UNIVERSITÀ DELLA CALABRIA
Dipartimento di Ingegneria Civile

Lorenzo Leonetti

Multiscale approaches for failure analyses of composite materials

Tesi di Dottorato in Ingegneria dei Materiali e delle Strutture
sezione: Scienza delle Costruzioni
Scuola Pitagora in Scienze Ingegneristiche
Ciclo XXVI (2010-2013)
S.S.D. ICAR 08

Coordinatore: prof. Renato S. Olivito

Tutor: prof. Fabrizio Greco




UNIVERSITÀ DELLA CALABRIA

La presente tesi è cofinanziata con il sostegno della Commissione Europea, Fondo Sociale Europeo e della Regione Calabria. L'autore è il solo responsabile di questa tesi e la Commissione Europea e la Regione Calabria declinano ogni responsabilità sull'uso che potrà essere fatto delle informazioni in essa contenute.

Lorenzo Leonetti

Abstract

Fiber-reinforced composite materials are being increasingly adopted in place of metallic elements in many structural applications of civil, automotive and aeronautical engineering, owing to their high stiffness-to-weight and strength-to-weight ratios, resistance to environmental deterioration and ability to form complex shapes.

However, in many practical situations, composite materials experience different kinds of failure during their manufacturing processes and/or in-services, especially for laminate configurations, where damage phenomena are rather complex, involving both intralaminar mechanisms (e.g. matrix cracking, fiber splitting and interface debonding between fiber and matrix) and interlaminar mechanisms (e.g. delamination between plies).

These damage mechanisms, which take place at the microscopic scale in conjunction with eventual contact interaction between crack faces, strongly influence the macroscopic structural behavior of composites, leading to a highly nonlinear post-peak response associated with a gradual loss of stiffness prior to failure. As a consequence, a proper failure analysis of a composite material subjected to such microstructural evolution should require a numerical model able to completely describe all its microscopic details; however fully microscopic models are not pursued in practice due to their large computational cost.

To overcome this problem, homogenization techniques have increasingly gained in importance, based on either classical micromechanical or periodic homogenization approaches; if combined each other, these models are able to

deal with both periodic and nonperiodic (e.g. random) composite microstructures. According to these approaches, also referred to as sequential multiscale methods, a "one-way" bottom-up coupling is established between the microscopic and macroscopic problems. As a consequence, such methods are efficient in determining the macroscopic behavior of composites in terms of stiffness and strength, but have a limited predictive capability for problems involving damage phenomena. To overcome these limitations, two classes of multiscale methods have been proposed in the literature: computational homogenization schemes and concurrent multilevel approaches.

Computational homogenization approaches, also referred to as semiconcurrent approaches, are very efficient in many practical cases, also for only locally periodic composites, especially when implemented in a finite element setting, as in the FE^2 method. The key idea of such approaches is to associate a microscopic boundary value problem with each integration point of the macroscopic boundary value problem, after discretizing the underlying microstructure. The macrostrain provides the boundary data for each microscopic problem (*macro-to-micro transition* or *localization* step). The set of all microscale problems is then solved and the results are passed back to the macroscopic problem in terms of overall stress field and tangent operator (*micro-to-macro transition* or *homogenization* step). Localization and homogenization steps are carried out within an incremental-iterative nested solution scheme, thus the two-scale coupling remains of a weak type.

On the other hand, concurrent multiscale methods abandon the concept of scale transition in favor of the concept of scale embedding, according to which models at different scales coexist in adjacent regions of the domain. Such methods can be regarded as falling within the class of domain decomposition methods, since the numerical model describing the composite structure is decomposed into fine- and coarse-scale submodels, which are simultaneously solved, thus establishing a strong "two-way" coupling between different resolutions.

The present thesis aims to develop a novel multiscale computational strategy for performing complete failure analyses of composite materials starting

from crack initiation events, which usually occur at the microscopic level, up to the formation of macroscopic cracks, subjected to propagation and coalescence phenomena. To this end, two alternative models have been proposed, belonging to the classes of semiconcurrent and concurrent multiscale models, respectively.

Firstly, a novel computational homogenization scheme is described, able to perform macroscopic failure analyses of fiber-reinforced composites incorporating the microstructural evolution effects due to crack initiation and subsequent crack propagation process. A two-scale approach is used, in which coupling between the two scales is obtained by using a unit cell model with evolving microstructure due to mixed-mode crack initiation and propagation at fiber/matrix interface. The method allows local failure quantities (fiber/matrix interfacial stresses, energy release and mode mixity for an interface crack) to be accurately obtained in an arbitrary cell from the results of the macroscale analysis, and, consequently, crack initiation and propagation at fiber/matrix interface to be predicted. Crack initiation at fiber/matrix interface is simulated by using a coupled stress and energy failure criterion, whereas crack propagation is analyzed by means of a mode mixity dependent fracture criterion taking advantage of a generalization of the *J*-integral technique in conjunction with a component separation method for computing energy release rate and mode mixity. The evolving homogenized constitutive response of the composite solid is determined in the context of deformation-driven microstructures, based on the crack length control scheme able to deal with unstable branches of the equilibrium path, such as snap-back and snap-through events; moreover, the micro-to-macro transition is performed by adopting periodic boundary conditions, based on the assumed local periodicity of the composite.

The second approach proposed in this thesis consists in a novel concurrent multiscale model able to perform complete failure analyses of fiber-reinforced composite materials, by using a non-overlapping domain decomposition method in a finite element tearing and interconnecting (FETI) framework in combination with an adaptive strategy able to continuously update the fine-scale subdomain around a propagating macroscopic crack. The continuity at

the micro-macro interface, characterized by nonmatching meshes, is enforced by means of Lagrange multipliers. When modeling fracture phenomena in composites, the competition between fiber/matrix interface debonding and kinking phenomena from and towards the matrix is accounted for, whereas continuous matrix cracking is described by using a shape optimization strategy, based on a novel moving mesh approach. A key point of the proposed approach is adaptivity, introduced into the numerical model by a heuristic zoom-in criterion, allowing to push the micro-macro interface far enough to avoid the strong influence of spurious effects due to interface nonmatching meshes on the structural response. It is worth noting that this heuristic zoom-in criterion is uniquely based on geometric considerations.

Numerical calculations have been performed by using both the proposed approaches, with reference to complete failure analyses of fiber-reinforced composite structures subjected to different global boundary conditions, involving both uniform and non-uniform macroscopic gradients. The validity of the proposed multiscale models has been assessed by comparing such numerical results with those obtained by means of a direct numerical simulation, considered as a reference solution. Numerical results have shown a good accuracy, especially for the proposed concurrent multiscale approach; moreover, this model has been proved to be more suitable for handling problems involving damage percolation in large composite structures and, at the same time, managing boundary layer effects.

Sommario

I materiali compositi fibrorinforzati sono sempre più impiegati in svariate applicazioni strutturali dell'ingegneria civile, meccanica ed aeronautica, in virtù delle loro notevoli caratteristiche meccaniche (elevati valori di rigidezza e resistenza, peso ridotto, resistenza ai fattori ambientali e versatilità di impiego).

In pratica, tuttavia, i materiali compositi sono soggetti a diversi tipi di danneggiamento durante le operazioni di produzione e/o in esercizio, in particolare nel caso dei laminati, caratterizzati da complessi meccanismi sia di tipo intralaminare (fessurazione della matrice, rottura delle fibre, *debonding* fibra/matrice) che di tipo interlaminare (delaminazione tra differenti strati).

Tali meccanismi di danno, che avvengono a livello microscopico e sono spesso accompagnati da fenomeni di contatto tra le facce delle fessure (*crack*), influenzano il comportamento macroscopico del composito, che è quindi caratterizzato da una risposta strutturale fortemente non-lineare cui corrisponde una riduzione di rigidezza prima di un eventuale completo collasso. Pertanto, al fine di simulare correttamente i diversi meccanismi di danneggiamento e le loro mutue interazioni, sarebbe opportuno costruire un modello meccanico in grado di riprodurre tutti i dettagli della microstruttura; ovviamente un siffatto modello si configura come non realizzabile nella pratica corrente, a causa dell'elevato onere computazionale richiesto.

Al fine di risolvere tale problema, sono stati proposti diversi metodi basati sulle ormai ampiamente utilizzate tecniche di omogeneizzazione; tali ap-

procci, che si basano su concetti di micromeccanica e/o su metodi di perturbazione multi-scala, consentono di studiare il comportamento globale di microstrutture periodiche e non, senza modellarne esplicitamente tutti i dettagli; tali metodi, se applicati in maniera sequenziale, consentono di stabilire un accoppiamento debole "a senso unico" tra la scala macroscopica e quella microscopica. Di conseguenza, tali metodi sono ampiamente usati per determinare le proprietà globali in termini di rigidezza e resistenza, ma possiedono una limitata capacità predittiva nel caso di problemi che interessano fenomeni di danneggiamento. Al fine di superare tali limitazioni, due nuove classi di metodi multi-scala vengono impiegate con sempre maggiore interesse nella comunità scientifica per studiare i fenomeni non-lineari nei materiali compositi e nei mezzi eterogenei in generale: gli schemi di omogeneizzazione computazionale e gli approcci multi-scala cosiddetti "concorrenti" (*concurrent* nella letteratura anglosassone).

I primi, chiamati anche approcci di tipo "semiconcurrent", sono molto efficaci se utilizzati in sinergia con il metodo degli elementi finiti; l'idea che sta alla base di tali metodi consiste nell'associare un problema al contorno microscopico ad ogni punto di integrazione del problema al contorno macroscopico discretizzato con una mesh rada. La macro-deformazione fornisce i dati necessari per applicare le condizioni al contorno per ogni problema microscopico; in questa prima fase (detta di *localizzazione*), viene stabilita una transizione tra le scale, da quella macroscopica verso quella microscopica. In seguito, i problemi microscopici vengono risolti in maniera completamente disaccoppiata, e le relative informazioni vengono trasferite alla macro-scala in termini di macro-tensione ed operatore tangente; questa fase è quella che viene usualmente denominata *omogeneizzazione* in senso stretto.

Al contrario, i metodi multi-scala concorrenti abbandonano il concetto di transizione di scala per accogliere quello di incorporamento di risoluzioni differenti nel medesimo modello numerico (*scale embedding*). Tali approcci ricadono nell'ampia classe dei metodi di decomposizione del dominio, caratterizzati dalla risoluzione simultanea di problemi descritti a differenti risoluzioni, che risultano, così, fortemente accoppiati.

Nel presente lavoro di tesi sono stati investigati differenti approcci multi-scala volti a condurre analisi al collasso di materiali compositi, partendo dall'innesco di microfratture fino alla formazione di crack macroscopici, soggetti ai fenomeni di propagazione e coalescenza. A tal fine, sono stati proposti due modelli alternativi, appartenenti alle due suddette classi di metodi multi-scala.

Il primo modello proposto consiste in uno schema di omogeneizzazione computazionale in grado di effettuare analisi a collasso macroscopiche di compositi fibrorinforzati con microstruttura in evoluzione per innesco e propagazione di microfratture; in particolare, è stato adoperato un approccio a due scale, in cui l'accoppiamento tra le suddette scale è ottenuto mediante l'introduzione di un modello di cella unitaria (*unit cell*) soggetta a fenomeni di innesco e propagazione di fratture all'interfaccia caricate in modo misto. Il metodo proposto consente di determinare le quantità che descrivono il danneggiamento a livello locale (tensioni all'interfaccia fibra/matrice, energia di rilascio ed angolo di modo misto per un crack all'interfaccia) per una cella unitaria arbitraria, a partire dai risultati di un'analisi macroscopica; in questo modo, è possibile simulare numericamente il comportamento non-lineare del composito. Nel dettaglio, l'innesco di una frattura all'interfaccia è descritto impiegando un criterio ibrido tensionale ed energetico, mentre la sua successiva propagazione è guidata da un criterio puramente energetico, che incorpora gli effetti di modo misto sulla tenacità dell'interfaccia; l'energia di rilascio ed i relativi fattori di intensificazione degli sforzi sono stati calcolati utilizzando una generalizzazione dell'integrale *J* per i mezzi eterogenei, in sinergia con una tecnica di estrazione dei contributi di modo I e II. La risposta strutturale omogeneizzata è numericamente guidata da un algoritmo di tipo *path-following* basato sulla lunghezza totale del crack (*crack length control scheme*); tale strategia consente di seguire percorsi di equilibrio instabile nell'ipotesi di caricamento quasi-statico. Inoltre, la transizione micro-macro su cui si basa l'intero metodo multi-scala è condotta imponendo condizioni al contorno periodiche per il problema microscopico, assumendo implicitamente una periodicità locale del composito.

Il secondo modello proposto consiste in un metodo multi-scala concorrente in grado di effettuare analisi al collasso di compositi fibrorinforzati, fino a completa separazione, coincidente con la totale perdita di capacità portante; tale metodo si basa su un approccio FETI (Finite Element Tearing and Interconnecting) inquadrabile all'interno dei metodi di decomposizione del dominio di tipo *non-overlapping*. I principali ingredienti del metodo sono: l'utilizzo della tecnica dei moltiplicatori di Lagrange per imporre la condizione di continuità tra mesh non combacianti, relative ai sottodomini discretizzati a scale differenti; lo studio della competizione tra debonding all'interfaccia fibra/matrice e diramazione nella matrice; l'impiego di mesh mobili per imporre il criterio della massima energia di rilascio come un problema di ottimizzazione strutturale; l'introduzione di un criterio di zoom adattivo di tipo euristico, basato su considerazioni puramente geometriche, in grado di incorporare il modello microscopico solo nelle regioni del modello macroscopico interessate da fenomeni di danneggiamento, assegnando, invece, una descrizione macroscopica alle regioni sufficientemente lontane dai crack.

Un'adeguata sperimentazione numerica è stata condotta per entrambi i metodi proposti, con riferimento ad analisi al collasso di strutture composite fibrorinforzate soggette a svariate condizioni di carico, in grado di generare gradienti macroscopici uniformi e non; tali risultati, in termini di risposta strutturale globale, sono stati opportunamente validati effettuando confronti con simulazioni numeriche dirette, in cui la microstruttura del composito è stata esplicitamente simulata e presa in considerazione come modello di riferimento. I risultati numerici hanno mostrato l'accuratezza dei metodi proposti nel valutare la risposta strutturale fortemente non-lineare dei compositi, evidenziando, altresì, la maggiore versatilità del modello di tipo *concurrent* nel risolvere problemi caratterizzati da percolazione del danno dovuta alla coalescenza dei microcrack, e soggetti agli effetti di bordo, che usualmente influenzano la configurazione dei crack all'innesco e nelle prima fasi di propagazione del danno.

Contents

Introduction

1 Literature review

In the last two decades fiber-reinforced composite structures have been used more extensively in many civil, mechanical, naval and aerospace applications, essentially due to their high stiffness-to-weight and strength-to-weight ratios and the possibility to induce anisotropy in their overall mechanical properties by varying fiber orientation and fiber volume fraction. In civil engineering, fiber-reinforced plastics (FRP) have been employed to rehabilitate and retrofit reinforced concrete structures, as well as masonry and steel structures, by virtue of their attractive properties in terms of mechanical strength and durability to environmental exposure conditions (see, for instance, [1-7]).

Despite their excellent characteristics, composite materials suffer from a number of shortcomings, such as brittleness, high thermal and residual stresses, low interfacial bonding strength and toughness, which may induce the process of unstable cracking under different loading conditions, due to the

presence of imperfection in material strength, fatigue, yielding and production defects. These failures can cause extensive damage accompanied by a significant reduction in stiffness and load-carrying capacity, decreased ductility and the possibility of abrupt collapse mechanisms.

Moreover, composite materials are employed in thin shape configurations which are susceptible to various types of defects; indeed, in many practical situations, cracking can initiate and propagate during manufacturing processes and/or in-services, especially for laminate configurations, for which damage phenomena are rather complex, involving both intralaminar mechanisms (e.g. matrix cracking, fiber splitting and interface debonding between fiber and matrix) and interlaminar mechanisms (e.g. delamination between plies).

These damage mechanisms, together with eventual contact interaction between crack faces, which strongly influence the macroscopic structural behavior of composites, and lead to the highly nonlinear post-peak response associated to a gradual loss of stiffness prior to failure, take place at the microscopic scale. As a consequence, a proper failure analysis of a composite material subjected to such microstructural evolution should require a numerical model able to completely describe all its microscopic details; however fully microscopic models are not pursued in practice due to the large computational cost, and direct numerical simulations usually refer to a limited portion of the structural sample, regarded as a critical “hotspot” towards damage and fracture phenomena. Most of the studies based on direct approaches are carried out by using various numerical methods (standard finite element method, boundary element method, extended finite element method, Voronoi cell finite element method, cohesive/volumetric finite element method, discrete element method) dealing with a microscopic description of damage initiation and/or propagation (see, for instance, [8-13]).

On the other hand, simplified models are often used to predict failure in composite materials with satisfactory accuracy, without requiring the explicit modeling of the given microstructure. The aim of these models, belonging to

the wide class of continuum damage models, is to provide macroscopic non-linear constitutive laws developed within a rigorous framework by means of the formalism of the thermodynamics of irreversible processes.

The simplest way to describe damage is to use a scalar damage variable, as proposed by Kachanov [14]; such a representation, in which the damage variable is essentially interpreted as a measure of the effective surface density of the microcavities, is not able to model the directionality of microcracks. On the other hand, the more general tensorial representation of damage seems to be more suitable when handling crack propagation in heterogeneous media, since microcracks usually propagate in different directions depending on the load history, geometry, boundary conditions, and material properties. Several damage models have been proposed, describing damage by means of a second-order or a fourth-order tensor (see, for instance, [15] and [16], respectively).

The application of continuum damage models to fiber-reinforced composite materials leads to additional difficulties due to their anisotropic behavior; indeed crack orientations are not only induced by the loads, geometry and boundary conditions, but also by the material morphology. Furthermore the presence of fiber/matrix interfaces weaker than the surrounding materials induces interfacial debonding, which causes some preferred patterns in the crack path.

Two main approaches have been extensively used to define damage models for composite materials, i.e. mesoscopic models and homogenization models. Mesoscopic models treat the composite lamina or sub-laminate as a homogeneous material (see, for instance, [17] and [18]). They are suitable for large scale computation, especially when diffuse damage localizes in narrow bands leading to the nucleation of macrocracks. In most cases, however, failure mechanisms in composites are intrinsically interrelated with their microscopic inhomogeneity, and thus the application of macroscopic fracture criteria may result in an unrealistic estimation of crack trajectories and load-carrying capacity. On the other hand, homogenization models aim to predict the overall mechanical response of composites on the basis of the properties of

the different individual constituents at the microscopic level, by establishing relationships between the microstress and microstrain fields and the corresponding macrovariables.

Homogenization models have increasingly gained in importance due to their better flexibility and accuracy with respect to mesoscopic models. Strictly speaking, homogenization denotes the mathematical techniques for the asymptotic analysis of physical media with periodic microstructure, developed my many authors (see, for instance, [19] and [20]). In this framework, the macroscopic domain is supposed to be entirely occupied by the spatial repetition of a unit cell, which plays the same role of the representative volume element (RVE) usually adopted in micromechanical approaches [21]. In classical homogenization schemes, also referred to as first-order schemes, however, the large spatial gradients in macroscopic fields cannot be resolved due to supposed validity of the principle of scale separation, therefore they are not suited for studying strain localization phenomena which commonly affect the macroscopic behavior of composites; moreover softening behaviors cannot be properly analyzed because of the mesh dependence at the macroscopic scale due to the ill-posedness of the macroscopic boundary value problem, as shown in [22].

In order to partially overcome such limitations, other homogenization paradigms have been proposed in the literature, such as the higher-order homogenization and the continuous-discontinuous homogenization schemes. The first one has been adopted in [23, 24] for transferring higher-order kinematics from the microscale to the macroscale, by incorporating a length scale defined by the RVE size into the model; it can handle moderate localization bands, but cannot be used for a complete softening analysis. The latter one essentially relies on the proper incorporation of a localization band at the macroscopic scale and it has been adopted by many authors (see, for instance, the approaches proposed in [25] and [26]).

Both continuous and continuous-discontinuous homogenization paradigms are usually adopted within the more general framework of multiscale methods. Following Belytschko and Song [27], such methods can be classified

in three main groups depending on the type of coupling between the microscale and macroscale problems: hierarchical (or sequential), semiconcurrent and concurrent methods.

In hierarchical methods, the following steps have to be performed: (i) identification of a representative volume element (RVE), whose individual constituents are assumed to be completely known, with their constitutive properties; (ii) formulation of the microscopic boundary conditions to be applied to the RVE; (iii) computation of the output macrovariables from the results of the microscopic boundary value problem associated with the RVE (*micro-to-macro transition* or *homogenization*); (iv) determination of the numerical constitutive laws, relating each other the input and output macrovariables. Since during the micro-to-macro transition step the information is passed from lower to higher scales, a "one-way" bottom-up coupling is established between the microscopic and macroscopic problems. As a consequence, such methods are efficient in determining the macroscopic behavior of composites in terms of stiffness and strength, but have a limited predictive capability for problems involving the above-mentioned damage phenomena (see, for instance, [28]).

When dealing with microscopic nonlinear phenomena due to evolving defects whose spatial configuration is not known a priori, however, a two-way coupling between micro- and macrovariables is required, i.e. the homogenized properties have to be computed "on the fly" during the microstructural evolution due to damage phenomena. Semiconcurrent methods, also referred to as computational homogenization approaches, especially when implemented in a finite element setting, as in the FE^2 method [29], have been proved to be very efficient in such cases, also for only locally periodic composites. The key idea of such approaches is to associate a microscopic boundary value problem with each integration point of the macroscopic boundary value problem, after discretizing the underlying microstructure. The macroscopic strain provides the boundary data for each microscopic problem (*macro-to-micro transition* or *localization* step). The set of all microscale problems is then solved and the results are passed back to the macroscopic problem in terms of overall stress field and tangent operator (*micro-to-macro transition* or *homogenization*

step). Localization and homogenization steps are carried out within an incremental-iterative nested solution scheme, thus the two-scale coupling remains of a weak type.

Other similar approaches have been proposed, in which an RVE is attached to every macroelement of the coarse problem rather than to each Gauss point (see, for instance, [30] and [31]); these approaches allows to overcome the dependence of the macroscopic problem solution on the coarse mesh size in the case of overall mechanical behaviors exhibiting softening.

Concurrent multiscale methods abandon the concept of scale transition in favor of the concept of scale embedding, according to which models at different scales coexist in adjacent regions of the domain. Such methods can be regarded as falling within the class of domain decomposition methods, since the numerical model describing the composite structure is decomposed into fine- and coarse-scale submodels, which are simultaneously solved, thus establishing a strong "two-way" coupling between different resolutions. Most of concurrent multiscale methods can be classified in overlapping and non-overlapping methods (see, for instance, [32] and [33], respectively). Overlapping methods seem to be more suitable for coupling continuum and discrete models, as in MAAD approach [34], whereas non-overlapping methods are preferred when dealing with pure continuum models. Concurrent schemes are more suitable than the previously described approaches for tackling damage percolation at the macroscale.

A number of concurrent approaches have been proposed in the literature, able to deal with failure analyses of heterogeneous materials, taking advantage of an adaptive framework for triggering the zoom-in procedure in an optimal manner (see, for instance, [35-38]).

Alternative multiscale approaches, which fall in the range between hierarchical methods and the more advanced concurrent and computational homogenization techniques, have been proposed in the literature. For instance, a variational multiscale approach able to predict failure in fiber reinforced composite by cohesive crack propagation has been proposed in [39], whereas a multiscale eigenelement method for the analysis of periodical composite

structures has been introduced in [40]. Moreover, the progressive failure process for composite laminates has been studied in [41] by using a multiscale nonlinear modeling technique incorporating a micromechanical elastic-plastic bridging constitutive model.

2 Motivation and objectives of the thesis

From the micromechanical point of view, the computational homogenization approach must take into account that microscopic damage phenomena, such as void growth, micro-cracking and interfacial debonding often involving contact interaction between crack faces, greatly influence the macroscopic response of the heterogeneous material. In fact, even if the constitutive response of each individual phase is assumed to be linearly elastic, the evolution of the microstructural configuration due to damage evolution and contact mechanisms produces a strongly nonlinear constitutive behavior at the macroscopic level [42-44]. Moreover, in the case of long fiber-reinforced laminates it is essential to perform a microscopic interlaminar analysis using a homogenization approach taking into account that laminae are heterogeneous materials, since microscopic failures, such as matrix cracking and delamination, often occur at the interfaces between the laminae and may lead to the macroscopic failure of laminates (see [45, 46]).

Additional nonlinearities in the macroscopic material response of a heterogeneous material arise due to crack initiation process. Typically, in a multiphase material such as fiber-reinforced composites, crack initiation may occur at originally undamaged interfaces between different phases or within a homogeneous constituent, usually the weak and soft one. The former kind of failure initiation is usually favored over the latter, since usually typically stress concentrations occur at inclusion/matrix interfaces, especially when a stiff inclusion (fiber) is embedded in a softer matrix. On the other hand, matrix cracking is a typical example of the latter kind of failure initiation mode. The coalescence of these microcracks leads to the formation of macrocracks in the material and may produce a catastrophic collapse of the heterogeneous solid. Crack initiation analysis can be developed by using the coupled stress-energy

approach originally introduced in [47] and subsequently extended in [48, 49] in order to study fracture onset in proximity of singularities and stress concentrations.

Another issue in failure analysis of composite materials is to determine the residual strength at a given strain level; this often requires tracing the whole equilibrium path, if computations are carried out in a quasistatic setting. The well-known arc-length method [50], which represents the standard method for dealing with geometrical nonlinearities in solid mechanics, is not suitable for studying structural problems involving material instabilities due to strain localization, and therefore other methods have been proposed, such as the crack mouth opening control scheme [51], the total strain control scheme [52], and the dissipation based arc-length method [53].

The present thesis aims to develop a multiscale computational strategy for performing complete failure analyses of composite materials starting from crack initiation events, which usually occur at the microscopic level, up to the formation of macroscopic cracks, subjected to propagation and coalescence phenomena. To this end, two alternative models have been proposed, belonging to the classes of semiconcurrent and concurrent multiscale models, respectively.

In the first part of this thesis, a novel computational homogenization scheme is described, able to perform macroscopic failure analyses of fiber-reinforced composites incorporating the microstructural evolution effects due to crack initiation and subsequent crack propagation processes. A two-scale approach is used, in which coupling between the two scales is obtained by using a unit cell model with evolving microstructure due to mixed-mode crack initiation and propagation at fiber/matrix interface. This method allows local failure quantities (fiber/matrix interfacial stresses, energy release and mode mixity for an interface crack) to be obtained accurately in an arbitrary cell from results of the macroscale analysis, and, consequently, crack initiation and propagation at fiber/matrix interface to be predicted. Crack initiation is studied by generalizing the coupled stress and energy failure criterion to the case of mixed-mode interfacial fracture, whereas crack propagation is analyzed by

means of a mode mixity-dependent fracture criterion taking advantage of a generalization of the *J*-integral technique [54] in conjunction with the component separation method, introduced in [55] to compute energy release rate and mode mixity. The evolving homogenized constitutive response of the composite solid is determined in the context of deformation-driven microstructures, based on the *crack length control scheme* proposed in [56], and the micro-to-macro transition is performed by adopting periodic boundary conditions, based on the assumed local periodicity of the composite. This methodology is implemented for two-dimensional composite structures by using a finite element formulation incorporating a novel strategy for automatic simulation of arbitrary crack initiation. The effectiveness of the proposed approach is then investigated by means of numerical macroscopic failure analyses of matrix/fiber composite structures. The accuracy is evaluated by means of comparisons with direct numerical simulations adopting a fine-scale modeling of the composite structure.

In the second part of this thesis, a novel concurrent multiscale model able to perform complete failure analyses of fiber-reinforced composite materials is presented, by using a non-overlapping domain decomposition method in a finite element tearing and interconnecting (FETI) framework [33, 57] in conjunction with an adaptive strategy able to continuously update the fine-scale subdomain around a propagating macroscopic crack. The continuity at the micro-macro interface, characterized by nonmatching meshes, is enforced in a weak form; different choices for the associated Lagrange multipliers lead to different types of micro-macro connection; in this thesis, both collocation and mortar methods have been considered. When modeling fracture phenomena in composites, the competition between fiber/matrix interface debonding and kinking phenomena from and towards the matrix is accounted for, whereas the continuous matrix cracking is described by using a novel shape optimization strategy, based on a moving mesh approach inspired by similar existing methodologies (see, for instance, [58] and [59]). Adaptivity is considered to be a necessary ingredient of the proposed technique, in order to obtain the accuracy of a fully microscopic model and the efficiency of a coarsely meshed model

at the same time; indeed the crack path is not known a priori, thus the zone of interest, for which a microscopic resolution is needed, has to be continuously updated following the propagating crack tip. This strategy, which falls into the wide class of *adaptive model refinement* techniques [60], shares some similarities with the classical *adaptive mesh refinement* strategies, but it is more efficient when dealing with highly heterogeneous solids. The main aspect of this strategy is to push the interface far enough to avoid the strong influence of spurious effects due to interface nonmatching meshes on the structural response. It is worth noting that this heuristic zoom-in criterion is uniquely based on geometric considerations, even if more sophisticated approaches are already existent in the literature (see, for instance, [61]), involving indicators for strain localization and loss of periodicity. The effectiveness of the proposed approach is then investigated by performing complete macroscopic failure analyses of matrix/fiber composite structures in the presence of an initial macrocrack, and the accuracy is evaluated by means of comparisons with direct numerical simulations adopting fully-meshed models.

3 Outline of the thesis

In Chapter 1 an introduction about the main damage mechanisms in composite materials is given, with a particular attention devoted to their numerical modeling at different scales; in detail, an overview of existing computational methods to model fracture and damage in brittle and quasibrittle composite materials is given for both intralaminar and interlaminar mechanisms. Since usually at least two scales are involved when studying such problems, the chapter focuses on the distinction between macroscopic and microscopic damage models. Classical homogenization techniques and multiscale methods are presented as effective tools to build *microscopically informed* constitutive laws for composites, able to deal with the interaction between different damage mechanisms, which cannot be analyzed by using a single-scale model.

Chapter 2 is devoted to a review of multiscale approaches for composite materials with evolving microstructure. In the first part, the main classical ho-

mogenization techniques are presented; two basic approaches for homogenization are discussed: the *average field theory*, in which the effective mechanical properties are determined as relations between the averaged microfields, and the *asymptotic homogenization theory*, in which the effective properties emerge as relations between microfields and macrofields naturally derived from a multiscale perturbation method applied to periodic structures. These two approaches, based on micromechanical and mathematical concepts, respectively, can be combined to derive a hybrid theory susceptible to be applied to a more general class of materials, including those exhibiting periodic, locally periodic, nonperiodic and random microstructures. In the latter part of the chapter, a review of existing multiscale methods is given, following a classification based on the type of coupling between the microscopic and the macroscopic levels.

In Chapter 3 the proposed computational homogenization approach is presented, addressed to the failure analysis of locally periodic fiber-reinforced composite materials, and taking into account microcrack initiation and propagation in the same numerical model. In the first part of this chapter the numerical techniques employed to perform homogenization/localization steps as well as to simulate crack initiation and propagation in bimaterial systems are described in detail. The latter part is devoted to the numerical simulation performed in order to investigate the capability of the proposed model in predicting failure mechanisms in composites, related to microcrack initiation and propagation phenomena; the obtained numerical results refer to the nonlinear mechanical response of 2D periodic fiber-reinforced composite structures subjected to transverse loading.

In Chapter 4, the proposed multiscale model able to perform complete failure analyses of fiber-reinforced composite materials is presented. In the first part of this chapter, a discussion about the theoretical framework is given, with particular attention devoted to the description of non-overlapping domain decomposition methods in a finite element tearing and interconnecting (FETI) framework as well as of the moving mesh approach employed to simulate

crack propagation along a path not known *a priori*. In the second part, a detailed description of the proposed multiscale approach is provided, in which the employed adaptive framework is highlighted, together with its implementation details within a commercial finite element simulation code. Finally, the third part presents some numerical results obtained via the proposed method and their validation by means of comparisons with direct numerical simulations.

This thesis ends with Chapter 5, which summarizes the main finding of this work and discusses the comparisons between the two proposed approaches; finally some concluding remarks are given, together with some future perspectives of this work.

1

Damage and fracture processes in composite materials: concepts and modeling techniques

Composite materials are widely used in many structural applications because of their attractive properties, such as high strength-to-weight and stiffness-to-weight ratios, resistance to environmental deterioration and ability to form complex shapes. However, composite material experience different kinds of damage and fracture phenomena due to the presence of manufacturing-induced microscopic defects. In order to investigate the load-carrying capacity of composites, it is therefore necessary to properly model the development of damage. This chapter will be devoted to the description of the main damage mechanisms in composites, and their modeling at different scales.

In Section 1.1 the main features of composite materials are recalled, with particular attention to polymer matrix composites reinforced with long fibers, usually denoted as *fiber-reinforced polymers* (or FRPs in short); Section 1.2 presents a description of the different damage mechanisms which usually affect the overall behavior of such materials; Sections 1.3 and 1.4 present a review of the main modeling approaches for describing damage in composite materials at the macroscale and microscale, respectively; finally, in Section 1.5, an introduction to multiscale approaches is given, in which the need for coupling different length scales is highlighted.

1.1 Definition and characteristics of composite materials

Composite materials (or shortened to *composites*), are systems consisting of two or more component materials (*phases*) with significantly different physical and/or chemical properties and distinguishable interfaces between them. In most composite materials, one phase is usually continuous and is called *matrix*, whereas the other phases are usually discontinuous and are called *inclusions*; since the latter are generally stiffer and stronger than the matrix, they are referred to as *reinforcement*. Sometimes, an additional phase, called *interphase*, exists between the matrix and the inclusions, essentially due to the chemical interactions which take place between them.

Matrix and reinforcement play different roles depending on the type of composite materials. In the case of high-performance structural composites, a continuous-fiber reinforcement is adopted, thus determining their strength and stiffness in the direction of the fibers; therefore, the main roles of the matrix phase are to provide protection for the fibers and to transfer local stresses from one fiber to another. On the other hand, in the case of medium-performance composites, the reinforcement, commonly made of short fibers or particles, provides only local strengthening and minimal changes in stiffness; as a consequence, the matrix governs the overall mechanical properties of the composite material.

Many classification systems are available for composites, based on the matrix and fiber materials, the type of the reinforcement, the manufacturing processes, the structural configuration, and so on; comprehensive lists of composites and their physical properties can be found in specialized publications [6, 62], technical standards (see [63] for Italian standards), and material science books and handbooks, e.g. [64]. Although the matrix can be made of different materials (including plastics, metals, or ceramics), the present work is entirely devoted to polymer matrix composites (PMCs).

The matrices commonly used in PMCs can be either thermosets or thermoplastics. Upon curing, thermosets (polyester, vinyl ester, epoxy, phenolic, etc.) form a highly cross-linked three-dimensional molecular network, exhibiting good resistance to high temperatures; moreover, they are characterized by low viscosity, allowing an excellent impregnation of the fiber reinforcement and high processing speeds; the counterpart in using this kind of matrices is that too high temperatures (about 175°C for epoxy resins) cause a degradation process due to the rupture of covalent bonds between polymeric chains. On the contrary, thermoplastic resins (PMMA, nylon, polyethylene, polypropylene, polycarbonate, etc.) can be reshaped as many times as necessary, due to the weakness of the bonds between polymeric chains (Van der Waals and hydrogen interactions), but have high viscosity at processing temperatures, which makes the impregnation of the fiber reinforcement more difficult. As a consequence, thermosets (especially epoxies and polyesters) have been the principal polymer matrix materials for several decades; however, advanced thermoplastics like polyetheretherketone (PEEK) and polyphenylene sulfide (PPS) are now receiving considerable attention for their excellent toughness and low moisture absorption properties, their recyclability and their resistance to higher temperatures (up to 250°C for PEEK matrices).

With regard to the reinforcement, long fiber (or *continuous* fiber) configuration is preferred because most materials are much stronger and stiffer in fiber form than in bulk form. As a general rule, the smaller the diameter of the fibers, the higher their strength: this is attributed to the sharp reduction in the

Table 1.1 Typical properties of the most common fibers for FRPs.

Fiber	Tensile strength [GPa]	Elongation [%]	Elastic modulus [GPa]	Poisson's ratio	Density [g/cm^3]
Glass fibers					
E-glass	3.45	4.4	72.4	0.22	2.50–2.59
S-glass	4.80	5.3	85.0	0.22	2.46–2.49
R-glass	4.40	5.2	86.0	0.15–0.26	2.55
C-glass	3.31	4.8	69.0	-	2.56
D-glass	2.50	4.7	55.0	-	2.14
Carbon fibers					
HT-S graphite	3.2	1.3	230	0.2	1.75
HM-S graphite	2.5	0.6	390	-	1.8
Polymeric fibers					
Kevlar 29	3.79	-	62.0	-	1.44
Kevlar 131	3.62	2.8	131	0.35	1.45
Kevlar 149	3.62	1.9	179	-	1.47

number and size of failure-inducing defects (usually surface defects, i.e. microcracks) during fabrication and handling, as conjectured by Griffith [65].

A large variety of fibers are available as reinforcement for composites; according to their chemical composition, they can be classified in organic and inorganic. The most common inorganic fibers are glass, carbon, boron, ceramic, mineral and metallic, whereas the organic fibers used in composites are polymeric fibers; Table 1.1 lists the typical properties of specific fibers, in terms of tensile strength, elongation, elastic modulus, Poisson's ratio, and density.

Glass, aramid and carbon fibers are the most commonly adopted in civil engineering, and the related composite systems are usually denoted by the acronyms GFRP, AFRP and CFRP, respectively. Glass fibers are used in low and medium performance composites because of their high tensile strength and low cost. They are limited in some practical applications due to their relatively low stiffness, low fatigue limit, and rapid degradation with exposure

to severe environmental conditions. Aramid (or Kevlar) fibers show higher stiffness and lower density, but are limited by very low compressive strength in the composite and high moisture absorption. Carbon (graphite) fibers cover a wide range of stiffness and strength values, depending on the processing temperatures. High strength and high stiffness carbon fibers (AS4, T300, C6000) are processed at temperatures between 1200°C and 1500°C. Ultrahigh stiffness graphite fibers (GY-70, Pitch) are processed at temperatures between 2000°C and 3000°C. The increase in stiffness is achieved at the expense of strength.

Since the fibers do not contribute to the strength in the transverse direction with respect to fibers, and the strength of the matrix is very low, continuous fiber composites are often made as laminate by stacking single sheets (*laminae*) of continuous fibers in different orientations to face all the applied loads with the desired strength and stiffness properties.

The nomenclature used for laminates is based on the specification of a standard lay-up sequence, also called *stacking sequence*; for regular laminates, i.e. laminates whose laminae have the same thickness, only the fiber orientations need to be specified. The standard stacking sequence lists orientation of the different plies, starting from the bottom of the laminate to the top, in a string separated by slashes. A laminate made of N laminae with different fiber orientations is represented as $\left[\theta_1/\theta_2/\cdots/\theta_N\right]$. The ith fiber orientation is considered to be positive if the angle θ_i is measured counterclockwise from the reference direction of the laminate; layers oriented at an angle different from 0° are referred to as *off-axis layers*.

If adjacent layers have the same orientation, they are usually grouped together, adding the total number of these layers to that particular orientation as a subscript; for instance, the sequences [0/0/0/90/90] and $[0_3/90_2]$ represent the same laminate. If a group of layers is repeated, then the number of repetitions is added as a subscript to the repeating group enclosed in parenthesis; for the laminate $[0_2/(0_2/45_2/90)_3/0_2]$, sandwiched between two layers of 0° on the bottom and two layers of 0° on the top, the group $0_2/45_2/90$ is repeated three times. Moreover, angle-ply combinations like $[\theta/-\theta]$ can be denoted by $[\pm\theta]$.

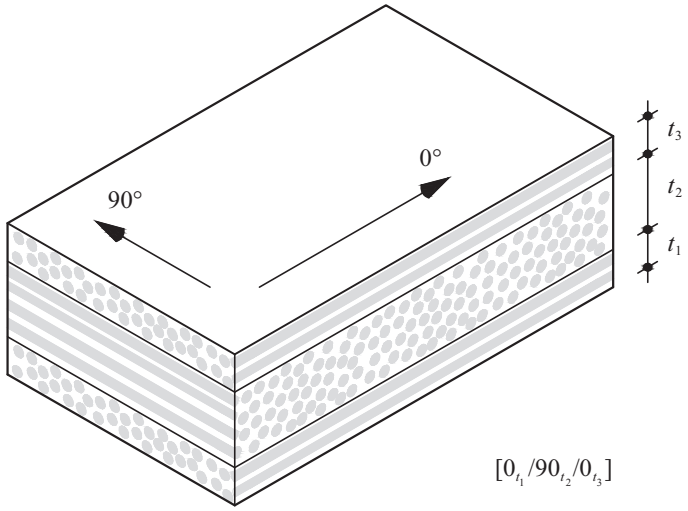

Fig. 1.1 Schematic representation of a cross-ply laminate.

A laminate is *symmetric* if the fiber orientations of its bottom half are mirror images of the fiber orientations above its mid-plane; in the case of symmetric laminates with an even number of layers, an abbreviated notation is used, which consists in giving only half of the stacking sequence and adding a subscript S; for example, the sequences [30/0/0/30] and $[30/0]_S$ represent the same laminate. On the other hand, in the case of symmetric laminates with an odd number of plies, the direction of the central ply is overlined, as shown in the following example: the laminate [0/0/90/0/0] is replaced by $[0_2/\overline{90}]_S$. Symmetric laminates deserve a special attention because their mechanical behavior is more desirable for practical applications.

A common type of laminate is the *cross-ply* laminate, whose laminae are oriented only at 0° and 90° (see Fig. 1.1). The main advantage of such laminates is simplicity of construction; in the case of symmetric staking sequence, the transverse deflection of a cross-ply laminate can be obtained treating such laminate as an orthotropic, homogenous plate. Moreover, symmetric cross-ply laminates do not experience coupling between shear and extension, nor do they have coupling between twisting and bending.

1.2 Damage mechanisms in fiber-reinforced composites

One of the most important factors affecting the load-carrying capacity of fiber-reinforced composite materials is the presence of internal defects (such as voids, microcracks, impurities and other structural imperfections), which can exist as initial defects (induced by manufacturing processes) and/or can initiate and propagate in response to the applied external loads.

In the case of monolithic materials normally exhibiting a brittle or quasi-brittle behavior, such as polymers, ceramics and glass, suitable failure analyses are usually performed by using fracture mechanics concepts; according to the classical energy-based criterion introduced by Griffith [65], failure problems for homogenous materials can be formulated in terms of fracture toughness, regarded as a measure of their resistance to a single crack growth.

In the case of composite materials, the damage process is, however, much more complex, due to the existence of at least two microconstituents with different mechanical properties in terms of strength and stiffness. The main feature of damage in composite materials, in contrast to monolithic materials, consists in the multiplicity of cracking in various shapes, sizes and orientations which depend not only on the material properties of the different phases, but also on their geometrical arrangement.

Since fiber-reinforced composite materials are usually made of different laminae bonded together, damage and fracture may occur in a variety of failure modes, which can be classified in *intralaminar* and *interlaminar* failure modes.

1.2.1 Intralaminar damage mechanisms

Intralaminar damage mechanisms refer to in-plane irreversible processes produced by the presence of distributed microcracks and voids inside each lamina. These mechanisms usually occur in the early stages of damage in composite materials, and are characterized by multiple cracking phenomena in a relevant portion of the ply. In the following a brief description of the most common intralaminar damage mechanisms is given.

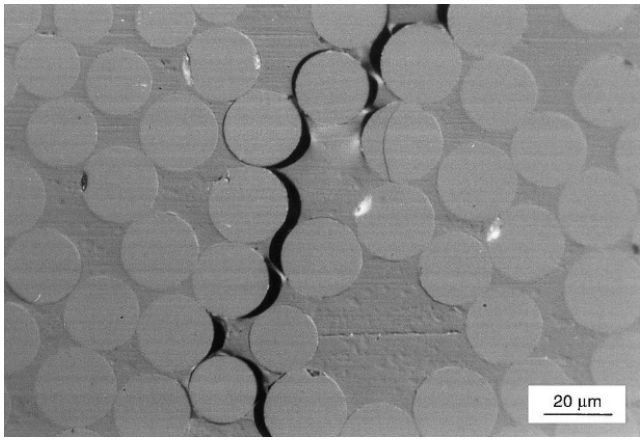

Fig. 1.2 Transverse crack at the macroscopic scale in a fiber-reinforced composite. Reprinted from [66].

Fiber/matrix interfacial debonding

One of the most important intralaminar mechanisms is the fiber/matrix *interfacial debonding*, because fibers, which are usually much stiffer than the surrounding matrix, usually act as stress concentrators. The interface plays a significant role in stress transfer between fiber and matrix; as a consequence, the performance of a fiber-reinforced composite is strongly influenced by the properties of the interfaces: if the fibers are weakly bonded to the matrix, debonding takes place at relatively low levels of the external load, leading to a diffuse transverse cracking before complete failure. On the other hand, in the case of strong fiber/matrix interface, transverse cracking is delayed and the composite experiences a catastrophic failure because of fiber fracture. Fig. 1.2 shows a transverse crack at the microscopic scale, originated by the coalescence of several interfacial cracks associated with debonding phenomena [66]. Several modeling approaches have been widely used to predict initiation and propagation of debonding, such as *shear lag* models [67], *linear elastic fracture mechanics* approaches [68], and *cohesive zone models* (CZM) [11].

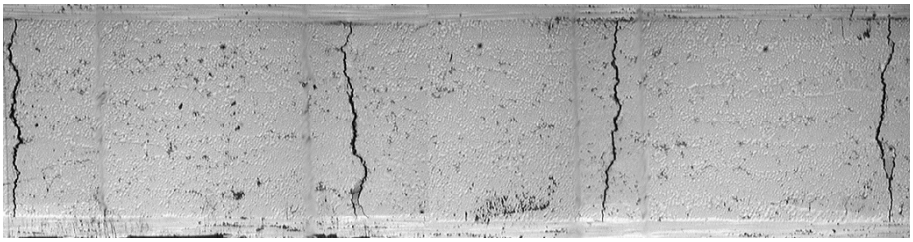

Fig. 1.3 Example of multiple matrix cracks observed in continuous fiber-reinforced laminates. Reprinted from [69].

Matrix microcracking

Matrix cracking is usually the first observed damage mechanism in fiber-reinforced composites. Indeed, in laminates with plies in different orientations, microscopic cracks can arise from defects in a given ply and grow traversing the thickness of the ply and running parallel to the fibers in that ply; such matrix cracks, also referred to as *transverse cracks* or *intralaminar cracks* are found to be caused by tensile loading, fatigue loading, as well as by thermal loading [69]. They can originate from debonded interfaces or manufacturing-induced defects such as voids and inclusions [70]. Two main different approaches can be found in the literature, able to predict formation and growth of matrix microcracking, inspired by finite fracture mechanics (FFM) [71] and continuum damage models (CDM) (see, for instance, [72]), respectively. Although matrix cracking does not lead directly to structural failure, it can result in significant degradation in material stiffness and can also induce more important damage mechanisms, such as delamination and fiber breakage, and give pathways for entry of fluids. Fig. 1.3 shows matrix cracks observed on the free edges of continuous fiber laminates induced by fatigue loads.

Fiber breakage

The complete failure of a fiber-reinforced composite subjected to a tensile loading in the fiber direction arises from breakage of fibers; the individual

fibers fail at their weak points and a stress redistribution occurs, affecting other fibers in the neighborhood of the broken fibers and possibly breaking some. The statistical character of fiber breakage process is essentially due to the nonuniformity of fiber strength along the fiber and the stress redistribution; indeed a larger amount of fibers break per unit volume close to the interface where the ply cracks terminate than away from the interface. The ultimate tensile strength of a ply within a general laminate is difficult to predict from the tensile strength of individual fibers, due to the statistical nature of fiber failure and the progression of fiber failure [73, 74]. Several experimental results highlighted that the fracture toughness of a composite depends not only on the fracture properties of individual microconstituents, but also on the efficiency of interfacial bonding [75].

Fiber microbuckling

In the case of unidirectional fiber-reinforced composite materials loaded in compression, failure is essentially driven by the fiber microbuckling. Such a mechanism is often difficult to capture, because in practical composites the manufacturing process tends to cause misalignment of fibers, inducing localized kinking. The kinking process, which is of plastic type, is driven by local shear, which depends on the initial misalignment angle [76].

Void growth

A composite material may contain a great amount of manufacturing-induced defects, involving the fibers (e.g. fiber misalignment, irregular fiber distribution in the cross section, fiber breakage), the matrix (e.g. voids and microcracks), and the interfaces (e.g. debonding and delamination phenomena). Voids represent one of the primary defects which can be found in all types of composite materials, regardless of material properties, microstructural arrangements and manufacturing processes. The nucleation of voids cannot be prevented, even if can be controlled by some manufacturing parameters, such as vacuum pressure, cure temperature, cure pressure, and resin viscosity. The presence of microscopic voids, even at low volume fractions, is shown to have

a notable influence of the effective material properties, especially in the transverse direction; their shape, size and distribution also play a significant role in determining material degradation, in terms of overall stiffness. Moreover, voids lead to non-negligible local inelastic deformations, acting as precursors to initiation of damage processes; in other words, the matrix phase undergoes ductile fracture due to nucleation, growth and coalescence of voids and cavities, leading to the formation of macroscopic matrix cracks and/or favoring the initiation of fiber/matrix debonding.

1.2.2 Interlaminar damage mechanisms

The most important interlaminar damage mechanisms is interlaminar cracking, i.e. cracking in the interfacial plane between two adjacent plies in a laminate; such mechanism, also referred to as *delamination*, causes separation of the plies (laminae). Delamination, which usually occurs at free edges, such as holes, or at an exposed surface through the thickness, is one of the most common failure modes in layered composite materials, consisting in a progressive reduction of their structural performances, until their final collapse.

Several modeling strategies can be found in the literature about initiation and propagation of delamination phenomena, involving both analytical and numerical methods (see, for instance, [77-79] and [80, 81], respectively), by means of macroscopic laws, representing the phenomenological or micromechanics-based constitutive interfacial behavior.

In the case of negligible material nonlinearities, analytical and numerical methods based on Linear Elastic Fracture Mechanics (LEFM) have been proved to be effective in predicting delamination phenomena, such as the Virtual Crack Closure Technique (VCCT) (see, for instance, Rybicki and Kanninen [82] and Raju [83]), the *J*-integral method (Rice [84], Gurtin [85]), the virtual crack extension method (Hellen [86]), and the stiffness derivative method (Parks [87]). These techniques are used to determine the components of the total energy release rate. However, the application of classical fracture mechanics requires the presence of an initial crack, therefore the onset problem cannot be properly analyzed in this context; to this end, stress-based local

approaches have been frequently used to detect delamination onset before performing a crack propagation analysis.

In the fracture mechanics setting, the propagation of an existing delamination in composite materials have been investigated by several authors; many works have shown that, when mixed-mode conditions are involved, the decomposition of the total energy release rate into mode I, mode II and mode III contributions becomes a necessary task due to the dependence of interface toughness on the mode mixity [88].

Another approach to the delamination problem consists in the application of the so-called *cohesive zone model* (CZM), whose origin goes back to the works of Dugdale [89] and Barenblatt [90]. Cohesive zone models make use of traction-separation laws and may also directly manage the partition of the energy release rate the in the case of mixed-mode crack propagation. Cohesive interface elements have been widely used to simulate delamination phenomena in composite materials [81, 91-94], due to their capabilities to encompass both crack initiation and propagation and to model multiple cracking, without the need for computationally expensive crack path-following algorithms.

1.2.3 Interaction between damage mechanisms in cross-ply laminates

The intrinsic microstructural complexity of fiber-reinforced composite materials reflects that of damage mechanisms which affect their overall behavior; indeed failure in composite materials is strongly affected by the interaction between damage mechanics which are usually described at different resolutions by different physical and numerical models.

In the last two decades the biggest interest has been focused on delamination phenomena, even if this damage mechanism cannot be considered of primary importance in each case during the life period of a composite. The probable reason is that delamination is a phenomenon easily visible at the macroscopic level, and therefore it is considered a crucial factor for the determination of serviceability for a laminate. However, delamination is often very close to the final failure and it is always preceded by a progressive process of matrix deterioration.

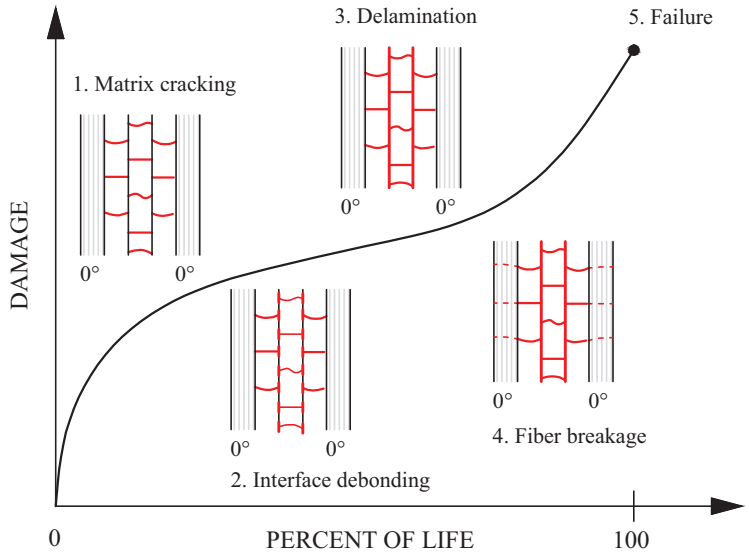

Fig. 1.4 Development of damage in composite laminates.

Matrix damage in off-axis plies, also referred to as *transverse cracking* and already described in Section 1.2.1, is the first stage in the progressive damage process, occurring during a considerable part of the life period; moreover, it can be considered as a source for other consecutive damage mechanisms involving different length scales. The direct consequence of matrix cracking is a notable reduction in strength and stiffness. Moreover, the ply cracks may induce a local interlaminar cracking due to the stress concentration at the matrix crack tips near the interface; the resulting delamination can grow and separate the region between two adjacent ply matrix cracks.

In the following the development of damage in cross-ply laminates is described in detail; Fig. 1.4 shows a schematic representation of the damage evolution due to tensile loading, highlighting five identifiable mechanisms numbered in order of occurrence. Although this behavior comes from experimental results, based on fatigue tests performed by several authors [95-97], it is considered to be valid also for quasistatic loading conditions [98].

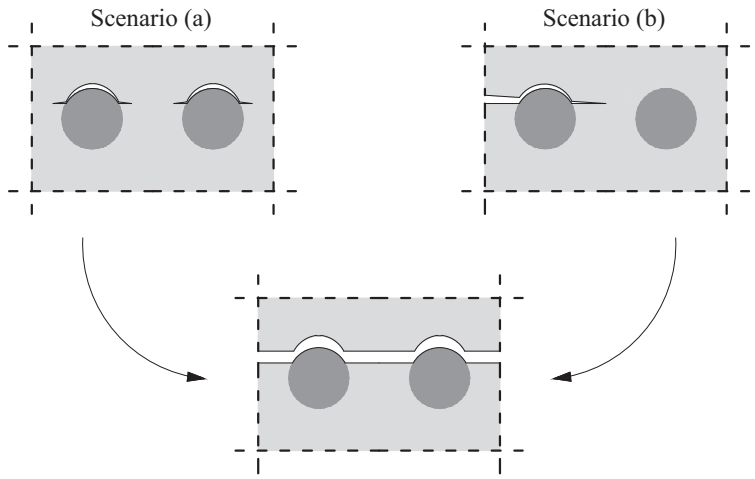

Fig. 1.5 Two alternative scenarios for transverse cracking: (a) matrix cracking induced by fiber/matrix debonding; (b) interfacial debonding induced by propagating matrix cracks.

In the early stage of damage accumulation, each layer whose fibers are aligned in a transverse direction with respect to the applied load is dominated multiple cracking; indeed, microcracks arise from microscopic defects such as voids, areas with high fiber density or regions characterized by a high resin content. Two possible scenarios of cracking can be identified, as shown in Fig. 1.5. In the first one, marked by (a), microcracks nucleate at fiber/matrix interfaces, regarded as the weakest component of the microstructure; then, debonding progresses along these interfaces until a critical state is reached, after which microcracks are subjected to kinking phenomena, inducing cracking into the matrix. Such matrix cracks then coalesce generating a continuous fiber-to-fiber crack. In the second scenario, marked by (b), matrix cracking is assumed to be the first mechanism; once nucleated, matrix cracks tend to propagate towards the fibers, inducing interfacial debonding. Also in this case, a continuous fiber-to-fiber takes place. The occurrence of either of these scenarios depends on the transverse local stress states, which in turn depend on several factors, such as the fiber volume fraction, the distribution of fiber diameters, the inter-fiber spacing, etc. The typical damage configuration observed

in cross sections in the early stage of damage accumulation, already shown in Fig. 1.2, may refer to both the considered scenarios, being a combination of matrix cracking and fiber/matrix debonding. Tensile tests performed on cross-ply laminates in a quasistatic manner have shown that the transverse cracks appear typically for an applied strain ranging from 0.4 to 1.0% (in glass/epoxy and carbon/epoxy systems).

The thickness of the ply subjected to microcracking also has a notable influence of the amount of axial strain which corresponds to transverse crack initiation. A systematic investigation of the thickness effect on cracking in $\left[0_m/90_n\right]_s$ laminates has been presented by Garrett et al. in [99], with reference to glass/polyester systems, and by Parvizi et al. in [100] for glass/epoxy systems.

The initiated cracks tend to propagate along the fiber/matrix interfaces and across the matrix in un unstable manner, spanning the thickness and width of the transverse plies, but are usually arrested at interfaces with adjacent plies of different orientation [101] (e.g. at $90/0$ interfaces for cross-ply laminates). Continued loading leads to the nucleation of progressively more cracks between the already existing cracks. Experimental studies have shown that once the ply cracks have reached the interface, they often grow along the fiber direction through the laminate width in an unstable manner, and are thus indicated as “tunneling cracks”.

Once the ply cracking has initiated, more and more ply cracks appear in between existing cracks, leading to an increase in the crack density [102]; as the crack spacing between adjacent cracks decreases, the cracks begin to interact, providing a “shielding effect”, which tends to reduce the stresses between two adjacent cracks. As a consequence, for increasing levels of load, the rate of cracking decreases until saturation of crack density (see Fig. 1.6).

Reifsnider et al. [103] described this microcrack saturation as a material state, called *characteristic damage state* (CDS), which does not depend on load history, environment, or thermal stresses.

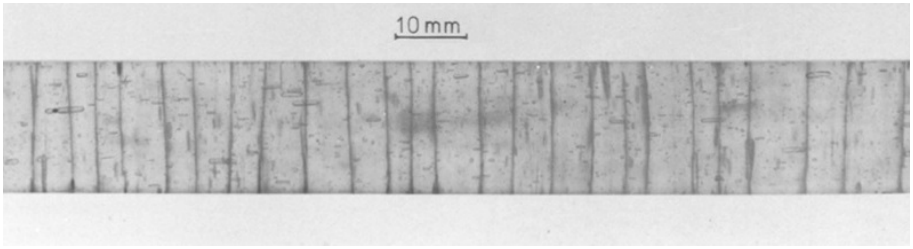

Fig. 1.6 Saturation of progressive microcracking in GFRP. Reprinted from [99].

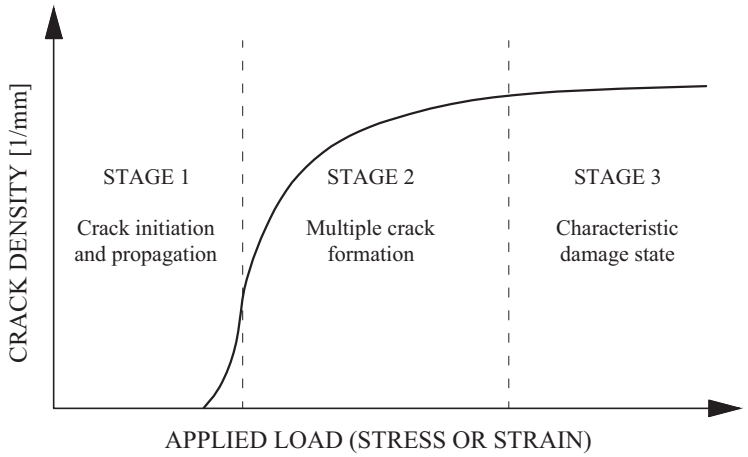

Fig. 1.7 Qualitative behavior of the damage evolution curve for ply cracking in laminates, as obtained from experiments.

A typical damage evolution curve for ply cracking based on experimental results is shown in Fig. 1.7; three main stages can be recognized: crack initiation and propagation through laminate width, multiple crack formation, saturation of progressive cracking.

Subsequent loading causes initiation of cracks in the transverse direction with respect to the primary (intralaminar) cracks, referred to as *secondary cracks*; these cracks are small in size and they can give rise to interlaminar damage phenomena. At first, the initiated interlaminar cracks are small, isolated and distributed in the interlaminar planes; subsequently, some interlam-

inar cracks merge leading to large scale delamination. Thus, the laminate experiences a significant loss in integrity in those regions; further development of damage is highly localized, and involves extensive fiber breakage. The final failure event is manifested by the formation of a failure path through the locally failed regions, and characterized by a highly stochastic behavior.

The interaction between intralaminar and interlaminar damage modes has been studied by many authors, whose works are devoted to the description of the strong coupling between transverse matrix cracking inside layers and delamination between layers [104-107].

1.3 Macroscale modeling of damage

Strength-based failure criteria are commonly used to predict failure in composite materials. A large number of continuum-based criteria have been proposed to predict the onset of different damage mechanisms occurring in composites [108-110]; only in a few cases, depending on the material, the geometry and the loading conditions, they are able to predict final structural collapse.

The development of damage, regarded as continuous stiffness degradation, can be more easily predicted by using the *continuum damage mechanics* (CDM), which represents the macroscopic effects of the microscopic cracking through an internal state variable (*damage variable*). The damage variable is derived from physically based evolution laws within the framework of thermodynamics and continuum mechanics.

The term “continuum damage” was introduced by Kachanov [14] to describe the deterioration of homogeneous, isotropic continua. In its original formulation, the continuum damage model had no physical, nor geometrical interpretation; it was characterized by a scalar *damage parameter* α which could change within the range [0,1], with $\alpha = 1$ and $\alpha = 0$ for the initial undamaged state and the final completely damaged state, respectively.

For composite material this approach is often insufficient to describe the variation of mechanical properties of damaging materials, as a scalar repre-

sentation of the damage state cannot properly represent the orientation of defects. A proper form of the stiffness matrix for anisotropic damaged materials was proposed by Chaboche [111, 112], by introducing a fourth-order tensor as a damage variable.

By means of continuum damage mechanics, a problem of damage and fracture caused by the development of distributed cavities and/or microcracks can be properly analyzed in the framework of continuum mechanics by performing the following steps:

1. A (scalar or tensorial) *damage variable* $\mathfrak{D}(\mathbf{x})$ is introduced to represent the damage state at any material point $\mathbf{x}$ of the composite material.

2. An equation governing the development of the damage variable (called *evolution equation*) is formulated in a thermodynamically consistent manner, e.g. by means of *generalized standard materials* approach.

3. A *constitutive equation*, describing the mechanical behavior of the damaged material, is obtained.

4. The macroscopic boundary value problem is solved by using these equations.

The definition of the fourth-order damage tensor $\mathbb{D}$ can be obtained by extending the notion of scalar damage variable $D = 1 - \alpha$, which represent the damage state in terms of the variation of an elastic modulus. Let the fourth-order elastic moduli tensor of the undamaged and damaged materials be denoted by $\mathbb{C}_0$ and $\mathbb{C}(\mathbb{D})$, respectively. Then the elastic constitutive equations of these materials are given by

$$\boldsymbol{\sigma} = \mathbb{C}_0 : \boldsymbol{\varepsilon}, \quad \boldsymbol{\sigma} = \mathbb{C}(\mathbb{D}) : \boldsymbol{\varepsilon}, \tag{1.1}$$

where $\boldsymbol{\sigma}$ and $\boldsymbol{\varepsilon}$ are the stress and strain tensors, and the symbol : denotes the double contraction. In this setting, the following transformation between elastic moduli is supposed:

$$\mathbb{C}(\mathbb{D}) = (\mathbb{I} - \mathbb{D}) : \mathbb{C}_0, \tag{1.2}$$

where $\mathbb{I}$ denotes the fourth-order identity tensor. Thus the fourth-order damage tensor $\mathbb{D}$ is given by the following relation:

$$\mathbb{D} = \mathbb{I} - \mathbb{C}(\mathbb{D}) : \mathbb{C}_0^{-1}. \tag{1.3}$$

It can be shown that the damage tensor $\mathbb{D}$ is asymmetric. To overcome this difficulty, Chaboche proposed a new fourth-order symmetric damage tensor $\widehat{\mathbb{D}}$ and employed an alternative transformation:

$$\mathbb{C}\left(\widehat{\mathbb{D}}\right) = \frac{1}{2}\left[\left(\mathbb{I} - \widehat{\mathbb{D}}\right) : \mathbb{C}_0 + \mathbb{C}_0 : \left(\mathbb{I} - \widehat{\mathbb{D}}\right)\right]. \tag{1.4}$$

Macroscopic constitutive equations derived for softening materials can be either *phenomenological* or *micromechanical*. In the latter case, based on the combination of micromechanics and continuum damage theory, suitable overall constitutive laws can be informed by the crack evolution at the microscopic scale [113-116].

1.4 Microscopic modeling of damage

The complexity of cracking patterns at the microscopic level in composite materials is essentially due to the presence of multiple microconstituents, arranged in various geometric configurations, having different properties in terms of strength and stiffness; indeed, the strain softening induced by damage localization gives rise to a stress redistribution, leading to a very complex stress state in the final damage stages. As a consequence, conventional con-

tinuum mechanics-based numerical models at the macroscopic scale, essentially based on a *stationary* microstructure, are generally not able to accurately predict the development of damage until the final laminae/laminates collapse.

An alternative strategy to predict failure in composites consists in modeling all the microstructural details of the material, in order to investigate the interaction of microcracks with the different microconstituents (i.e. phases, interfaces, and other defects); several methods have been developed to model damage and fracture at the microscopic scale, such as the *extended finite element method*, the *discrete element method*, the *lattice element method*, the *cohesive/volumetric finite element method*, the *regularized damage models*, and the *element erosion method*. In the following the above-mentioned methods are briefly described.

1.4.1 The extended finite element method (X-FEM)

The extended finite element method, presented in [117-119], allows for the crack modeling, without requiring any remeshing technique; based on a level set representation, a crack can be modeled independently of the mesh by enriching the finite element approximation by step functions and asymptotic near-tip fields. The displacement field for a single crack in a two-dimensional body can be written as:

$$\begin{aligned}\mathbf{u}^h(\mathbf{x}) = &\sum_{i\in I} \mathbf{u}_i \phi_i(\mathbf{x}) + \sum_{i\in L} \mathbf{a}_i \phi_i(\mathbf{x}) H(\mathbf{x}) \\ &+ \sum_{i\in M_1} \phi_i(\mathbf{x}) \left(\sum_{j=1}^{4} \mathbf{b}_{i,1}^j F_1^j(\mathbf{x}) \right) \\ &+ \sum_{i\in M_2} \phi_i(\mathbf{x}) \left(\sum_{j=1}^{4} \mathbf{b}_{i,2}^j F_2^j(\mathbf{x}) \right)\end{aligned} \tag{1.5}$$

where I is the set of all nodes in the mesh, $L \subset I$ is the subset of nodes that are enriched for the crack discontinuity, and $M_1 \subset I$ and $M_2 \subset I$ are the subsets of enriched nodes for the first and second crack tip, respectively (see

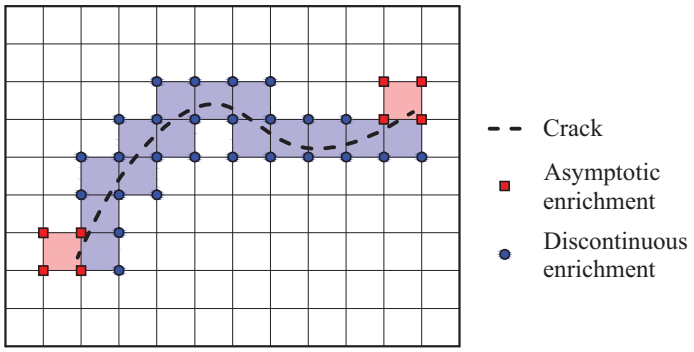

Fig. 1.8 X-FEM enriched nodes for a crack located on a regular 2D mesh.

Fig. 1.8). Moreover, $\mathbf{u}_i$ denotes the usual DOFs at node i; ϕ_i is the shape function associated with node i, $\mathbf{a}_i$ are the additional DOFs corresponding to the crack discontinuity, $\mathbf{b}^j_{i,1}$ and $\mathbf{b}^j_{i,2}$ ($j = 1, \ldots, 4$) are the additional DOFs for the first and second crack tip, respectively, and the near-tip functions $F^j_k(\mathbf{x})$ for the kth tip are given by

$$\left\{ \sqrt{r}\sin\left(\frac{\theta}{2}\right), \sqrt{r}\cos\left(\frac{\theta}{2}\right), \sqrt{r}\sin\left(\frac{\theta}{2}\right)\sin\theta, \sqrt{r}\cos\left(\frac{\theta}{2}\right)\sin\theta \right\}, \quad (1.6)$$

where (r, θ) are the local polar coordinates at the kth crack tip with $\theta = 0$ coinciding with the tangent to the crack at the considered tip.

The extended finite element method has been extended by Daux et al. [120] to the case of arbitrarily branched and intersecting cracks, and applied to study cracking phenomena in composite materials [10, 121].

1.4.2 The discrete element method (DEM)

The discrete element method (DEM) is a flexible method to study the mechanical behavior of materials characterized by evolving microstructures, due to its capability in predicting material reorganization at the microscopic scale as a direct consequence of applied loads.

In a DEM setting, a solid is regarded as a collection of rigid particles or blocks interacting with each other by means of different interaction laws in

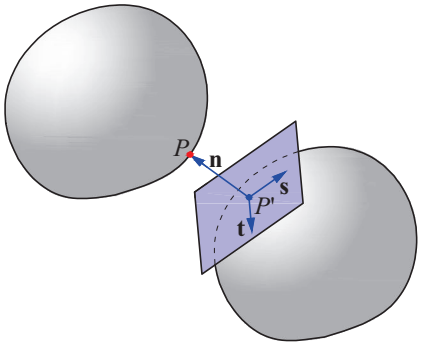

Fig. 1.9 Candidate and antagonist contactors and local frame for a contact pair.

both normal and tangential directions. Let $\{\Omega_m, m = 1, \ldots, N_b\}$ be a collection of N_b interacting 3D rigid bodies, each of which is in contact with one or more of its neighboring bodies. If the dynamic evolution of such a mechanical system is assumed to me sufficiently smooth, its motion can be described in a global reference by means of the following spatial semi-discretization (written in *compact matrix notation*):

$$\mathbf{M}(\mathbf{q}, t)\ddot{\mathbf{q}} = \mathbf{F}_{\text{int}}(\dot{\mathbf{q}}, \mathbf{q}, t) + \mathbf{F}_{\text{ext}}(t) + \mathbf{r}, \tag{1.7}$$

where $\mathbf{q} \in \mathbb{R}^N$ denotes the vector of generalized degrees of freedom (whose size is $N = 6N_b$), $\dot{\mathbf{q}}$ is the vector of generalized velocities, $\mathbf{F}_{\text{int}}(\dot{\mathbf{q}}, \mathbf{q}, t)$ denotes the vector containing the internal forces (for deformable bodies) and the nonlinear inertial terms, $\mathbf{F}_{\text{ext}}(t)$ represents the external forces, $\mathbf{r}$ is the vector of contact forces, and $\mathbf{M}(\mathbf{q}, t)$ is the mass matrix. Initial and boundary conditions must be added to completely describe the evolution of the considered system.

Contacts are regarded as binary interactions, i.e. each interaction involves only two bodies (or portions of them), referred to as *candidate* and *antagonist contactors* and denoted by Ω_i and Ω_j, respectively. If all bodies are strictly convex bodies, each interaction locus may be considered as punctual; in this case, a unique pair of points $P \in \partial\Omega_i$ and $P' \in \partial\Omega_j$ can be identified, which minimizes the distance between the two contactors (see Fig. 1.9). For each contact pair $\alpha = (i, j)$, a local frame $(\mathbf{t}_\alpha, \mathbf{s}_\alpha, \mathbf{n}_\alpha)$ is introduced, with $\mathbf{n}_\alpha$ the outer

unit normal vector of the antagonist boundary in P' and $(\mathbf{t}_\alpha, \mathbf{s}_\alpha)$ two vectors lying in its tangential plane; it allows to define the local variables g_α, $\mathbf{U}_\alpha$ and $\mathbf{R}_\alpha$, which denote the gap (i.e. the algebraic distance between two different bodies), the contact relative velocity and local contact force, respectively.

The following general kinematic relationships can be established between local and global variables for a given contact α:

$$\mathbf{U}_\alpha = \mathbf{H}^*_\alpha(\mathbf{q})\dot{\mathbf{q}}, \tag{1.8}$$

where $\mathbf{H}^*_\alpha(\mathbf{q})$ is a linear mapping from $\mathbb{R}^N$ to $\mathbb{R}^3$ (see [122] for additional details); by virtue of duality considerations, the local contact force $\mathbf{R}_\alpha$ is mapped on the corresponding unknown $\mathbf{r}_\alpha$ expressed in the global frame, as follows:

$$\mathbf{r}_\alpha = \mathbf{H}_\alpha(\mathbf{q})\mathbf{R}_\alpha, \tag{1.9}$$

where $\mathbf{H}_\alpha(\mathbf{q})$ is the transpose of $\mathbf{H}^*_\alpha(\mathbf{q})$. These mappings can be written in an assembled form, leading to define the operators $\mathbf{H}(\mathbf{q})$ and $\mathbf{H}^*(\mathbf{q})$:

$$\begin{aligned} \mathbf{H}(\mathbf{q}) \,:\, \mathbf{R} = \{\mathbf{R}_\alpha\} \rightarrow \mathbf{r} = \sum_{\alpha=1}^{N_c} \mathbf{H}_\alpha(\mathbf{q})\mathbf{R}_\alpha \\ \mathbf{H}^*(\mathbf{q}) \,:\, \dot{\mathbf{q}} \rightarrow \mathbf{U} = \{\mathbf{U}_\alpha\} = \{\mathbf{H}^*_\alpha(\mathbf{q})\dot{\mathbf{q}}\}, \end{aligned} \tag{1.10}$$

where N_c is the number of contacts.

In the discrete element method, the attention is focused on the interaction laws which account for the different physical and chemical phenomena occurring at the touching boundaries, such as unilateral contact, friction and cohesion; as an example, only the frictionless unilateral contact is considered, which implies that the different bodies cannot interpenetrate. For each contact α, this unilateral constraint is enforced by using the classical Signorini condition, here formulated in terms of relative velocities (the subscript α is omitted for the sake of simplicity): assuming an initial gap $g(t_0) \geq 0$ and for all $t > t_0$, if $g(t) \leq 0$, then

$$\begin{aligned} R_N &= \mathbf{R}^{\mathrm{T}}\mathbf{n} \geq 0 \\ U_N &= \mathbf{U}^{\mathrm{T}}\mathbf{n} \geq 0 \\ U_N R_N &= 0, \end{aligned} \tag{1.11}$$

otherwise $\mathrm{R}_N = 0$; eq. (1.11) represents an *implicit* interaction law[1], i.e. it cannot be expressed as $\mathbf{R} = \mathbf{R}(g, \mathbf{U})$. Due to the nonsmooth nature of contact phenomena, the classical Euler-Lagrange equation (1.7) must be reformulated to describe collisions and other events for which velocity discontinuities are to be expected, generally referred to as *shocks*.

In the following, the approach proposed by Moreau [123] is briefly recalled, in the framework of the *nonsmooth contact dynamics* (NSCD); after assuming that $t \to \dot{\mathbf{q}}(t)$ and $t \to \mathbf{U}(t)$ belong to the space of functions of *locally bounded variation* (LBV) and loads are represented by *measures*, Eq. (1.7) can be replaced by the following differential measure equation:

$$\begin{aligned} \mathbf{M}(\mathbf{q}, t)\, \mathrm{d}\dot{\mathbf{q}} &= \mathbf{F}_{\mathrm{int}}\left(\dot{\mathbf{q}}^{+}, \mathbf{q}, t\right) \mathrm{d}t + \mathbf{F}_{\mathrm{ext}}(t)\, dt + \mathrm{d}\mathbf{p} \\ \mathbf{q}(t) &= \mathbf{q}(t_0) + \int_{t_0}^{t} \dot{\mathbf{q}}^{+}\, \mathrm{d}t, \end{aligned} \tag{1.12}$$

where $\mathrm{d}t$ is the Lebesgue measure on $\mathbb{R}$, $\mathrm{d}\dot{\mathbf{q}}$ is the differential measure of $\dot{\mathbf{q}}$, and $\mathrm{d}\mathbf{p}$ is the nonnegative measure of the contact impulse; both $\mathrm{d}\dot{\mathbf{q}}$ and $\mathrm{d}\mathbf{p}$ are regarded as sums of two contributions (*smooth* and *nonsmooth*), the latter one representing the effects of a finite number of shocks occurring at times t_i:

[1] Any implicit (nonsmooth) interaction law can be transformed into an equivalent explicit (smooth) law by *regularization*, after introducing additional parameters without any physical interpretation. In the case of unilateral contact, the constraint condition can be enforced by the *penalty* approach, which introduces an artificial stiffness k, chosen to be sufficiently large to keep the interpenetration admissible. Moreover, the use of smooth interaction laws requires reasonably small time steps, leading to high computational costs, especially for complex mechanical systems characterized by a huge number of collisions.

$$\begin{aligned} \mathrm{d}\dot{\mathbf{q}} &= \ddot{\mathbf{q}}\,\mathrm{d}t + \sum\nolimits_i \left(\dot{\mathbf{q}}^+(t_i) - \dot{\mathbf{q}}^-(t_i)\right)\,\delta(t_i) \\ \mathrm{d}\mathbf{p} &= \mathbf{r}\,\mathrm{d}t + \sum\nolimits_i \mathbf{p}_i\,\delta(t_i), \end{aligned} \tag{1.13}$$

where $\dot{\mathbf{q}}^+(t_i) - \dot{\mathbf{q}}^-(t_i)$ is the difference between the right continuous and the left continuous functions associated with the LBV function $\dot{\mathbf{q}}$ at time t_i, $\mathbf{p}_i$ is the *percussion* at time t_i, and $\delta(t_i)$ denotes the Dirac measure at time t_i.

When shocks occur in a collection of rigid bodies, the equation of motion (1.12) (together with initial and boundary conditions) and the interaction laws are not enough to completely describe the mechanical evolution; indeed rather complicated phenomena, such as local elastic or plastic deformation, wave propagation, and long distance effects, usually take place in the neighborhood of contact points. As a consequence, additional phenomenological laws must be prescribed, referred to as *shock laws*, which relates the local quantities (velocity, contact force, energy) evaluated after impact to the corresponding quantities computed before, by means of different *coefficients of restitution*.

A numerical strategy to solve Eq. (1.12) has been developed in [122], starting from its integration over an arbitrary time step (even reduced to a shock instant):

$$\begin{aligned} \mathbf{M}\left(\dot{\mathbf{q}}_{i+1} - \dot{\mathbf{q}}_i\right) &= \overbrace{\int_{t_i}^{t_{i+1}} \left(\mathbf{F}_{\mathrm{int}}(\dot{\mathbf{q}}, \mathbf{q}, t) + \mathbf{F}_{\mathrm{ext}}(t)\right)\,\mathrm{d}t}^{\mathbf{p}_{\mathrm{free}}} + \mathbf{p}_{i+1} \\ \mathbf{q}_{i+1} &= \mathbf{q}_i + \int_{t_i}^{t_{i+1}} \dot{\mathbf{q}}\,\mathrm{d}t, \end{aligned} \tag{1.14}$$

where $\mathbf{p}_{i+1} = \int_{t_i}^{t_{i+1}} \mathrm{d}\mathbf{p}$ denotes the total impulsion over the time step (regarded as an unknown). Choosing the θ-method as time integration scheme, one obtains the following equations:

$$\begin{aligned}\mathbf{M}\left(\dot{\mathbf{q}}_{i+1}-\dot{\mathbf{q}}_i\right) &= h\theta\Big(\mathbf{F}_{\text{int}}\left(\dot{\mathbf{q}}_{i+1},\mathbf{q}_{i+1},t_{i+1}\right)+\mathbf{F}_{\text{ext}}\left(t_{i+1}\right)\Big)\\ &\quad + h(1-\theta)\left(\mathbf{F}_{\text{int}}(\dot{\mathbf{q}}_i,\mathbf{q}_i,t_i)+\mathbf{F}_{\text{ext}}(t_i)\right)+\mathbf{p}_{i+1}\\ \mathbf{q}_{i+1} &= \mathbf{q}_i + h\left(\theta\dot{\mathbf{q}}_{i+1}+(1-\theta)\dot{\mathbf{q}}_i\right),\end{aligned} \tag{1.15}$$

where $h = t_{i+1} - t_i$ is the step size and $\theta \in [0,1]$. Such scheme is implicit (except for $\theta = 0$), and, if $\theta \in [0.5,1]$, it is unconditionally stable; moreover if $\theta = 0.5$ the scheme (also referred to as Crank-Nicolson method) is conservative for smooth evolution problems, i.e. no spurious solutions are generated.

The commonly used contact solver in the NSCD method is the nonlinear Gauss-Seidel (NLGS) nesting; considering the local system to be solved for each contact α:

$$\begin{aligned}\mathbf{U}_\alpha &= \mathbf{U}_{\alpha,free} + \mathbf{W}_{\alpha\alpha}\mathbf{R}_\alpha + \sum_{\beta\neq\alpha}\mathbf{W}_{\alpha\beta}\mathbf{R}_\beta\\ \mathbf{f}(g_\alpha,\mathbf{U}_\alpha,\mathbf{R}_\alpha) &= \mathbf{0},\end{aligned} \tag{1.16}$$

the contributions due to any other contact ($\beta \neq \alpha$) are frozen taking updated values if $\beta < \alpha$ or old values if $\beta > \alpha$.

The discrete element method, in the above described formulation, has been widely devoted to the analysis of granular materials, such as sands, rocks, soils, hot mix asphalt and concrete [124-127]. In recent years, the DEM approach has been extended to model composite materials: for instance, Khattab et al. [128] developed a DEM model using the image-based shape structure to predict the compressive response of carbon fiber-reinforced polymer composites; Yang et al. [129] used a DEM approach to simulate mechanical process of microbond test of fiber-reinforced composites; Khattak and Khattab [130] studied the micromechanical behavior of carbon fiber-reinforced polymer composites under tensile loading, representing the different microconstituents (fibers and matrix) as clusters of small bonded discrete elements.

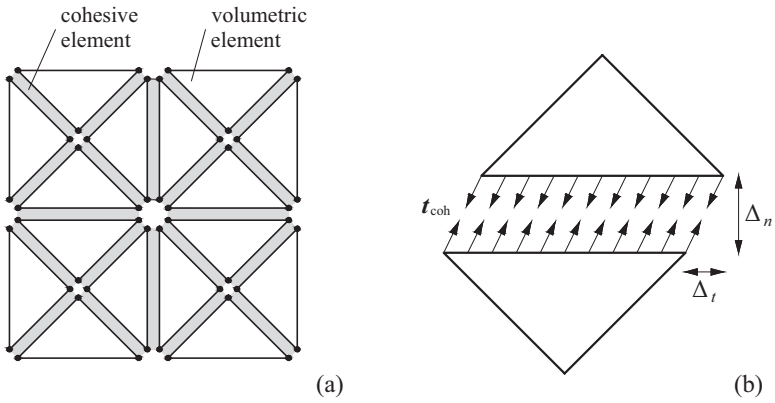

Fig. 1.10 Cohesive/volumetric finite element method: (a) cross-triangle quadrilateral mesh; (b) two-node cohesive interface element.

A generalization of the discrete element method, referred to as *lattice element method* (LEM) has been developed to deal with the case of rigid particles embedded in a deformable continuous phase (i.e. the matrix), like in cemented granular materials and composites (see, for instance, [131, 132]). This method relies on 1D element-meshing of the continuous phase, based on a triangular lattice which can be either regular or irregular. Several rheological models can be used to describe the behavior of the lattice, such as spring-like or beam-like elements.

1.4.3 The cohesive/volumetric finite element method

The cohesive/volumetric finite element (CVFE) scheme, introduced by Xu and Needleman [133], consists in a combination of conventional (volumetric) finite elements and of interfacial (cohesive) elements; the volumetric elements are used to characterize the mechanical response of the bulk material, whereas the cohesive elements are introduced between the volumetric finite elements to simulate the initiation and propagation of multiple cracks in the considered solid (see Fig. 1.10a).

In this framework, damage phenomena are modeled by using suitable phenomenological cohesive failure laws characterizing the evolution of the interfacial elements. The choice of the cohesive model plays a fundamental role in the simulation of the fracture process; the most simple formulation is the bilinear rate-independent *intrinsic* law introduced by Geubelle and Baylor [134].

The implementation of the CVFE scheme is based on the following form of the principle of virtual work:

$$\int_{\Omega} \boldsymbol{\sigma} : \delta\boldsymbol{\varepsilon} \, \mathrm{d}V - \int_{\partial_t\Omega} \mathbf{t} \cdot \delta\mathbf{u} \, \mathrm{d}S - \int_{\Gamma} \mathbf{t}_{\mathrm{coh}} \cdot \delta\boldsymbol{\Delta} \, \mathrm{d}S = 0, \tag{1.17}$$

where the first two contribution in the left-hand side represent the (bulk) internal and the external virtual works, respectively, whereas the third contribution is associated with the cohesive tractions $\boldsymbol{t}_{\mathrm{coh}}$ acting on the internal cohesive surface Γ; moreover, $\boldsymbol{\Delta}$ denotes the displacement jump across a pair of cohesive surfaces, as shown in Fig. 1.10b.

In this manner, nucleation, propagation and coalescence of cracks during the deformation process is an outcome of the simulation; an important feature of this model consists in its capability of predicting microcrack patterns and evolution of crack densities, without requiring additional criteria.

However, the introduction of interfacial elements based on the intrinsic cohesive zone model adds some artificial compliance to the finite element model, which can alter the overall mechanical response, especially in a dynamic setting; moreover, the fracture path strongly depends on the mesh geometry and size [135]. Several attempts have been made to avoid this mesh sensitivity; various authors have proposed semi-empirical criteria for the initial slope in order to define “invisible” CZMs at the macroscopic scale [136-138]; Blal et al. [139] proposed a generalization of these criteria to three dimensional cases and to any type of loading, giving also a rigorous explication of the above-mentioned semi-empirical results.

In [12] the cohesive/volumetric combined approach has been used to simulate the overall mechanical behavior of a representative sample of a metal

matrix composite (a Zircaloy-4 plate with rectangular hydride inclusions), regarded as a collection of (rigid or deformable) individual fibers embedded into a continuous matrix, discretized by using a mesh, whose elements are separated by suitable cohesive interface elements.

1.4.4 The regularized damage models

Continuum damage mechanics is also used to model the development of damage and cracking at the microscopic scale. In classical approaches, referred to as *local* approaches, the stress state at a certain point depends only on the state variable at that point, according to the classical assumption of *locality*.

In the case of quasibrittle materials, whose damage constitutive models usually involve *softening*, local continuum formulations lead to several pathological consequences: (i) the softening region is infinitely small; (ii) the load-displacement curve always exhibits snap-back, independently of the size of the structure and of the ductility of the material; (iii) the total amount of energy dissipated during the failure process is zero. From a mathematical point of view, the above-mentioned features are associated with the so-called *loss of ellipticity* of the governing differential equation; on the other hand, from a numerical point of view, this ill-posedness causes a spurious sensitivity of the results to the size of the finite element mesh.

In order to overcome such drawbacks, several *nonlocal* approaches have been developed [140-142], based on generalized continuum theories incorporating a *characteristic length* and preventing strain localization. In detail, nonlocal models of the integral type consist in replacing a certain variable by its nonlocal counterpart obtained by weighted averaging over a spatial neighborhood of each point. Given a local field $f(\mathbf{x})$ in the domain Ω, the corresponding nonlocal field is defined as

$$\overline{f}(\mathbf{x}) = \int_{\Omega} \alpha(\mathbf{x}, \mathbf{y}) f(\mathbf{y}) \, \mathrm{d}\mathbf{y}, \tag{1.18}$$

where $\alpha(\mathbf{x}, \mathbf{y})$ is a given nonlocal weight function.

Other regularized damage models have been proposed, such as the explicit gradient and the implicit gradient formulations (see [143, 144] for additional details), which can be considered as the differential counterpart of integral nonlocal formulations, as well as the methods based on the introduction of viscous regularizations in the framework of rate-dependent materials.

1.4.5 The erosion approaches to fracture

The easiest way to deal with discrete fracture is the *element erosion* scheme [145-147], since it does not require any representation of the crack's topology; however, it is well-known that this method, in its original formulation, suffers from an extreme mesh sensitivity and cannot be used for dynamic fracture.

For brittle fracture, Pandolfi and Ortiz [148] derived a novel eigenerosion approach, in which a finite element can be either intact or completely failed according to the fulfillment of a suitable energy criterion. In the first case, the element shows an elastic behavior, whereas in the latter case it is eroded from the finite element model. The starting point consists in formulating the three-dimensional crack tracking problem (based on classical Griffith's criterion) as the minimization of the dissipation functional

$$F(\mathbf{u}, K, t) = \underbrace{\Pi(\mathbf{u}, K, t)}_{\text{bulk}} + \underbrace{\mathscr{G}_c |K|}_{\text{surface}} \tag{1.19}$$

at every time, subjected to monotonic loading; in Eq. (1.19), Π is the potential energy of the body, $\mathscr{G}_c$ is the fracture energy, and $|K|$ denotes the area of the crack set K. In order to overcome the difficulty of minimizing with respect to the crack set K, which is numerically cumbersome, the problem is reformulated in terms of *eigendeformations*, by introducing the following extended energy:

$$\Pi^*(\mathbf{u}, \boldsymbol{\varepsilon}^*, t) = \int_\Omega W(\boldsymbol{\varepsilon}(\mathbf{u}) - \boldsymbol{\varepsilon}^*)\, \mathrm{d}V - \int_{\partial_t \Omega} \mathbf{t} \cdot \mathbf{u}\, \mathrm{d}S, \tag{1.20}$$

where the eigendeformations $\boldsymbol{\varepsilon}^*$ are restricted to be of the form

$$\boldsymbol{\varepsilon}^* = (\boldsymbol{\delta} \otimes_s \mathbf{n})\delta_K. \tag{1.21}$$

In Eq. (1.21), $\boldsymbol{\delta}$ denotes the opening displacement field across K, $\mathbf{n}$ is the unit normal to K, $\otimes_s$ is the symmetric part of the tensor product $\otimes$, and δ_K represents a distribution concentrated over the crack set K. The minimization of Π^* with respect to the opening displacement field $\boldsymbol{\delta}$ allows to obtain a displacement field that satisfy zero traction boundary conditions over the crack set:

$$\Pi(\mathbf{u}, K, t) = \inf_{\delta} \Pi^*(\mathbf{u}, \boldsymbol{\varepsilon}^*, t), \tag{1.22}$$

and thus, a new formulation of the original minimization problem can be obtained, by means of a regularization of the extended energy (1.20), leading to the element erosion scheme, in which the eigendeformation is restricted in a binary sense. These scheme is not convergent, due to a geometrical reason: when the crack is not aligned with the mesh, the amount of fracture energy is overestimated as the crack shows a jagged path in accordance with the given mesh. Schmidt et al. [149] proposed the following regularized dissipation functional, thus eliminating the spurious mesh dependency:

$$F_\epsilon(\mathbf{u}, \boldsymbol{\varepsilon}^*, t) = \int_\Omega W(\boldsymbol{\varepsilon}(\mathbf{u}) - \boldsymbol{\varepsilon}^*)\, \mathrm{d}V - \int_{\partial_t \Omega} \mathbf{t} \cdot \mathbf{u}\, \mathrm{d}S + \mathscr{G}_c \frac{|K_\epsilon|}{2\epsilon}, \tag{1.23}$$

where ϵ is a small regularization parameter; K_ϵ is the ϵ-neighborhood of K, shown in Fig. 1.11 (see [148] for additional details).

The authors have shown that this scheme converges to Griffith's model with increasing mesh refinement; moreover it seems to be insensitive to mesh size and orientation.

1.5 Multiple length scales in damage modeling

Material failure in heterogeneous materials is an intrinsically multiscale process; damage initiates at a fine scale, e.g. due to the loss of cohesion between

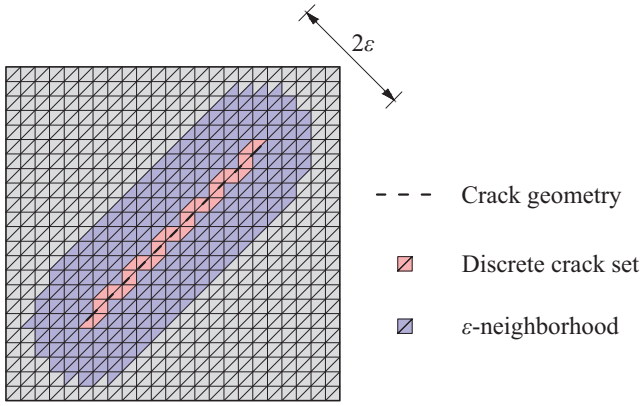

Fig. 1.11 Regularization of the discrete crack path by means of the ε-neighborhood construction.

the different microconstituents, leading to the appearance of zones with highly localized deformations at the macroscopic level. Therefore modeling of damage phenomena at the microscopic and macroscopic scales in a separate manner does not lead to accurate numerical results, since the interaction between damage mechanisms at different scales cannot be properly taken into account. The increasing computational capabilities available to designers and researchers have encouraged the development of the so-called *multiscale methods*, on the basis of the intuitive notion that the physical phenomena occurring at the lower scales determine the material response at the higher scales. Fiber-reinforced composites and, more generally, heterogeneous materials appear to be natural candidates for this kind of modeling.

Since in a heterogeneous medium, the microscopic heterogeneities are embedded in the matrix, overall (mechanical) properties must be defined at a scale much larger than the size of such heterogeneities; this leads to the main idea that, at a proper scale, a *representative volume element* exists such that the properties of interest can be computed by appropriate averaging over this volume. The classical micromechanical approaches rely on this concept.

These approaches are valid only for stationary microstructures, whose characteristic size does not change under external loading; in the case of strain

localizations, characterized by the transition from a diffuse damage configuration to localized fracture events, more sophisticated multiscale approaches are needed, based on information passing from the microscale to the macroscale, and vice versa.

A wide literature about multiscale methods exists, addressed to the theoretical aspects, as well to the practical applications in modeling damage phenomena in composite materials; in Chapter 2, a review of the main approaches is proposed, without having the claim of being exhaustive.

2

Multiscale approaches for composite materials with evolving microstructure: a review

As widely discussed in Chapter 1, composite materials cannot be considered homogeneous at the microscopic scale, consisting of different microconstituents with evolving material and geometric properties; thus, the macroscopic mechanical behavior of such structures appears to be rather complex and characterized by nonuniformity, anisotropy and nonlinearity due to several damage mechanisms.

Fully microscopic models are not pursued in practice due to their large computational cost, and thus simplified models are commonly used to predict failure in composite materials with satisfactory accuracy.

Two main approaches have been extensively used to define damage models for composite materials, i.e. *mesoscopic models* and *homogenization models*. In the first case, the composite is treated as a homogenous material and its behavior is described by a macroscopic phenomenological damage law; therefore, in most cases, the use of mesoscopic models may result in an unrealistic estimation of crack trajectories and load-carrying capacity. In the latter case, the overall mechanical response of composites is predicted on the basis of the properties of the different individual constituents at the microscopic level, by establishing relationships between the microstress and microstrain fields and the corresponding macrovariables.

Homogenization techniques, discussed in Section 2.1, have increasingly gained in importance due to their better flexibility and accuracy with respect to mesoscopic models; moreover, they are usually adopted within the more general framework of *multiscale methods*, which are more suitable for studying damage and other nonlinear phenomena in heterogeneous media; an overview of such methods is given in Section 2.2.

2.1 Overview of homogenization techniques

Micromechanics-based methods aim to predict the *effective* (averaged) properties by understanding the fundamental concepts of composite materials and their relevant damage phenomena. In the micromechanics-based analysis, a composite material is simplified in a model based on a widely accepted *homogenization process*. This is achieved by replacing a heterogeneous microstructure by an *equivalent homogenized material*.

In order to obtain the effective behavior of a heterogeneous material, there exist two basic approaches for homogenization: the *average field theory* (also referred to as *mean field theory*), in which the effective mechanical properties are determined as relations between the averaged microfields, and the *asymptotic homogenization theory*, in which the effective properties emerge as relations between the microfields and macrofields naturally derived from a multiscale perturbation method.

2.1.1 Average field theory

The average field theory plays a central role in *micromechanics*, whose main purpose is to obtain the overall mechanical properties associated with an infinitesimal material neighborhood from the parameters which characterize its microstructure. For a complete theoretical treatment of micromechanics and analytical homogenization methods, one can refer to the works of Mura [150], Nemat-Nasser and Hori [151], Suquet [152], Torquato [153], Milton [154].

2.1.1.1 Definition of RVE

The starting point of the average field theory is a proper definition of the concept of *representative volume element* (RVE). Different definitions of RVE can be found in the literature, according to the specific purpose (theoretical, numerical or experimental):

a) The RVE is "a sample that (a) is structurally entirely typical of the whole mixture on average, and (b) contains a sufficient number of inclusions for the apparent overall moduli to be effectively independent of the surface values of traction and displacement, so long as these values are *macroscopically uniform*" (Hill, [155]).

b) The RVE is a "reference cube […] which is large compared to the size of non-homogeneities, yet small compared to the whole body. Then the volume average of a quantity such as displacement, strain, stress or phase volume fraction is the same for the whole body and the reference cube" (Hashin and Shtrikman, [156]).

c) An optimal choice for the RVE is a material sample that "includes the most dominant features that have first-order influence on the overall properties of interest and, at the same time, yields the simplest model. This can only be done through a co-

ordinated sequence of microscopic (small-scale) and macroscopic (continuum-scale) observation, experimentation, and analysis" (Nemat-Nasser and Hori, [151]).

d) The RVE is "the smallest material volume element of the composite for which the usual spatially constant *overall modulus* macroscopic constitutive representation is a sufficiently accurate model to represent mean constitutive response" (Drugan and Willis, [157]).

e) A correct definition of RVE requires "(a) *statistical homogeneity* and *ergodicity* of the material; these two properties assure the RVE to be *statistically representative* of the macroresponse; (b) some scale L of the material domain, sufficiently large relative to the microscale d (inclusion size) so as to ensure the *independence of boundary conditions*". According to these hypotheses, an RVE is "well defined in two situations only: (i) unit cell in a periodic microstructure, and (ii) volume containing a very large (mathematically infinite) number of microscale elements (e.g. molecules, grains, crystals), possessing ergodic properties" (Ostoja-Starzewski, [158]).

f) The determination of the RVE size "is by no means straightforward. It depends on the material under consideration, but also on the structure sensitivity of the physical quantity that is measured. Often, *elastic moduli* are taken as the governing parameter […] Also other macroscopic quantities can be taken. […] the peak load or the energy dissipation may be used" (Stroeven et al., [159]).

g) The RVE size "should be large enough with respect to the individual grain size in order to define overall quantities such as

stresses and strains, but it should be small enough in order not to hide macroscopic heterogeneity" (Evesque, [160]).

h) The RVE size can be defined as the "minimum size of a microstructural cell that fulfills the requirement of statistical homogeneity. As such, it is a *lower bound*: larger microstructural cells behave similarly while smaller microstructural cells do not" (Gitman et al., [22]).

i) A microscopic sample is considered to be an RVE when it fulfills all the following requirements: "an increase in its size does not lead to considerable differences in the homogenized properties, the microscopic sample is large enough so that the homogenized properties are independent of the microstructural randomness, and its size is much smaller than the macroscopic dimension" (Nguyen et al., [26]).

As may be inferred from these definitions, to quantify the concept of RVE, three length scales are necessary: one is the macroscopic scale (or *macroscale*), denoted by L_{macro}, which corresponds to the characteristic size of the considered solid, described as a continuum; the second is the microscopic scale (or *microscale*), denoted by L_{micro}, which corresponds to the smallest microconstituent (*microelement*) whose properties and shape are supposed to have a direct influence on the overall response of the continuum infinitesimal material neighborhood; the third scale, denoted by L_{RVE}, is an intermediate scale (also referred to as mesoscopic scale or *mesoscale*), which corresponds to the size of the RVE. These three scales are related to each other thought the following inequalities:

$$L_{\text{micro}} \ll L_{\text{RVE}} \ll L_{\text{macro}} \tag{2.1}$$

according to the well-known MMM (*micro-meso-macro*) principle[1], proposed by Hashin [161], also referred to as *principle of scale separation*.

Concerning the RVE determination in practical cases, three main approaches can be distinguished which are based on:

- *experimental observations*, by combining basic morphological tools with image analysis techniques to describe the geometrical dispersion of the considered medium (see, for instance, [162]);
- *analytical approaches*, as in [157], where an explicit nonlocal constitutive equation is employed;
- *numerical methods*, by combining finite element simulations and statistical analyses as a *post-processing* step (see, for instance, [163]).

2.1.1.2 Problem setting

Consider the linear elasticity problem for a random heterogeneous material occupying the open bounded set $\Omega \subset \mathbb{R}^3$, under the assumptions of small displacements and quasistatic loading. According to the principle of scale separation, this standard continuum, which is generally regarded as a manifold of material points with (global) position vectors $\overline{\mathbf{x}}$, is now supposed to consist of a manifold of RVEs centered at $\overline{\mathbf{x}}$ (the overbar refers to the macroscopic scale); any representative volume element is denoted by Ω_{RVE}, and a local reference Cartesian coordinate system is introduced to locate the material points inside the RVE at the microscopic level (see Fig. 2.1).

[1] Eq. (2.1) is rigorously valid only in the case of random distribution of inhomogeneities; on the contrary, for ordered (e.g. periodic) microstructures the first inequality is replaced by $L_{\mathrm{micro}} < L_{\mathrm{RVE}}$, i.e. the scale separation between the microscopic and mesoscopic scales is no longer required, leading to the introduction of the concept of *repeating cell* instead of the RVE.

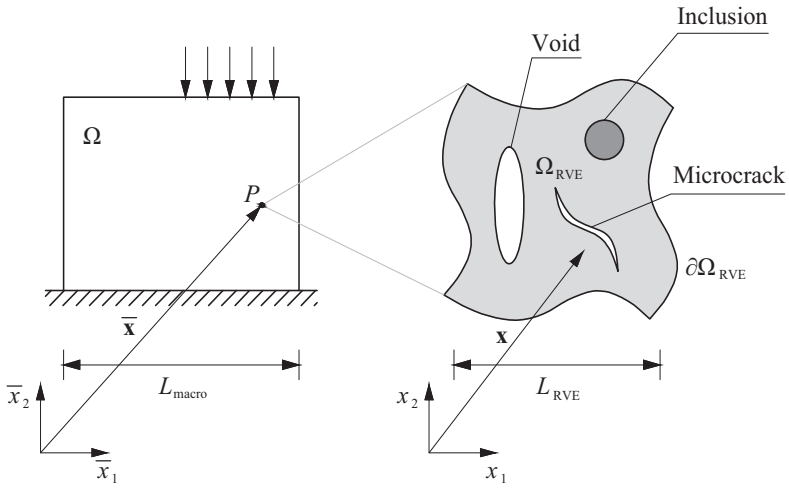

Fig. 2.1 Schematic representation of a random heterogeneous material.

The domain of each RVE associated with the infinitesimal neighborhood of $\overline{\mathbf{x}}$ is assumed to consist of a solid part $\Omega^{(s)}_{\mathrm{RVE}}$ and a void part $\Omega^{(v)}_{\mathrm{RVE}}$:

$$\Omega_{\mathrm{RVE}} = \Omega^{(s)}_{\mathrm{RVE}} \cup \Omega^{(v)}_{\mathrm{RVE}}, \tag{2.2}$$

where $\Omega^{(v)}_{\mathrm{RVE}}$ may consist of cracks and holes which can, in general, be subjected to self-contact or may be filled with a pressurized fluid. However, for the sake of simplicity, contact between the crack faces is not considered in the following; furthermore, only RVEs whose void part does not interest the RVE boundary are considered.

The scope of homogenization is to compute the *effective moduli tensor* $\overline{\mathbb{C}}$ at each point $\overline{\mathbf{x}}$ of the composite, such that:

$$\overline{\boldsymbol{\sigma}} = \overline{\mathbb{C}} : \overline{\boldsymbol{\epsilon}}, \tag{2.3}$$

where $\overline{\boldsymbol{\epsilon}}$ and $\overline{\boldsymbol{\sigma}}$ are the macroscopic strain and stress of the composite; $\overline{\boldsymbol{\epsilon}}$ and $\overline{\boldsymbol{\sigma}}$ are regarded as the unweighted volume average of the corresponding microscopic fields $\boldsymbol{\epsilon}(\mathbf{x})$ and $\boldsymbol{\sigma}(\mathbf{x})$ over the RVE attached to $\overline{\mathbf{x}}$, as will be shown in Sections 2.1.1.3 and 2.1.1.4.

2.1.1.3 RVE kinematics

The starting point of the classical micromechanical theory of heterogeneous materials is the assumption that the strain tensor $\overline{\boldsymbol{\varepsilon}}$ at a point $\overline{\mathbf{x}}$ of the macrocontinuum is the *unweighted volume average* of the so-called microscopic strain field $\boldsymbol{\varepsilon}$ over the RVE associated with $\overline{\mathbf{x}}$:

$$\overline{\boldsymbol{\varepsilon}} = \langle \boldsymbol{\varepsilon}(\mathbf{x}) \rangle_{\Omega_{\mathrm{RVE}}} = \frac{1}{|\Omega_{\mathrm{RVE}}|} \int_{\Omega_{\mathrm{RVE}}} \boldsymbol{\varepsilon}(\mathbf{x}) \, \mathrm{d}V, \tag{2.4}$$

where $\langle \cdot \rangle_{\Omega_{\mathrm{RVE}}}$ is the volume average operator, $|\cdot|$ is the Lebesgue measure, defining the conventional volume in the Euclidean space $\mathbb{R}^3$, and $\mathbf{x}$ denotes the position of a material point inside the RVE with respect to the fixed local frame (see Fig. 2.1).

The microscopic strain field $\boldsymbol{\varepsilon}$ must fulfill the following compatibility equation:

$$\boldsymbol{\varepsilon} = \nabla \otimes_s \mathbf{u}, \tag{2.5}$$

where $\otimes_s$ is the symmetric part of the tensor product $\otimes$, and $\mathbf{u}$ denotes the microscopic displacement field of the RVE. It should be noted that, in the presence of voids inside the RVE, Eq. (2.4) is valid only in a generalized sense, because the microscopic displacement and strain fields are not defined over the void subdomain $\Omega^{(v)}_{\mathrm{RVE}}$; a rigorous general definition of macroscopic strain is:

$$\overline{\boldsymbol{\varepsilon}} = \frac{1}{|\Omega_{\mathrm{RVE}}|} \left(\int_{\Omega^{(s)}_{\mathrm{RVE}}} \boldsymbol{\varepsilon}(\mathbf{x}) \, \mathrm{d}V + \int_{\partial\Omega^{(v)}_{\mathrm{RVE}}} \mathbf{u} \otimes_s \mathbf{n} \, \mathrm{d}S \right), \tag{2.6}$$

where $\mathbf{n}$ denotes the outer unit normal vector at $\mathbf{x} \in \partial\Omega^{(v)}_{\mathrm{RVE}}$ (see [151] for additional details).

By applying the divergence theorem to Eq. (2.4) and taking into account the symmetry of the gradient operator, the macroscopic strain field can be expressed in terms of the boundary displacements $\mathbf{u}$ on $\partial\Omega_{\mathrm{RVE}}$, as follows:

$$\overline{\boldsymbol{\varepsilon}} = \frac{1}{|\Omega_{\mathrm{RVE}}|} \int_{\partial\Omega_{\mathrm{RVE}}} \mathbf{u} \otimes_s \mathbf{n} \, \mathrm{d}S, \tag{2.7}$$

where **n**, here, denotes the outer unit normal vector at $\mathbf{x} \in \partial\Omega_{\mathrm{RVE}}$. The assumption (2.7) naturally defines a constraint on the possible displacement fields of the RVE, i.e. only fields **u** satisfying Eq. (2.7) can be said to be kinematically admissible. Formally, a microscopic displacement field **u** is kinematically admissible if:

$$\mathbf{u} \in \mathscr{V}, \tag{2.8}$$

where the *set of kinematically admissible microscopic displacements* $\mathscr{V}$ is defined as:

$$\mathscr{V} \equiv \left\{ \mathbf{v} \in H^1(\Omega) \mid \frac{1}{|\Omega_{\mathrm{RVE}}|} \int_{\partial\Omega_{\mathrm{RVE}}} \mathbf{v} \otimes_s \mathbf{n} \, \mathrm{d}S = \overline{\boldsymbol{\varepsilon}} \right\}, \tag{2.9}$$

where H^1 is the Sobolev space[2].

Without loss of generality, the microscopic displacement field $\mathbf{u}(\mathbf{x})$ can be assumed to be a function of the macroscopic strain $\overline{\boldsymbol{\varepsilon}}$, and expressed as the sum of a linear part $\overline{\boldsymbol{\varepsilon}}\mathbf{x}$, representing a homogenous deformation, and of a correction part $\mathbf{w}(\mathbf{x})$ associated with a nonhomogeneous deformation, also referred to as *fluctuation field*, i.e.

$$\mathbf{u}(\mathbf{x}) = \overline{\boldsymbol{\varepsilon}}\mathbf{x} + \mathbf{w}(\mathbf{x}). \tag{2.10}$$

In accordance with the additive split (2.10), the microscopic strain field is decomposed as follows:

[2] The Sobolev space $H^1(\Omega)$ is defined as the space of functions which belong to the space $L^2(\Omega)$ of square-integrable functions on Ω, together with their first-order derivatives (intended in a distributional sense), i.e. $H^1(\Omega) = \left\{ \mathbf{w}(\mathbf{x}) \in L^2(\Omega) : \nabla\mathbf{w}(\mathbf{x}) \in L^2(\Omega) \right\}$.

$$\boldsymbol{\varepsilon}(\mathbf{x}) = \overline{\boldsymbol{\varepsilon}} + \nabla \otimes_s \mathbf{w}, \tag{2.11}$$

where the homogenous contribution coincides with the macroscopic strain.

By substituting Eq. (2.10) into Eq. (2.7), one can obtain after some manipulations:

$$\frac{1}{|\Omega_{\mathrm{RVE}}|} \int_{\partial\Omega_{\mathrm{RVE}}} \mathbf{w} \otimes_s \mathbf{n} \, \mathrm{d}S = \mathbf{0}, \tag{2.12}$$

leading to the following constraint, which is equivalent to the constraint (2.8):

$$\mathbf{w} \in \mathscr{V}_0, \tag{2.13}$$

where:

$$\mathscr{V}_0 \equiv \left\{ \mathbf{v} \in H^1(\Omega) \mid \int_{\partial\Omega_{\mathrm{RVE}}} \mathbf{v} \otimes_s \mathbf{n} \, \mathrm{d}S = \mathbf{0} \right\} \tag{2.14}$$

is the vector space of kinematically admissible displacement fluctuations of the RVE.

2.1.1.4 Equilibrium of the RVE and definition of average stress

In order to derive the equilibrium equations for the RVE, let $\boldsymbol{\sigma} = \boldsymbol{\sigma}(\mathbf{x})$ denote the *microscopic stress* field. Assuming that body forces are negligible[3] and that the RVE is subjected to an external traction field $\mathbf{t} = \mathbf{t}(\mathbf{x})$ on its external boundary $\partial\Omega_{\mathrm{RVE}}$, the principle of virtual work establishes that the RVE is in equilibrium if and only if the variational equation

[3] The assumption of zero body forces appears to be realistic in most practical cases; indeed, the surface forces are usually much greater than the body forces, due to large surface to volume ratio in micromechanics, according to the principle of scale separation.

$$\int_{\Omega_{\mathrm{RVE}}^{(s)}} \boldsymbol{\sigma} : (\nabla \otimes_{\mathrm{s}} \delta\mathbf{u})\, \mathrm{d}V = \int_{\partial\Omega_{\mathrm{RVE}}} \mathbf{t} \cdot \delta\mathbf{u}\, \mathrm{d}S \qquad \forall \delta\mathbf{u} \in \mathscr{V}^* \tag{2.15}$$

holds, where $\delta\mathbf{u}$ is a *virtual displacement*, acting as a test function in a variational setting, and $\mathscr{V}^*$ is an appropriate space of virtual displacements of the RVE, coinciding with $\mathscr{V}_0$.

For sufficiently regular fields $\boldsymbol{\sigma}$, the variational formulation (2.15) can be written in the following equivalent strong formulation of the equilibrium equation:

$$\begin{cases} \nabla \cdot \boldsymbol{\sigma}(\mathbf{x}) = \mathbf{0} & \forall \mathbf{x} \in \Omega_{\mathrm{RVE}}^{(s)} \\ \boldsymbol{\sigma}(\mathbf{x}) \cdot \mathbf{n} = \mathbf{t} & \forall \mathbf{x} \in \partial\Omega_{\mathrm{RVE}} \end{cases} \tag{2.16}$$

where $\mathbf{n}$ is the outer unit normal vector to the RVE boundary.

From duality arguments it follows that the macroscopic stress tensor $\overline{\boldsymbol{\sigma}}$ at a point $\overline{\mathbf{x}}$ of the macrocontinuum is the *unweighted volume average* of the so-called microscopic stress field $\boldsymbol{\sigma}$ over the RVE associated with $\overline{\mathbf{x}}$:

$$\overline{\boldsymbol{\sigma}} = \langle \boldsymbol{\sigma}(\mathbf{x}) \rangle_{\Omega_{\mathrm{RVE}}} = \frac{1}{|\Omega_{\mathrm{RVE}}|} \int_{\Omega_{\mathrm{RVE}}} \boldsymbol{\sigma}(\mathbf{x})\, \mathrm{d}V. \tag{2.17}$$

Eq. (2.17) is valid only in a generalized sense, because the microscopic stress is not defined over the void subdomain $\Omega_{\mathrm{RVE}}^{(v)}$; thus it can be replaced by

$$\overline{\boldsymbol{\sigma}} = \frac{1}{|\Omega_{\mathrm{RVE}}|} \int_{\Omega_{\mathrm{RVE}}^{(s)}} \boldsymbol{\sigma}(\mathbf{x})\, \mathrm{d}V. \tag{2.18}$$

The macroscopic stress can be alternatively expressed in terms of RVE boundary tractions; by applying the divergence theorem to Eq. (2.18), combined with the identity $\nabla \otimes \mathbf{x} = \mathbf{I}$ (where $\mathbf{I}$ denotes the second-order identity tensor), one obtains after manipulations

$$\int_{\Omega^{(s)}_{\mathrm{RVE}}} \boldsymbol{\sigma}(\mathbf{x})\,\mathrm{d}V = \int_{\partial\Omega_{\mathrm{RVE}}} (\boldsymbol{\sigma}\cdot\mathbf{n})\otimes\mathbf{x}\,\mathrm{d}S - \int_{\Omega^{(s)}_{\mathrm{RVE}}} (\nabla\cdot\boldsymbol{\sigma})\otimes\mathbf{x}\,\mathrm{d}V. \tag{2.19}$$

Then, introducing the strong form (2.16) of equilibrium equations, the following expression for the homogenized stress, exclusively in terms of RVE boundary tractions, is obtained:

$$\overline{\boldsymbol{\sigma}} = \int_{\partial\Omega_{\mathrm{RVE}}} \mathbf{t}\otimes\mathbf{x}\,\mathrm{d}S. \tag{2.20}$$

It is worth noting that the average stress must be independent of the origin of the local coordinate system, therefore it is meaningful only if the prescribed surface tractions are self-equilibrating.

2.1.1.5 Hill-Mandel's macro-homogeneity principle

The Hill-Mandel's *macro-homogeneity principle* plays a fundamental role in the formulation of multiscale constitutive models (see [151]); based on physical arguments, it establishes that the power of the macroscopic stress must equal the volume average of the power of the microscopic stress over the RVE, i.e. at any RVE configuration characterized by an equilibrate stress state $\boldsymbol{\sigma}$, the identity

$$\overline{\boldsymbol{\sigma}} : \dot{\overline{\boldsymbol{\varepsilon}}} = \frac{1}{|\Omega_{\mathrm{RVE}}|}\int_{\Omega^{(s)}_{\mathrm{RVE}}} \boldsymbol{\sigma} : \dot{\boldsymbol{\varepsilon}}\,\mathrm{d}V \tag{2.21}$$

must hold for any kinematically admissible microscopic strain rate field $\dot{\boldsymbol{\varepsilon}}$; in the present setting, a microscopic strain rate is said to be kinematically admissible if

$$\dot{\boldsymbol{\varepsilon}} = \dot{\overline{\boldsymbol{\varepsilon}}} + \nabla\otimes_s \dot{\mathbf{w}} \qquad \dot{\mathbf{w}}\in\mathscr{V}^*, \tag{2.22}$$

where $\mathscr{V}^*$ is the prescribed space of kinematically admissible fluctuation velocities.

This principle follows directly from the definitions of average strain (2.4) and average stress (2.18), which allows to decompose the microscopic stress and strain rate fields as follows[4]:

$$\begin{aligned} \boldsymbol{\sigma}(\mathbf{x}) &= \overline{\boldsymbol{\sigma}} + \boldsymbol{\sigma}^*(\mathbf{x}) \\ \dot{\boldsymbol{\varepsilon}}(\mathbf{x}) &= \dot{\overline{\boldsymbol{\varepsilon}}} + \dot{\boldsymbol{\varepsilon}}^*(\mathbf{x}) \end{aligned} \tag{2.23}$$

where $\boldsymbol{\sigma}^*(\mathbf{x})$ and $\dot{\boldsymbol{\varepsilon}}^*(\mathbf{x})$ are the zero-mean fluctuations of $\boldsymbol{\sigma}(\mathbf{x})$ and $\dot{\boldsymbol{\varepsilon}}(\mathbf{x})$, respectively, i.e.

$$\begin{aligned} \int_{\Omega^{(s)}_{\mathrm{RVE}}} \boldsymbol{\sigma}^*(\mathbf{x})\, \mathrm{d}V &= \mathbf{0} \\ \int_{\Omega^{(s)}_{\mathrm{RVE}}} \dot{\boldsymbol{\varepsilon}}^*(\mathbf{x})\, \mathrm{d}V &= \mathbf{0}. \end{aligned} \tag{2.24}$$

By using Eqs. (2.23) and (2.24), the averaged microstructural work in the right-hand side of Eq. (2.21) may be expressed as follows:

$$\frac{1}{|\Omega_{\mathrm{RVE}}|} \int_{\Omega^{(s)}_{\mathrm{RVE}}} \boldsymbol{\sigma} : \dot{\boldsymbol{\varepsilon}}\, \mathrm{d}V = \overline{\boldsymbol{\sigma}} : \dot{\overline{\boldsymbol{\varepsilon}}} + \frac{1}{|\Omega_{\mathrm{RVE}}|} \int_{\Omega^{(s)}_{\mathrm{RVE}}} \boldsymbol{\sigma}^* : \dot{\boldsymbol{\varepsilon}}^*\, \mathrm{d}V. \tag{2.25}$$

Thus, Eq. (2.21) holds provided that the following condition is satisfied:

$$\frac{1}{|\Omega_{\mathrm{RVE}}|} \int_{\Omega^{(s)}_{\mathrm{RVE}}} \boldsymbol{\sigma}^* : \dot{\boldsymbol{\varepsilon}}^*\, \mathrm{d}V = 0, \tag{2.26}$$

which can be expressed in an different form by applying the divergence theorem:

[4] An alternative approach, based on the *variational theory of homogenization*, consists in deriving the definition of macroscopic stress from the Hill-Mandel's principle, regarded as an assumption of the theory; according to this approach, the external surface tractions $\mathbf{t}$ are required to be *purely reactive*. That is, they are considered as reactions to the kinematical constraints imposed upon the RVE and cannot be prescribed arbitrarily.

$$\frac{1}{|\Omega_{\mathrm{RVE}}|}\int_{\partial\Omega_{\mathrm{RVE}}}\left(\mathbf{t}-\overline{\boldsymbol{\sigma}}\cdot\mathbf{n}\right)\cdot\left(\mathbf{u}-\dot{\overline{\boldsymbol{\varepsilon}}}\cdot\mathbf{x}\right)\mathrm{d}V=0. \tag{2.27}$$

It can be shown that if Ω_{RVE} is a subdomain of a material consisting of similar microstructures, the left-hand side of Eq. (2.27) decays to zero as the size of Ω_{RVE} increases; thus the Hill-Mandel's principle holds when a sufficiently large RVE is taken from a composite with a *statistically homogenous* microstructure. From a physical point of view, statistical homogeneity means that the probability of finding a phase at a microscopic point inside the RVE does not depend on the macroscopic point to which the RVE is attached.

Moreover Eq. (2.27) suggests the following conditions satisfying the Hill-Mandel's principle (2.21):

$$\begin{cases}\mathbf{u}=\overline{\boldsymbol{\varepsilon}}\cdot\mathbf{x} & \text{(linear boundary displacements)}\\ \mathbf{t}=\overline{\boldsymbol{\sigma}}\cdot\mathbf{n} & \text{(uniform boundary tractions)}\end{cases} \tag{2.28}$$

even if Ω_{RVE} is not statistically homogeneous. A third type of boundary condition, i.e. the so-called *mixed orthogonal boundary condition*, is also possible, in which one specifies both tractions and displacements on the boundary. Each of these boundary conditions, if applied to an arbitrary microstructure whose size is $L_{\mathrm{RVE}}<\infty$ results is a different overall stiffness tensor.

Moreover, the following universal inequalities are valid for the strain fields of a common volume average

$$\langle\boldsymbol{\varepsilon}^{\sigma}:\mathbb{C}:\boldsymbol{\varepsilon}^{\sigma}\rangle_{\Omega_{\mathrm{RVE}}}\leq\langle\boldsymbol{\varepsilon}^{g}:\mathbb{C}:\boldsymbol{\varepsilon}^{g}\rangle_{\Omega_{\mathrm{RVE}}}\leq\langle\boldsymbol{\varepsilon}^{\varepsilon}:\mathbb{C}:\boldsymbol{\varepsilon}^{\varepsilon}\rangle_{\Omega_{\mathrm{RVE}}}, \tag{2.29}$$

where $\boldsymbol{\varepsilon}^{\varepsilon}$, $\boldsymbol{\varepsilon}^{g}$, and $\boldsymbol{\varepsilon}^{\sigma}$ are the strain fields with a common volume average when Ω_{RVE} is subjected to linear displacement boundary conditions, general (possibly mixed) boundary conditions, and uniform traction boundary conditions, respectively.

The limit $L_{\mathrm{RVE}}\to\infty$ results in the mesoscale properties converging towards the uniquely defined *effective stiffness tensor* $\overline{\mathbb{C}}$ of the representative volume element [164], as shown in Fig. 2.2.

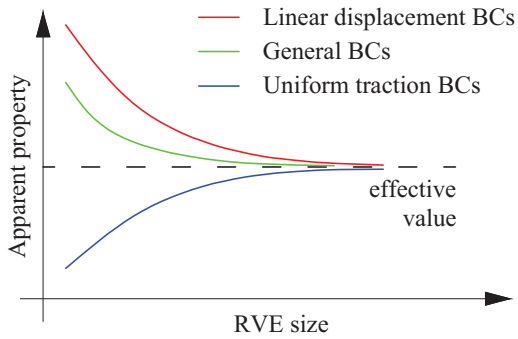

Fig. 2.2 Convergence of the apparent properties to the effective values with increasing RVE size for different types of BCs.

2.1.1.6 Effective moduli tensor for a two-phase composite material

Here, a two-phase composite material is considered, made of inclusions embedded in a continuous matrix; both matrix and reinforcements are assumed to be linearly elastic and isotropic, and reinforcements are perfectly bonded to the matrix, and randomly oriented and distributed. For such a composite, the effective elasticity tensor $\overline{\mathbb{C}}$ appearing in Eq. (2.3) can be expressed in terms of a *strain concentrator tensor* $\mathbb{A}$, which relates the average strain of the inclusion phase $\overline{\boldsymbol{\varepsilon}}_I$ to that of the composite $\overline{\boldsymbol{\varepsilon}}$, through $\overline{\boldsymbol{\varepsilon}}_I = \mathbb{A} : \overline{\boldsymbol{\varepsilon}}$, as follows:

$$\overline{\mathbb{C}} = \mathbb{C}_M + f(\mathbb{C}_I - \mathbb{C}_M) : \mathbb{A}, \tag{2.30}$$

where $\mathbb{C}_M$ and $\mathbb{C}_I$ are the elasticity tensors of the matrix and inclusion phases, respectively, and f is the volume fraction of the inclusion phase.

In the average field theory, the strain concentration tensor can be analytically estimated by means of various averaging schemes, such as the *dilute distribution* scheme, the *self-consistent method*, or the *Mori-Tanaka method*, based on the Eshelby's *equivalence principle* (see [151] for additional details). The main assumption in the dilute model is that a single inclusion is embedded in an infinite matrix subjected to a remote loading, thus neglecting the interaction between the different inclusions. In the self-consistent model, a single

inclusion is embedded in an infinite equivalent medium, whose properties are not known a priori; therefore it usually requires an iterative solution scheme. In the Mori-Tanaka model, the strain (or stress) field in the matrix is, at a sufficient distance from an inclusion, approximated by a constant strain (or stress) field.

These analytical and semi-analytical models are often reduced to specific cases; thus, *numerical* approaches have proved to be more suitable for describing the overall behavior of composite materials, since no restriction about geometry, material properties, number of phases, and size, is required. These models are based on approximate techniques, such as *unit cell methods* [165], *windowing approaches* [166], or *embedded cell approaches* [167]; these techniques are able to model heterogeneous materials by means of discrete models, by using approximation techniques such as the finite element method.

2.1.2 Theory of asymptotic homogenization

Although the traditional physical approach of the average field theory is very intuitive, it is not able to uniquely define the effective mechanical properties; in particular, the effective moduli tensor $\overline{\mathbb{C}}$ may depend on the choice of the sample size, or the boundary conditions.

The mathematical theory of homogenization, developed since the 1970s, is used as an alternative approach to obtain the effective properties of the equivalent homogenized material [19, 20]; it is a limit theory which takes advantage of the asymptotic expansion and the assumption of periodicity to replace the original differential equations with rapidly oscillating coefficients, with differential equations whose coefficients are constant or slowly varying, such that the related solution is close to that of the original problem.

In the framework of the mathematical theory of homogenization, rather than considering a single heterogeneous material with a given length scale ε, the problem is embedded in a sequence of similar problems with asymptotically decreasing values of the length scale (i.e. $\varepsilon \to 0$); then, the moduli tensor of the limit problem is said to be the *effective* or *homogenized* moduli tensor.

This apparently more complex approach has the advantage of uniquely defining the homogenized properties. Furthermore, the approximation made by using the effective properties instead of the actual heterogeneous properties can be rigorously justified by computing the resulting error.

2.1.2.1 Basic principles

In this section the linear elastic boundary value problem (BVP) of a composite material subjected to a quasistatic loading, is considered. Let Ω be the region occupied by the composite, defined as a bounded open set in $\mathbb{R}^N$ with $N \geq 1$ the space dimension; its boundary $\partial\Omega = \partial_t\Omega \cup \partial_u\Omega$ is supposed to be Lipschitz continuous such that $\partial_t\Omega \cap \partial_u\Omega = \varnothing$ and the measure of $\partial_u\Omega$ is greater than zero to avoid rigid-body motions. Such structure is subjected to a system of body forces $\mathbf{f}$, and of surface forces $\mathbf{t}$ on $\partial_t\Omega$, whereas a prescribed displacement $\overline{\mathbf{u}}$ is applied on $\partial_u\Omega$. The domain Ω is highly heterogeneous, and exhibits a periodic microstructure whose length scale l is defined by a small parameter $\varepsilon \equiv \frac{l}{L} \ll 1$, with L the characteristic size of the macroscopic problem. Thus, the considered domain can be regarded as the union of translated homotheties of a *repeating cell*. The choice of the repeating cell depends on the specific microstructure, but is not unique. In the literature, the most common repeating cell is the unit cube $[0, 1)^N$, which is also used is the present work, under the name of *repeating unit cell* (RUC)[5], usually denoted by Y (see Fig. 2.3).

The considered problem is characterized by the existence of two separated length scales associated with the macroscopic and microscopic phenomena. This *separation of scales* can be formally expressed by introducing two sets of dimensionless coordinates, $\mathbf{x}^* = \frac{\mathbf{x}}{L}$ and $\mathbf{y}^* = \frac{\mathbf{x}}{l}$, where $\mathbf{x}$ is the dimen-

[5] The only topological requirement for a repeating cell is its *paving property*, according to which the whole space $\mathbb{R}^N$ can be covered by the disjoint union of translated copies of Y. For instance, the unit square is the simplest repeating cell for microstructures made of a periodically distributed square array, whereas hexagonal repeating cells are most suitable for describing honeycomb-like microstructures or the cross-sections of large wire ropes.

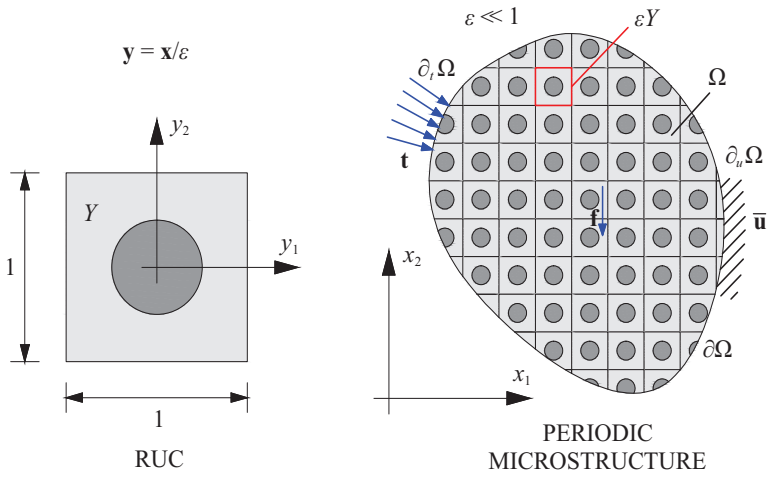

Fig. 2.3 Elasticity problem for a heterogeneous medium exhibiting a periodic microstructure and associated repeating unit cell (RUC).

sional variable: the global coordinate $\mathbf{x}^*$ (also called macroscopic or *slow* variable) refers to the whole body Ω, whereas the stretched local coordinate $\mathbf{y}^*$ (also referred to as microscopic or *fast* variable) is defined in such a way that $\mathbf{y}^* = \mathbf{x}^*/\varepsilon \in Y$; in the following these dimensionless variables are simply denoted by $\mathbf{x}$ and $\mathbf{y}$, respectively.

By virtue of the repetitiveness of the microscopic constituents, the elastic properties are fully described if they are defined over a single period Y related to coordinate system $\mathbf{y}$. Let $\mathbb{C}(\mathbf{y})$ be the (fourth-order) elasticity tensor on Y, which is generally discontinuous in $\mathbf{y}$ (to model the jump in elastic properties from one phase to the other). The function $\mathbb{C} : Y \to \mathbb{R}^{N\times N\times N\times N}$ is extended by Y-periodicity to the entire macroscopic domain Ω, leading to the following definition for the elasticity tensor at any material point $\mathbf{x}$ of the considered body:

$$\mathbb{C}^{\varepsilon}(\mathbf{x}) := \mathbb{C}\left(\frac{\mathbf{x}}{\varepsilon}\right), \tag{2.31}$$

where the superscript ε is used to indicate the dependence of the elastic properties on the length scale of the microstructure.

Therefore, the stress, strain and displacement fields, denoted by $\boldsymbol{\sigma}$, $\boldsymbol{\varepsilon}$ and $\mathbf{u}$, respectively, are assumed to be rapidly varying, and the equilibrium state of the heterogeneous material (under the assumption of small deformations) is described by the following system of equations:

$$\begin{aligned} -\nabla \cdot \boldsymbol{\sigma}^{\varepsilon} &= \mathbf{f}^{\varepsilon} \\ \boldsymbol{\sigma}^{\varepsilon} &= \mathbb{C}^{\varepsilon} : \boldsymbol{\varepsilon}^{\varepsilon} \qquad \forall \mathbf{x} \in \Omega \\ \boldsymbol{\varepsilon}^{\varepsilon} &= \nabla \otimes_s \mathbf{u}^{\varepsilon} \end{aligned} \tag{2.32}$$

with associated boundary conditions:

$$\begin{aligned} \boldsymbol{\sigma}^{\varepsilon} \cdot \mathbf{n} &= \mathbf{t} \qquad \forall \mathbf{x} \in \partial_t \Omega \\ \mathbf{u}^{\varepsilon} &= \overline{\mathbf{u}} \qquad \forall \mathbf{x} \in \partial_u \Omega \end{aligned} \tag{2.33}$$

where $\otimes_s$ is the symmetric part of the tensor product, and $\mathbf{n}$ is the unit normal to the boundary. Since each component does not need to be isotropic, $\mathbb{C}$ represents any fourth-order tensor that is bounded and positive-definite, i.e. there exist two constants $\alpha, \beta \in \mathbb{R}^+$ with $\alpha \leq \beta$ such that

$$\alpha \|\boldsymbol{\xi}^{\mathrm{sym}}\|^2 \leq \frac{1}{2}\boldsymbol{\xi} : \mathbb{C} : \boldsymbol{\xi} \leq \beta \|\boldsymbol{\xi}^{\mathrm{sym}}\|^2 \quad \forall \mathbf{x} \in \Omega, \forall \boldsymbol{\xi} \in \mathbb{R}^{N \times N}, \tag{2.34}$$

where $\boldsymbol{\xi}^{sym} := \frac{1}{2}\left(\boldsymbol{\xi} + \boldsymbol{\xi}^{\mathrm{T}}\right)$. Moreover, the elastic constants of the solid are assumed to have the following symmetries: $C_{ijhk} = C_{jihk} = C_{ijkh} = C_{hkij}$.

From a mathematical point of view, problem (2.32) together with boundary conditions (2.33) is well posed; in other words, if the source term $\mathbf{f}(\mathbf{x})$ belongs to the space $L^2(\Omega)$ of square-integrable functions on Ω, then the Lax-Milgram theorem implies existence and uniqueness of the solution $\mathbf{u}$ in the Sobolev space $H^1(\Omega)$.

Here it should be noticed that it is not allowed to apply the divergence operator in Eq. (2.32), because the elasticity tensor is not differentiable (in the case of microstructure made of two different constituents, $\mathbb{C}$ is defined as a

piecewise constant function over Y). As a consequence, it is more advisable to formulate the considered BVP in a variational sense; thus, the *principle of virtual displacements* can be stated in index notation, as follows: find $\mathbf{u}^\epsilon \in \mathscr{V}$ such that

$$\int_\Omega C^\epsilon_{ijhk} \frac{\partial u^\epsilon_h}{\partial x_k} \frac{\partial v_i}{\partial x_j} \, \mathrm{d}\Omega = \int_\Omega f^\epsilon_i v_i \, \mathrm{d}\Omega + \int_{\partial_t\Omega} t_i v_i \, \mathrm{d}S \tag{2.35}$$

for any test function $\mathbf{v} \in \mathscr{V}_0$, where

$$\begin{aligned} \mathscr{V} &= \left\{ \mathbf{v} \in H^1(\Omega) \,:\, \mathbf{v}|_{\partial_u\Omega} = \overline{\mathbf{u}} \right\} \\ \mathscr{V}_0 &= \left\{ \mathbf{v} \in H^1(\Omega) \,:\, \mathbf{v}|_{\partial_u\Omega} = \mathbf{0} \right\}. \end{aligned} \tag{2.36}$$

At first sight, if the domain Ω is reasonably simple, one can use a classical finite element method to solve the problem. However, it is clear that the spatial discretization needs to capture the oscillations of the elasticity tensor $\mathbb{C}^\epsilon$, and of the displacement field $\mathbf{u}^\epsilon$, thus the adopted mesh should have a linear size $h \ll \epsilon$. For very small values of ϵ it is not realistic to mesh the entire domain and assemble the discretized version of Eq. (2.35); therefore it is preferable to average or homogenize the properties of Ω, in order to obtain an approximation of $\mathbf{u}^\epsilon$ on a coarse mesh.

2.1.2.2 Asymptotic expansions and equilibrium equations

The method of two-scale asymptotic expansions postulates that the solution $\mathbf{u}^\epsilon$ to a problem with periodic microstructure is expressed as a series in integer powers of the microscale parameter ϵ (see [168-170]):

$$\mathbf{u}^\epsilon(\mathbf{x}) = \sum_{i=0}^{+\infty} \epsilon^i \mathbf{u}^i(\mathbf{x}, \mathbf{y}), \quad \mathbf{y} = \mathbf{x}/\epsilon, \tag{2.37}$$

where each term $\mathbf{u}^i : \Omega \times Y \to \mathbb{R}^N$, which is a function of both variables $\mathbf{x}$ and $\mathbf{y}$, has the same periodicity as $\mathbb{C}^\epsilon$ with respect to $\mathbf{x}$.

Since it is known that any field variable $\Phi(\mathbf{x}, \mathbf{y})$ depends on the two length scales, the (total) spatial gradient of Φ is obtained by using the following *chain rule*:

$$\nabla\Phi(\mathbf{x}, \mathbf{y}) = \big(\nabla_x\Phi + \varepsilon^{-1}\nabla_y\Phi\big)(\mathbf{x}, \mathbf{y}), \tag{2.38}$$

where ∇_x and ∇_y are the gradients with respect to the first and second arguments of $\Phi(\mathbf{x}, \mathbf{y})$, respectively; Eq. (2.38) can be rewritten by components as follows:

$$\frac{\mathrm{d}}{\mathrm{d}x_i}\big(\Phi(\mathbf{x}, \mathbf{y})\big) = \frac{\partial\Phi}{\partial x_i} + \frac{1}{\varepsilon}\frac{\partial\Phi}{\partial y_i}. \tag{2.39}$$

Therefore, by introducing the expansion (2.37) and the chain rule (2.39) into Eq. (2.35), the strain field tensor may be expressed as follows:

$$\begin{aligned}\int_\Omega C^\varepsilon_{ijhk}\Bigg\{&\frac{1}{\varepsilon^2}\frac{\partial u^0_h}{\partial y_k}\frac{\partial v_i}{\partial y_j} + \frac{1}{\varepsilon}\left[\left(\frac{\partial u^0_h}{\partial x_k} + \frac{\partial u^1_h}{\partial y_k}\right)\frac{\partial v_i}{\partial y_j} + \frac{\partial u^0_h}{\partial y_k}\frac{\partial v_i}{\partial x_j}\right]\\ &+ \left[\left(\frac{\partial u^0_h}{\partial x_k} + \frac{\partial u^1_h}{\partial y_k}\right)\frac{\partial v_i}{\partial x_j} + \left(\frac{\partial u^1_h}{\partial x_k} + \frac{\partial u^2_h}{\partial y_k}\right)\frac{\partial v_i}{\partial y_j}\right]\\ &+ \varepsilon(\dots)\Bigg\}\,\mathrm{d}\Omega = \int_\Omega f^\varepsilon_i v_i\,\mathrm{d}\Omega + \int_{\partial_t\Omega} t_i v_i\,\mathrm{d}S\end{aligned} \tag{2.40}$$

for any $\mathbf{v} \in \mathscr{V}_{\Omega\times Y}$, where

$$\begin{aligned}\mathscr{V}_{\Omega\times Y} = \{&\mathbf{v}(\mathbf{x}, \mathbf{y}) \in \Omega\times Y \,:\, \mathbf{v}(\cdot, \mathbf{y})\ Y\text{-periodic};\\ &\mathbf{v}|_{\partial_u\Omega} = \mathbf{0};\ \mathbf{v}\ \text{smooth enough}\big\}.\end{aligned} \tag{2.41}$$

Similarly, $\mathscr{V}_\Omega$ and $\mathscr{V}_Y$ are defined as

$$\begin{aligned}\mathscr{V}_\Omega &= \big\{\mathbf{v}(\mathbf{x}) \in \Omega \,:\, \mathbf{v}|_{\partial_u\Omega} = \mathbf{0};\ \mathbf{v}\ \text{smooth enough}\big\}\\ \mathscr{V}_Y &= \{\mathbf{v}(\mathbf{x}) \in Y \,:\, \mathbf{v}(\mathbf{y})\ Y\text{-periodic};\ \mathbf{v}\ \text{smooth enough}\}.\end{aligned} \tag{2.42}$$

If it is assumed that the functions are smooth enough so that the limit for $\varepsilon \to 0^+$ of all integrals exists, Eq. (2.40) holds if the terms of the same power of ε are equal to zero. Therefore

$$\frac{1}{\varepsilon^2}\int_\Omega C^\varepsilon_{ijhk}\frac{\partial u^0_h}{\partial y_k}\frac{\partial v_i}{\partial y_j}\,\mathrm{d}\Omega = 0 \tag{2.43}$$

$$\frac{1}{\varepsilon}\int_\Omega C^\varepsilon_{ijhk}\left[\left(\frac{\partial u^0_h}{\partial x_k}+\frac{\partial u^1_h}{\partial y_k}\right)\frac{\partial v_i}{\partial y_j}+\frac{\partial u^0_h}{\partial y_k}\frac{\partial v_i}{\partial x_j}\right]\mathrm{d}\Omega = 0 \tag{2.44}$$

$$\begin{aligned}\int_\Omega C^\varepsilon_{ijhk}\left[\left(\frac{\partial u^0_h}{\partial x_k}+\frac{\partial u^1_h}{\partial y_k}\right)\frac{\partial v_i}{\partial x_j}+\left(\frac{\partial u^1_h}{\partial x_k}+\frac{\partial u^2_h}{\partial y_k}\right)\frac{\partial v_i}{\partial y_j}\right]\mathrm{d}\Omega \\ = \int_\Omega f^\varepsilon_i v_i\,\mathrm{d}\Omega + \int_{\partial_t\Omega} t_i v_i\,\mathrm{d}S\end{aligned} \tag{2.45}$$

for any $\mathbf{v} \in \mathscr{V}_{\Omega\times Y}$. Considering that, for a Y-periodic function $\Psi(\mathbf{y})$

$$\lim_{\varepsilon\to 0^+}\int_\Omega \Psi\left(\frac{\mathbf{x}}{\varepsilon}\right)\mathrm{d}\Omega \to \frac{1}{|Y|}\int_\Omega\int_Y \Psi(\mathbf{y})\,\mathrm{d}Y\,\mathrm{d}\Omega, \tag{2.46}$$

multiplying Eq. (2.43) by ε^2 and taking the limit for $\varepsilon \to 0^+$, one obtains:

$$\frac{1}{|Y|}\int_\Omega\int_Y C_{ijhk}\frac{\partial u^0_h}{\partial y_k}\frac{\partial v_i}{\partial y_j}\,\mathrm{d}Y\,\mathrm{d}\Omega = 0 \quad \forall \mathbf{v} \in \mathscr{V}_{\Omega\times Y}. \tag{2.47}$$

Since $\mathbf{v}$ is an arbitrary function, it is useful to choose $\mathbf{v} = \mathbf{v}(\mathbf{y})$, i.e. $\mathbf{v} \in \mathscr{V}_Y$. After integrating by parts and applying the divergence theorem to the integral in Y, and using periodicity conditions on the opposite faces of the cube Y, one obtains from Eq. (2.47)

$$\frac{1}{|Y|}\int_\Omega\int_Y\left[-\frac{\partial}{\partial y_j}\left(C_{ijhk}\frac{\partial u^0_h}{\partial y_k}\right)\right]v_i\,\mathrm{d}Y\,d\Omega = 0 \quad \forall \mathbf{v} \in \mathscr{V}_{\Omega\times Y}. \tag{2.48}$$

It follows that the boundary value problem of the first term $\mathbf{u}^0$ of the expansion of the original solution $\mathbf{u}^\epsilon$ in the unit cell Y is:

$$-\frac{\partial}{\partial y_j}\left(C_{ijhk}\frac{\partial u_h^0}{\partial y_k}\right)=0 \quad \mathbf{y}\in Y. \tag{2.49}$$

A problem of type

$$\frac{\partial}{\partial y_j}\left(C_{ijhk}\frac{\partial \Phi(\mathbf{y})}{\partial y_k}\right)=F(\mathbf{y}) \quad \mathbf{y}\in Y \tag{2.50}$$

has unique solution Φ in $\mathscr{V}_Y$ (defined up to an additive constant), for a regular F, if and only if

$$\frac{1}{|Y|}\int_Y F(y)\,\mathrm{d}Y=0. \tag{2.51}$$

From this fact, and using Eq. (2.49), it directly follows that

$$\mathbf{u}^0(\mathbf{x},\mathbf{y})=\mathbf{u}^0(\mathbf{x}). \tag{2.52}$$

In other words, the first term of the asymptotic expansion $\mathbf{u}^\epsilon$ depends only on the macroscopic scale $\mathbf{x}$. Introducing (2.52) into (2.44), multiplying by ϵ, taking the limit for $\epsilon\to 0^+$ and using the property (2.46), one obtains

$$\int_\Omega \frac{1}{|Y|}\left[\int_Y C_{ijhk}\left(\frac{\partial u_h^0(\mathbf{x})}{\partial x_k}+\frac{\partial u_h^1}{\partial y_k}\right)\frac{\partial v_i}{\partial y_j}\,\mathrm{d}Y\right]\mathrm{d}\Omega=0 \tag{2.53}$$

for any $\mathbf{v}\in\mathscr{V}_{\Omega\times Y}$. Since (2.53) it is satisfied for any $\mathbf{v}$, by choosing $\mathbf{v}=\mathbf{v}(\mathbf{y})$ it follows:

$$\int_Y C_{ijhk}\left(\frac{\partial u_h^0(\mathbf{x})}{\partial x_k}+\frac{\partial u_h^1}{\partial y_k}\right)\frac{\partial v_i(\mathbf{y})}{\partial y_j}\,\mathrm{d}Y=0 \quad \forall\mathbf{v}\in\mathscr{V}_Y. \tag{2.54}$$

Introducing (2.52) into (2.45) and taking the limit for $\epsilon\to 0^+$, one obtains

$$\int_\Omega \left\{ \frac{1}{|Y|} \int_Y C_{ijhk} \left[\left(\frac{\partial u_h^0}{\partial x_k} + \frac{\partial u_h^1}{\partial y_k} \right) \frac{\partial v_i}{\partial x_j} + \left(\frac{\partial u_h^1}{\partial x_k} + \frac{\partial u_h^2}{\partial y_k} \right) \frac{\partial v_i}{\partial y_j} \right] \mathrm{d}Y \right\} \mathrm{d}\Omega = \int_\Omega \left(\frac{1}{|Y|} \int_Y f_i v_i \, \mathrm{d}Y \right) \mathrm{d}\Omega + \int_{\partial_t \Omega} t_i v_i \, \mathrm{d}S \tag{2.55}$$

for any $\mathbf{v} \in \mathscr{V}_{\Omega \times Y}$. Now, a statement of equilibrium at the macroscopic scale can be obtained by considering Eq. (2.45) and choosing $\mathbf{v} = \mathbf{v}(\mathbf{x})$:

$$\int_\Omega \left[\frac{1}{|Y|} \int_Y C_{ijhk} \left(\frac{\partial u_h^0}{\partial x_k} + \frac{\partial u_h^1}{\partial y_k} \right) \mathrm{d}Y \right] \frac{\partial v_i(\mathbf{x})}{\partial x_j} \, \mathrm{d}\Omega = \int_\Omega \left(\frac{1}{|Y|} \int_Y f_i \, \mathrm{d}Y \right) v_i(\mathbf{x}) \, \mathrm{d}\Omega + \int_{\partial_t \Omega} t_i v_i(\mathbf{x}) \, \mathrm{d}S \tag{2.56}$$

for any $\mathbf{v} \in \mathscr{V}_\Omega$.

If in Eq. (2.45) it is assumed $\mathbf{v} = \mathbf{v}(\mathbf{y})$, then it follows:

$$\int_\Omega \left[\frac{1}{|Y|} \int_Y C_{ijhk} \left(\frac{\partial u_h^1}{\partial x_k} + \frac{\partial u_h^2}{\partial y_k} \right) \frac{\partial v_i(\mathbf{y})}{\partial x_j} \, \mathrm{d}Y \right] \mathrm{d}\Omega = \int_\Omega \left(\frac{1}{|Y|} \int_Y f_i v_i(\mathbf{y}) \, \mathrm{d}Y \right) \mathrm{d}\Omega \quad \forall \mathbf{v} \in \mathscr{V}_Y \tag{2.57}$$

or equivalently,

$$\int_Y C_{ijhk} \left(\frac{\partial u_h^1}{\partial x_k} + \frac{\partial u_h^2}{\partial y_k} \right) \frac{\partial v_i(\mathbf{y})}{\partial x_j} \, \mathrm{d}Y = \int_Y f_i v_i(\mathbf{y}) \, \mathrm{d}Y, \quad \forall \mathbf{v} \in \mathscr{V}_Y, \tag{2.58}$$

which represents the equilibrium of the unit cell at the microscopic level.

By solving the set of equations (2.54), (2.56) and (2.58), the "full" solution in terms of $\mathbf{u}^0$, $\mathbf{u}^1$ and $\mathbf{u}^2$ can be obtained. However, if only the first order terms are needed, solving (2.54) and (2.56) yields the "full" solution for $\mathbf{u}^\epsilon$; the term $\mathbf{u}^0$ represents, essentially, the macroscopic mechanical behavior, whereas the term $\mathbf{u}^1$ represents the microscopic behavior.

2.1.2.3 Determination of effective elastic moduli

In the theory of periodic homogenization, it is assumed that

$$u_h^1(\mathbf{x},\mathbf{y}) = \chi_h^{lm}(\mathbf{x},\mathbf{y})\frac{\partial u_l^0(\mathbf{x})}{\partial x_m} + \tilde{u}_h^1(\mathbf{x}), \tag{2.59}$$

where χ_h^{lm} is the so-called *characteristic function*, regarded as an unknown Y-periodic tensor of the third order. Inserting Eq. (2.59) into Eq. (2.54) leads to

$$\int_Y \left(C_{ijhk}\frac{\partial u_h^0(\mathbf{x})}{\partial x_k} + C_{ijhk}\frac{\partial \chi_h^{lm}(\mathbf{x},\mathbf{y})}{\partial y_k}\frac{\partial u_l^0(\mathbf{x})}{\partial x_m}\right)\frac{\partial v_i(\mathbf{y})}{\partial y_j}\,\mathrm{d}Y = 0. \tag{2.60}$$

Since $u_l^0(\mathbf{x})$ is independent of $\mathbf{y}$ and

$$C_{ijhk}\frac{\partial \chi_h^{lm}(\mathbf{x},\mathbf{y})}{\partial y_k}\frac{\partial u_l^0(\mathbf{x})}{\partial x_m} = C_{ijlm}\frac{\partial \chi_l^{hk}(\mathbf{x},\mathbf{y})}{\partial y_m}\frac{\partial u_h^0(\mathbf{x})}{\partial x_k}, \tag{2.61}$$

it follows from Eq. (2.60):

$$\int_Y C_{ijlm}\frac{\partial \chi_l^{hk}(\mathbf{x},\mathbf{y})}{\partial y_m}\frac{\partial v_i(\mathbf{y})}{\partial y_j}\,\mathrm{d}Y = -\int_Y C_{ijhk}\frac{\partial v_i(\mathbf{y})}{\partial y_j}\,\mathrm{d}Y. \tag{2.62}$$

The characteristic function χ_h^{lm} can be obtained by solving Eq. (2.62) together with the periodic boundary conditions of $u_h^1(\mathbf{x},\mathbf{y})$. In the case of a three-dimensional model of composite material, if the repeating cell is the unit cube shown in Fig. 2.4, the six faces $(f_1,\ldots,f_6)$ are described by

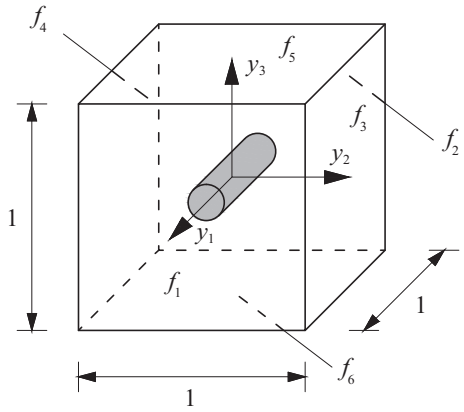

Fig. 2.4 Cube-shaped repeating unit cell (RUC) for three-dimensional periodic homogenization.

$$
\begin{aligned}
(y_1, y_2, y_3)|_{f_1,f_2} &= \left(\mp\frac{1}{2}, y_2, y_3\right) \\
(y_1, y_2, y_3)|_{f_3,f_4} &= \left(y_1, \mp\frac{1}{2}, y_3\right) \\
(y_1, y_2, y_3)|_{f_5,f_6} &= \left(y_1, y_2, \mp\frac{1}{2}\right).
\end{aligned}
\tag{2.63}
$$

The above-mentioned periodic boundary conditions can be written as

$$
\begin{aligned}
u_h^1(\mathbf{x}, \mathbf{y})\big|_{f_1} &= u_h^1(\mathbf{x}, \mathbf{y})\big|_{f_2} \\
u_h^1(\mathbf{x}, \mathbf{y})\big|_{f_3} &= u_h^1(\mathbf{x}, \mathbf{y})\big|_{f_4} \\
u_h^1(\mathbf{x}, \mathbf{y})\big|_{f_5} &= u_h^1(\mathbf{x}, \mathbf{y})\big|_{f_6}
\end{aligned}
\tag{2.64}
$$

with $h = 1,2,3$; inserting (2.59) into (2.64) one obtains

$$\begin{aligned}
\left[\chi_h^{lm}(\mathbf{x},\mathbf{y})\frac{\partial u_l^0(\mathbf{x})}{\partial x_m}+\tilde{u}_h^1(\mathbf{x})\right]_{f_1} &= \left[\chi_h^{lm}(\mathbf{x},\mathbf{y})\frac{\partial u_l^0(\mathbf{x})}{\partial x_m}+\tilde{u}_h^1(\mathbf{x})\right]_{f_2}\\
\left[\chi_h^{lm}(\mathbf{x},\mathbf{y})\frac{\partial u_l^0(\mathbf{x})}{\partial x_m}+\tilde{u}_h^1(\mathbf{x})\right]_{f_3} &= \left[\chi_h^{lm}(\mathbf{x},\mathbf{y})\frac{\partial u_l^0(\mathbf{x})}{\partial x_m}+\tilde{u}_h^1(\mathbf{x})\right]_{f_4}\\
\left[\chi_h^{lm}(\mathbf{x},\mathbf{y})\frac{\partial u_l^0(\mathbf{x})}{\partial x_m}+\tilde{u}_h^1(\mathbf{x})\right]_{f_5} &= \left[\chi_h^{lm}(\mathbf{x},\mathbf{y})\frac{\partial u_l^0(\mathbf{x})}{\partial x_m}+\tilde{u}_h^1(\mathbf{x})\right]_{f_6}.
\end{aligned} \tag{2.65}$$

Since $\tilde{u}_h^1(\mathbf{x})$ is independent of $\mathbf{y}$ and the macroscopic strains are arbitrarily uniform, Eq. (2.64) can be rewritten as

$$\begin{aligned}
\chi_h^{lm}(\mathbf{x},\mathbf{y})\big|_{f_1} &= \chi_h^{lm}(\mathbf{x},\mathbf{y})\big|_{f_2}\\
\chi_h^{lm}(\mathbf{x},\mathbf{y})\big|_{f_3} &= \chi_h^{lm}(\mathbf{x},\mathbf{y})\big|_{f_4}\\
\chi_h^{lm}(\mathbf{x},\mathbf{y})\big|_{f_5} &= \chi_h^{lm}(\mathbf{x},\mathbf{y})\big|_{f_6}.
\end{aligned} \tag{2.66}$$

Therefore, the characteristic functions can be uniquely determined by solving Eq. (2.62) with associated boundary conditions (2.66). Finally, by inserting (2.59) into (2.56), one obtains

$$\begin{aligned}
&\int_\Omega \overline{C}_{ijhk}(\mathbf{x})\frac{\partial u_h^0(\mathbf{x})}{\partial x_k}\frac{\partial v_i(\mathbf{x})}{\partial x_j}\,\mathrm{d}\Omega\\
&\qquad = \int_\Omega b_i(\mathbf{x})v_i(\mathbf{x})\,\mathrm{d}\Omega + \int_{\partial_t\Omega} t_i(\mathbf{x})v_i(\mathbf{x})\,\mathrm{d}S \quad \mathbf{x}\in\Omega
\end{aligned} \tag{2.67}$$

where

$$\overline{C}_{ijhk}(\mathbf{x}) = \frac{1}{|Y|}\int_Y \left(C_{ijhk} + C_{ijlm}\frac{\partial \chi_l^{hk}}{\partial y_m}\right)\mathrm{d}Y \tag{2.68}$$

Table 2.1 Comparison between the average field theory and the homogenization theory

	Average field theory	Homogenization theory
Microscopic displacement	$\mathbf{u}$	$\mathbf{u}^0 + \varepsilon \boldsymbol{\chi}^1 : (\nabla_X \otimes \mathbf{u}^0)$
Microstrain	$\boldsymbol{\varepsilon} = \nabla_x \otimes_s \mathbf{u}$	$\boldsymbol{\varepsilon}^0 = (\mathbb{I} + \nabla_x \otimes_s \boldsymbol{\chi}^1) : (\nabla_X \otimes_s \mathbf{u}^0)$
Microstress	$\boldsymbol{\sigma} = \mathbb{C} : (\nabla_x \otimes \mathbf{u})$	$\boldsymbol{\sigma}^0 = \mathbb{C} : (\mathbb{I} + \nabla_x \otimes \boldsymbol{\chi}^1) : (\nabla_X \otimes \mathbf{u}^0)$
Microscopic displacement	$\overline{\mathbf{u}} = \int \phi_V \mathbf{u} \, \mathrm{d}V$	$\mathbf{u}^0$
Macrostrain	$\overline{\boldsymbol{\varepsilon}} = \nabla_X \otimes_s \overline{\mathbf{u}}$	$\langle \boldsymbol{\varepsilon}^0 \rangle = \nabla_X \otimes_s \mathbf{u}^0$
Macrostress	$\overline{\boldsymbol{\sigma}} = \overline{\mathbb{C}} : \overline{\boldsymbol{\varepsilon}}$	$\langle \boldsymbol{\sigma}^0 \rangle = \overline{\mathbb{C}}^0 : \langle \boldsymbol{\varepsilon}^0 \rangle$
Effective elasticity	$\overline{\mathbb{C}} = \mathbb{C}_M + f(\mathbb{C}_I - \mathbb{C}_M) : \mathbb{A}$	$\overline{\mathbb{C}} = \langle \mathbb{C} : (\mathbb{I} + \nabla_x \otimes \boldsymbol{\chi}^1) \rangle$

$$b_i(\mathbf{x}) = \frac{1}{|Y|} \int_Y f_i(\mathbf{x}, \mathbf{y}) \, \mathrm{d}Y. \tag{2.69}$$

Eq. (2.67) represents the macroscopic equilibrium, whereas $\overline{C}_{ijhk}(\mathbf{x})$ denotes the tensor of homogenized (effective) elastic constants.

2.1.3 Hybrid micromechanical theory

Both the mean field theory and the mathematical theory of homogenization have been widely used to estimate the effective moduli of heterogeneous materials starting from the geometric arrangement and the material properties of the different microconstituents. As pointed out by Hori and Nemat-Nasser [21], when applying the singular perturbation of the microscopic fields, the resulting fields of $O(\varepsilon^0)$ and their averages taken over the RUC correspond to the microscopic and macroscopic fields of the mean field theory, respectively; see Table 2.1 for the comparison of the field variables of $O(\varepsilon^0)$ with the corresponding variables of the mean field theory.

There are, however, two main differences between these two theories. The first difference relies on the modeling approach: the mathematical theory of homogenization makes use of a repeating unit cell under the assumption of perfect periodicity, whereas the mean field theory considers a representative volume element under the assumption of statistical homogeneity. The second difference is that the homogenization theory can manage higher-order terms in the singular perturbation expansion, leading to the definition of more sophisticate schemes (*higher-order homogenization* schemes).

Despite these differences, the homogenization theory can be also applied to heterogeneous materials exhibiting nonperiodic microstructures; in this case, the higher order terms can be computed by taking advantage of the average field theory applied to suitable microstructural models (see [21] for the complete treatment of higher-order terms).

Another interesting comparison between formal asymptotic homogenization and volume averaging has been recently proposed by Davit et al. in [171], whose aim is to bridge the gap between the two considered theories.

2.2 Overview of multiscale methods

As widely discussed in Chapter 1, the overall structural behavior of composite materials is strongly influenced by several damage mechanisms, which take place at the microscopic scale in conjunction with eventual contact interaction between crack faces, leading to a highly nonlinear post-peak response associated with a gradual loss of stiffness prior to failure. As a consequence, a proper failure analysis of a composite material subjected to such microstructural evolution should require a numerical model able to completely describe all its microscopic details; however fully microscopic models cannot be pursued in practice due to the large computational cost, and thus simplified models are need to predict failure in composite materials with satisfactory accuracy.

Two classes of multiscale problems can be recognized, when studying the mechanical behavior of heterogeneous structures [172]. The first class con-

tains the so-called problems of type A, i.e. the problems involving local defects or singularities, such as dislocations, cracks, shocks, and boundary layers, for which a macroscopic model is sufficient for most of the physical domain, and a fine-scale model is only needed in the neighborhood of the singularities or heterogeneities. The second class of problems (called type B problems) are those for which a microscopic model is needed everywhere either as a complement to or as a replacement of the macroscopic model; an example of type B problem is a standard mechanical system for which a macroscopic constitutive phenomenological law is missing.

The standard approach for type A problems is to use a *domain decomposition method* (DDM), since the physical domain is split in two subdomains resolved at different scales; the main task in this approach is a suitable coupling at the interface between the subdomains. The standard approach for type B problems is to couple the macro- and micro-models everywhere in the computational domain, as in the heterogeneous multiscale method (HMM) [172]. It is worth noting that for type A problems, the macro-micro coupling is localized, whereas for type B problems, the scale transition is performed over the whole computational domain.

Before describing multiscale methods in more detail, an overview of different types of approach is given; multiscale methods are usually classified as either hierarchical or concurrent.

Hierarchical methods (see Fig. 2.5a) are most widely used and computationally the most efficient. In these methods, the response of a representative volume element under prescribed microscopic boundary conditions is first computed over a range of expected inputs of the macrostrain $\boldsymbol{\varepsilon}_M$, and from these a constitutive law is extracted. For linear response, this process is extremely simplified since homogenized quantities can be effectively computed by virtue of the robust theory of linear homogenization, sometimes without requiring numerical microscopic models. On the other hand, for strongly nonlinear problems, hierarchical models become less effective, especially if the fine-scale response is path-dependent. It is worth noting that in the case of failure events, standard hierarchical models are no longer valid.

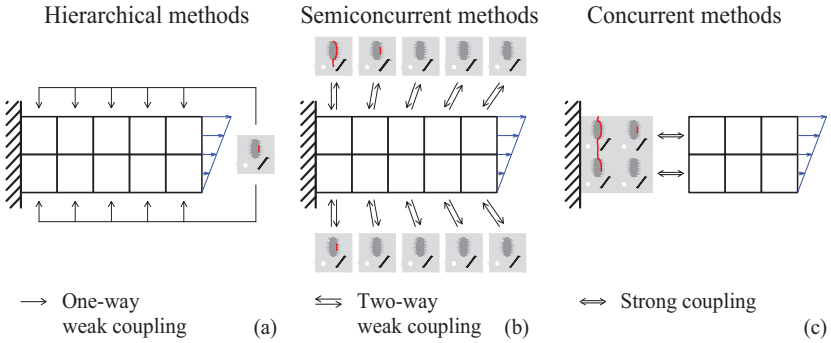

Fig. 2.5 Classification of multiscale methods according to [27].

Concurrent methods are characterized by the presence of a fine-scale model embedded into the coarse-scale model, which is directly and strongly coupled to it, as shown in Fig. 2.5c. In order to restore the continuity conditions between the two submodels, both compatibility and momentum balance are enforced across the interface. Such models are effective when the subdomain where a higher-order description is required, is small compared to the whole domain.

As pointed out by Belytschko and Song [27], several multiscale methods fall in an intermediate class between hierarchical and concurrent methods. These methods, referred to as *semiconcurrent methods*, allow to compute the fine-scale model response for a specific input required by the coarse-scale model and pass the information to the coarser scale during the simulation of the coarse-scale model, as shown in Fig. 2.5b. A classical semiconcurrent approach is the FE^2 method [29, 173], in which a fine-scale finite element model is used to compute the coarse-scale stresses for each Gauss point in the coarse-scale mesh.

2.2.1 Hierarchical methods

In hierarchical multiscale methods, a macroscopic constitutive model is assumed with parameters determined by fitting the data obtained as the result of the boundary value problem of a microscopic sample whose microstructure is

explicitly modeled. In the literature, these numerical homogenization techniques, also referred to as *unit cell methods*, are particularly useful for modeling composite materials since they enable the development of the so-called *micromechanically informed constitutive models* that can be used in structural computations. Due to the assumption on the type of macroscopic constitutive law, these methods are not suitable for handling nonlinear problems with evolving microstructures; on the other hand, these methods are attractive for large scale computations, since finite element computations at the microscale are performed a priori.

In hierarchical models (also referred to as *sequential models*), the following steps have to be performed:

i. identification of a representative volume element (RVE) or a repeating unit cell (RUC), for random or periodic structures, respectively, whose individual constituents are assumed to be completely known, with their constitutive properties;

ii. formulation of the microscopic boundary conditions to be applied to the RVE;

iii. computation of the output macroscopic variables from the results of the microscopic boundary value problem associated with the RVE (*micro-to-macro transition* or *homogenization*);

iv. determination of the numerical constitutive law, relating each other the input and output macroscopic variables.

Since during the micro-to-macro transition step the information is passed from lower to higher scales, a “one-way” bottom-up coupling is established between the microscopic and macroscopic scales. As a consequence, such methods are efficient in determining the macroscopic behavior of composites in terms of stiffness and strength, but have a limited predictive capability for problems involving damage phenomena.

Many studies have been addressed to the macroscopic constitutive behavior of composite materials with microscopic defects (see, for instance, [42, 43, 174-177]). In many works, the damage configuration is fixed, since for a pure micromechanical model, the evolution of damage configuration cannot be predicted (see [174, 175]); more general approaches consider a random distribution of fiber/matrix debonding [176] or cohesive cracks [43], include damage evolution effects into the macroscopic constitutive response by means of brittle interface models [177], or continuum damage models at the microscale [178].

More recently, a nonlinear micromechanical model incorporating contact effects and based on homogenization techniques, interface models and fracture mechanics concepts has been proposed in [44, 54], where the damage configuration is not assumed *a priori*, but driven by a fracture criterion. By using this hierarchical model, accurate nonlinear macroscopic constitutive laws are obtained, taking into account the evolution of the microstructural configuration associated with crack growth and contact phenomena at the microscale.

2.2.2 Semiconcurrent methods

When dealing with microscopic nonlinear phenomena due to evolving defects whose spatial configuration is not known a priori, however, a "two-way" coupling between micro- and macrovariables is required, i.e. the homogenized properties have to be updated during the microstructural evolution due to damage phenomena. In semiconcurrent multiscale methods, also referred to as *computational homogenization* methods, the macroscopic constitutive response of a heterogeneous material is determined "on the fly" during simulation; these methods have been widely used to predict the mechanical behavior of microstructured materials, due to their flexibility. The most important approaches are those proposed by Guedes and Kikuchi [168], Miehe et al. [179], Feyel and Chaboche [29], Kouznetsova et al. [23].

Another approach which can be considered as an *information passing* method is the *multiscale finite element method* (MsFEM); this method, originally developed by Hou and Wu [180], is able to solve partial differential equations with rapidly oscillating coefficients. The central idea of this method is to introduce a set of fine-scale finite element basis functions, which are obtained by solving suitable fine-scale problems for every element of a given mesh; these basis functions incorporate the needed information about the microstructure of the problem.

In the following a special attention is devoted to the large class of approaches inspired by the multilevel finite element (FE^2) method introduced by Feyel and Chaboche [29]. This method has been proved to be very efficient in such cases, also for only locally periodic composites. The key idea of such approaches is to associate a microscopic boundary value problem to each integration point of the macroscopic boundary value problem, after discretizing the underlying microstructure. The macroscopic strain provides the boundary data for each microscopic problem (*macro-to-micro transition* or *localization* step). The set of all microscale problems is then solved and the results are passed back to the macroscopic problem in terms of overall stress field and tangent operator (*micro-to-macro transition* or *homogenization step*). Localization and homogenization steps are carried out within an incremental-iterative nested solution scheme, thus the two-scale coupling remains of a weak type. An advantage of semiconcurrent methods over hierarchical methods is that a framework for storing the macroscopic constitutive response is not needed.

In the original formulation of the method, based on a classical first-order homogenization and summarized in Section 2.2.2.1, however, the large spatial gradients in macroscopic fields cannot be resolved due to supposed validity of the principle of scale separation, therefore they are not suited for studying strain localization phenomena which commonly affect the macroscopic behavior of composites; moreover, softening behaviors cannot be properly analyzed because of the mesh dependence at the macroscopic scale due to the ill-posedness of the macroscopic boundary value problem, as shown in [22].

In order to overcome such limitations, other homogenization paradigms have been proposed in the literature, such as the *higher-order computational homogenization* schemes, the *coupled volume* multiscale method and the *continuous-discontinuous computational homogenization* schemes, illustrated in Sections 2.2.2.2, 2.2.2.3 and 2.2.2.4, respectively.

2.2.2.1 Multilevel finite element (FE^2) method

The FE^2 method has been introduced by Feyel in [29] and consists in describing the mechanical behavior of heterogeneous structures. After choosing two relevant mechanical scales (referred to as *microscale* and *macroscale*), the FE^2 method can be adopted, based on three main ingredients:

i. The identification of a representative volume element (RVE);

ii. A localization rule able to obtain the local solution inside the RVE, for any given macroscopic strain;

iii. A homogenization rule giving the macroscopic stress tensor, starting from the micromechanical stress state.

In this setting, macroscopic phenomenological relationships are not required, even in the case of nonlinear behaviors; indeed, the macroscopic response arises directly from the calculation at the microscopic level.

The FE^2 method is applied by means of a nested solution scheme sketched in Fig. 2.6; for each step of the macroscopic incremental-iterative procedure, and for each macroscopic integration point, the macroscopic strain $\overline{\boldsymbol{\varepsilon}}$ is computed based on the current (iterative) macroscopic displacement field. Then, $\overline{\boldsymbol{\varepsilon}}$ is passed to the microscopic level, and used to define the boundary conditions to be applied to the RVE attached to the respective macroscopic integration point. After solving every RVE problem, the macroscopic stress tensor $\overline{\boldsymbol{\sigma}}$ is obtained in a post-processing step. Thus, the macroscopic equilibrium can be evaluated, and the next iterations are performed until equilibrium is

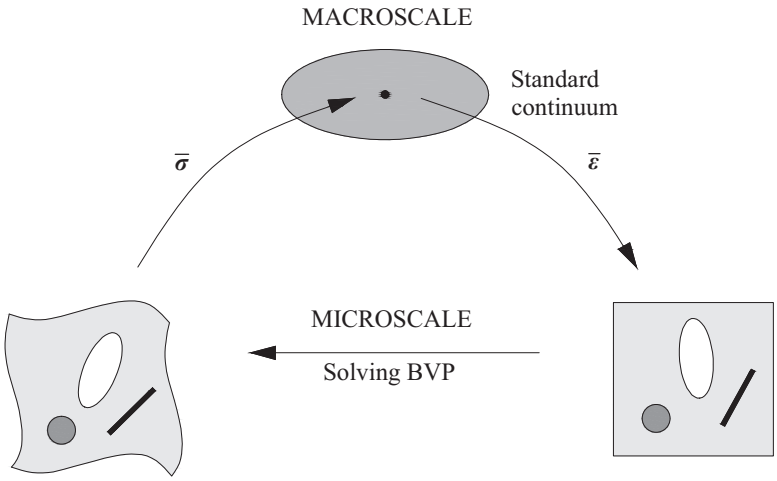

Fig. 2.6 First-order computational homogenization scheme.

achieved; after this, the calculations can be continued for the next load increment.

The multilevel finite element method is intrinsically parallel; indeed, all RVE calculations for one macroscopic iteration can be performed simultaneously without any exchange of information between them. Thus, even if this method is computationally costly, the use of parallel processors for the RVE analyses would significantly reduce the total calculation time.

2.2.2.2 Higher-order computational homogenization

In this section the second-order computational scheme, proposed by Kouznetsova et al. [23] to extend the classical computational techniques, is illustrated. This technique adopts not only the macrostrain tensor (as in first-order schemes) but also its gradient to prescribe the essential boundary conditions on the representative volume element of the given microstructure, leading to a second-order continuum macroscopic model.

Let Y be a representative volume element (RVE) of a composite microstructure attached to a material point $\overline{\mathbf{X}}$ of the homogenized continuum, denoted by Ω. Assuming large displacements, a nonlinear deformation map χ is

considered, describing the transformation inside the RVE from the undeformed macroscopic state (identified by the microscopic position vector $\mathbf{X}$) to the deformed state (identified by $\mathbf{x}$), i.e. $\mathbf{x} = \chi(\mathbf{X})$. The averaging of the RVE is performed by considering the microconstituents within the RVE as *first-order continua*, for which the deformation is described by the microstrain gradient tensor $\mathbf{F}$ defined as:

$$\mathbf{F} = \nabla_X \otimes \mathbf{x}. \tag{2.70}$$

The starting point of this approach is to express the microscopic variation $\mathbf{x}(\mathbf{X})$ by means of a Taylor series expansion of the macroscopic fields in the neighborhood of a macroscopic material point $\overline{\mathbf{X}}$:

$$\mathbf{x} = \overline{\mathbf{F}} \cdot \mathbf{X} + \frac{1}{2}\overline{\boldsymbol{\mathcal{G}}} : (\mathbf{X} \otimes \mathbf{X}) + O\left(\mathbf{X}^3\right), \tag{2.71}$$

where $\overline{\mathbf{F}} = \nabla_{\overline{X}} \otimes \overline{\mathbf{x}}$ is the macrostrain gradient tensor, and the third-order tensor $\overline{\boldsymbol{\mathcal{G}}}$ is introduced as:

$$\overline{\boldsymbol{\mathcal{G}}} = \nabla_{\overline{X}} \otimes \overline{\mathbf{F}} = \nabla_{\overline{X}} \otimes \left(\nabla_{\overline{X}} \otimes \overline{\mathbf{x}}\right) \tag{2.72}$$

representing its Lagrangian macroscopic gradient. It should be noted that $\overline{\boldsymbol{\mathcal{G}}}$ possesses the minor symmetry $\overline{G}_{ijk} = \overline{G}_{ikj}$. All the higher-order terms in Eq. (2.71), represented by $O\left(\mathbf{X}^3\right)$, are regarded as an unknown microscopic fluctuation field $\mathbf{w}$, which represents the fine scale contribution in the kinematics. Therefore, Eq. (2.71) can be rewritten as follows:

$$\mathbf{x} = \overline{\mathbf{F}} \cdot \mathbf{X} + \frac{1}{2}\overline{\boldsymbol{\mathcal{G}}} : (\mathbf{X} \otimes \mathbf{X}) + \mathbf{w}. \tag{2.73}$$

It is worth noting that the first-order expansion suffices, i.e. $\overline{\boldsymbol{\mathcal{G}}} = \mathbf{0}$ whenever scale separation is valid, whereas the second-order case is needed when homogeneous macroscopic deformation within the RVE cannot be assumed. The microscopic deformation gradient tensor $\mathbf{F}$ is easily obtained as

$$\mathbf{F} = \nabla_X \otimes \mathbf{x} = \overline{\mathbf{F}} + \overline{\boldsymbol{\mathcal{G}}} : (\mathbf{1} \otimes_s \mathbf{X}) + \nabla_X \otimes \mathbf{w}, \tag{2.74}$$

where $\mathbf{1}$ is a vector of all ones and $\otimes_s$ denotes the symmetric part of the dyadic product.

Then, the boundary value problem on the RVE level, completed by proper generalized periodic boundary conditions, is formulated as a standard problem of quasistatic equilibrium in a classical continuum framework. The equilibrium equation for the considered RVE (in the case of neglected body forces) takes the form:

$$\nabla_X \cdot \mathbf{P} = \mathbf{0}, \tag{2.75}$$

where $\mathbf{P}$ is the first Piola-Kirchhoff stress tensor.

After solving the microscopic BVP, the macroscopic first Piola-Kirchhoff stress tensor $\overline{\mathbf{P}}$ and a higher-order stress tensor $\overline{\boldsymbol{\mathcal{Q}}}$ (a third-order tensor), defined as the work conjugate of the gradient $\overline{\boldsymbol{\mathcal{G}}}$ of the deformation gradient tensor, are obtained by using the following extension of the Hill-Mandel condition:

$$\frac{1}{|\Omega_{\mathrm{RVE}}|} \int_{\Omega_{\mathrm{RVE}}} \mathbf{P} : \delta\mathbf{F} \, \mathrm{d}\mathbf{X} = \overline{\mathbf{P}} : \delta\overline{\mathbf{F}} + \overline{\boldsymbol{\mathcal{Q}}} \vdots \delta\overline{\boldsymbol{\mathcal{G}}}. \tag{2.76}$$

It follows, after some manipulations:

$$\begin{aligned} \overline{\mathbf{P}} &= \frac{1}{|\Omega_{\mathrm{RVE}}|} \int_{\Omega_{\mathrm{RVE}}} \mathbf{P} \, \mathrm{d}\mathbf{X} \\ \overline{\boldsymbol{\mathcal{Q}}} &= \frac{1}{|\Omega_{\mathrm{RVE}}|} \int_{\Omega_{\mathrm{RVE}}} \mathbf{P} \otimes_{\mathrm{s}} \mathbf{X} \, \mathrm{d}\mathbf{X}. \end{aligned} \tag{2.77}$$

The second-order computational homogenization is applied by means of a nested solution scheme sketched in Fig. 2.7; for each step of the macroscopic incremental-iterative procedure, and for each macroscopic integration point, the macroscopic deformation gradient tensor $\overline{\mathbf{F}}$ and its gradient $\overline{\boldsymbol{\mathcal{G}}}$ are computed based on the current (iterative) macroscopic displacement field. Then,

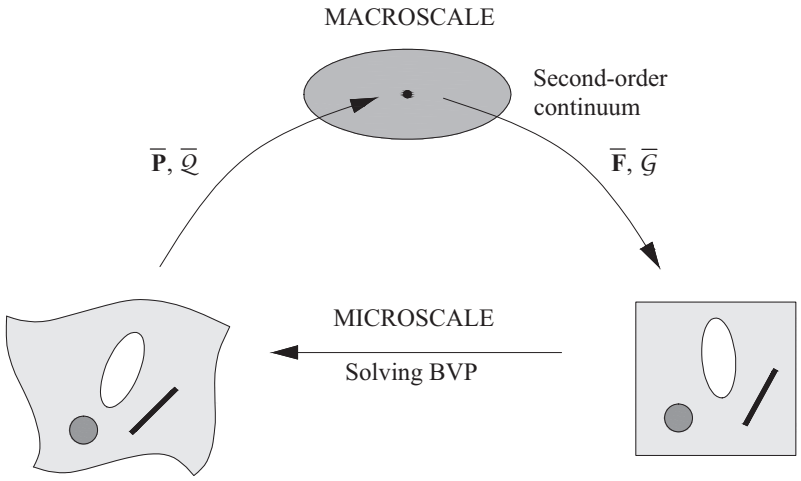

Fig. 2.7 Second-order computational homogenization scheme.

$\overline{\mathbf{F}}$ and $\overline{\mathcal{G}}$ are passed to the microscopic level, and used to define the boundary conditions to be applied to the RVE attached to the respective macroscopic integration point. After solving every RVE problem, the macroscopic stress tensor $\overline{\mathbf{P}}$ and the higher-order stress tensor $\overline{\mathcal{Q}}$ are obtained by using Eq. (2.77). Thus, the macroscopic internal nodal forces can be computed, the higher-order equilibrium can be evaluated, and the next iterations are performed until equilibrium is achieved; after this, the calculations can be continued for the next load increment.

The inclusion of strain gradients and higher-order stresses automatically results in the introduction of a length scale parameter in the macroscopic response; this allows to overcome the dependence on the macroscopic discretization, but does not solve the RVE size dependence in the case of softening behaviors, as shown in [30].

2.2.2.3 Coupled volume multiscale method

A different approach has been proposed by Gitman et al. [30], referred to as *coupled volume multiscale method*, able to resolve simultaneously the mac-

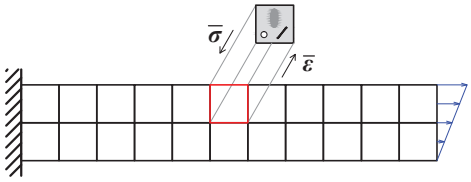

Fig. 2.8 Coupled volume multiscale approach.

roscale discretization sensitivity and the RVE size dependence. The main feature of this method is that an RVE is not linked to an infinitely small macroscopic material point, but associated with a macroelement, whose size equals the RVE size, as sketched in Fig. 2.8.

The coupled volume approach abandons the principle of scale separation and a model parameter (the RVE size) is linked to a numerical parameter (the mesh size); since this approach does not rely upon the existence of an RVE, it can also be used in the presence of softening behaviors.

If used in combination with the fracture energy-based approach, the coupled volume method shows two different effects: on one hand, while considering different mesh sizes at the macroscopic scale and keeping the RVE size constant, an increase in the mesh density corresponds to an increase in the brittleness of the overall mechanical response; on the other hand, while keeping the mesh size at the macroscopic scale constant and varying the RVE size, the dependence on the RVE size is obtained: the smaller the RVE size the less brittle the macroscopic response becomes. This dependency is understood as a material constitutive behavior.

By linking the mesh size to the RVE size, the macroscopic mesh dependence is balanced by different constitutive behaviors arising from different RVE sizes; as a consequence, the macroscopic response shows neither macroscopic mesh dependency nor RVE size dependency.

2.2.2.4 Continuous-discontinuous computational homogenization

Continuous-discontinuous homogenization methods refer to computational homogenization models in which the bulk and discontinuities at the macroscale are coupled to RVE problems. These approaches arise directly from the discontinuous homogenization schemes, developed in the context of computational homogenization to obtain the behavior of cracks at the macroscopic level from nested microscale computations performed on a sample representing the fully resolved microstructure of a thin layer.

Homogenization towards intrinsic cohesive laws has been introduced by Matouš et al. [181], where microscopic failure is described by a continuum damage model; a similar work has been presented by Alfaro et al. [182], where microscopic failure is modeled by using discrete cohesive microcracks. On the other hand, homogenization towards extrinsic cohesive laws has been adopted by Verhoosel et al. [183] and Nguyen et al. [184], to model random heterogeneous materials exhibiting discrete cracking and band localization, respectively.

The main scope of continuous-discontinuous homogenization approaches consists in performing the transition from diffusive microcracks to localized macrocracks as usually observed; generally speaking, a macrocrack is injected at the macrocontinuum point associated with a certain representative volume element (RVE), when a material instability (a crack and/or a shear band) is detected within this RVE.

One of the first computational homogenization models able to deal with strain localization problems is that by Massart et al. [185] in the context of masonry cracking; other approaches have been proposed by Belytschko et al. [25] for composite materials, by Souza et al. [186] for random viscoelastic materials, and by Nguyen et al. [187] for random heterogeneous solids. These approaches share some common features, but they differ in the description of failure at both the microscopic and macroscopic scales: in [185] localization bands are used to model microscopic failure, whereas embedded crack bands are employed to describe macroscopic failure; in [186] both microscopic and

macroscopic failure is simulated by using cohesive zone models; in [25] macroscopic failure is described by traction-free cracks, whereas one cohesive crack is used to model microscopic failure; in [187] cohesive zone models are used to describe macroscopic failure, whereas for the microscopic failure a diffuse localization band is employed.

In the following, a particular attention is devoted to summarize the main features of the approaches proposed in [25] and [187], i.e. the *multiscale aggregating discontinuity* (MAD) approach and the *failure zone averaging scheme*, respectively.

Multiscale aggregating discontinuity (MAD) method

Basically, the multiscale aggregating discontinuity (MAD) approach, proposed by Belytschko et al. [25], is a computational homogenization method applied to the failure analysis of heterogeneous solids; the essential feature of this method is the injection of a macroscopic discontinuity which is equivalent to the material instabilities (such as cracks or shear bands) occurring in the microscopic model. This is possible by removing the subdomain of the microscopic model in which the material loses convexity from the domain used to compute the average strain and stress. This macroscopic discontinuity is described by the extended finite element method (X-FEM).

Given an RVE in its reference configuration, denoted by Ω_0^m, the domain of the so-called *perforated unit cell* is

$$\widetilde{\Omega}_0^m = \Omega_0^m / \Omega_0^{\mathrm{loc}}, \tag{2.78}$$

where Ω_0^{loc} is the subdomain of the unit cell where the material is not convex (i.e. susceptible to strain localization); all averaging operations are performed over the perforated unit cell, and thus, any cohesive stress is excluded during this step. The macroscale deformation gradient $\mathbf{F}^M$ and the macroscale first Piola-Kirchhoff stress $\mathbf{P}^M$ are defined as the averages of the microscale deformation gradient $\mathbf{F}^m$ and the microscale first Piola-Kirchhoff stress $\mathbf{P}^m$ over the perforated unit cell, respectively:

$$\begin{aligned}\mathbf{F}^M &= \langle \mathbf{F}^m \rangle = \frac{1}{\left|\widetilde{\Omega}_0^m\right|} \int_{\widetilde{\Omega}_0^m} \mathbf{F}^m \, \mathrm{d}\Omega \\ \mathbf{P}^M &= \langle \mathbf{P}^m \rangle = \frac{1}{\left|\widetilde{\Omega}_0^m\right|} \int_{\widetilde{\Omega}_0^m} \mathbf{P}^m \, \mathrm{d}\Omega,\end{aligned} \tag{2.79}$$

where $\langle \cdot \rangle$ denotes the averaging operation.

The constant deformation modes used in the first-order homogenization scheme are not able to properly describe the deformation of a unit cell in the presence of a growing microcrack; thus two hourglass modes are added to considered model. In order to handle this additional modes, two generalized strains $\mathbf{q} = \left[q_1, q_2\right]$ and two corresponding generalized stresses $\mathbf{Q} = [Q_1, Q_2]$ are added to the kinematic and dynamic descriptions at the macroscopic scale. These extra generalized stresses and strains are assumed to be energetically consistent with the work in the perforated unit cell:

$$\mathbf{P}^M \,:\, \delta\mathbf{F}^M + \mathbf{Q} \cdot \delta\mathbf{q} = \frac{1}{\left|\widetilde{\Omega}_0^m\right|} \int_{\widetilde{\Omega}_0^m} \mathbf{P}^m \,:\, \delta\mathbf{F}^m \, \mathrm{d}\Omega. \tag{2.80}$$

It is worth noting that these additional modes are introduced coherently with the approach proposed by Kouznetsova et al. [23].

Failure zone averaging scheme

In [187], Nguyen et al. have proposed a novel averaging scheme, called *failure zone averaging scheme* for which the existence of an RVE for heterogeneous quasibrittle materials with softening behavior has been proved. This technique is able to obtain homogenized stress-strain relationships which are objective with respect to the micro-sample size. In the following, the subscripts m and M refer to the micro- and macroscale, respectively.

The macrocrack initiation criterion is based on the loss of positive definiteness of the homogenized material tangent matrix $\mathbb{D}_M$,whereas the orientation of the nucleating macrocrack is determined using a macrostress-based criterion.

At the beginning of the analysis, periodic BCs are used for the bulk RVEs; when strain localization occurs at the critical RVE, a macrocrack is inserted at the macroelement associated with this bulk RVE. The cohesive RVEs attached to Gauss points on the crack are now subjected to semi-periodic BCs.

Damage at the microscopic scale is modeled by a regularized isotropic damage model:

$$\boldsymbol{\sigma}_m = (1-\omega)\mathbb{C}_m : \boldsymbol{\varepsilon}_m, \tag{2.81}$$

where ω is the scalar damage parameter and the fourth-order tensor $\mathbb{C}$ is the elastic moduli tensor; damage is governed by the following phenomenological law:

$$\omega = 1 - \frac{\kappa}{\kappa_c}\left[1 - \alpha + \alpha e^{-\beta(\kappa-\kappa_c)}\right], \quad \kappa \geq \kappa_c, \tag{2.82}$$

where α, β and κ_c denote the residual stress, the softening slope and the damage threshold, respectively. The variable κ is a scalar measure of the largest strain ever reached during the loading history, defined by the following loading function f:

$$f = \overline{\varepsilon}_{\text{eq}} - \kappa, \tag{2.83}$$

where $\overline{\varepsilon}_{\text{eq}}$ is the nonlocal equivalent strain, according to the gradient enhanced models.

Then, the *active damaged domain* Ω_d, i.e. the region containing Gauss points which are damaged and loading, is defined; mathematically, Ω_d is:

$$\Omega_d = \{\mathbf{x} \in \Omega_m : \omega(\mathbf{x}) > 0, f(\mathbf{x}) = 0\}, \tag{2.84}$$

where Ω_m denotes the RVE domain.

After this, the homogenized stresses and strains are defined as the volume averages of the microscopic stresses and strains over Ω_d, respectively:

$$\begin{aligned} \overline{\boldsymbol{\sigma}}_{\text{dam}} &= \frac{1}{|\Omega_d|}\int_{\Omega_d} \boldsymbol{\sigma}_m \, \mathrm{d}\Omega \\ \overline{\boldsymbol{\varepsilon}}_{\text{dam}} &= \frac{1}{|\Omega_d|}\int_{\Omega_d} \boldsymbol{\varepsilon}_m \, \mathrm{d}\Omega, \end{aligned} \tag{2.85}$$

It is worth noting that Eq. (2.85) should be used only after development of a failure band, i.e. after the peak.

A macroscopic cohesive law can be extracted from the microscopic response within the active damaged domain which is independent of the micro-sample size. The displacements due to damage $\mathbf{u}_{\text{dam}}$ is given as

$$\mathbf{u}_{\text{dam}} = \overline{\boldsymbol{\varepsilon}}_{\text{dam}} \cdot (l\mathbf{n}), \tag{2.86}$$

where l is the averaged width of the localization band, equal to $|\Omega_d|/h$; then, the macrocrack opening $[\![\mathbf{u}_M]\!]$ is defined as

$$[\![\mathbf{u}_M]\!] = \mathbf{u}_{\text{dam}} - \mathbf{u}^0_{\text{dam}}, \tag{2.87}$$

where $\mathbf{u}^0_{\text{dam}}$ is the damage opening corresponding to the maximum traction, in order to obtain an initially rigid macroscopic traction-opening relationship.

The micro-to-macro transition is based on the following equation

$$\frac{1}{wh}\int_{\Omega_d} \boldsymbol{\sigma}_m \,:\, \delta\boldsymbol{\varepsilon}_m \, d\Omega = \frac{1}{w}\mathbf{t}_M \cdot \delta\mathbf{u}_{\text{dam}}, \tag{2.88}$$

where w and h are the RVE dimensions; Eq. (2.88) represents a modified version of the well-known Hill-Mandel principle. The final micro-macro connection is given by

$$\mathbf{u}_R = (w - l)\mathbf{C}_0^{-1} \cdot \mathbf{t}_M + [\![\mathbf{u}_M]\!] + \mathbf{u}^0_{\text{dam}}, \tag{2.89}$$

where $\mathbf{u}_R$ is the total displacement of the RVE, and the second-order tensor $\mathbf{C}_0^{-1}$ is the projection of the compliance $\mathbb{C}_0^{-1}$ on the crack plane, with $\mathbb{C}_0$ being the elasticity tensor evaluated in the undeformed RVE.

During the macroscale analysis, the following system of equation has to be solved for $\mathbf{u}_m$ and $\mathbf{t}_M$ by using a Newton-Raphson iteration for the Gauss points on the crack, having a jump $[\![\mathbf{u}_M]\!]$:

$$\begin{aligned} \mathbf{f}_{\text{int}}(\mathbf{u}_m) &= \mathbf{f}_{\text{ext}}([\![\mathbf{u}_M]\!]) \\ \mathbf{u}_R(\mathbf{u}_m) &= \left[w - l(\mathbf{u}_m)\right]\mathbf{C}_0^{-1} \cdot \mathbf{t}_M + [\![\mathbf{u}_M]\!] + \mathbf{u}_{\text{dam}}^0, \end{aligned} \tag{2.90}$$

where $\mathbf{f}_{\text{int}}$ and $\mathbf{f}_{\text{ext}}$ are the microscopic internal and external force vectors.

2.2.3 Concurrent models

The main feature of concurrent multiscale methods consists in embedding a microscopic model into the macroscopic one, leading to a strong coupling between different length scales; thus two main issues must be addressed in practical application of these methods, i.e. (i) suitable handling the coupling between the fine-scale and the coarse-scale models, and (ii) finding efficient strategies for adding adaptivity during the fine-scale additions to the principal model, in order to reduce the computational costs.

Several concurrent methods have been proposed, based on different theoretical approaches and numerical strategies. According to the length scales involved in the considered physical problem, different choices can be made about the nature of the fine-scale models: on one hand, the microscopic model can be a discrete (molecular or atomistic) model, as in the *macroscopic atomistic ab initio dynamics* (MAAD) approach [188], the *quasi-continuum* (QC) method [189], the *atomistic-to-continuum* (AtC) coupling technique [190], and the *bridging domain* method [191]; on the other hand, the fine-scale model can be described as a continuum [35, 37, 61].

Concurrent multiscale methods can be regarded as falling within the class of *domain decomposition methods* (DDMs), since the numerical model describing the composite structure is decomposed into a fine- and coarse-scale

sub-models, which are simultaneously solved, thus establishing a strong "two-way" coupling between different resolutions. In classical domain decomposition methods, the computational domain is divided into smaller subdomains to be simultaneously solved, and a computational strategy is required to make sure that the solutions on different subdomains match each other. Most of concurrent multiscale methods can be classified in overlapping and non-overlapping methods.

In most multiscale models, two or more continuum models are strongly coupled each other, allowing to perform accurate simulations at the microscopic scale within the so-called *zone of interest*, which is usually adaptively updated during calculations [35, 37, 38].

A heterogeneous multiscale model consisting of several subdomains describing the material at different length scales is considered. Mesoscale models, characterized by a nonlinear material behavior, are only used in those zones of the structure in which damage takes place; on the contrary, undamaged regions of the structure are simulated at the macroscale assuming a linear elastic material behavior characterized by effective material parameters. Such an approach combines the advantages of both scales, i.e. the numerical efficiency of macroscale models and the accuracy of microscale models.

Moreover, concurrent multiscale methods are able to deal with boundary layer effects in a natural way, by replacing the coarse-scale model with a fine-scale one where periodicity conditions are no longer valid, as in the vicinity of free edges or applied loads or constraints.

One of the crucial points in concurrent multiscale methods is the connection between macro- and microscale subdomains; Fig. 2.9 shows the portion of a concurrent multiscale model in the vicinity of a coupling boundary Γ_c between a macroscale subdomain Ω_M and a microscale subdomain Ω_m. Three different methods can be applied to connect subdomains with nonmatching finite element discretization. If a collocation method is used, displacement compatibility of the subdomains is enforced in a strong sense, i.e.

$$\mathbf{u}_M(\mathbf{x}) - \mathbf{u}_m(\mathbf{x}) = \mathbf{0} \quad \forall \mathbf{x} \in \Gamma_c = \Omega_M \cap \Omega_m, \tag{2.91}$$

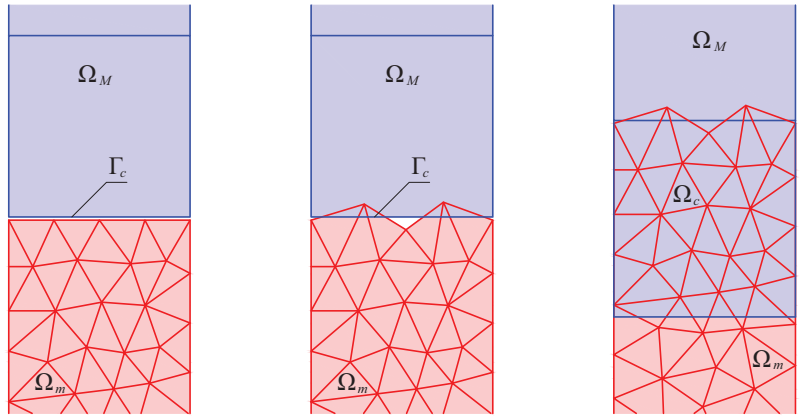

Fig. 2.9 Three alternative types of micro-macro connection in concurrent multiscale methods.

where $\mathbf{u}_M$ and $\mathbf{u}_m$ are the displacements of the subdomains Ω_M and Ω_m, respectively. In a weak coupling approach, realized by the mortar method [192] or the Arlequin method [32], the coupling condition (2.91) is only satisfied in an average sense; in the first case the compatibility equation is

$$\int_{\Gamma_c} \big(\mathbf{u}_M(\mathbf{x}) - \mathbf{u}_m(\mathbf{x})\big)\, \mathrm{d}\mathbf{x} = 0 \qquad \Gamma_c = \Omega_M \cap \Omega_m, \tag{2.92}$$

whereas, in the latter case

$$\int_{\Omega_c} \big(\mathbf{u}_M(\mathbf{x}) - \mathbf{u}_m(\mathbf{x})\big)\, \mathrm{d}\mathbf{x} = 0 \qquad \Omega_c = \Omega_M \cap \Omega_m, \tag{2.93}$$

where Ω_c represents the so-called *gluing zone*.

3

A computational homogenization model for failure analyses of composite materials

As widely discussed in Chapter 2, when studying the mechanical response of composite materials, multiscale modeling is essential to account for the spatial variability of their structural properties at both the macro- and microscales. To this end, a novel two-scale finite element approach is proposed, addressed to the failure analysis of locally periodic fiber-reinforced composite materials, taking into account microcrack initiation and propagation in the same model.

Coupling between the two scales is obtained by using a unit cell model with evolving microstructure due to crack initiation and propagation at the fiber/matrix interface and/or within the matrix. An innovative computational

technique has been introduced to perform localization and homogenization exchanges between the two scales during microstructural damage evolution. The proposed method is able to predict local failure quantities in an arbitrary cell from the results of the macroscopic analysis. These local quantities are then adopted to predict crack initiation and propagation by using fracture mechanics concepts.

Section 3.1 deals with the theoretical background directly used in the present work, focusing on the information passing between the *homogenization* and *localization* steps. In Section 3.2 the modeling techniques employed to simulate crack initiation and propagation processes are described in detail. Then, in Section 3.3, a hierarchical (numerical) homogenization strategy is presented as a preliminary step, for computing the effective mechanical properties of composite materials with evolving microcracking, taking advantage of a combination of homogenization concepts and fracture mechanics criteria presented in Sections 3.1 and 3.2. In Section 3.4 the above-mentioned innovative two-scale semiconcurrent approach devoted to the failure analysis of composite materials is discussed, together with the main computational details that clarify its practical implementation in a finite element setting. Then, Section 3.5 is devoted to the numerical evaluation of effective moduli for a unit cell undergoing fiber/matrix debonding and matrix cracking, performed by using the hierarchical strategy presented in Section 3.3. Finally the numerical simulations reported in Section 3.6 focus on the mechanical response of 2D periodic fiber-reinforced composite structures in order to investigate the capability of the model proposed in Section 3.4 in predicting failure mechanisms related to the crack initiation and propagation at the microstructural level. Moreover, comparisons between multiscale numerical simulations (MNS) and direct numerical simulations (DNS) have been carried out in order to assess the validity of the semiconcurrent approach.

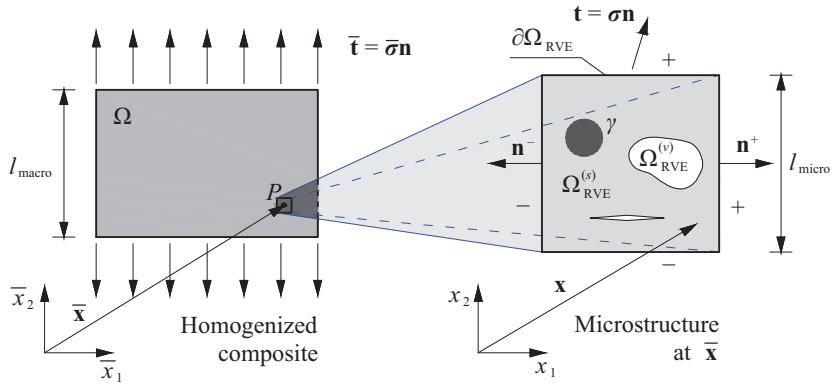

Fig. 3.1 Parallelepiped-shaped representative volume element of a heterogeneous microstructure containing microcavities, microcracks and inclusions, associated with an infinitesimal neighborhood of a material point $\bar{\mathbf{x}}$.

3.1 Setting of the homogenization problem

In the present work a first-order homogenization scheme is adopted to evaluate the homogenized behavior at a macroscopic point $\bar{\mathbf{x}}$ of a heterogeneous solid, as a function of geometry and constitutive properties of the different phases. In this homogenization procedure, an isolated RVE, whose volume is denoted by $\Omega_{\mathrm{RVE}} \subset \mathbb{R}^3$, is attached to the point $\bar{\mathbf{x}}$ and identified at microstructural scale of heterogeneities (see Fig. 3.1). A solid portion $\Omega^{(s)}_{\mathrm{RVE}}$ and a void portion $\Omega^{(v)}_{\mathrm{RVE}}$ form this volume, namely $\Omega_{\mathrm{RVE}} = \Omega^{(s)}_{\mathrm{RVE}} \cup \Omega^{(v)}_{\mathrm{RVE}}$, and the latter part is assumed to include microscopic discontinuities (cracks, interface debonding and/or cavities).

In the conventional homogenization approach, the characteristic length l_{micro} of the RVE scale must be significantly small with respect to the macroscopic scale length l_{macro} of the macroscopic structure and applied load. This assumption is not strictly necessary when a multiscale approach is adopted, although the accuracy of the macroscopic analysis generally increases as the ratio of the RVE size to the macroscopic zone of interest approaches zero.

Assuming that macroscopic constitutive response of the microstructure is based on an equilibrium state neglecting body forces and assuming small displacements, the homogenized stress and strain fields, denoted respectively by $\overline{\boldsymbol{\sigma}}$ and $\overline{\boldsymbol{\varepsilon}}$, at the macroscopic scale can be obtained from the corresponding variables at the microscopic scale by using averaging formulas [151, 193]:

$$\begin{aligned} \overline{\boldsymbol{\sigma}} &= \langle \boldsymbol{\sigma} \rangle_{\Omega_{\mathrm{RVE}}} = \frac{1}{|\Omega_{\mathrm{RVE}}|} \int_{\partial\Omega_{\mathrm{RVE}}} \mathbf{t} \otimes \mathbf{x} \, \mathrm{d}S \\ \overline{\boldsymbol{\varepsilon}} &= \langle \boldsymbol{\varepsilon} \rangle_{\Omega_{\mathrm{RVE}}} = \frac{1}{|\Omega_{\mathrm{RVE}}|} \int_{\partial\Omega_{\mathrm{RVE}}} \mathbf{u} \otimes_s \mathbf{n} \, \mathrm{d}S, \end{aligned} \tag{3.1}$$

where $\otimes_s$ denotes the symmetric part of the tensor product $\otimes$ and $\mathbf{n}$ is the outward normal at $\mathbf{x} \in \partial\Omega_{\mathrm{RVE}}$. As already stated in Section 2.1.1.5, the condition for statistical homogeneity, according to the Hill-Mandel's principle, assumes the equivalence of strain energy for the actual and homogenized structures. Thus, for a statically admissible stress field $\boldsymbol{\sigma}(\mathbf{x})$ and a kinematically admissible strain field $\boldsymbol{\varepsilon}(\mathbf{x})$,

$$\langle \boldsymbol{\sigma} : \boldsymbol{\varepsilon} \rangle_{\Omega_{\mathrm{RVE}}} = \langle \boldsymbol{\sigma} \rangle_{\Omega_{\mathrm{RVE}}} : \langle \boldsymbol{\varepsilon} \rangle_{\Omega_{\mathrm{RVE}}}. \tag{3.2}$$

The microscopic stress $\boldsymbol{\sigma}(\mathbf{x})$ and strain $\boldsymbol{\varepsilon}(\mathbf{x})$ fields satisfying the macro-homogeneity condition (3.2) may be obtained by solving the BVP for the each RVE with three alternate boundary conditions on $\partial\Omega_{\mathrm{RVE}}$:

a) Uniform traction: $\mathbf{t}(\mathbf{x}) = \overline{\boldsymbol{\sigma}} \cdot \mathbf{n}(\mathbf{x})$
b) Linear displacement: $\mathbf{u}(\mathbf{x}) = \overline{\boldsymbol{\varepsilon}} \cdot \mathbf{x}$
c) Periodic fluctuation: $\mathbf{u}(\mathbf{x}) = \overline{\boldsymbol{\varepsilon}} \cdot \mathbf{x} + \mathbf{w}(\mathbf{x}) = \overline{\boldsymbol{\varepsilon}} \cdot \mathbf{x} + \mathbf{w}\left(\mathbf{x} + \mathbf{k} \cdot \hat{\mathbf{L}}\right)$,

where $\mathbf{k}$ is a 3×3 array of integers and $\hat{\mathbf{L}} = \left[\widehat{L}_1, \widehat{L}_2, \widehat{L}_3\right]^{\mathrm{T}}$ is the period of the fluctuation field $\mathbf{w}$, interpreted as local perturbation to the macrostrain-based displacement field.

Under the assumptions of linearly hyperelastic microconstituents, convex microscopic strain energy and neglected contact forces, the homogenization condition can be obtained by means of the following minimization problem:

$$\overline{W}\left(\overline{\boldsymbol{\varepsilon}}\right) = \inf_{\mathbf{w}\in\mathscr{A}\left(\overline{\boldsymbol{\varepsilon}}\right)} \frac{1}{|\Omega_{\mathrm{RVE}}|} \int_{\Omega_{\mathrm{RVE}}^{(s)}} W(\boldsymbol{\varepsilon}(\mathbf{w}), \mathbf{x})\, \mathrm{d}V, \tag{3.3}$$

where $\mathscr{A}\left(\overline{\boldsymbol{\varepsilon}}\right)$ denotes the space of admissible fluctuations satisfying the three above-mentioned alternative constraints, assumed to be a subset of the Sobolev space $H^1\left(\Omega_{\mathrm{RVE}}^{(s)}\right)$. By solving the minimization problem (3.3) under the constraints derived from (3.2), it follows that the macrostress $\overline{\boldsymbol{\sigma}}$ and effective moduli tensor $\overline{\mathbb{C}}$ are defined in terms of the first and second derivatives of the macrostress potential with respect to the macrostrain, respectively:

$$\overline{\boldsymbol{\sigma}} = \frac{\partial \overline{W}}{\partial \overline{\boldsymbol{\varepsilon}}}, \quad \overline{\mathbb{C}} = \frac{\partial^2 \overline{W}}{\partial \overline{\boldsymbol{\varepsilon}}^2}, \tag{3.4}$$

where derivatives are taken in the Gâteaux sense.

When frictionless unilateral contact is taken into account, the minimization problem (3.3) has to be modified in order to incorporate the kinematical unilateral contact condition. In detail, the unilateral contact condition can be enforced by introducing a new space $\mathscr{K}\left(\overline{\boldsymbol{\varepsilon}}\right)$ of admissible fluctuations:

$$\mathscr{K}\left(\overline{\boldsymbol{\varepsilon}}\right) = \left\{\mathbf{w} \in \mathscr{A}\left(\overline{\boldsymbol{\varepsilon}}\right) \mid [\![w_n]\!] \leq 0 \text{ on } \Gamma_c\right\}, \tag{3.5}$$

where Γ_c denotes the union of crack faces, $w_n = \mathbf{w} \cdot \mathbf{n}$ is the normal component of the fluctuation field with respect to crack faces, and $[\![\cdot]\!]$ denotes the jump of the enclosed quantity evaluated as the difference between the values computed on the negative and positive side of the contact interface, as shown in Fig. 3.2.

As a consequence of the inequality constraint (3.5), the minimization problem leads to a variational inequality; when frictionless unilateral contact occurs, the macroscopic constitutive behavior of the composite becomes nonlinear but remains hyperelastic (i.e. rate- and path-independent). In fact, the

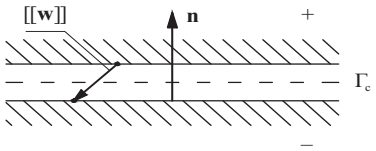

Fig. 3.2 Notation employed to define the admissible fluctuation fields when contact between crack faces must be considered in the homogenization problem.

contact area is not known a-priori but is dependent only on the direction of the prescribed macrostrain, implying that the effective moduli tensor $\overline{\mathbb{C}}$ satisfies the relation $\overline{\mathbb{C}}\left(\lambda\overline{\boldsymbol{\varepsilon}}\right) = \overline{\mathbb{C}}\left(\overline{\boldsymbol{\varepsilon}}\right)$ for any strictly positive real number λ (see [175] for additional details).

Assuming that each constituent phase in Ω_{RVE} is made of linear elastic material with a convex strain energy function, the following relationship between the macroscopic strain energy functions for the considered boundary conditions has been established:

$$\overline{\boldsymbol{\varepsilon}} : \overline{\mathbb{C}}_{\mathrm{UT}} : \overline{\boldsymbol{\varepsilon}} \leq \overline{\boldsymbol{\varepsilon}} : \overline{\mathbb{C}}_{\mathrm{PF}} : \overline{\boldsymbol{\varepsilon}} \leq \overline{\boldsymbol{\varepsilon}} : \overline{\mathbb{C}}_{\mathrm{LD}} : \overline{\boldsymbol{\varepsilon}}, \tag{3.6}$$

where $\overline{\mathbb{C}}_{\mathrm{UT}}$, $\overline{\mathbb{C}}_{\mathrm{PF}}$, $\overline{\mathbb{C}}_{\mathrm{LD}}$ are the macroscopic (or *effective*) moduli tensors evaluated respectively with uniform traction (UT), periodic fluctuation (PF) and linear displacement (LD) boundary conditions; it is worth noting that in Eq. (3.6) the same prescribed macroscopic (or averaged) strain $\overline{\boldsymbol{\varepsilon}}$ for each boundary conditions is assumed. The proof of Eq. (3.6) is given in [151], in the absence of contact; however, as shown in [54], Eq. (3.6) remain valid also in the presence of frictionless unilateral contact.

The apparent properties obtained by application of uniform strain BCs on a microstructural cell usually overestimate the actual effective properties, while the uniform traction boundary conditions lead to their underestimation. It has been verified by a number of authors (see [54, 164, 194], for instance) that, for a given RVE size, periodic BCs provide a better estimation of the

overall properties than the uniform strain and uniform traction boundary conditions. This statement also holds if the given microstructure does not really have geometrical periodicity [164]. Furthermore, increasing the size of the RVE leads to a convergence of the results obtained with reference to the different boundary conditions to the actual effective properties of the composite material.

Unlike classical homogenization approaches, based on classical bottom-up coupling between the different scales, an important issue in the framework of multiscale modeling is recovering the microscopic fields from the results of the macroscopic solution. In fact, a second coupling, which is of the top-down type, allows the evolution of local variables to be evaluated at the scale of the microstructure from the known macroscopic variables, by a process termed *localization*. In order to obtain this scale bridging, the local equilibrium problem of the RVE subjected to boundary conditions depending on the macroscopic deformation tensor is solved with reference to periodic boundary conditions to gives a local solution which usually is a good approximation of the actual one. When the composite material is periodic the microscopic scale response can be obtained by identifying the RVE with a representative unit cell (RUC).

3.2 Modeling of microcrack initiation and propagation

Most of the existent semiconcurrent multiscale models assume that the microscopic damage can be modeled by using either a continuum damage model [181] or a cohesive zone model (see, for instance, [183]); these approaches are effective, robust, and easy to implement, and they are able to manage both initiation and propagation of damage in a same numerical model. However special techniques are usually required to avoid the sensitivity of the numerical results on the mesh size and orientation.

Here a different strategy is pursued, in the framework of *Finite Fracture Mechanics* (FFM) for crack initiation analysis, and of *Linear Elastic Fracture*

Mechanics (LEFM) for crack propagation analysis: crack initiation and propagation are simulated separately, by using different phenomenological criteria at the microscopic scale, as described in the following.

3.2.1 Microcrack initiation analysis

In the present work, fracture phenomena are supposed to involve only the matrix and the material interfaces, whereas the fibers are supposed to be infinitely strong[1]. Under this hypothesis, a crack can initiate either within the matrix or at an interface; in the first scenario, crack initiation occurs at the interface, considered to be the weakest component, whereas in the second scenario, in the presence of a stronger interface, crack initiates within the matrix.

Crack initiation is simulated in two steps. In the first one, the *onset point* $P(\mathbf{x}_{\text{onset}})$, i.e. the critical point at which crack initiation occurs, is detected, within the matrix ($\mathbf{x}_{\text{onset}} \in \Omega_m$) or at the fiber/matrix interface ($\mathbf{x}_{\text{onset}} \in \Gamma$). The well-known *maximum principal stress criterion* can be adopted in the former case, whereas Ye's *quadratic failure criterion* in the latter, which accounts for the interaction between the normal and tangential stresses, assuming an infinite strength in compression (see [195] for additional details):

$$\begin{aligned} \mathbf{x}_{\text{onset}} &= \arg\max_{\mathbf{x}\in\Omega_m} \left(\frac{\sigma_1}{\sigma_c^m}\right) && \text{(within the matrix)} \\ \mathbf{x}_{\text{onset}} &= \arg\max_{\mathbf{x}\in\Gamma} \left[\left(\frac{\langle\sigma\rangle}{\sigma_c^\gamma}\right)^2 + \left(\frac{\tau}{\tau_c^\gamma}\right)^2\right] && \text{(at the interface)} \end{aligned} \tag{3.7}$$

where σ_1 is the maximum principal stress within the matrix, σ_c^m is the tensile strength of the matrix, σ and τ denote the normal and tangential interfacial stresses, σ_c^γ and τ_c^γ are the corresponding strengths, and $\langle\cdot\rangle$ denotes the Macaulay brackets, used to describe the ramp function[2].

[1] This assumption appears to be likely, since fibers are generally stronger than the surrounding matrix in most bimaterial systems.

[2] As fracture is caused by a material instability, a more rigorous approach for

In the second step, a generalization of the coupled stress- and energy-based criterion proposed by Leguillon is adopted to simulate the crack onset process. The basic idea of this approach consists in using simultaneously a stress-based criterion and an energy-based one, since either of them represents a necessary but not sufficient condition for the crack onset (see [47] for details). As a matter of fact, the only use of a stress criterion allows to find the minimum value of the applied load leading to rupture, but cannot lead to an explicit determination of the size of the originated crack. On the other hand, the application of the energy-based criterion (according to Griffith's approach) necessarily requires a pre-existing crack; as a consequence, it is not possible to determine the initial crack length associated to the nucleation process. Therefore, when using only one criterion, the crack initiation problem can be solved after artificially introducing a characteristic length, according to the theory of *critical distances* (see [196] for additional details).

If the load factor β_c associated with Eq. $(3.7)_1$ is smaller than the one associated with Eq. $(3.7)_2$, assuming the sudden onset of a matrix crack of finite length, as shown in Fig. 3.3a, the proposed approach consists in the simultaneous application of both the stress- and energy-based criteria, in combination with an additional criterion, able to predict the direction of crack initiation. Thus, crack initiation occurs starting from the already identified onset point, if at a neighboring point the stress criterion is satisfied, the potential energy released during the nucleation of a virtual crack, emanated from the crack onset point to this point, here called *incremental energy release* (IER), reaches its critical value and the IER weighted with respect to its critical value, assumes a maximum value among all possible crack onset directions. The appli-

studying crack initiation phenomena would require a suitable definition of *loss of ellipticity* (or *loss of material stability*) at any material point. After defining the so-called *acoustic tensor* $\mathbf{Q} = \mathbf{n} \cdot \mathbb{D} \cdot \mathbf{n}$ for a given material point with tangent moduli tensor $\mathbb{D}$ and for any direction $\mathbf{n}$, this point is considered to be stable whenever the minimum eigenvalue of $\mathbf{Q}$ is strictly positive, and unstable otherwise.

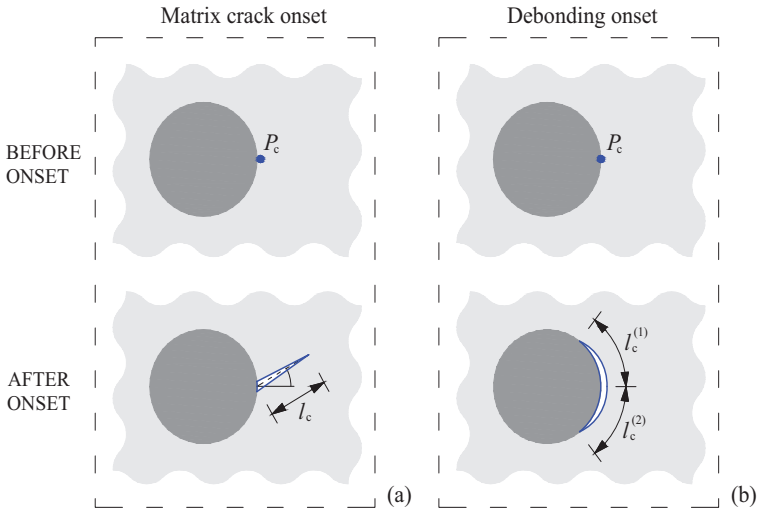

Fig. 3.3 Two scenarios for crack initiation in fiber-reinforced composites: (a) matrix crack emanated from the fiber boundary in the case of strong interface; (b) interface crack nucleation in the case of weak interface.

cation of this approach provides the following system of three (typically nonlinear) equations for three unknowns: the length l_c of the nucleated crack, the crack initiation angle θ_c and the critical load factor β_c required for its onset:

$$\begin{cases} \sigma_{r\theta}(\beta_c, l_c, \theta_c) = \sigma_c^m \\ \mathscr{E}(\beta_c, l_c, \theta_c) = \mathscr{E}_c^m \\ \theta_c = \arg\max_{\theta} \left(\dfrac{\mathscr{E}}{\mathscr{E}_c^m} \right) \end{cases} \tag{3.8}$$

where $\sigma_{r\theta}$ denotes the circumferential stress, $\mathscr{E}$ is the incremental energy release[3], defined by applying the incremental version of Griffith's criterion:

[3] In the spirit of the *finite fracture mechanics*, the incremental energy release can be also defined as the integral of classical energy release rate over the total crack length.

$$\mathscr{E}(\beta_c, l_c, \theta_c) = -\Delta\Pi(\beta_c, l_c, \theta_c) = -\left[\Pi^*(\beta_c, l_c, \theta_c) - \Pi(\beta_c)\right], \tag{3.9}$$

with Π and Π^* denoting the potential energy before and after the crack onset, respectively; $\mathscr{E}_c^m$ is the incremental energy release for the crack initiation within the matrix, defined as

$$\mathscr{E}_c^m = \mathscr{G}_c^m l_c, \tag{3.10}$$

for a homogeneous and isotropic material, where $\mathscr{G}_c^m$ is the fracture energy of the matrix. In practice, the system (3.8) can be solved through an iterative method, by testing different values of crack length and crack direction at initiation; thus, a rigorous approach requires a high computational cost due to the need of remeshing for each trial couple (l_c, θ_c).

A significant reduction in numerical effort comes from the assumption that crack initiation occurs at the fiber/matrix interface (see Fig. 3.3b): this is a likely scenario, because interfaces, which act as stress concentrators in bi-material systems those matrix is softer than inclusions, usually represent the weakest component. Under this hypothesis, pursued in the present work, the dependence on the crack angle disappears, and the system (3.8) becomes:

$$\begin{cases} \left(\dfrac{\langle\sigma\left(\beta_c, l_c^{(1)}\right)\rangle}{\sigma_c^\gamma}\right)^2 + \left(\dfrac{\tau\left(\beta_c, l_c^{(1)}\right)}{\tau_c^\gamma}\right)^2 = 1 & \text{at tip 1} \\ \left(\dfrac{\langle\sigma\left(\beta_c, l_c^{(2)}\right)\rangle}{\sigma_c^\gamma}\right)^2 + \left(\dfrac{\tau\left(\beta_c, l_c^{(2)}\right)}{\tau_c^\gamma}\right)^2 = 1 & \text{at tip 2} \\ \mathscr{E}\left(\beta_c, l_c^{(1)}, l_c^{(2)}\right) = \mathscr{E}_c^\gamma\left(l_c^{(1)}, l_c^{(2)}\right) \end{cases} \tag{3.11}$$

where $l_c^{(1)}$ and $l_c^{(2)}$ denote the two partial crack lengths measured from the onset point, such that $l_c = l_c^{(1)} + l_c^{(2)}$, and $\mathscr{E}_c^\gamma$ is the critical value for the interfacial IER; since Eq. $(3.11)_3$ represents an energy-based (global) criterion, the incremental energy release can be regarded as the sum of contributions arising from

the two tips [49]:

$$\mathscr{E}_c^{\gamma}\left(l_c^{(1)}, l_c^{(2)}\right) = \int_0^{l_c^{(1)}} \mathscr{G}_c^{(1)}\big(\psi(l)\big)\,\mathrm{d}l + \int_0^{l_c^{(2)}} \mathscr{G}_c^{(2)}\big(\psi(l)\big)\,\mathrm{d}l, \qquad (3.12)$$

where $\mathscr{G}_c^{(1)}$ and $\mathscr{G}_c^{(2)}$ are the toughness functions for tip 1 and 2, respectively, expressed in terms of the mode mixity by relations of the type (3.29).

It is worth noting that Eqs. $(3.11)_1$ and $(3.11)_2$ establish an explicit relationship between $l_c^{(1)}$ and $l_c^{(2)}$; therefore, they cannot be chosen independently of each other, suggesting a suitable numerical method to solve the nonlinear system (3.11), as discussed in Section 3.3.1.

3.2.2 Microcrack propagation analysis

In the present work, microcrack propagation phenomena are supposed to involve only the matrix and the material interfaces, whereas the fibers are supposed to be infinitely strong. Moreover, both matrix and interfaces are of brittle character, thus the size of fracture process zone can be neglected, according to the classical framework of *linear elastic fracture mechanics* (LEFM) [197]; given a 2D heterogeneous domain Ω containing a crack of finite length l, Griffith's classical energy-based fracture criterion suggests a quasi-static rate-independent model for crack propagation, expressed by means of the well-known Kuhn-Tucker conditions:

$$\begin{aligned} &\dot{l} \geq 0 \\ &\mathscr{G}(l) - \mathscr{G}_c \leq 0 \\ &(\mathscr{G}(l) - \mathscr{G}_c)\dot{l} = 0 \end{aligned} \qquad (3.13)$$

where $\dot{l}$ is the rate of the crack length, $\mathscr{G}$ denotes the energy release rate associated to l, and $\mathscr{G}_c$ is its critical value, also referred to as fracture energy, which is considered as a material constant for crack tips embedded in isotropic homogeneous phases or as a function of the mode mixity for interface cracks.

In the present work, a *crack length control scheme* [56] is adopted: the crack propagation process is modeled by incrementally extending the given crack of a small amount Δl; this incremental strategy requires a suitable choice for Δl, having to be much smaller than a characteristic length of the microstructure, e.g. the diameter of the fibers (a fixed value is generally chosen for the whole crack propagation process, but adaptively computed increments are also possible, in order to properly capture locally tortuous crack paths).

For each value of l, the elasticity problem is solved for a unit external load factor; the actual load factor β_c (also referred to as *critical load factor*) is subsequently determined, by enforcing the quasi-static crack propagation criterion $\mathcal{G}(l) = \mathcal{G}_c$ at each step. By virtue of the supposed linearity of the problem, the resulting load control equation can be written in the form:

$$\beta_c^2 \hat{\mathcal{G}}(l) - \mathcal{G}_c = 0, \tag{3.14}$$

from which the critical load factor is obtained:

$$\beta_c = \sqrt{\mathcal{G}_c / \hat{\mathcal{G}}(l)}, \tag{3.15}$$

where $\hat{\mathcal{G}}$ denotes the energy release rate per unit load factor associated with l.

This technique, sketched in Fig. 3.4, is essentially used to simplify the analysis by avoiding the need for developing a dedicated algorithm capable to deal with nonsmooth Kuhn-Tucker conditions. In detail, a path-following constraint based on the crack length (acting as a damage parameter), allows to achieve two main advantages: (i) the thermodynamically consistent irreversibility condition $\dot{l} \geq 0$ is automatically satisfied, and (ii) the instability phenomena commonly occurring during the damage propagation in composites, such as snap-back and snap-through events, can be properly studied[4].

[4] A variety of control types can be applied to trace quasistatic nonlinear load-displacement curves, based on different constraint equations to be used in an incremental-iterative scheme. For geometrically nonlinear problems the well-known arc-length method, developed by Riks [50], is well suited as a structural equilibrium path-

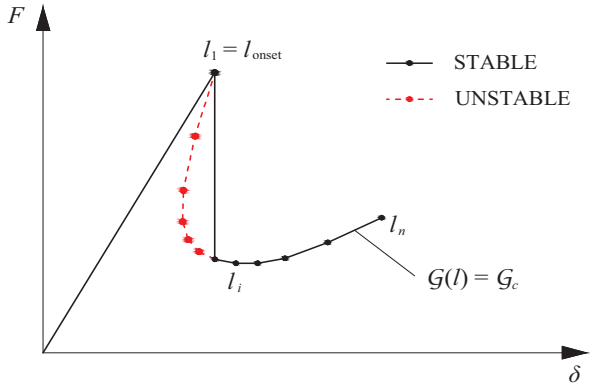

Fig. 3.4 Crack length control scheme: load-displacement curve in the presence of a snap-back instability.

In the presence of multiple crack tips, the propagation process is assumed to be controlled by the total crack length, i.e. the sum of lengths of all cracks; coherently, the total amount of crack increments is set equal to a fixed value Δl_{tot} at each simulation step. At a general step, the length of each active crack tip is increased by:

$$\Delta l_i = \frac{\Delta l_{\text{tot}}}{n_{\text{act}}}, \quad i = 1, \dots, n_{\text{act}}, \tag{3.16}$$

where n_{act} is the number of active tips at the beginning of step $j + 1$; it can be determined by a stability analysis at the end of step j. As explained in [198], since the algorithm is explicit and the propagation criterion and the equilibrium equations are implemented by an operator-split approach, the proposed

following strategy; however, for structures exhibiting materially nonlinear phenomena like strain localization and cracking, softening can lead to failure of the arc-length method, if localization affects only a few degrees of freedom involved in the constraint equation. Other suitable continuation method for path-dependent materials are, for instance, the crack mouth opening control scheme[51], the total strain control scheme [52], and the dissipation based arc-length method [53].

method is only conditionally stable, and therefore Δl_{tot} must be chosen sufficiently small. At the beginning of each step, a unit load is applied to the system and the FE analysis is performed. The most critical crack tip, i.e. the crack tip with maximum value of $\hat{\mathcal{G}}^{(i)} / \mathcal{G}_c^{(i)}$, is then detected; the critical load parameter β_c is chosen so that the energy release rate for the considered crack tip reaches its critical value. The critical load parameter β_c for linear elastic materials is defined as:

$$\beta_c = \sqrt{\inf_{i=1,\dots,n_{\text{tip}}} \left(\frac{\mathcal{G}_c^{(i)}}{\hat{\mathcal{G}}^{(i)}} \right)}. \tag{3.17}$$

If $\mathcal{G}^{(i)}$ is close to $\mathcal{G}_c^{(i)}$ for more than one tip, a very small error in the determination of the stress intensity factors can prevent a crack tip from propagating, leading to a wrong prediction of the crack propagation pattern. Therefore, a tolerance can be introduced while applying the propagation criterion. The set of competing crack tips is denoted by N_{comp} and defined as:

$$N_{\text{comp}} = \left\{ i \in \left\{1, \dots, n_{\text{tip}}\right\} \text{ such that } \frac{\mathcal{G}_c^{(i)} - \mathcal{G}^{(i)}}{\mathcal{G}_c^{(i)}} \leq \varepsilon_{\mathcal{G}} \right\}, \tag{3.18}$$

where the tolerance $\varepsilon_{\mathcal{G}}$ is chosen based on the accuracy of evaluation of the stress intensity factors. As the energy release rate is computed by the *J*-integral technique (see Section 3.3.2.3), in the present work $\varepsilon_{\mathcal{G}}$ is always set equal to 1%. In general, the propagating cracks can be detected from the set of competing crack tips by carrying out a stability analysis, as described in [198]. However, in the present work the stability analysis has been avoided, since in the numerical experiments, it is assumed that the two considered competing crack tips do not interact each other.

3.2.2.1 Microcrack propagation along a fiber/matrix interface

Once initiated, an interfacial crack tends to propagate along the interface as a fiber/matrix debonding. Thus, the general problem of an interfacial crack in a bimaterial system is considered; the governing analytical solution for a plane

interface crack between two elastic isotropic materials was obtained by Williams [199] and results in a singular, oscillating stress field as the crack tip is approached. The stress singularity is of the order of $r^{-1/2+i\varepsilon}$, where r is the distance from the crack tip, i is the imaginary unit, and ε is the bimaterial constant defined as:

$$\varepsilon = \frac{1}{2\pi} \ln \left\{ \frac{\kappa_1/\mu_1 + 1/\mu_2}{\kappa_2/\mu_2 + 1/\mu_1} \right\} \tag{3.19}$$

with

$$\kappa_j = \begin{cases} 3 - 4\nu_j & \text{plane strain} \\ \left(3 - \nu_j\right)/\left(1 + \nu_j\right) & \text{plane stress} \end{cases} \tag{3.20}$$

where ν_j and μ_j denote the Poisson's ratio and the shear modulus of the material j, respectively.

A complex stress intensity factor was introduced by Rice and Sih [200], according to the following definition:

$$K = K_1 + iK_2 = |K| e^{i\psi^*}, \tag{3.21}$$

where ψ^* is the phase angle (also referred to as mode mixity of K). The stress field ahead of the crack tip at the interface ($\theta = 0$), at a distance r is given by:

$$\sigma_{yy} + i\tau_{xy} = \frac{K}{\sqrt{2\pi r}} r^{i\varepsilon}, \tag{3.22}$$

where σ_y and τ_{xy} are the tensile and shear stress components (see Fig. 3.5).

The oscillatory solution implies: (i) coupling between fracture modes, and (ii) interpenetration of crack faces adjacent to the crack tip; as a consequence, the oscillatory solution does not capture the actual behavior close to the crack tip, associated with contact and phenomena. Several approaches have been proposed to manage the oscillating singularity, such as the *contact model* introduced by Comninou [201], but they are not able to determine the crack tip mode mixity. The concept of a *small-scale contact zone* has been proposed by

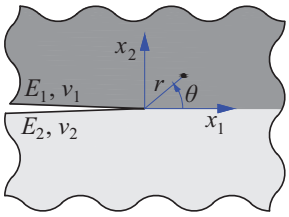

Fig. 3.5 Geometry and notation for an interfacial crack.

Rice to circumvent interpenetration of crack faces and allows the oscillatory solution to be valid in the so-called K-annulus, defined as the region close to the crack tip dominated by the asymptotic singular field, outside the nonlinear contact zone.

Furthermore, K_1 and K_2 cannot be interpreted as mode I and mode II stress intensity factors, due to the above-mentioned coupling between fracture modes; thus an alternative definition of interfacial *stress intensity factors* (SIFs) was introduced by Rice [202], using the concept of *reference length*:

$$\sigma_{yy} + i\tau_{xy} = \frac{K_{\mathrm{I}} + iK_{\mathrm{II}}}{\sqrt{2\pi r}} \left(\frac{r}{l_{\mathrm{ref}}} \right)^{i\varepsilon}, \tag{3.23}$$

where K_{I} and K_{II} are SIFs of classical type based on a reference length l_{ref} arbitrarily chosen to normalized the oscillatory singular term[5]; it is worth not-

[5] As pointed out in [88], it is useful to distinguish between a choice based on an in-plane length L of the specimen geometry, such as the crack length, and a choice based on a material length scale, such as the size of the fracture process zone. The former choice is used to describe the mixed-mode character of an interfacial crack in bimaterial systems, without any assumptions about the material fracture behavior, whereas the latter is more suitable for interpreting the mixed-mode fracture data. In the present work, according to the choice of a material-based reference length (also referred to as *characteristic length*), l_{ref} necessarily lies within the zone of dominance of the K-field.

ing that K_{I} and K_{II} are not analogous to independent fracture modes I (opening) and II (in-plane shear) for homogenous materials, since a reference length needs to be specified.

The SIFs of classical type K_{I} and K_{II} in Eq. (3.23) are related to the complex K in Eq. (3.22) as follows:

$$K_{\mathrm{I}} + iK_{\mathrm{II}} = Kl_{\mathrm{ref}}^{i\varepsilon} = |K|e^{i\psi}, \tag{3.24}$$

where ψ is the mode mixity of $Kl_{\mathrm{ref}}^{i\varepsilon}$, which can be rewritten as

$$\psi = \tan^{-1}\left(\frac{K_{\mathrm{II}}}{K_{\mathrm{I}}}\right) = \tan^{-1}\left(\frac{\mathfrak{I}\left(Kl_{\mathrm{ref}}^{i\varepsilon}\right)}{\mathfrak{R}\left(Kl_{\mathrm{ref}}^{i\varepsilon}\right)}\right) \tag{3.25}$$

with $\mathfrak{R}(\cdot)$ and $\mathfrak{I}(\cdot)$ denoting the real and imaginary parts, respectively.

On the other hand, the relative displacements between the crack faces can be evaluated by the following expression:

$$\delta_y + i\delta_x = \frac{8}{(1+2i\varepsilon)E^*\cosh(\pi\varepsilon)}(K_{\mathrm{I}} + iK_{\mathrm{II}})\sqrt{\frac{r}{2\pi}}\left(\frac{r}{l_{\mathrm{ref}}}\right)^{i\varepsilon}, \tag{3.26}$$

where δ_y and δ_x are the relative normal and tangential crack tip displacements with respect to the crack tip propagation direction, r is the distance from the crack tip at which the relative displacements are evaluated, and the equivalent Young's modulus E^* for the bimaterial system is defined as

$$\frac{1}{E^*} = \frac{1}{2}\left(\frac{1}{E_1'} + \frac{1}{E_2'}\right) \tag{3.27}$$

with $E_j' = E_j$ for plane stress and $E_j' = E_j/\left(1-\nu_j^2\right)$ for plane strain.

Furthermore, the total strain energy release rate $\mathcal{G}^{\gamma}$ for an interface crack is not oscillatory and can be expressed as [203]:

$$\mathcal{G}^{\gamma} = \frac{1}{E^*\cosh^2(\pi\varepsilon)}|K|^2, \tag{3.28}$$

where $|K|^2 = K_1^2 + K_2^2 = K_\mathrm{I}^2 + K_\mathrm{II}^2$; according to Griffith's criterion, at fracture load, $\mathcal{G}^\gamma$ is equal to the toughness of the interface $\mathcal{G}_c^\gamma$. The following phenomenological criterion is employed to characterize the interface toughness (see [88]):

$$\mathcal{G}_c^\gamma\big(\psi(l_\mathrm{ref})\big) = \mathcal{G}_{Ic}^\gamma\big\{1 + \tan^2\big[(1-\lambda)\psi(l_\mathrm{ref})\big]\big\}, \tag{3.29}$$

where $\mathcal{G}_{Ic}^\gamma$ denotes the fracture mode I toughness, λ is a fracture mode sensitivity parameter that adjusts the influence of mode II contribution, and ψ is the mode mixity as defined by Eq. (3.25).

3.2.2.2 Competition between interfacial debonding and kinking out of an interface

When a crack propagates along the fiber/matrix interface, it is loaded in mixed mode and can kink out of the interface under a certain combination of loading condition and geometric configuration; moreover it is expected that it will stay on the interface only if this mechanism is energetically favored over kinking towards the matrix, in the spirit of the maximum energy release rate criterion [204].

He and Hutchinson have proposed that a crack propagates along an interface if the ratio of the energy release rates at the interface and in the bulk material is larger than the ratio of the respective values of the fracture toughness, i.e.

$$\frac{\mathcal{G}^\gamma}{\mathcal{G}_\mathrm{max}^m} > \frac{\mathcal{G}_\mathrm{c}^\gamma(\psi)}{\mathcal{G}_c^m}, \tag{3.30}$$

otherwise, it kinks out of the interface; in Eq. (3.30) $\mathcal{G}_\mathrm{max}^m$ denotes the maximum of $\mathcal{G}^m$ with respect to kink angle for a given ψ.

If $\mathcal{G}_c^m$ is sufficiently large, compared to $\mathcal{G}_\mathrm{c}^\gamma(\psi)$, the crack will never kink into the matrix; on the other hand, when $\mathcal{G}_\mathrm{c}^\gamma(\psi)$ and $\mathcal{G}_c^m$ are comparable, there will be a loading range $0 \le \psi \le \psi^*$ such that the crack stays in the interface, whereas for $\psi > \psi^*$ the interface crack will kink into the matrix.

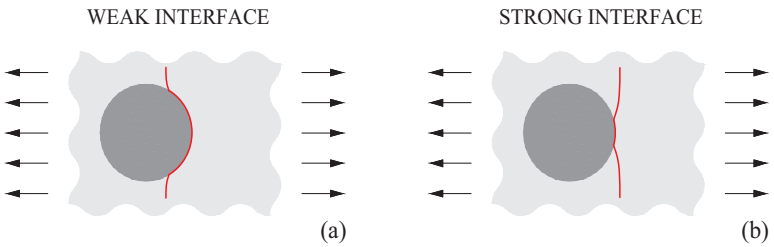

Fig. 3.6 Crack configuration after kinking in the case of (a) weak interface and of (b) strong interface.

As a consequence, the debonding lengths at kinking are strongly influenced by the interface toughness, which depends on the adhesion mechanisms governing the fiber/matrix bond. In the case of weak interfaces, kinking takes place after wide interface portions affected by debonding, as sketched in Fig. 3.6a; conversely, in the case of strong interfaces, kinking prevails over debonding and the total crack configuration appears almost completely as a matrix crack, as shown in Fig. 3.6b.

3.2.2.3 Microcrack propagation within the matrix

Matrix microcracking is driven by the *maximum energy release rate criterion*, which states that a crack will propagate so as to maximize the energy release. Since, by definition, $\mathcal{G} = \Pi'(l) = \partial\Pi/\partial l$, this criterion is equivalent to saying that cracks grow so as to minimize the potential energy of the solid, matching with the thermodynamic idea that equilibrium systems seek their local energy minima.

Wu [204] studied the propagation problem for 2D cracks under mixed-mode loading conditions, by considering a straight crack of finite length l extended by a small kink of length $\Delta l \ll l$ in a certain direction defined by the finite angle θ, starting from the pre-existing crack tip. According to the maximum energy release rate criterion, the crack will kink at the angle θ_c if

$$\frac{\partial \mathcal{G}(\theta_c)}{\partial \theta} = 0, \qquad \frac{\partial^2 \mathcal{G}(\theta_c)}{\partial \theta^2} < 0, \qquad \mathcal{G}(\theta_c) = \mathcal{G}_c, \tag{3.31}$$

where $\mathcal{G}(\theta) \equiv \lim_{\Delta l \to 0} \frac{1}{\Delta l}(\Pi^* - \Pi)$, with Π and Π^* denoting the potential energy for the original and kinked crack, respectively. For loading in pure mode I, the resulting value for θ_c is zero, whereas for loading in pure mode II, one obtains $|\theta_c| = \theta_{\max} \approx 75.2°$, where the sign of θ_c depends on the sign of the stress intensity factor K_{II}; for mixed-mode loading, θ_c must fulfill the following conditions: $-\theta_{\max} < \theta_c < 0$ for $K_{\mathrm{II}} > 0$ and $0 < \theta_c < \theta_{\max}$ for $K_{\mathrm{II}} < 0$.

3.3 Effective properties of composite materials with evolving microcracking

In this section, the strategy for obtaining the effective mechanical properties of periodic composite materials undergoing microcrack initiation and propagation, introduced in [44, 54], is presented. This method is based on the combination of a classical first-order homogenization method and a path-following strategy based on the crack length, already discussed in Sections 3.1 and 3.2. With reference to the repeating unit cell (RUC) of a two-dimensional periodic microstructure, subjected to a prescribed macrostrain $\overline{\boldsymbol{\varepsilon}}$, the effective moduli tensor for a given damage configuration, depending on the crack length l and on the macrostrain direction $\hat{\overline{\boldsymbol{\varepsilon}}} = \overline{\boldsymbol{\varepsilon}} / \left\| \overline{\boldsymbol{\varepsilon}} \right\|$, due to the nonlinearities induced by contact, can be determined by using Eq. $(3.4)_2$. Therefore, the macroscopic constitutive law can be written as:

$$\overline{\boldsymbol{\sigma}} = \overline{\mathbb{C}}\left(\hat{\overline{\boldsymbol{\varepsilon}}}, l\right) : \overline{\boldsymbol{\varepsilon}}, \tag{3.32}$$

where $\overline{\mathbb{C}} \equiv \left(C_{ijhk}\right)$ denotes the macroscopic secant moduli tensor.

Starting from the crack configuration at its onset, the use of the classical fracture criterion, expressed as a constraint equation of type (3.14), together with the kinking criterion (3.30) and the maximum energy release criterion (3.31) when needed, leads to obtain a nonlinear damage evolution relationship

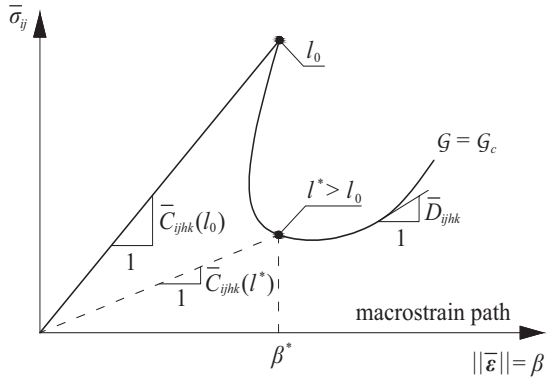

Fig. 3.7 Macroscopic constitutive law in the presence of evolving cracks.

between the prescribed macrostrain and the crack length, i.e. $l = l\left(\bar{\boldsymbol{\varepsilon}}\right)$. As a consequence, the macroscopic stress-strain relation becomes highly nonlinear and depends on the macrostrain history.

Taking the derivative of Eq. (3.32) with respect to a time-like parameter t, the following incremental constitutive relationship is obtained:

$$\begin{aligned} &\dot{\bar{\boldsymbol{\sigma}}} = \bar{\mathbb{D}}\left(\bar{\boldsymbol{\varepsilon}}\right) : \dot{\bar{\boldsymbol{\varepsilon}}} \\ &\bar{D}_{ijhk}\left(\bar{\boldsymbol{\varepsilon}}\right) = \bar{C}_{ijhk}\left(l\left(\bar{\boldsymbol{\varepsilon}}\right)\right) + \frac{\partial \bar{C}_{ijmn}\left(l\left(\bar{\boldsymbol{\varepsilon}}\right)\right)}{\partial \bar{\varepsilon}_{hk}} \bar{\varepsilon}_{mn} \end{aligned} \tag{3.33}$$

where $\bar{\mathbb{D}} \equiv \left(\bar{D}_{ijhk}\right)$ is the macroscopic incremental (tangent) moduli tensor, the "over-dot" denotes time derivative, and $\dot{l} > 0$ is assumed. Eq. (3.33) accounts for the evolutionary change in stiffness with progressive cracking, and for $\dot{l} \leq 0$, i.e. during unloading, the second term at the right hand side of Eq. $(3.33)_2$ vanishes. Both $\bar{C}_{ijhk}\left(\bar{\boldsymbol{\varepsilon}}\right)$ and $\bar{D}_{ijhk}\left(\bar{\boldsymbol{\varepsilon}}\right)$ appearing in Eq. (3.33) are represented in Fig. 3.7.

For a prescribed macrostrain path $\beta\hat{\bar{\boldsymbol{\varepsilon}}}$, controlled by a parameter $\beta > 0$ (serving as a load factor), the energy release rate for a given crack length is computed; by recalling the linearity of the problem, the computed energy release rate satisfies the following equation:

$$\mathcal{G}\left(\beta\hat{\overline{\boldsymbol{\varepsilon}}}, l\right) = \beta^2 \mathcal{G}\left(\hat{\overline{\boldsymbol{\varepsilon}}}, l\right); \tag{3.34}$$

thus, the damage evolution criterion provides the critical load factor as

$$\beta_c = \sqrt{\mathcal{G}_c \,/\, \mathcal{G}\left(\hat{\overline{\boldsymbol{\varepsilon}}}, l\right)}, \tag{3.35}$$

and the macroscopic moduli can be obtained as functions of the macrostrain $\beta_c \hat{\overline{\boldsymbol{\varepsilon}}}$, when the fracture criterion is imposed.

The nonlinear macroscopic stress-strain relation (3.32) for a prescribed macrostrain path has been determined by calculating the macroscopic strain by Eq. (3.35) and the corresponding stress by Eq. $(3.1)_1$ as a function of the crack length, assuming a monotonic damage growth. In detail, by considering only two-dimensional repeating unit cells (RUCs), three different macrostrain path can be considered:

$$\begin{cases} \hat{\overline{\boldsymbol{\varepsilon}}}_1^{\pm} = \pm \mathbf{e}_1 \otimes \mathbf{e}_1 \\ \hat{\overline{\boldsymbol{\varepsilon}}}_2^{\pm} = \pm \mathbf{e}_2 \otimes \mathbf{e}_2 \\ \hat{\overline{\boldsymbol{\varepsilon}}}_3^{\pm} = \pm \dfrac{1}{2}(\mathbf{e}_1 \otimes \mathbf{e}_2 + \mathbf{e}_2 \otimes \mathbf{e}_1) \end{cases} \tag{3.36}$$

where the vectors $\mathbf{e}_1$ and $\mathbf{e}_2$ form a basis for $\mathbb{R}^2$, $\hat{\overline{\boldsymbol{\varepsilon}}}_1^{\pm}$ and $\hat{\overline{\boldsymbol{\varepsilon}}}_2^{\pm}$ are the uniaxial macrostrain paths along the directions x_1 and x_2, respectively, and $\hat{\overline{\boldsymbol{\varepsilon}}}_3^{\pm}$ is the shear macrostrain path; moreover the superscript $\pm$ denotes the positive (tensile) or negative (compressive) macrostrain path direction.

It can be shown that each component $\overline{\mathbb{C}}\left(\hat{\overline{\boldsymbol{\varepsilon}}}_h\right) \cdot \mathbf{e}_i \otimes \mathbf{e}_j$ $(h = 1,2,3)$ of the effective moduli tensor can be determined as the component $\overline{\sigma}_{ij}$ of the macroscopic stress tensor, eventually with the sign changed in the case of compressive loading, associated with the macrostrain path direction $\hat{\overline{\boldsymbol{\varepsilon}}}_h$.

By virtue of its minor symmetry, the macroscopic moduli tensor $\overline{\mathbb{C}}$ admits a matrix representation; thus, in Voigt notation, the macroscopic constitutive law (3.32) can be rewritten as:

$$\boldsymbol{\sigma}_V = \mathbf{C}\boldsymbol{\varepsilon}_V \tag{3.37}$$

with $\boldsymbol{\sigma}_V = (\sigma_{11}, \sigma_{22}, \sigma_{33}, \sigma_{23}, \sigma_{31}, \sigma_{12})^{\mathrm{T}}$, $\boldsymbol{\varepsilon}_V = (\varepsilon_{11}, \varepsilon_{22}, \varepsilon_{33}, 2\varepsilon_{23}, 2\varepsilon_{31}, 2\varepsilon_{12})^{\mathrm{T}}$ expressed as vectors, and $\mathbf{C}$ being a 6×6 matrix. By considering only the in-plane components along the directions x_1 and x_2, one obtains:

$$\mathbf{C} = \begin{bmatrix} C_{1111} & C_{1122} & C_{1112} \\ C_{2211} & C_{2222} & C_{2212} \\ C_{1211} & C_{1222} & C_{1212} \end{bmatrix}, \tag{3.38}$$

It is worth noting that $\mathbf{C}$ is symmetric due to the major symmetry of the moduli tensor $\mathbb{C}$, therefore only six (in-plane) components must be determined, in the case of anisotropic materials.

3.3.1 Finite element implementation

The variational problem of homogenization has been discretized by means of a displacement-based finite element (FE) approximation implemented by using the commercial software COMSOL Multiphysics®. A MATLAB® script has been developed and linked with the chosen simulation software environment in order to automate the entire numerical procedure for crack initiation and propagation, and COMSOL Multiphysics® has been used only to perform automatic remeshing for each new crack configuration, and to solve the microscopic boundary value problems for the given crack geometry; a nonlinear solution strategy has been adopted to deal with contact, based on the damped Newton method [205].

In this chapter, a single crack is supposed to originate along a predefined path, i.e. along the fiber/matrix interface; on the other hand, crack propagation occurs along a path which is not known a priori. Thus, two different *ad hoc* algorithms for determining the effective response of a composite during crack initiation and propagation, regarded as separated steps, are presented.

Based on the coupled criterion discussed in Section 3.2.1, the crack initiation algorithm for homogenization purposes, sketched in Fig. 3.8, is

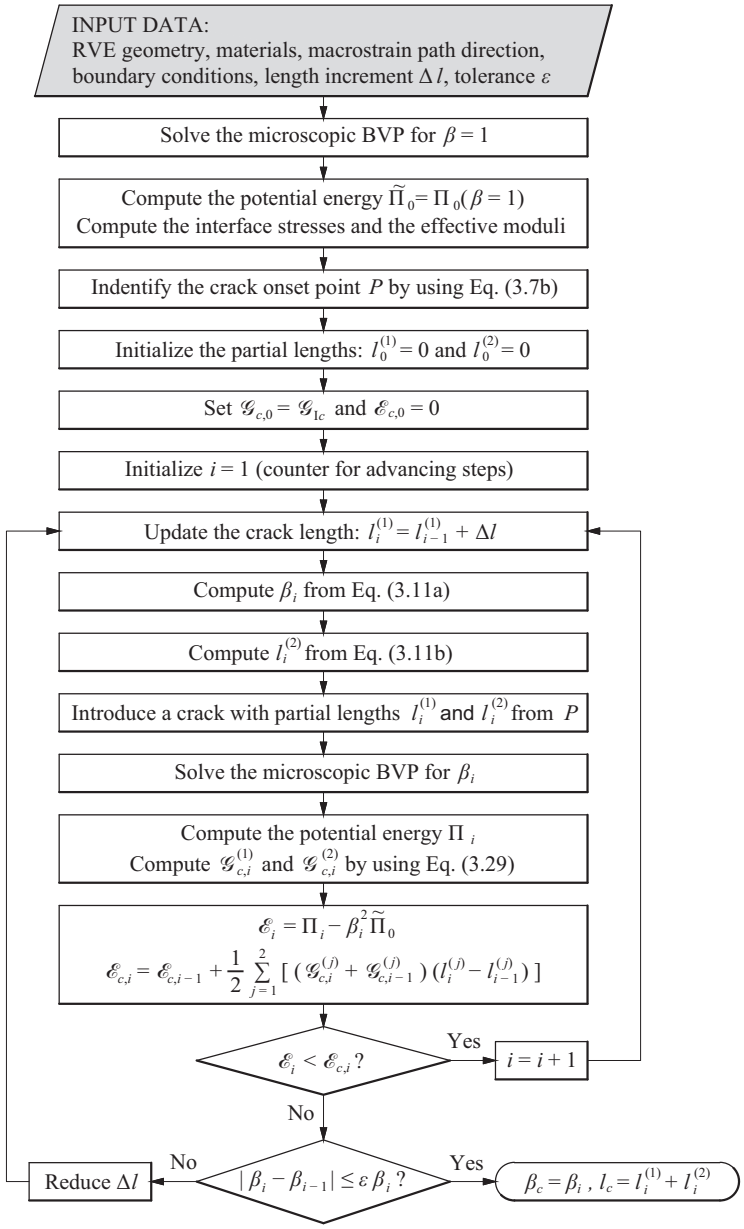

Fig. 3.8 Schematic representation of the crack initiation algorithm.

described in the following. Once the crack onset point is detected at the fiber/matrix interface by a stress analysis, the system (3.11) of equations associated with the stress- and energy-based criteria is solved as follows: for each trial value of $l_c^{(1)}$, the corresponding value of β_c is explicitly computed from $(3.11)_1$, then the corresponding value of $l_c^{(2)}$ is obtained by substituting the computed value of β_c into Eq. $(3.11)_2$. Then the tentative triplet $\left(\beta_c, l_c^{(1)}, l_c^{(2)}\right)$ is substituted into Eq. $(3.11)_3$ and the loop is repeated until this equation is satisfied (within a given small tolerance).

The crack propagation algorithm for homogenization purposes is developed, including the kinking criterion and the crack path tracking strategy, presented in Sections 3.2.2.2 and 3.2.2.3, respectively. In the case of multiple crack tips, three nested loops are needed: the outer one iterates over all the propagation steps, the intermediate one iterates over the set of existing crack tips, and the inner one iterates over a finite set of trial advancing crack directions, as shown in Fig. 3.9. The actual crack direction, uniquely defined by the kinking angle θ_c, is computed according to a generalization of the maximum energy release rate criterion to heterogeneous media, incorporating the abovementioned kinking criterion. Since trial crack advances are associated with geometry updates, at each iteration (local or global) remeshing is required.

3.3.2 Computational details

In this section some computational details are given, in order to clarify how the proposed approach has been implemented in a standard finite element setting. The topics covered in this section are the explicit description of cracks, the trail crack propagation algorithm, the adopted interface model for taking into account the frictionless unilateral contact, the adopted *J*-integral formulation for computing the energy release rate in heterogeneous solids, the extraction of the stress intensity factors (SIFs) from the *J*-integral, the extrusion operator for imposing periodic BCs over the RVE, and the numerical evaluation of macroscopic (effective) moduli tensor.

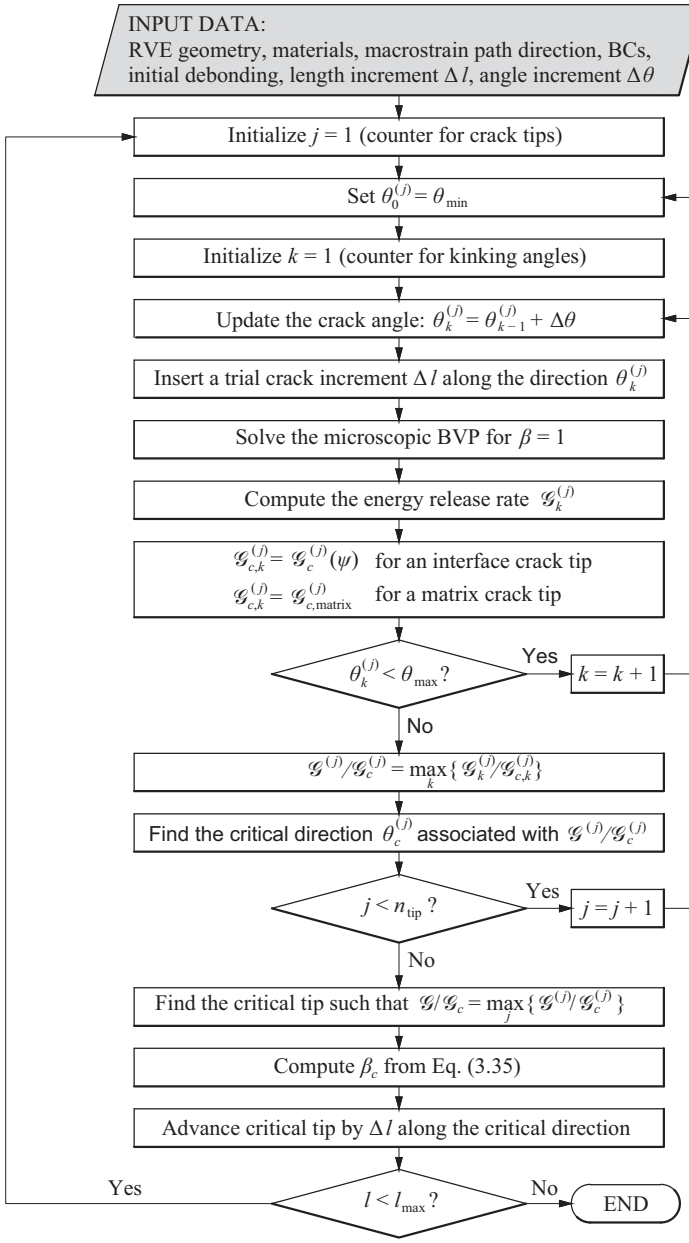

Fig. 3.9 Schematic representation of the crack propagation algorithm.

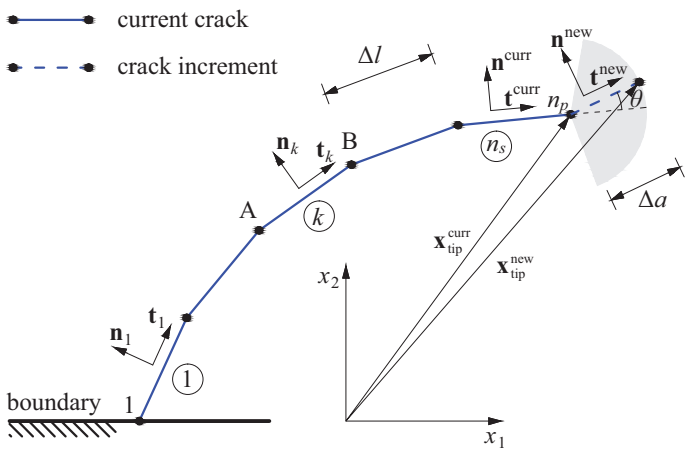

Fig. 3.10 Schematic representation of the explicit crack description.

3.3.2.1 Explicit description of cracks and trial crack propagation

In this section, the *explicit* description of cracks used in the present work will be described. A two-dimensional (discrete) crack is introduced by adding its boundaries in the geometric model; as the crack paths can be curvilinear, here each crack has been represented by a nonintersecting polygonal chain, whose straight line segments are of the same length Δl, chosen sufficiently small so that the crack path is accurate represented even in the presence of a finite number of kinks.

The polygonal chain describing the crack path for a given crack configuration is composed of n_s segments, as shown in Fig. 3.10, and thus defined by a set of points $P_i \in \mathbb{R}^2$, with $i \in \{1, \ldots, n_p\}$, related by a $n_s \times 2$ connectivity matrix $\mathbf{C}$. Each component C_{ij} of $\mathbf{C}$ refers to one of the points and hence, $1 \leq C_{ij} \leq n_p$.

In order to compute local quantities, such as the displacement jump between crack faces and the contact tractions, it is useful to define a local frame $(\mathbf{t}_k, \mathbf{n}_k)$ for each segment $k \in \{1, \ldots, n_s\}$ of the polygonal chain. Assuming that the segment k is between the points $A = \{x_1^A, x_2^A\}$ and $B = \{x_1^B, x_2^B\}$, the normal vector $\mathbf{n}_k$ can be expressed as:

$$\mathbf{n}_k = \begin{bmatrix} n_1^k \\ n_2^k \end{bmatrix} = \begin{bmatrix} -\left(x_2^B - x_2^A\right) \\ x_1^B - x_1^A \end{bmatrix} \Big/ \Delta l, \tag{3.39}$$

where Δl is the length of the segment. It is worth noting that the direction of the normal vector is implied by the order of the nodes in the connectivity matrix.

The end points of the polygonal chain describing the crack path are both crack tips in the case of an internal crack; on the contrary the crack tip can be either the first or the last point depending on the crack orientation. A local coordinate system $(\mathbf{t}^{\text{curr}}, \mathbf{n}^{\text{curr}}) \equiv (\mathbf{t}_k, \mathbf{n}_k)$ is introduced for the current tip (or tips), with k being the first and/or last segment of the polygonal chain.

During the advance of a crack (in both initiation and propagation processes), its geometry is updated, by adding a new segment starting from the current crack tip in a given direction $\mathbf{t}^{\text{new}}$; thus, the position of the new crack tip is expressed as follows

$$\mathbf{x}_{\text{tip}}^{\text{new}} = \mathbf{x}_{\text{tip}}^{\text{curr}} + \Delta a\, \mathbf{t}^{\text{new}}, \tag{3.40}$$

where Δa is the crack increment, chosen to be very small with respect to a characteristic size of the problem (e.g. the current crack length). It is usually assumed $\Delta a = \Delta l$; however, in the present work, Δa is set equal to $\Delta l / 10$, in order to reduce the computational cost of the initiation and propagation algorithms.

If the crack path is *known a priori*, $\mathbf{t}^{\text{new}}$ is fixed for each propagation step; conversely, the new crack direction can be expressed as a function of the kink angle θ, regarded as an unknown:

$$\mathbf{t}^{\text{new}} = \mathbf{R}(\theta)\, \mathbf{t}^{\text{curr}}, \tag{3.41}$$

where $\mathbf{R}(\theta)$ is a rotation matrix; thus, the application of the maximum energy release rate criterion leads to a one-dimensional optimization (minimization)

problem, where the optimization variable is the kink angle θ, and the objective function is the energy release rate (with the sign changed).

According to this method, several calculations are performed, by extending the given crack by a trial crack increment of fixed length Δa in different directions, and the energy release rate in computed for each trial crack. The crack direction is varied until a local maximum of the energy release rate has been found with sufficient precision; the optimum crack direction is then chosen for the next crack increment.

In order to find the optimum crack direction, a sequential line search method has been adopted[6]. In the numerical calculations, presented in Section 3.5, the increment $\Delta\theta$ of the kinking angle, is assumed equal to 1.0°, whereas the crack length increment Δl is chosen equal to $1 \times 10^{-2} h$ (with h the RVE size) in both the crack initiation and propagation processes.

It is worth noting that, since the direction of the trial cracks is arbitrary, a remeshing of the geometry is needed for each trial crack calculation to exactly enforce crack propagation on the nodes between finite elements.

3.3.2.2 Modeling of frictionless unilateral contact

In order to ensure uncoupling of the mesh nodes between the crack faces, an artificial geometric gap g is introduced into the numerical model, by using offset operations to the crack path described in Section 3.3.2.1. The parameter g has been chosen very small with respect to the crack increment Δl; here, g is set equal to $\Delta l / 100$. In this way, frictionless unilateral contact can be easily modeled as a set of multipoint constraints, numerically enforced by a penalty approach.

Unilateral contact without friction between crack faces has been incorporated into the numerical model by means of an interface model characterized

[6] More sophisticated minimization algorithms can be used, such as the *golden section method* or the *Brent's algorithm*; these algorithms start with a local minimum bracketed between two other values and refine the minimum position by decreasing the size of the bracketing interval.

by the following nonlinear constitutive law, written in the local frame $(\mathbf{t}_k, \mathbf{n}_k)$ for each crack segment:

$$\mathbf{t} = \mathbf{k}[\![\mathbf{u}]\!], \quad \mathbf{k} = \mathrm{diag}\{k_t, k_n\}, \tag{3.42}$$

where $t = \{t_t, t_n\}^{\mathrm{T}}$ is the traction vector, $[\![\mathbf{u}]\!] = \{[\![u_t]\!], [\![u_n]\!]\}^{\mathrm{T}}$ is the displacement jump between crack faces, k_t is always assumed to be zero, and k_n is

$$k_n = \frac{k}{2}(1 - \mathrm{sgn}[\![u_n]\!]), \tag{3.43}$$

where k is the so-called *penalty parameter*, which must be sufficiently large to ensure displacement continuity but not too high in order to overcome numerical ill conditioning of the global stiffness matrix; in the present numerical computations, it is assumed $kh = 1 \times 10^7 E_m$, where h is the RVE size and E_m denotes the Young's modulus of the matrix material.

It is worth noting that the gap parameter g is not directly involved in the interface model, unlike in more sophisticated contact search algorithms.

3.3.2.3 *J*-integral formulation

In the present work, the energy release rate $\mathcal{G}$ for a given damage configuration and a prescribed load factor β, is computed by means of the J-integral technique (see [84] for additional details). It has been rigorously proved that for a homogenous hyperelastic solid and a straight crack, $\mathcal{G}$ is equal to the value of the J-integral for any path enclosing the crack tip. On the contrary, for an inhomogeneous body and/or curved cracks, $\mathcal{G}$ is the limit value of the J-integral as the integration path approaches the crack tip (see [85]):

$$\mathcal{G}(\beta, l) = \lim_{\delta \to 0} \mathbf{e} \cdot \int_{\partial D_\delta} \left(W\mathbf{n} - \nabla \mathbf{u}^{\mathrm{T}} \boldsymbol{\sigma} \mathbf{n} \right) \mathrm{d}S, \tag{3.44}$$

where D_δ is a disc of radius δ centered at the crack tip, $\mathbf{n}$ is the outer unit normal vector to ∂D_δ, and $\mathbf{e}$ is the direction of crack propagation, as illustrated in Fig. 3.11.

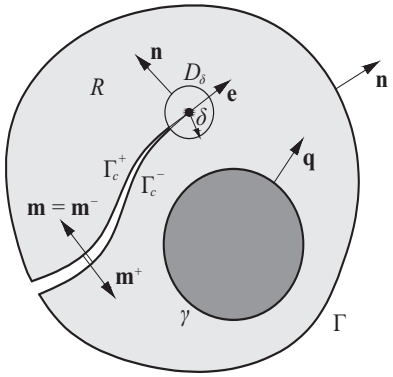

Fig. 3.11 Scheme of the *J*-integral path in its extended formulation.

Taking into account the material interfaces between the different microconstituents, and considering the tensor field $W\mathbf{I} - \nabla\mathbf{u}^{\mathrm{T}}\boldsymbol{\sigma}$ to be divergence-free, due to the absence of body forces, the application of the divergence theorem to a region R identified by an arbitrary path Γ surrounding the crack tip lead to a generalized formulation of the *J*-integral, introduced by Greco [54]; this formulation, which is valid for heterogeneous media composed of different homogeneous hyperelastic materials, and containing an arbitrarily shaped two-dimensional crack, can be written as follows (see Fig. 3.11):

$$\begin{aligned}\mathcal{G}(\beta, l) = \lim_{\delta\to 0} \mathbf{e} \cdot \Bigg[&\int_{\Gamma} \left(W\mathbf{n} - \nabla\mathbf{u}^{T}\boldsymbol{\sigma}\mathbf{n} \right) \mathrm{d}S \\ &+ \int_{\Gamma_c} \left[\!\left[W\mathbf{I} - \nabla\mathbf{u}^{\mathrm{T}}\boldsymbol{\sigma} \right]\!\right] \mathbf{m} \, \mathrm{d}S \\ &+ \int_{\gamma} \left[\!\left[W\mathbf{I} - \nabla\mathbf{u}^{\mathrm{T}}\boldsymbol{\sigma} \right]\!\right] \mathbf{q} \, \mathrm{d}S \Bigg],\end{aligned} \tag{3.45}$$

where Γ_c is the union of the two paths along the crack faces Γ_c^+ and Γ_c^-, γ is the union of the material interfaces, $\mathbf{n}$ is the outer unit normal to Γ, $\mathbf{m} = \mathbf{m}^-$ is the outer unit normal to the lower crack face, $\mathbf{q}$ is the outer unit normal to the material interfaces, and $[\![\cdot]\!]$ denotes the jump of the enclosed quantity evaluated as the difference between the values computed at the negative and positive sides of the crack or interface, e.g. $[\![\mathbf{u}]\!] = \mathbf{u}^- - \mathbf{u}^+$.

The path-independence of the *J*-integral is a very attractive property as far as finite element analyses are concerned, since the integration path can be chosen sufficiently away from the crack tip where the description of the stress and strain fields can be inaccurate owing to the high gradient of the near-tip singular elastic field; this property is preserved by this generalized formulation, but in a restricted sense, due to the presence of a limit operator in its definition.

If the material interfaces are aligned with **e** and the crack is straight, the last two terms in Eq. (3.45) vanish; in the general case, the second contribution to the second integral vanishes only when contact does not occur. Moreover, it is worth noting that in the neighborhood of the crack tip, the contribution coming from the second integral approaches zero since the normal to the crack face becomes perpendicular to the crack propagation direction. This avoids difficulties in the numerical evaluation of the jump quantities near the crack tip due to the stress singularities.

The numerical evaluation of the *J*-integral was implemented in the simulation environment by using *integration coupling variables* for postprocessing purposes. The integration coupling variable is defined as the integral expressed in Eq. (3.45) over the closed path Γ with a global destination (see [205] for additional details about integration coupling).

3.3.2.4 Extraction of SIFs from the *J*-integral for interface cracks

Crack propagation along the fiber/matrix interfaces is driven by the phenomenological criterion (3.29), which requires the accurate evaluation of the mode mixity, directly related to the ratio between stress intensity factors K_{I} and K_{II} by Eq. (3.25). Nishioka et al. [55] developed a *component separation method* of the *J*-integral for extracting the mixed-mode stress intensity factors of an interfacial tip; by using the ratio of the stress intensity factors ($\rho = K_{\mathrm{II}} / K_{\mathrm{I}}$), the *J*-integral can be expressed as

$$\mathscr{G} = \frac{1}{E^* \cosh^2(\pi\varepsilon)} K_{\mathrm{I}}^2 \left(1 + \rho^2\right). \tag{3.46}$$

Then, from Eq. (3.26), the ratio of the stress intensity factors can be related to the ratio of the relative displacements as follows:

$$\rho = \frac{K_{\mathrm{II}}}{K_{\mathrm{I}}} = \lim_{r \to 0} \left(\frac{1 - S\delta_y/\delta_x}{\delta_y/\delta_x + S} \right) \quad \text{with } S = \frac{\tan Q - 2\varepsilon}{1 + 2\varepsilon \tan Q}, \tag{3.47}$$

where $Q = \varepsilon \ln(r/l_{\mathrm{ref}})$. The ratio ρ can be only determined in the limit as r approaches zero, thus involving numerical complications associated with the oscillatory singularity. To this end, the following *special reference length* can be defined, by taking $\tan Q = 2\varepsilon$ in Eq. (3.47):

$$\bar{l}_{\mathrm{ref}} = r / e^{\varepsilon^{-1} \tan^{-1}(2\varepsilon)}, \tag{3.48}$$

which allows the ratio between the stress intensity factors to be accurately computed as:

$$\rho = \frac{\delta_x}{\delta_y}. \tag{3.49}$$

Using Eq. (3.49) in (3.46), the explicit formulas for the component separation method can be derived as:

$$\overline{K}_{\mathrm{I}} = \delta_y \sqrt{\frac{J E^* \cosh^2(\pi\varepsilon)}{\delta_y^2 + \delta_x^2}}, \quad \overline{K}_{\mathrm{II}} = \delta_x \sqrt{\frac{J E^* \cosh^2(\pi\varepsilon)}{\delta_y^2 + \delta_x^2}}. \tag{3.50}$$

Finally, the following transformation can be applied, in order to compute the stress intensity factors associated with the desired reference length l_{ref}:

$$\begin{Bmatrix} K_{\mathrm{I}}(l_{\mathrm{ref}}) \\ K_{\mathrm{I}}(l_{\mathrm{ref}}) \end{Bmatrix} = \begin{bmatrix} \cos\omega & -\sin\omega \\ \sin\omega & \cos\omega \end{bmatrix} \begin{Bmatrix} \overline{K}_{\mathrm{I}} \\ \overline{K}_{\mathrm{II}} \end{Bmatrix}, \quad \omega = \varepsilon \ln\left(l_{\mathrm{ref}} / \bar{l}_{\mathrm{ref}} \right). \tag{3.51}$$

The stress intensity factors computed through this technique are scarcely influenced by the choice of r, provided that the pair of considered nodes are located in the neighborhood of the propagating crack tip.

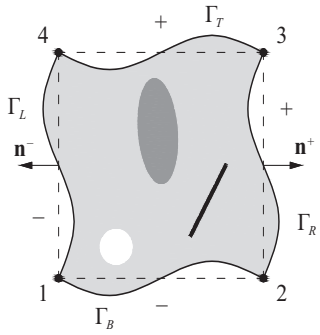

Fig. 3.12 RVE subjected to periodic boundary conditions.

3.3.2.5 Extrusion operator for periodic BCs over the RVE

As stated in Section 3.1, the typical periodic boundary conditions are usually expressed be the following relation:

$$\mathbf{u}(\mathbf{x}) = \overline{\boldsymbol{\varepsilon}} \cdot \mathbf{x} + \mathbf{w}(\mathbf{x}), \tag{3.52}$$

which cannot be directly applied in a finite element setting, since the microscopic fluctuation $\mathbf{w}(\mathbf{x})$ is generally unknown and dependent upon the applied loads. In practice, Eq. (3.52) is usually transformed into a certain number of explicit constraints between the corresponding finite element nodes on the opposite surfaces of the RVE; in the present work, an explicit form of periodic BCs in a 2D setting is used.

Consider an RVE as shown in Fig. 3.12 with four vertices numbered from 1 to 4. The displacements on a pair of opposite boundaries are

$$\begin{cases} \mathbf{u}_{14} = \overline{\boldsymbol{\varepsilon}} \cdot \mathbf{x}_{14} + \mathbf{w} \\ \mathbf{u}_{23} = \overline{\boldsymbol{\varepsilon}} \cdot \mathbf{x}_{23} + \mathbf{w} \end{cases} \quad \begin{cases} \mathbf{u}_{12} = \overline{\boldsymbol{\varepsilon}} \cdot \mathbf{x}_{12} + \mathbf{w} \\ \mathbf{u}_{43} = \overline{\boldsymbol{\varepsilon}} \cdot \mathbf{x}_{43} + \mathbf{w} \end{cases} \tag{3.53}$$

where $\mathbf{x}_{14}$, $\mathbf{x}_{23}$, $\mathbf{x}_{12}$, and $\mathbf{x}_{43}$ are the corresponding positions. In order to eliminate the periodic part $\mathbf{w}$, the displacement of one boundary can be subtracted from that of its opposite one, leading to the following relations:

$$\begin{cases} \mathbf{u}_{23} - \mathbf{u}_{14} = \overline{\boldsymbol{\varepsilon}} \cdot (\mathbf{x}_{23} - \mathbf{x}_{14}) \\ \mathbf{u}_{43} - \mathbf{u}_{12} = \overline{\boldsymbol{\varepsilon}} \cdot (\mathbf{x}_{43} - \mathbf{x}_{12}) \end{cases} \tag{3.54}$$

where the differences $(\mathbf{x}_{23} - \mathbf{x}_{14})$ and $(\mathbf{x}_{43} - \mathbf{x}_{12})$ are constants and equal to the length of the RVE sides. Since in the finite element analysis, at least one node of the RVE mesh has to be fixed in order to avoid rigid body motions, the vertices are directly constrained as $\mathbf{u}_i = \overline{\boldsymbol{\varepsilon}} \cdot \mathbf{x}_i$ ($i = 1,2,4$). Eq. (3.54) represents a set of linear multipoint constraints, which are easy to be enforced in most commercial finite element codes.

In the present work, the periodic boundary conditions (3.54) have been implemented by means of a *linear extrusion* coupling operator, already defined within the simulation environment used to perform the numerical computations, which allows to make available the displacement field on the opposite boundary faces of the RVE. This operator maps an expression defined on a source to an expression that can be evaluated in the destination; this mapping from destination to source is performed in two steps: (i) first, the destination (in this case the positive sides of the RVE) is orthogonally projected onto the linear space spanned by the destination vertices; (ii) then the linear space is mapped linearly to the source (in this case the negative sides of the RVE), so that each destination vertex is mapped to the corresponding source vertex (see [205] for additional details).

3.3.2.6 Numerical evaluation of the effective moduli

In classical homogenization, the macroscopic stress associated with an RVE is obtained by using Eq. (2.20); thus the accurate evaluation of boundary tractions is needed. To this end, the three microscopic boundary conditions discussed in Section 3.1 are converted into *weak constraints* by using suitable *Lagrange multipliers*. The Lagrange multiplier field, representing the traction vector on the boundary of the RVE, is available for postprocessing and provides an accurate value of macrostresses when integrated along the boundary.

Then, the effective (homogenized) moduli can be computed from the homogenized stress tensor by means of a numerical derivative using the central difference formula:

$$\begin{aligned}\overline{C}_{ijhk}\left(\beta\hat{\overline{\boldsymbol{\varepsilon}}}, l\right) &= \frac{\partial\overline{\sigma}_{ij}}{\partial\overline{\varepsilon}_{hk}}\left(\beta\hat{\overline{\boldsymbol{\varepsilon}}}, l\right) \\ &\cong \frac{\overline{\sigma}_{ij}\left(\beta\hat{\overline{\boldsymbol{\varepsilon}}} + \mathbf{e}_h \otimes \mathbf{e}_k \Delta\overline{\varepsilon}_{hk}\right) - \overline{\sigma}_{ij}\left(\beta\hat{\overline{\boldsymbol{\varepsilon}}} - \mathbf{e}_h \otimes \mathbf{e}_k \Delta\overline{\varepsilon}_{hk}\right)}{2\Delta\overline{\varepsilon}_{hk}},\end{aligned} \tag{3.55}$$

where $\Delta\overline{\varepsilon}_{hk}$ is a small increment of the strain $\overline{\varepsilon}_{hk}$. However, in practice, the secant moduli $\overline{C}_{ijhk}\left(\hat{\overline{\boldsymbol{\varepsilon}}}, l\right)$ are computed with reference to the initial configuration; this is valid also in presence of contact, after imposing the constraint condition for the relative displacement in the normal direction to crack faces $[\![u_n]\!] = 0$ within the contact area associated with the given macrostrain. Indeed, the contact area can be obtained by solving the microscopic boundary value problem driven by the macrostrain direction $\hat{\overline{\boldsymbol{\varepsilon}}}$, since it does not depend on the load parameter. When contact is not activated, the macroscopic moduli are obtained as:

$$\overline{C}_{ijhk} = \frac{1}{|\Omega_{\mathrm{RVE}}|}\int_{\partial\Omega_{\mathrm{RVE}}} C_{ilmn}\varepsilon^{hk}_{mn} n_l x_j \,\mathrm{d}S, \tag{3.56}$$

where C_{ilmn} are the microscopic moduli, and ε^{hk}_{mn} denotes the microscopic strain tensor associated with a prescribed unit macrostrain $\overline{\boldsymbol{\varepsilon}}^{hk} = \mathbf{e}_h \otimes_s \mathbf{e}_k$, with $\mathbf{e}_i$ unit vectors parallel to the coordinate axes x_i; since $C_{ilmn}\varepsilon^{hk}_{mn} n_l$ represents the boundary traction $\mathbf{t}^{hk}$ for the prescribed macrostrain path, the macroscopic moduli tensor $\overline{\mathbb{C}}$ can be easily obtained by integrating the product $\mathbf{t}^{hk} \otimes \mathbf{x}$ over the RVE boundaries.

3.4 A two-scale failure analysis of composite materials: computational implementation

As widely stated in Chapter 2, semiconcurrent multiscale methods allow to obtain an accurate description of the failure variables at different scales and to properly simulate microscopic nonlinear phenomena, taking advantage of a two-way coupling between the macroscopic problem and the microscopic problem defined over a representative volume element (RVE); this coupling derives from the step-by-step application of the micro-to-macro transition (homogenization step) and the macro-to-micro transition (localization step).

In this section, a novel semiconcurrent approach is proposed, incorporating the *homogenization* (micro-to-macro transition) and *localization* (macro-to-micro transition) steps in a FE^2-like computational scheme in order to analysis microcrack initiation and propagation phenomena in fiber-reinforced composite materials.

Unlike classical FE^2 approaches, the proposed method is able to overcome the macroscopic mesh size sensitivity in multiscale analysis of softening materials in a straightforward manner, without any regularization technique. The main feature of this approach is a direct coupling of the macroelement and RVE sizes, as adopted in *coupled volume* [30] or *coarse-graining* [27] approaches; however, differently from these method, for which the mesh size is set equal to the RVE size (i.e. $l_{\text{mesh}} = l_{\text{RVE}}$), the proposed strategy considers a periodic arrangement of unit cells in the macroscopic model, for which each cell is discretized by using the same coarse mesh, i.e. $l_{\text{mesh}} < l_{\text{RVE}}$. In this setting, each RVE is not attached to an integration point (Gauss point) of the macroscopic model, but it is associated with a coarse-meshed subdomain (of the same size as the RVE), whose boundary displacements are used to compute the macrostrain which drives the microscopic boundary value problem for each RVE, through the use of Eq. (3.1).

By virtue of the enriched kinematics during the micro-to-macro transition, with respect to classical FE^2-like approaches, the proposed strategy allows to account for the influence of macroscopic boundary layer effects and

the interaction between the different RVEs. Moreover, this approach is susceptible to further improvements by using the so-called *extrusion technique*. According to this technique, the displacements computed in the homogenized analysis are applied on the unit cell external boundary, instead of driving the microstructure by means of the macrostrain computed by integrating these displacements over the unit cell external boundary. However the use of the extrusion technique, in which pointwise boundary conditions derived from the homogenized analysis are applied to the microscopic problem, does not lead to appreciable improvements in accuracy for the cells away from the boundaries, for which, however, the relative errors are smaller than those located at the boundaries, as shown in [206] and [54].

Obviously, when dealing with separated scales ($l_{\mathrm{RVE}} \ll l_{\mathrm{macro}}$), the proposed strategy requires a large computational effort, like the other semiconcurrent methods, essentially due to the large number of microscopic BVPs to be solved; however, since these problems are not coupled to each other, parallelization is generally easy to implement.

Numerical computations have been performed for both crack initiation and propagation, with reference to a periodic 2D microstructure composed of a regular arrangement of unit cells, where fibers are initially perfectly bonded to the matrix. The variational problem of homogenization has been discretized by means of a displacement-based finite element (FE) approximation implemented by using the commercial software COMSOL Multiphysics®.

The multiscale computational procedure has been carried out taking advantage of a MATLAB® script, developed and linked with the chosen simulation software environment in order to automate the entire numerical procedure; COMSOL Multiphysics® has been used only to perform automatic remeshing for each new crack configuration, and to solve the boundary value problems for the given couples (β_c, l_c) at both the microscopic and macroscopic scales.

The *ad hoc* algorithms used to simulate crack initiation and propagation phenomena within the proposed multiscale computational scheme are discussed in the following.

3.4.1 Multiscale crack initiation analysis

A computational technique is here presented to find the location of the onset point and to estimate the critical load factor and the interface crack length at onset for a composite microstructure, from the results of a macroscopic analysis, by using the coupled energy- and stress-based criterion proposed in [47] and extended to the case of an interface crack in [49]. The procedure is carried out by performing the steps summarized in the following paragraph.

Multiscale crack initiation algorithm

STEP 1. Evaluate the homogenized moduli by solving the local boundary value problem of a single undamaged unit cell subjected to uniaxial and shear macrostrain paths for periodic BCs (a fine mesh is used to model the microstructure of the unit cell).

STEP 2. Analyze the composite structure subjected to a reference load by adopting the homogenized moduli obtained in step 1 (the structure is discretized by using a coarse mesh).

STEP 3. FOR each region of the macroscopic structure corresponding to a unit cell **DO**:

> **3.1.** Compute the macrostrain by integrating displacements obtained in step 2 over its external boundaries, according to Eq. $(3.1)_2$.
>
> **3.2.** Solve the local boundary value problem of the undamaged unit cell linked to the corresponding region of the macroscopic structure, by imposing the macrostrain computed in step 3.1 and using periodic boundary conditions.
>
> **3.3.** Evaluate the interface normal and tangential stresses inside the considered unit cell.

STEP 4. Identify the unit cell undergoing crack initiation as the one related to the minimum critical load parameter:

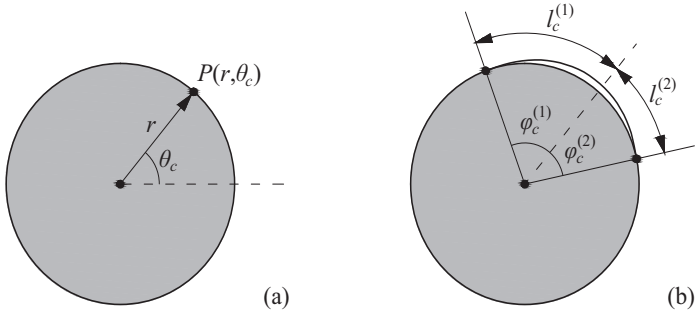

Fig. 3.13 Schematic representation of (a) onset point detection and (b) interface crack nucleation.

$$\beta_c = \sqrt{\sup_{i=1,\dots,n_{\mathrm{RVE}}} \left\{ \max_{\mathbf{x}\in\gamma_i} \left[\left(\frac{\langle \hat{\sigma}(\mathbf{x}) \rangle}{\sigma_c} \right)^2 + \left(\frac{\hat{\tau}(\mathbf{x})}{\tau_c} \right)^2 \right] \right\}}, \tag{3.57}$$

where γ_i denotes the fiber/matrix interface inside the ith unit cell, and n_{RVE} is the number of unit cells of the macroscopic model.

STEP 5. Given a polar coordinate system centered at the inclusion, find the onset point $P(r, \theta_c)$ inside the previously identified cell by using the stress-based criterion $(3.7)_2$ as follows (see Fig. 3.13a):

$$\theta_c = \arg\max_{\theta\in[0,2\pi]} \left\{ \left(\frac{\langle \hat{\sigma} \rangle}{\sigma_c} \right)^2 + \left(\frac{\hat{\tau}}{\tau_c} \right)^2 \right\}. \tag{3.58}$$

STEP 6. Estimate the critical load factor and the interface crack length at crack onset by employing the coupled failure criterion (3.11) within the considered unit cell linked to the relevant macroscopic region. Owing to the presence of two crack tips, this step requires the solution of a system of three nonlinear algebraic equations for the unknowns $\left(\beta_c, l_c^{(1)}, l_c^{(2)}\right)$, usually performed by iterations (see Fig. 3.13b); given a suitable initial value for the interface crack length l_c^{init} and a small enough increment Δl, set the current value l_c^{curr} of

the crack length at onset equal to l_c^{init} and **DO WHILE** the criterion (3.11) is not satisfied:

6.1. Compute the tentative values of $l_c^{(1)}$ and $l_c^{(2)}$ by imposing the same equivalent stress state for both the tips; the trial couple $\left(l_c^{(1)}, l_c^{(2)}\right)$ is then the solution of the system:

$$\begin{cases} \left(\dfrac{\langle\hat{\sigma}^{(1)}\rangle}{\sigma_c}\right)^2 + \left(\dfrac{\hat{\tau}^{(1)}}{\tau_c}\right)^2 = \left(\dfrac{\langle\hat{\sigma}^{(1)}\rangle}{\sigma_c}\right)^2 + \left(\dfrac{\hat{\tau}^{(1)}}{\tau_c}\right)^2 . \\ l_c^{\text{curr}} = l_c^{(1)} + l_c^{(2)} \end{cases} \tag{3.59}$$

6.2. Explicitly calculate the corresponding value of β_c from any equation (3.11), by virtue of the linear relation between β and the interfacial stresses.

6.3. Insert a crack of finite length l_c^{curr} and solve the local problem of the damaged unit cell linked to the corresponding macroscopic region, by imposing the macrostrain computed in step 3.1 and applying periodic boundary conditions.

6.4. Compute the trial incremental energy release and its critical value with reference to a virtual process, required for the application of the criterion $(3.11)_3$.

6.5. Increase the current value of the crack onset length by the increment Δl.

STEP 7. Compute the effective crack length l_c at onset as the current value which first satisfies the coupled criterion, i.e. $l_c = l_c^{\text{init}} + n_{\text{iter}}\Delta l$, where n_{iter} denotes the number of iterations made in step 6.

It is worth noting that in the presence of contact phenomena, the procedure would become more complex, since the dependence of the homogenized moduli tensor on the macrostrain direction should be taken into account (see [54] for additional details). Additional simplifications arise from considering

the entire crack initiation process driven by the undamaged moduli; this is allowed because results have shown that assuming the undamaged moduli for the entire crack initiation process leads to negligible discrepancies with respect to the case in which the changes in the macroscopic moduli due to crack initiation are taken into account.

The homogenization/localization steps performed within the proposed multiscale algorithm for crack initiation are shown in the flowchart of Fig. 3.14.

3.4.2 Multiscale crack propagation analysis

The computational technique proposed to calculate the energy release rate values at the crack tips inside the damaging unit cell for a composite microstructure, from the results of the macroscopic analysis, is here presented. The following steps must be performed.

Multiscale crack propagation algorithm

STEP 1. Evaluate the undamaged homogenized moduli by solving the local problem of a single unit cell subjected to uniaxial and shear macrostrain paths for periodic boundary conditions; these moduli are used to model the constitutive behavior of those macroscopic regions corresponding to undamaged unit cells.

STEP 2. Given the crack length l_c at onset, the crack length increment Δl and the number n_{step} of crack propagation steps, set the current value l of the crack length as l_c and **FOR** $i = 1, \ldots, n_{\text{step}}$ **DO**:

> **2.1.** Evaluate the damaged homogenized moduli by solving the local problem of a single unit cell subjected to uniaxial and shear macrostrain directions for periodic boundary conditions and for the current value l of the crack length.

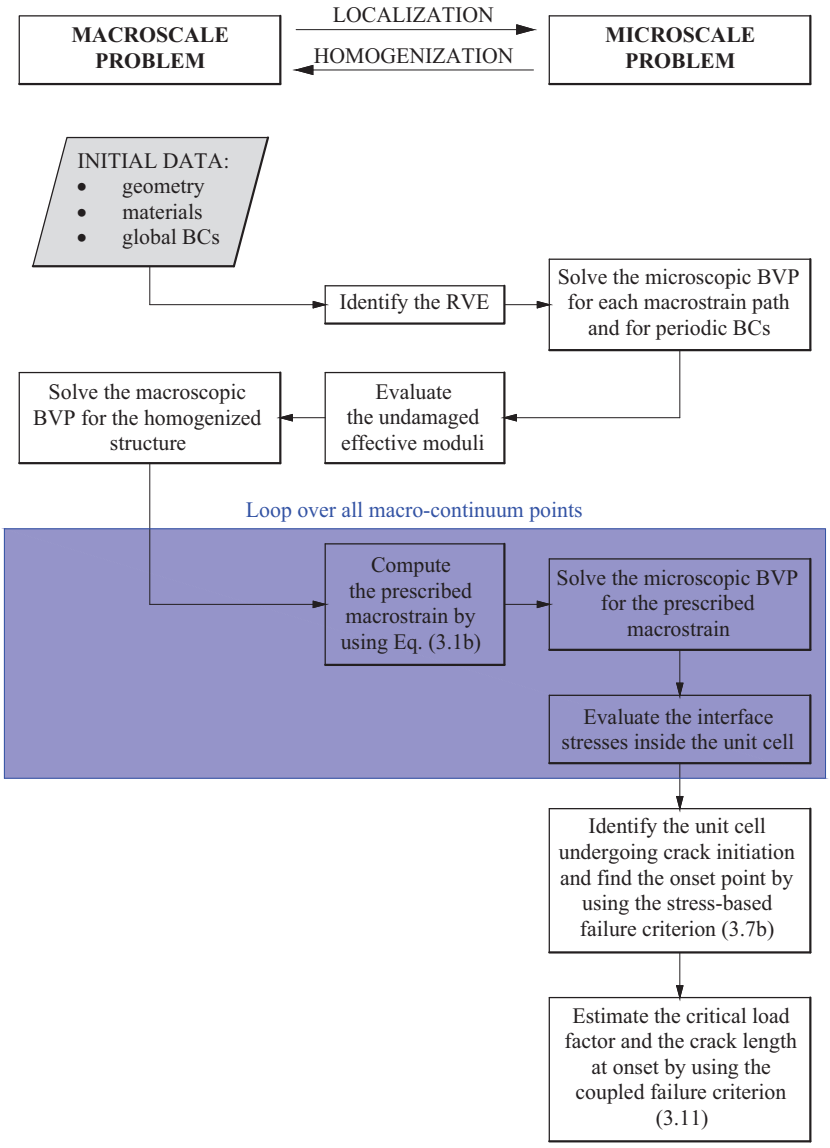

Fig. 3.14 Schematic representation of the two-scale coupling during crack initiation.

2.2. Analyze the composite structure subjected to a reference load by adopting the homogenized moduli obtained in steps 1 and 2.1 (the structure is discretized by using a coarse mesh).

2.3. Compute the macrostrain for the unit cell undergoing crack propagation by integrating displacements obtained in step 2.2 over its external boundaries, according to Eq. $(3.1)_2$.

2.4. Solve the local boundary value problem of the considered damaged unit cell, by imposing the macrostrain computed in step 2.3 and applying periodic boundary conditions.

2.5. Evaluate the local energy release rates $\mathcal{G}^{(1)}$ and $\mathcal{G}^{(2)}$ at both the crack tips of the damaged unit cell by means of the *J*-integral technique.

2.6. Set $\mathcal{G} = \sup\left\{\mathcal{G}^{(1)}, \mathcal{G}^{(2)}\right\}$ and estimate the critical load factor β_c by employing the Griffith's criterion within the considered unit cell.

2.7. IF $\left|\mathcal{G}^{(1)} - \mathcal{G}^{(2)}\right| / \mathcal{G} > \varepsilon_{\mathcal{G}}$

THEN:

The crack tip which corresponds to the higher energy release rate is advanced by the increment Δl.

ELSE:

Both the crack tips are advanced by the increment $\Delta l / 2$.

2.8. Increase the current value of the crack length by the increment Δl.

It is worth noting the importance of the step-by-step update of macroscopic moduli for the unit cell undergoing damage evolution during the homogenization procedure; as a matter of fact, results from calculations carried out by skipping this step showed an underestimation of the energy release rate for $\beta = 1$ and, consequently, an overestimation of the strength of the compo-

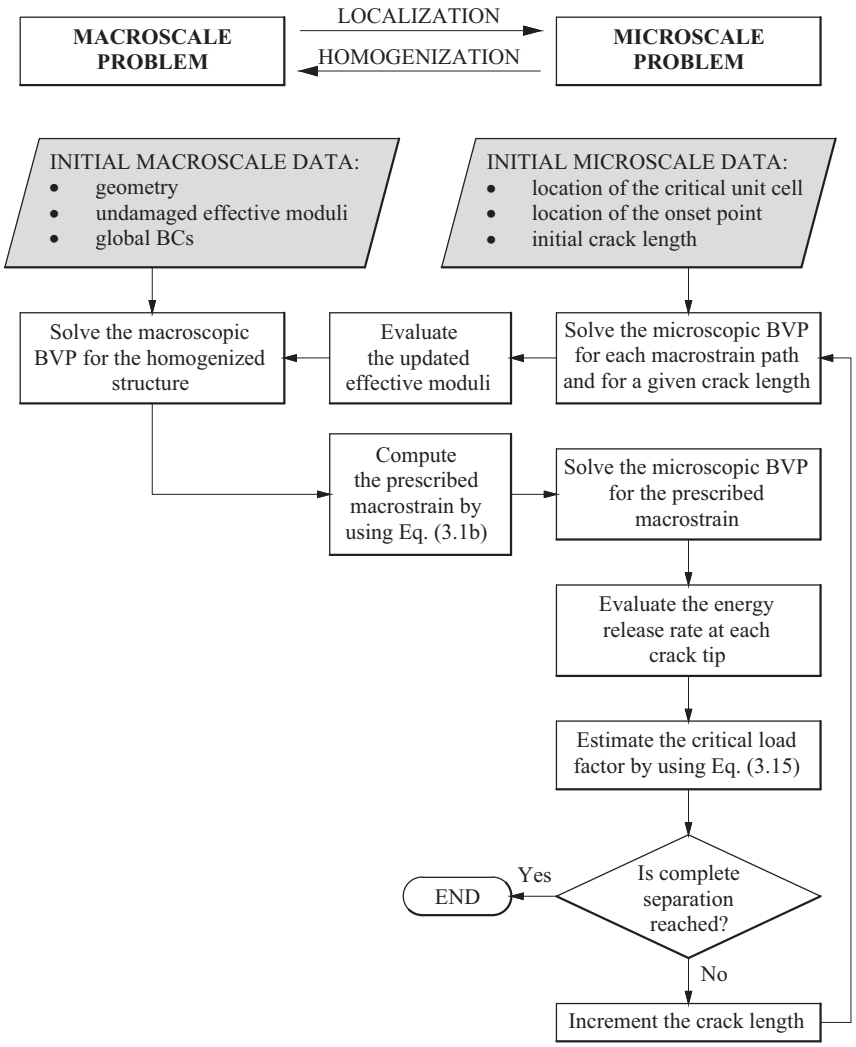

Fig. 3.15 Schematic representation of the two-scale coupling during crack propagation.

site. Thus, continuous homogenization/localization exchanges must be performed during the microstructural evolution, within the proposed multiscale algorithm, as highlighted in the flowchart shown in Fig. 3.15.

Finally, the computational details already given in Section 3.3.2 also refer to the present multiscale method.

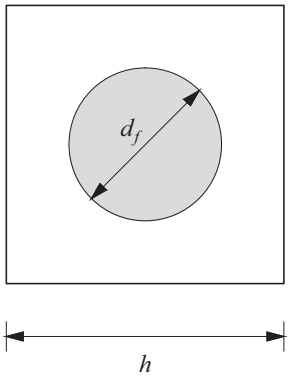

Fig. 3.16 2D unit cell model of a fiber-reinforced microstructure: stiff inclusion embedded in a soft matrix.

3.5 Macroscopic constitutive response of a fiber-reinforced composite: numerical experiments

This section is devoted to the numerical experiments carried out in order to assess the capability of the proposed homogenization scheme, described in Section 3.3, for estimating the macroscopic (effective) constitutive response of composite materials, with particular attention to transverse loading in unidirectional laminae.

Numerical experiments have been carried out with reference to a 2D periodic microstructure made of stiff cylindrical inclusions embedded in a soft matrix with initially undamaged fiber/matrix interfaces, regarded as a suitable model for a continuous fiber-reinforced composite material. A square unit repeating cell has been considered, consisting of a matrix including a rigid centered circular inclusion, as shown in Fig. 3.16. The side length of this unit cell is $h = 30$ μm, and the fiber diameter is $d_f = 0.5h$. Both matrix and inclusions are made of homogeneous isotropic linearly elastic materials, and they are bonded together along a perfect and brittle interface. The elastic constants are: $E_m = 2.79$ GPa and $\nu_m = 0.33$ for the matrix, $E_f = 70.8$ GPa and $\nu_f = 0.22$

for the fiber. The mode I fracture toughness for the matrix is assumed to be $\mathcal{G}_c = 100$ J/m^2, whereas the interface is characterized by four failure parameters: the tensile and shear strengths, equal to 90 and 120 MPa, respectively, the fracture mode I toughness $\mathcal{G}_c$, assuming the value of 2 J/m^2, unless otherwise indicated, and the fracture mode-sensitivity parameter λ which adjusts the influence of mode II contribution, here adopted equal to 0.3. The reference length l_{ref}, introduced to evaluate the mode mixity, is set as 1×10^{-2} μm, whereas the distance $\overline{r}$ from the crack tip, at which the displacement jump is evaluated, is assumed to be equal to 2×10^{-3} μm. The special reference length $\overline{l}_{\text{ref}}$, needed to avoid difficulties in obtaining accurate numerical results for the component separation method described in Section 3.3.2.4, is assumed equal to 2.746×10^{-4} μm. Plane strain conditions are always assumed in the finite element model.

Two different prescribed macrostrain path directions have been considered to obtain the macroscopic moduli: a uniaxial mode case $\hat{\overline{\boldsymbol{\varepsilon}}}_1^{\pm} = \pm(\mathbf{e}_1 \otimes \mathbf{e}_1)$ and a shear mode $\hat{\overline{\boldsymbol{\varepsilon}}}_s = 1/\sqrt{2}\,(\mathbf{e}_1 \otimes_s \mathbf{e}_2)$, where the superscript $\pm$ denotes the tensile or compressive macrostrain path direction. In order to analyze the influence of the interfacial toughness on the macroscopic structural response for the shear macrostrain path, both the case of a weak and strong fiber/matrix interface have been examined, by assuming the values 2 J/m^2 and 20 J/m^2 for $\mathcal{G}_{\text{Ic}}$, respectively. Moreover, the influence of inclusion size and of fiber volume fraction on the macroscopic constitutive response has been analyzed by considering increasing values for d_f with $d_f / h = 0.5$ and increasing values for h at fixed d_f, respectively. Finally, the effects of loading along the fiber direction on the macroscopic properties of the composite have been investigated in the context of generalized plane strain conditions.

3.5.1 Uniaxial macrostrain path

For the uniaxial tensile macrostrain path direction, contact does not occur and crack faces do not overlap. As already stated in Section 3.2.1, the onset point is assumed to be located along the fiber/matrix interface, which plays the role of a stress concentrator. The application of the coupled stress- and energy-

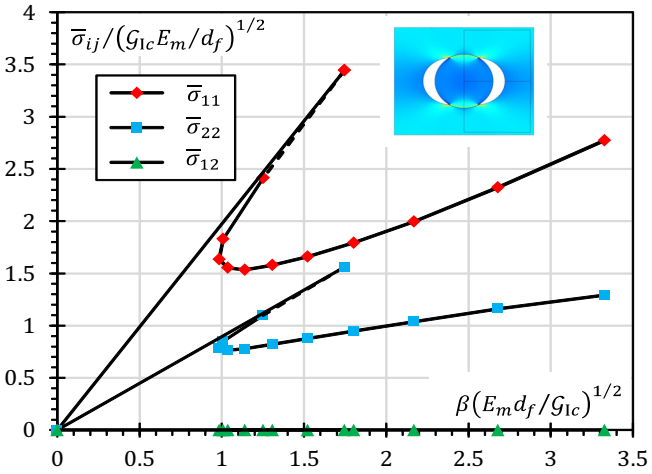

Fig. 3.17 Uniaxial tensile macrostrain path direction: dimensionless macroscopic stresses versus macroscopic strain parameter.

based criterion leads to predict the initiation of debonding with two interface cracks symmetrically located with respect to the vertical axis of symmetry of the unit cell.

As shown in Fig. 3.17, the macroscopic response is characterized by an initially unstable behavior followed by a stable one, with the consequent possibility of crack arrest for a prescribed macrostrain; a snap-through event is predicted, associated with the transition from an unstable to a stable crack propagation. Moreover, the macroscopic constitutive law exhibits an orthotropic symmetry; indeed the macroscopic shear stresses are practically zero within errors related to the numerical FE discretization. The first point shown in the macrostress curves refers to the crack onset load level and is assumed to be located along the initial loading curve associated with the undamaged microstructure.

This change in the stability behavior can be justified on the basis of the plot of total energy release rate to interface toughness curve ratio versus crack length, which is characterized by an initial increasing behavior followed by a decreasing one (see Fig. 3.18), related to increasing values of the mode mixity

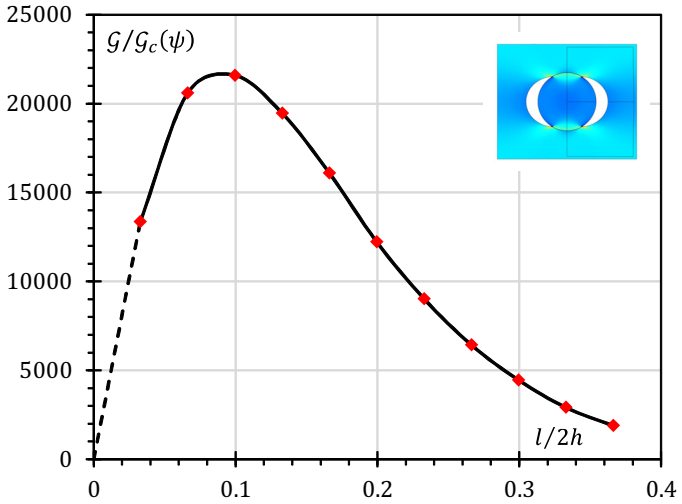

Fig. 3.18 Uniaxial tensile macrostrain path direction: behavior of the total energy release rate to interface toughness function ratio for a prescribed unit macrostrain as the crack semi-length increases.

for increasing debonding lengths. It is worth noting that the energy release rate assumes identical values at the four crack tips, due to the double symmetry; moreover the crack length here adopted refers to the debonding semi-length of one of the two symmetric interface cracks.

Fig. 3.19 shows how the macroscopic moduli are strongly dependent on the crack length, with the maximum loss of stiffness exhibited by $\overline{C}_{1111}$.

The compressive negative macrostrain path direction leads to a more complex microstructure evolution. Crack onset points are located in the neighborhood of the intersections of the unit cell diagonals with the matrix/fiber interface. As a consequence, crack initiation occurs with the abrupt formation of four identical interface cracks characterized by two different lengths for each crack tip. The system of four initiated interface cracks is characterized by a double symmetry about the vertical and horizontal central axes of the unit cell. With reference to the upper right interface crack, the upper crack tip is

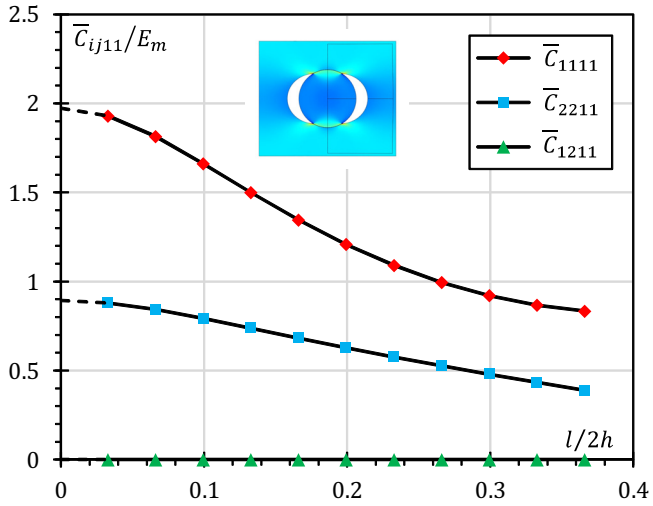

Fig. 3.19 Uniaxial tensile macrostrain path direction: effective moduli versus crack semi-length.

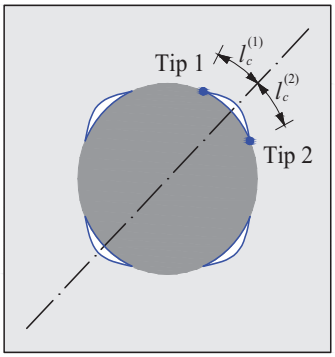

Fig. 3.20 Initiation of four identical interface cracks characterized by two different lengths for each crack tip in the case of the uniaxial compressive macrostrain path direction.

associated to the length $l_c^{(1)}$, whereas the lower one to the length $l_c^{(2)}$ (see Fig. 3.20).

By applying proper symmetry conditions, the crack initiation problem can be solved by using Eq. (3.11), which accounts for the introduction of two crack

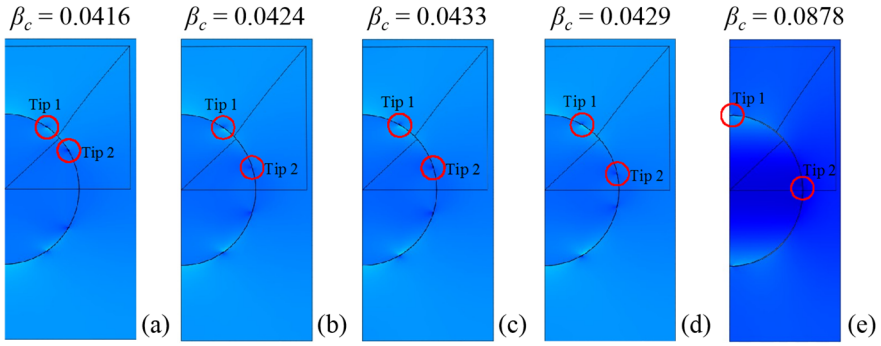

Fig. 3.21 Evolution of one half of the unit cell for the compressive uniaxial macrostrain path: the marked circles highlight the crack tip positions.

tips at the same time; this leads to a system of three nonlinear equations in as many unknowns, namely the two partial lengths l_1 and l_2, and the macrostrain load factor β; the first two equations derive from the interface stress failure criterion evaluated at the lengths l_1 and l_2, whereas the third one comes from the incremental energy criterion referred to the total length $l_1 + l_2$. Once nucleated, the crack propagates in such a way that the two tips advance alternately due to their mutual interaction, as depicted in Fig. 3.21.

After the crack onset, corresponding to a strong snap-back instability, the overall constitutive response of the composite exhibits a sharp snap-through, as shown in Fig. 3.22, where the propagation steps illustrated in are also indicated.

This behavior can be highlighted by considering the curve of the normalized energy release rates at the critical crack tip for increasing values of the total crack length and for a unit prescribed macrostrain; indeed, by plotting the maximum of the dimensionless energy release rates for the two crack tips as a function of $l_1 + l_2$, a stable crack propagation behavior can be observed, except for the initial step (see Fig. 3.23).

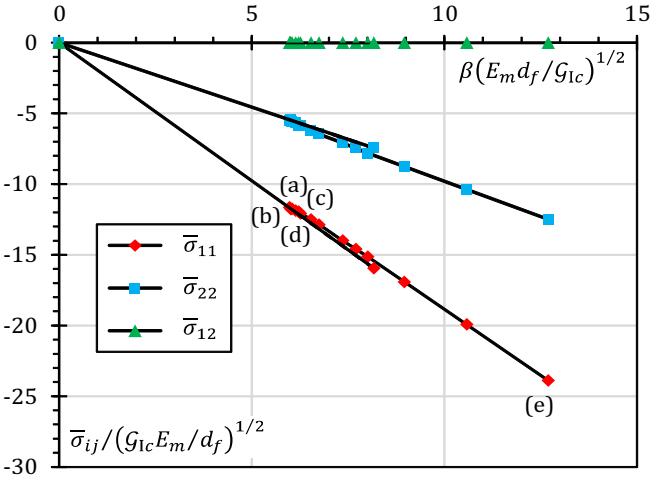

Fig. 3.22 Uniaxial compressive macrostrain path direction: dimensionless macroscopic stresses versus macroscopic strain parameter.

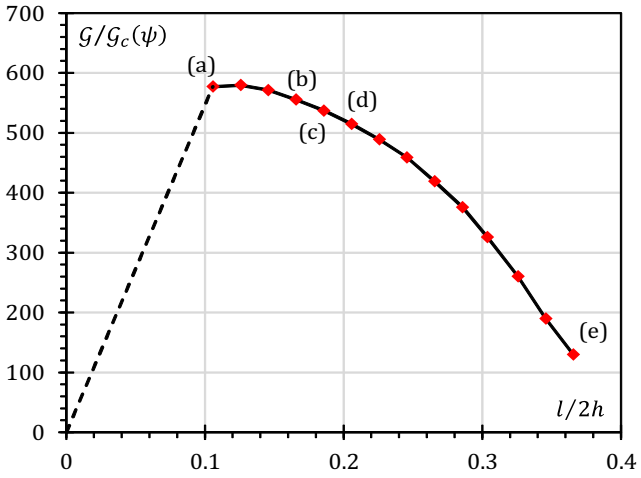

Fig. 3.23 Uniaxial compressive macrostrain path direction: behavior of the maximum energy release rate to interface toughness function ratio for a prescribed unit macrostrain as the dimensionless total crack length increases.

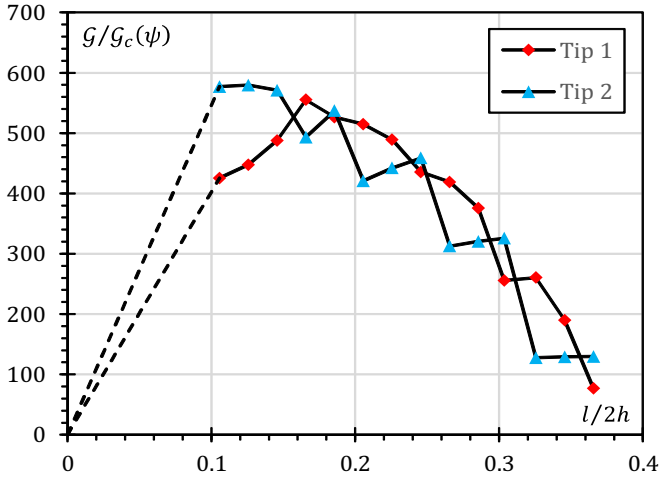

Fig. 3.24 Uniaxial compressive macrostrain path direction: energy release rate to interface toughness function ratio for a prescribed unit macrostrain as a function of the total crack length for both crack tips.

The alternating crack advance can be easily observed by considering the plot of the normalized energy release rates at the two crack tips for increasing values of the total crack length, shown in Fig. 3.24, exhibiting a jagged behavior corresponding to the change of the critical tip.

In Fig. 3.25, the behavior of the mixity angle for both crack tips as a function of the total crack length is presented; the numerical results show that ψ seems to be almost independent of the crack length; it is worth noting that the mode mixity for both tips are different in sign due to the different sliding between crack faces.

As expected, the macroscopic moduli are weakly dependent on the microcrack length, and the macroscopic behavior is characterized by an orthotropic symmetry (see Fig. 3.26).

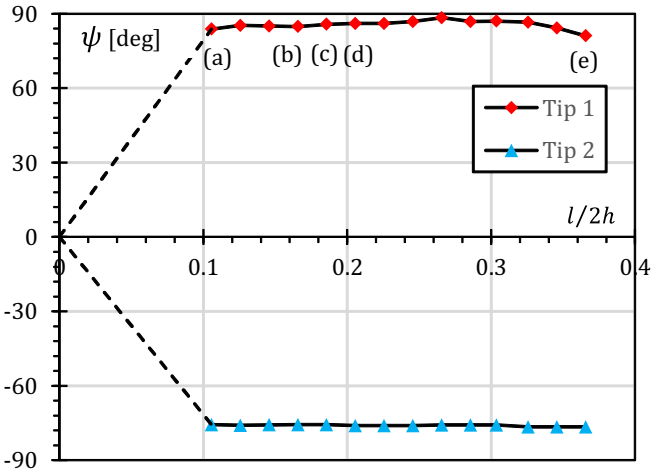

Fig. 3.25 Uniaxial compressive macrostrain path direction: mixity angle as a function of the total crack length for both crack tips.

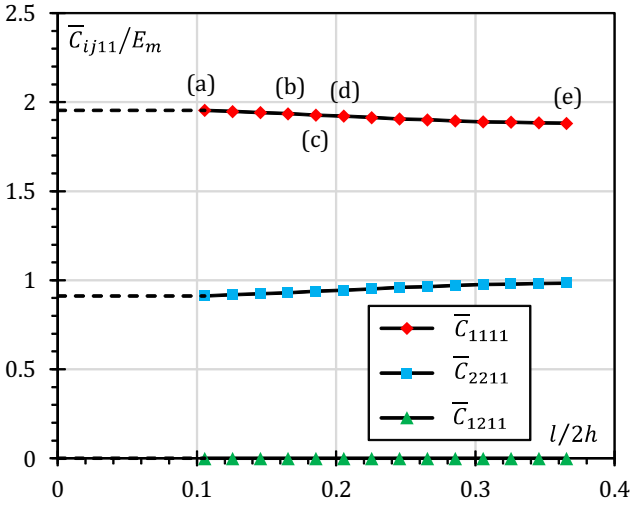

Fig. 3.26 Uniaxial compressive macrostrain path direction: macroscopic moduli versus crack length.

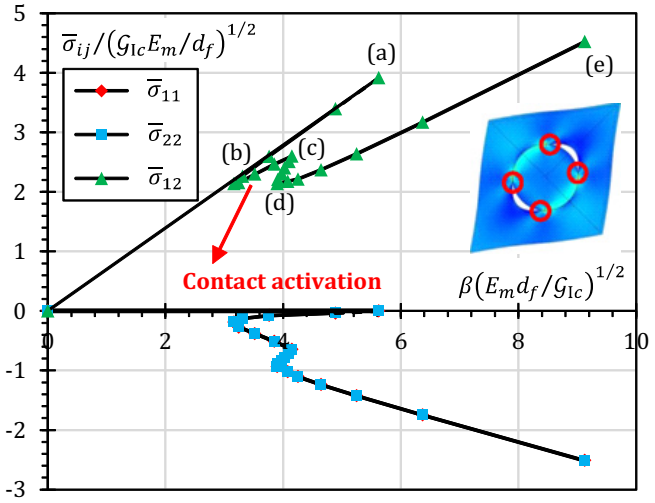

Fig. 3.27 Shear macrostrain path direction: macroscopic moduli versus crack length.

3.5.2 Shear macrostrain path

For the prescribed shear macrostrain path direction, the crack initiation occurs with two interface cracks symmetrically located along a diagonal of the unit cell. Because of the combined effect of contact activation and mixed-mode loading conditions for large debonding angles, the overall response shows a double snap-through behavior (Fig. 3.27) as confirmed by the two local maxima exhibited by the curve of the normalized energy release rate, shown in Fig. 3.28. At the beginning, a stabilizing effect is highlighted, essentially due to the combined action of both contact phenomena and relevant mode II contributions to the total ERR during the mixed-mode crack propagation. Then, the sign inversion of the mode mixity causes an initially unstable effect, followed by a recover in strength, due to the strong influence of contact. In this case, elastic moduli are strongly dependent on the interface crack length (Fig. 3.29), and do not show an orthotropic symmetry.

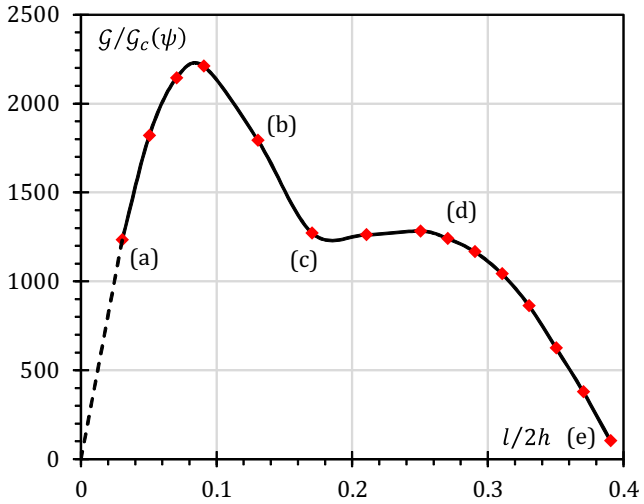

Fig. 3.28 Shear macrostrain path direction: total energy release rate to interface toughness function ratio for a prescribed unit macrostrain as the crack semi-length increases.

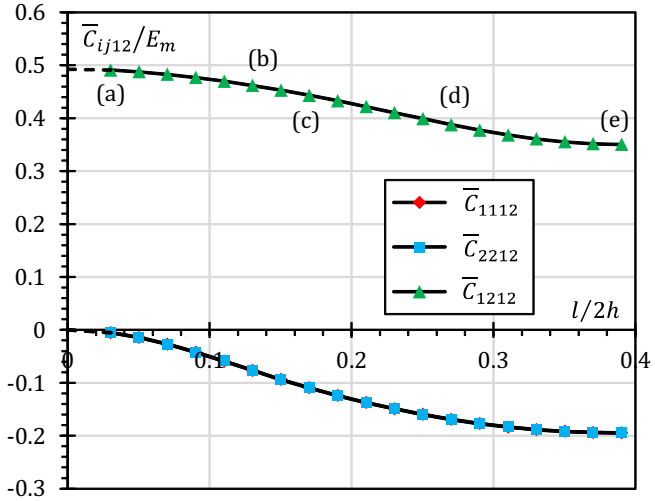

Fig. 3.29 Shear macrostrain path direction: macroscopic moduli versus crack length.

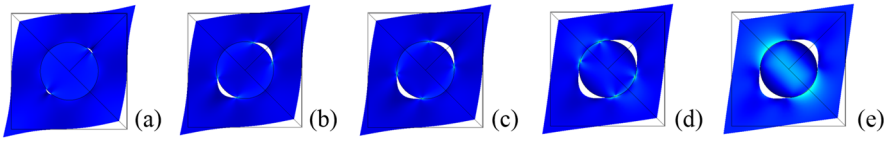

Fig. 3.30 Microstructural evolution in the case of weak fiber-matrix interface.

Fig. 3.30 shows the microstructure evolution by using the deformed configuration of the unit cell associated with five steps of crack propagation. The final stage of the macroscopic response is characterized by a deformed configuration where the fiber is completely debonded from the matrix and in contact along a large portion of its interface (see Fig. 3.30e).

In order to analyze the influence of the interfacial toughness on the macroscopic constitutive response, the case of a strong fiber/matrix interface is also investigated ($\mathcal{G}_{Ic} = 20$ J/m^2). An increase of the mode I interface toughness leads the existent crack to kink out of the interface toward the matrix for sufficiently large crack debonding lengths. Once kinked, the mechanical behavior is driven by the mode I toughness of the matrix. Kinking is favored over interface advancing, because the mode II propagation, which requires a higher energy level to be activated, prevails for sufficiently large debonding angles. Fig. 3.31 shows the dimensionless ERR behavior with reference to the actual propagation behavior (kinking) and for an imposed (*fictitious*) interface crack propagation (debonding). In the former case, the plotted quantity is the ratio between the ERR (for the interface crack) and the interface toughness curve, whereas in the latter, the ratio between the maximum ERR (with respect to the kinked crack angle) and the mode I fracture toughness of the matrix. It can be observed that kinking occurs at the beginning of the propagation process for $l/h = 0.1532$. By comparing Figs. 3.31 and 3.28, it can be noticed that the effect of increasing interface toughness is favorable, leading to higher strength values of the composite at crack onset. Even in this case, moduli are strongly dependent on the interface crack length (see Fig. 3.32). The macroscopic constitutive response is characterized by a small snap-through followed

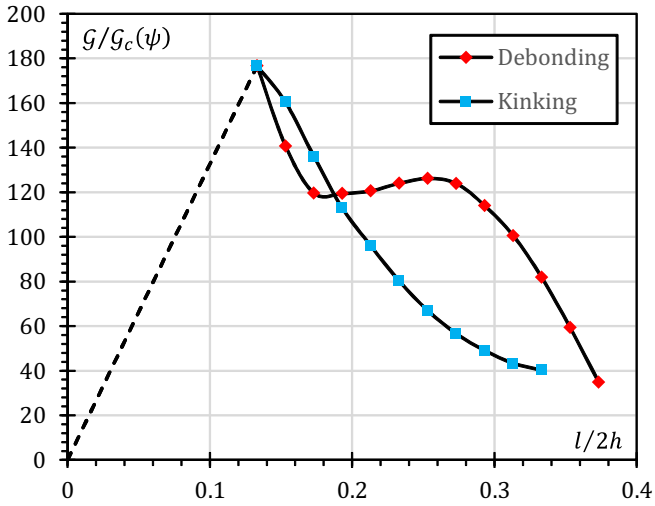

Fig. 3.31 Strong fiber/matrix interface for the shear macrostrain path direction: energy release rate for a prescribed unit macrostrain as the crack semi-length increases.

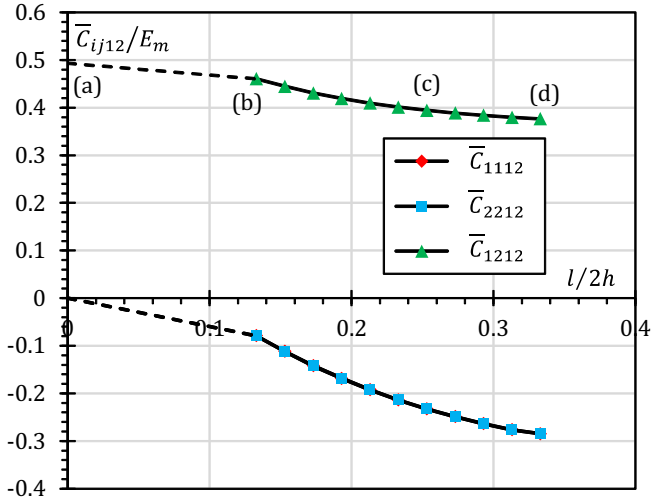

Fig. 3.32 Strong fiber/matrix interface for the shear macrostrain path direction: macroscopic moduli versus crack semi-length.

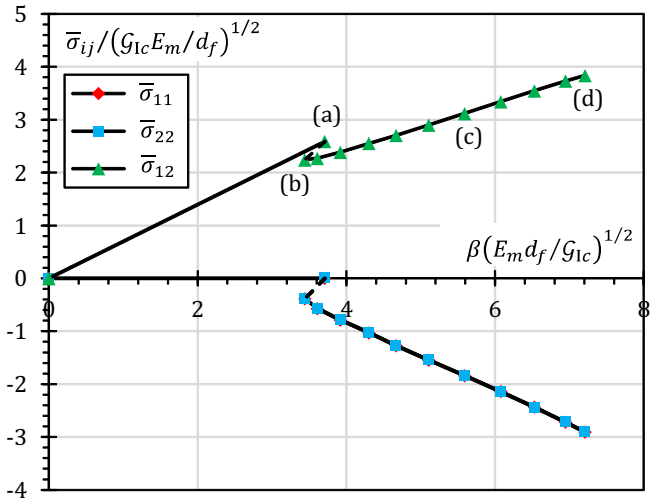

Fig. 3.33 Strong fiber/matrix interface for the shear macrostrain path direction: macroscopic stresses versus macroscopic strain parameter.

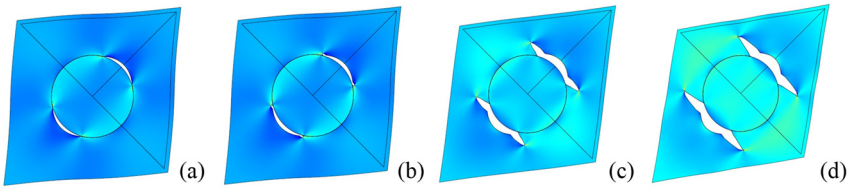

Fig. 3.34 Microstructural evolution in the case of strong fiber-matrix interface.

by a stable crack propagation, as shown in Fig. 3.33, and the macroscopic behavior does not show an orthotropic symmetry. Fig. 3.34 shows the microstructure evolution by means of the deformed configuration of the unit cell for increasing values of the load parameter.

3.5.3 Influence of inclusion size and of fiber volume fraction on the macroscopic constitutive laws

In order to investigate the ability of the proposed approach to predict size effects in the considered matrix/inclusion system, the influence of fiber size and

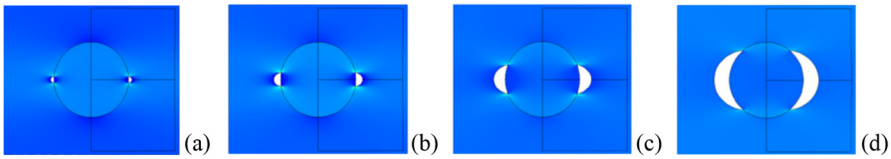

Fig. 3.35 Crack configuration at onset for different values of fiber diameter: (a) $d_f = 20$ μm, (b) $d_f = 10$ μm, (c) $d_f = 5$ μm, (d) $d_f = 2$ μm.

volume fraction on the macroscopic constitutive response is studied. Numerical experiments have been carried out, with reference to four different values of fiber diameter, namely $d_f = 20, 10, 5, 2$ μm (see Fig. 3.35).

In Figs. from 3.36 to 3.39 the macroscopic constitutive response for the analyzed fiber diameters is depicted, and the increasing behavior of the critical load factor at onset as the fiber diameter d_f decreases, is shown. Numerical results highlight an increasing behavior for the dimensionless crack semi-length $l/2h$ at onset as the fiber diameter decreases. Macroscopic constitutive laws are characterized by a transition from snap-through instability in the case of large fiber diameters to a stable mechanical response for smaller reinforcement sizes. In fact, whereas for large values of d_f (20, 10, 5 μm) the macroscopic constitutive response shows a snap-back (see Figs. from 3.36 to 3.38), for smaller values (2 μm) the snap-back does not occur and an increasing level of macrostrain is required for further interfacial crack propagation (see Fig. 3.39). Figs. from 3.40 to 3.43 show how the macroscopic moduli are strongly dependent on the interface crack length for all the considered fiber diameters.

The behavior of the dimensionless ERR for decreasing fiber diameters confirm the stabilizing size effect of the inclusion, as shown in Figs. from 3.44 to 3.47, which also highlight the decreasing behavior of the dimensionless ERR peak as the fiber diameter decreases, in accordance with the increasing load level required for interface crack propagation.

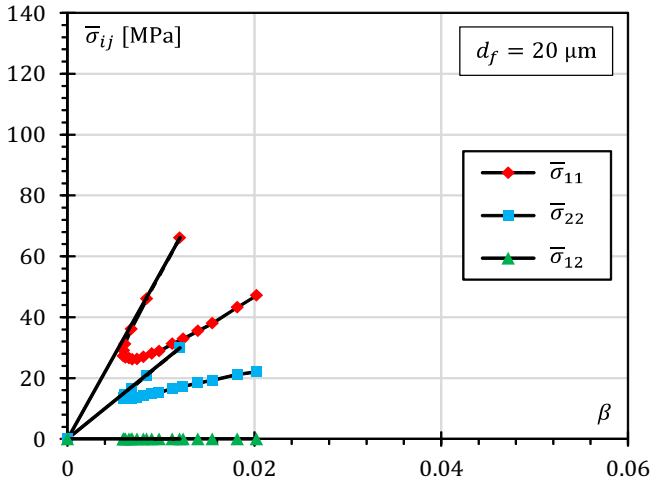

Fig. 3.36 Influence of the inclusion size on the macroscopic constitutive laws: $d_f = 20$ µm.

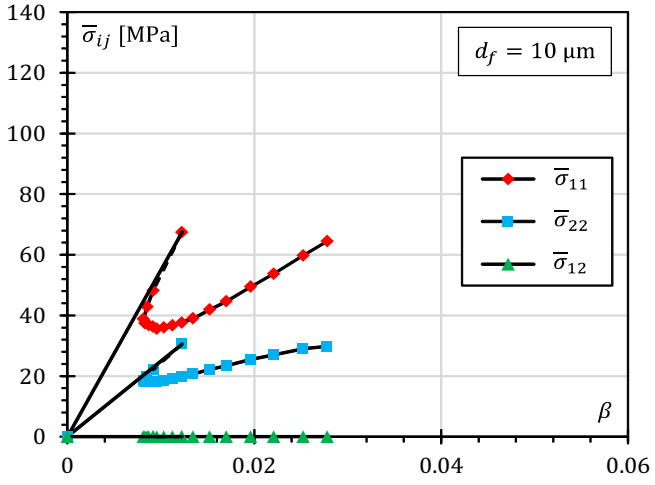

Fig. 3.37 Influence of the inclusion size on the macroscopic constitutive laws: $d_f = 10$ µm.

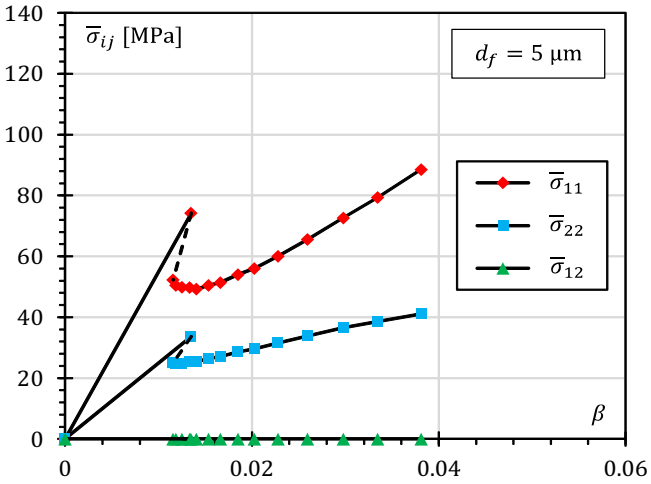

Fig. 3.38 Influence of the inclusion size on the macroscopic constitutive laws: $d_f = 5$ µm.

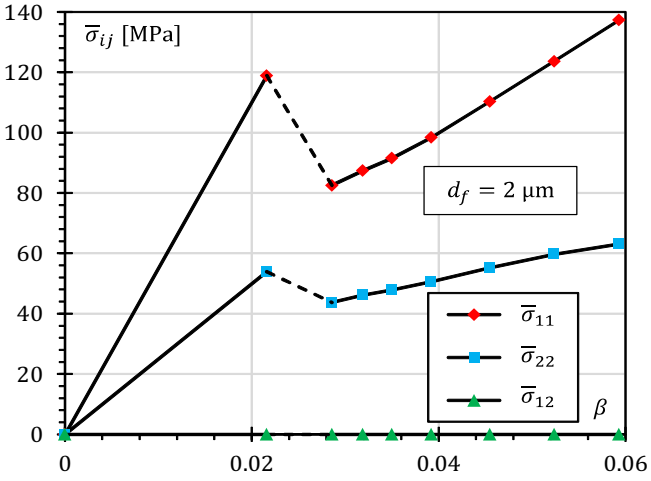

Fig. 3.39 Influence of the inclusion size on the macroscopic constitutive laws: $d_f = 2$ µm.

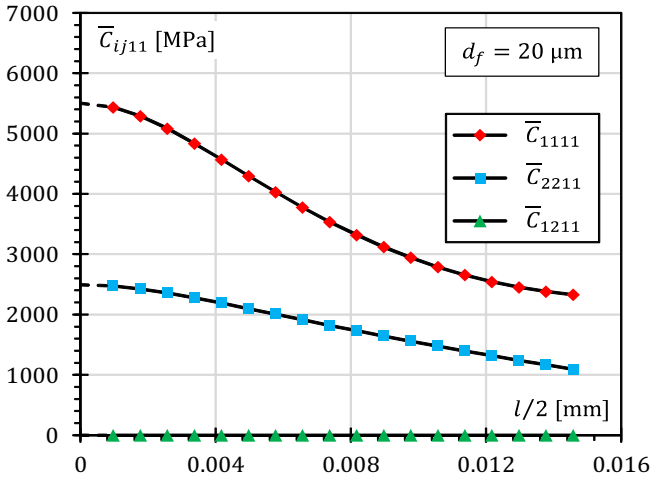

Fig. 3.40 Influence of the inclusion size on the macroscopic moduli: $d_f = 20$ μm.

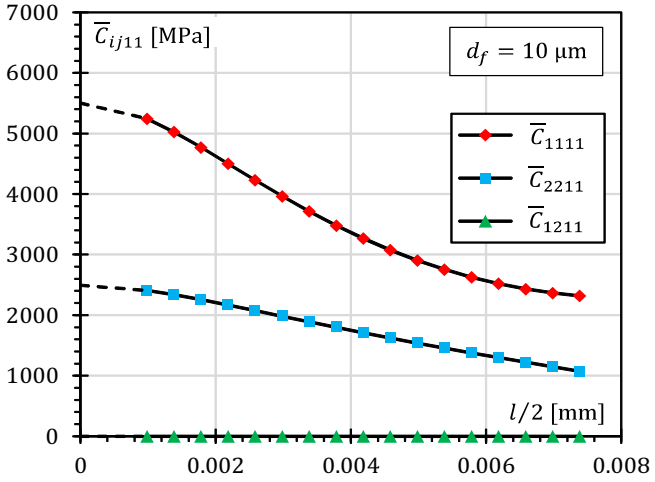

Fig. 3.41 Influence of the inclusion size on the macroscopic moduli: $d_f = 10$ μm.

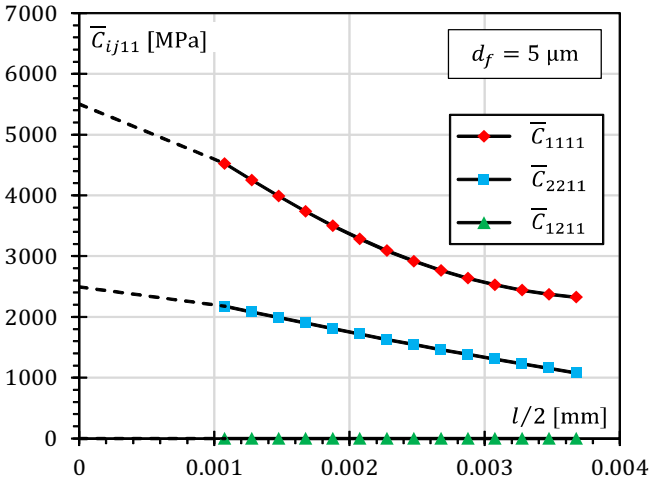

Fig. 3.42 Influence of the inclusion size on the macroscopic moduli: $d_f = 5$ μm .

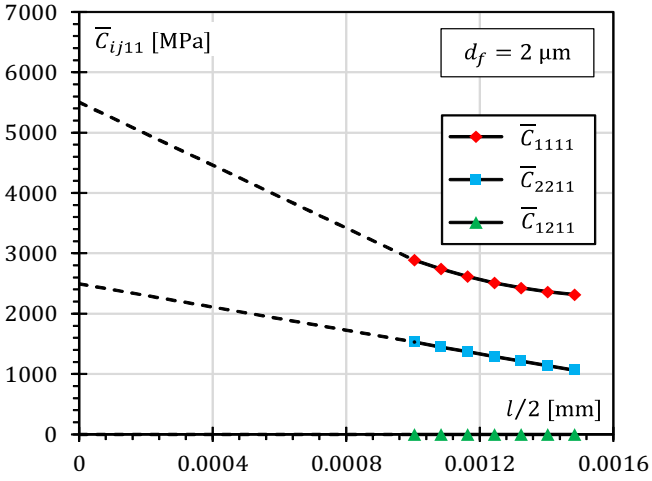

Fig. 3.43 Influence of the inclusion size on the macroscopic moduli: $d_f = 2$ μm .

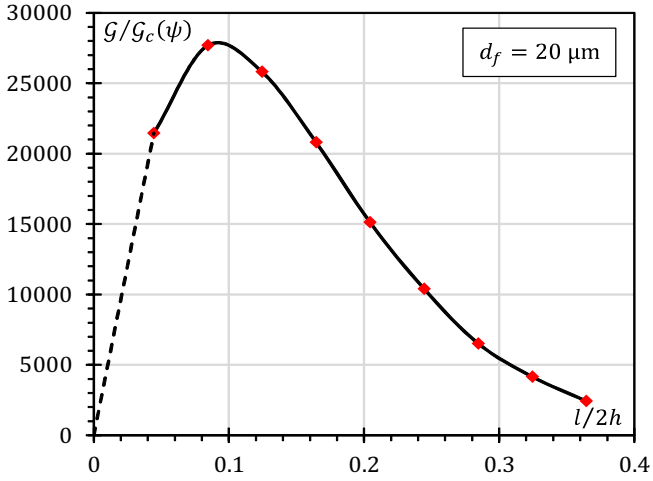

Fig. 3.44 Influence of the inclusion size on the energy release rate: $d_f = 20$ μm.

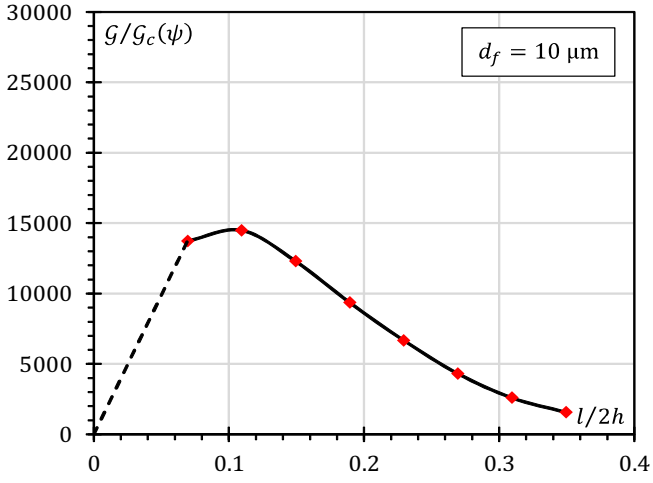

Fig. 3.45 Influence of the inclusion size on the energy release rate: $d_f = 10$ μm.

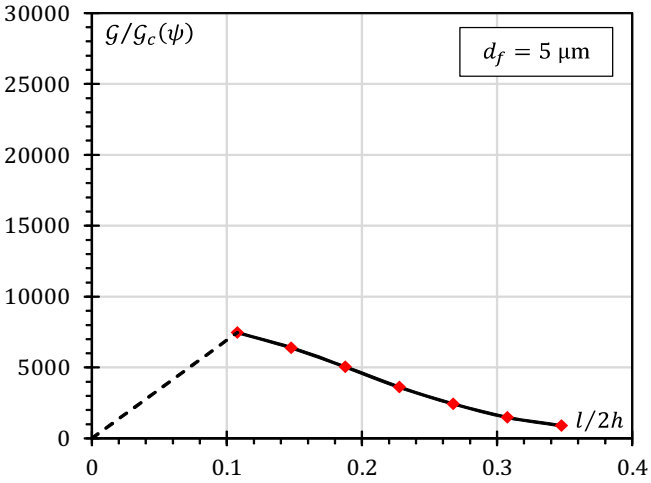

Fig. 3.46 Influence of the inclusion size on the energy release rate: $d_f = 5$ μm.

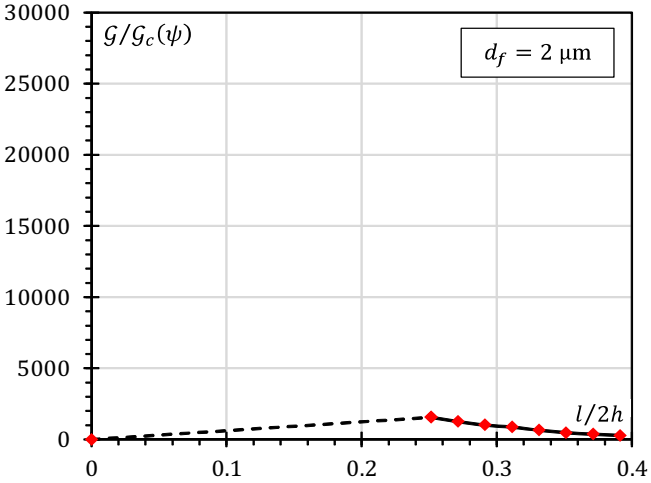

Fig. 3.47 Influence of the inclusion size on the energy release rate: $d_f = 2$ μm.

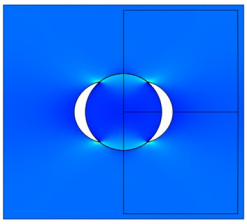
(a)

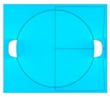
(b)

Fig. 3.48 Influence of the fiber volume fraction on the macroscopic properties: (a) $f_v = 10\%$, and (b) $f_v = 60\%$.

The effect of fiber volume fraction f_v on the macroscopic response is analyzed, by considering the six different values, i.e. 10, 20, 30, 40, 50, 60 μm (see Fig. 3.48). The fiber volume ratio has been changed by considering increasing values for h at fixed $d_f = 15$ μm. A sensitivity analysis with respect to fiber volume fraction has been performed, and results show that the crack semi-length at onset increases for increasing values of f_v; moreover for decreasing values of the fiber volume fraction, it asymptotically tends to a finite value (see Fig. 3.49).

Moreover Fig. 3.50 shows the macroscopic constitutive response for all the analyzed fiber volume fractions. A transition can be observed, from an unstable crack propagation behavior in the case of small fiber volume fraction to a stable one for larger fiber volume fractions ($f_v > 40\%$). Indeed, as the fiber volume fraction increases, an increasing level of macrostrain is required for the interface crack propagation. Fig. 3.50 also shows a moderate increasing behavior of the critical load factor at onset as the fiber volume fraction decreases.

3.5.4 Influence of loading along the fiber direction

In the present work the attention is focused on transverse cracking, which is one of the most common damage modes when the external loads are applied perpendicularly to fibers; thus, plane strain state is considered to be a proper approximation for failure analysis of composite materials. According to this

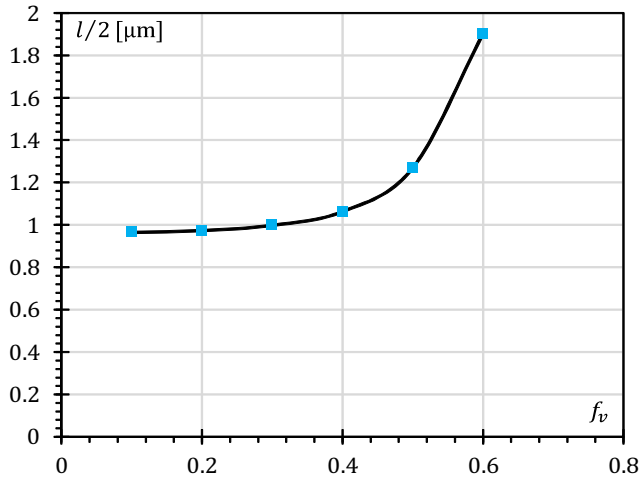

Fig. 3.49 Influence of the fiber volume fraction on the macroscopic properties: crack semi-length at onset versus fiber volume fraction.

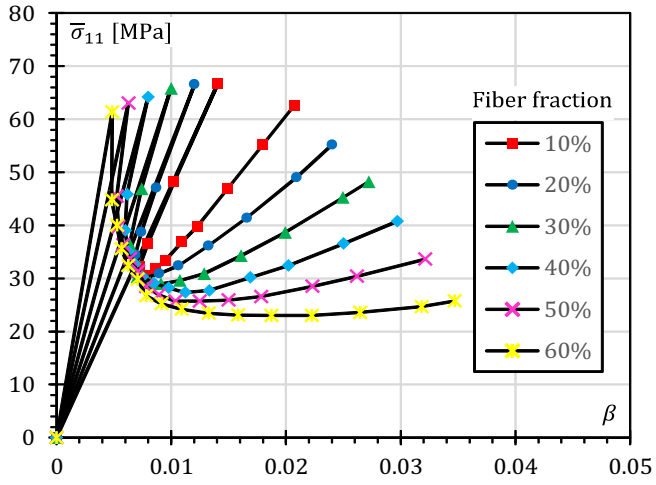

Fig. 3.50 Influence of the fiber volume fraction on the macroscopic properties: macroscopic stress versus load parameter for the analyzed fiber volume fractions.

model, crack is assumed of a through-the-width type, namely of infinite length in the out-of-plane direction (x_3). Consequently the assumption of plane strain exclude itself the possibility of out-of-plane loading conditions.

However, a generalized plane strain condition can be artificially modeled in the context of the present plane strain model in order to include the effect of loads applied along the fiber direction. The state of generalized plane strain is defined by the displacement field $u_1 = u_1(x_1, x_2)$, $u_2 = u_2(x_1, x_2)$ and $u_3 = \overline{\varepsilon}_{33} x_3$, where $\overline{\varepsilon}_{33}$ is the constant prescribed macrostrain in the fiber direction and rigid body motions are neglected. In order to simulate the above generalized plane strain model, an artificial initial strain in the out-of-plane direction is introduced such that the stress field for the plane strain and generalized plane strain problems are identical.

The strain ε_{33} in the out-of-plane direction can be written as the sum of the elastic and initial contributions, denoted by $\varepsilon_{33}^{\text{el}}$ and $\varepsilon_{33}^{\text{in}}$, respectively. For the generalized plane strain problem the strain must be equal to $\overline{\varepsilon}_{33}$ and the initial strain is assumed to be zero, i.e. $\varepsilon_{33} = \varepsilon_{33}^{\text{el}} = \overline{\varepsilon}_{33}$. For the present plane strain model the out-of-plane strain must vanish (i.e. $\varepsilon_{33} = \varepsilon_{33}^{\text{el}} + \varepsilon_{33}^{\text{in}} = 0$) and consequently the artificial initial strain which produces the same elastic strain in both the generalized and plane strain problems is $\varepsilon_{33}^{\text{in}} = -\overline{\varepsilon}_{33}$.

Since the crack is infinitely long in the fiber direction, loading along the fiber direction does not cause out-of-plane shear interface stresses (τ_{rz}) and only normal and tangential fiber/matrix interface stresses arise as in the case of loading only in the transverse plane. Consequently, the effect of loading along the x_3-direction on initiation and propagation of cylindrical fiber/matrix interface crack is driven by Poisson's effect and fracture mode III is not activated. Numerical calculations, carried out to investigate the effect of loading along the fiber direction on a composite microstructure loaded through a prescribed macrostrain having components in both x_1- and x_3-directions, have shown that compressive loading may lead to a notable increase in composite strength, whereas tensile loading gives a considerable decrease in strength, even if to a lesser degree. The macrostrain path involving both transverse and out-of-plane loading is defined by the following expression:

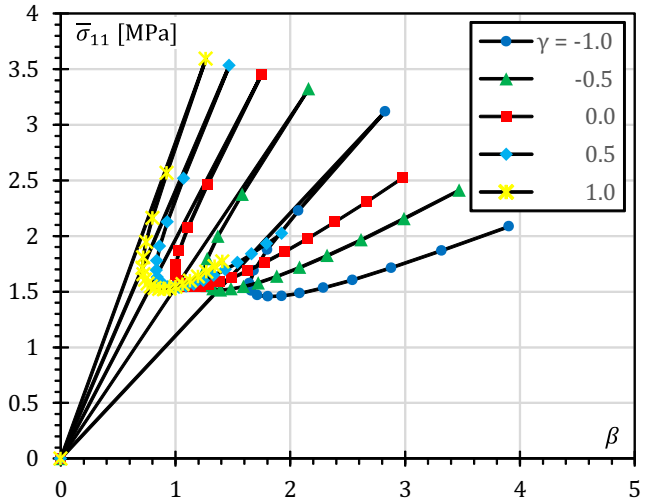

Fig. 3.51 Dimensionless macroscopic stresses versus macrostrain parameter for different levels of loading in the fiber direction.

$$\overline{\boldsymbol{\varepsilon}}_B = \pm\beta(\mathbf{e}_1 \otimes \mathbf{e}_1 + \gamma \mathbf{e}_3 \otimes \mathbf{e}_3) \qquad -1 \leq \gamma \leq 1\,, \tag{3.60}$$

where β is the macrostrain load parameter.

As a matter of fact, Fig. 3.51 shows that the macrostrain load parameter at crack onset β_c increases monotonically as the level of compression along the fiber direction increases, with a maximum relative difference with respect to the case of pure transverse loading ($\gamma = 0$) of about 62% attained for a fiber loading of the same level of the transverse one ($\gamma = 1$). On the other hand, in tension the macrostrain critical load parameter decreases, with a maximum relative difference with respect to the case of pure transverse loading within 28%. This behavior is also confirmed by the curves of the energy release rate to interface toughness function ratio versus interface crack length (see Fig. 3.52).

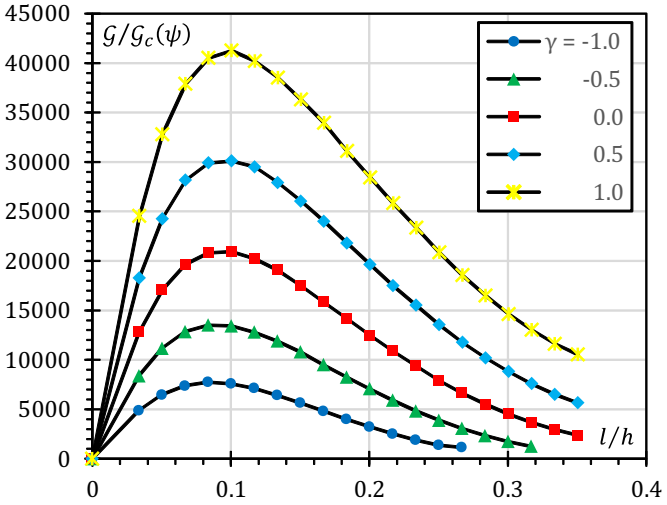

Fig. 3.52 Total energy release rate to interface toughness function ratio for a prescribed unit macrostrain as the crack semi/length increases for different levels of loading in the fiber direction.

Coherently, the plots of the macroscopic stress versus macrostrain load parameter show a stronger dependence on the level of loading in the fiber direction in compression in comparison with the tensile case, with a general decreasing trend of macrostresses as the level of loading along the fiber direction decreases.

3.5.5 Comparisons with existing models and assessment of the proposed methodology

In order to assess the accuracy of the proposed approach for determining energy release rate and fracture mode mixity for an interface crack inside a unit cell of a composite structure, described in Section 3.3, comparisons with results taken from [9] are here shown. Additional comparisons are carried out with reference to the procedure adopted to analyze kinking of a fiber/matrix crack leaving the interface and penetrating into the matrix.

Table 3.1 Material properties of the different microconstituents (fiber and matrix).

	Matrix (epoxy)	Fiber (glass)
Young's modulus	$E_f = 2.79 \times 10^9$ Pa	$E_f = 70.8 \times 10^9$ Pa
Poisson's ratio	$\nu_f = 0.33$	$\nu_f = 0.22$

The case of a single circular cylindrical inclusion embedded in an unbounded matrix subjected to a remote uniform uniaxial transverse tension, already studied in [9] is here analyzed. Plane strain state and isotropic linearly elastic microconstituents are considered; the material properties are listed in Table 3.1. The fiber radius a is set as 7.5 μm, and dimensionless results for ERR are obtained dividing the results by $\mathcal{G}_0 = \left[(1+\kappa_m)/8\mu_m\right]\sigma_0^2 a\pi$, where $\kappa_m = 3 - 4\nu_m$, μ_m is the shear modulus of the matrix, and σ_0 is the absolute value of the applied tension. In order to simulate the unbounded matrix a square sample of fiber reinforced material is considered with a side equal to $40a$.

Fig. 3.53 presents the evolution of the ERR (denoted by $\mathcal{G}$) and its mode components with the semi-debonding angle θ_d, as computed by using both the present approach and the one proposed in [9], whereas the behavior of the related fracture mode mixity is depicted in Fig. 3.54. The ERR mode I and II components, denoted by $\mathcal{G}_{\mathrm{I}}$ and $\mathcal{G}_{\mathrm{II}}$, respectively, are evaluated at the same reference length l_{ref} as in [9], by using the following formulas:

$$\mathcal{G} = \mathcal{G}_{\mathrm{I}} + \mathcal{G}_{\mathrm{II}}, \qquad \tan^2 \psi(l_{\mathrm{ref}}) = \frac{\mathcal{G}_{\mathrm{II}}(l_{\mathrm{ref}})}{\mathcal{G}_{\mathrm{I}}(l_{\mathrm{ref}})}, \tag{3.61}$$

Results highlight a good agreement in terms of both the total value of the ERR and mode mixity between the present model, based on the J-integral application in conjunction with the component separation method [55], and the

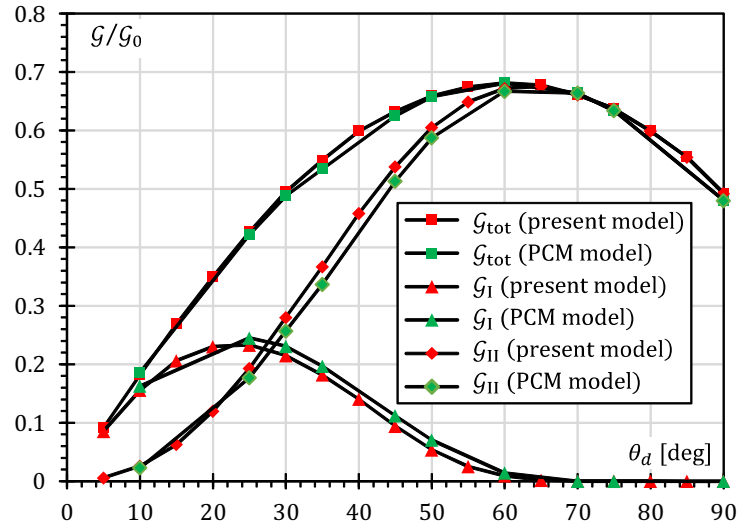

Fig. 3.53 Values of ERR for a fiber-matrix interface for different values of the semi-debonding angle.

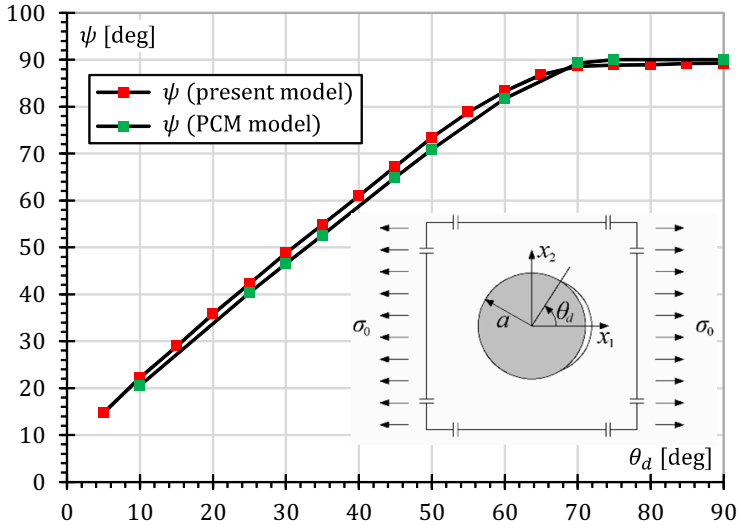

Fig. 3.54 Evolution of the fracture mode mixity with the semi-debonding angle.

Table 3.2 Relative percentage absolute errors for normalized ERR and fracture mode mixity between the present model and the PCM model [9].

θ_d (°)	% Absolute error	
	$\mathcal{G}/\mathcal{G}_0$	ψ (°)
10	2.24	7.92
25	0.986	4.79
30	1.44	4.83
35	2.79	4.29
45	1.19	3.56
50	0.113	3.54
60	0.031	1.95
70	0.422	0.79
75	0.512	1.25
90	2.54	0.83

model proposed by París, Correa and Mantič in [9] (here called PCM model), based on the BEM approach and the *virtual crack closure technique* (VCCT).

As matter of fact, the relative percentage errors in terms of both ERR and mode mixity, evaluated as $|(\mathcal{G}/\mathcal{G}_0) - (\mathcal{G}/\mathcal{G}_0)_{\text{PCM}}|/(\mathcal{G}/\mathcal{G}_0)_{\text{PCM}} \times 100$ and $|\psi - \psi_{\text{PCM}}|/\psi_{\text{PCM}} \times 100$ respectively, are reasonably small and within 2.54% for $\mathcal{G}$ and, except for very small semi-debonding angles for which the maximum error is 7.92%, within 4.83% for ψ, as shown in Table 3.2. With reference to the fracture mode mixity, the largest errors are obtained, as expected, for small semi-debonding angles, at which ψ attains very small values, due to the prevalence of mode I with respect to mode II. In these comparisons the quantities without subscripts refer to the results obtained by using the present model.

The relative differences shown in Table 3.2, which for fracture mode mixity appear larger than for ERR, depend on several aspects. As a matter of fact,

the determination of fracture mode mixity is extremely sensitive to the mesh adopted to discretize the near-tip zone and depends on the different strategies adopted to compute fracture mode mixity. In the present work the mode mixity is extracted by using the *J*-integral technique to compute the total ERR in conjunction with the component separation procedure introduced by Nishioka and co-workers [55], based on the crack tip opening displacements measured at a special reference length. On the other hand, in [9] a very accurate boundary element discretization is applied and the virtual crack closure method is adopted to compute ERR and its mode components. When the virtual crack closure technique is used, the total ERR as well as its component modes depend on the value of the crack extension length Δl and on the technique used to compute the crack closure integral (the crack closure method using two analysis steps may be used in place of the modified crack closure technique taking stresses and displacements from the opposite sides of the crack tip). Moreover, the ERR mode components show a nonconvergent behavior as Δl approaches zero when the oscillatory singularity is modeled and the crack closure integral must be carried out by adopting a sufficiently fine mesh near the crack tip.

On the other hand, the ERR mode components calculated by means of the component separation method depend only on the associated reference length scale l_{ref} and leads to stable and accurate numerical results for the stress intensity factors, due to the introduction of a special characteristic length in order to exclude the oscillatory and logarithmic singular terms.

As far as results for kinked cracks are concerned, the maximum ERR criterion is adopted, requiring kink crack modeling but being more accurate over other methodologies to predict the kink direction. On the other hand, a commonly used criterion is the one adopted in [9], based on the maximum circumferential stress (MCS criterion), requiring only the knowledge of the near-tip stress solution for the parent interface crack. Although these two criteria are conceptually different, for an isotropic elastic solid the kinking angle that maximizes ERR is nearly coincident with the kinking angle associated with the maximum circumferential stress [197]. On the other hand when kinking of

a crack at an interface between two materials characterized by a strong elastic mismatch is analyzed, significant differences may occur between different criteria [88]. As a consequence, once the procedure adopted to calculate ERR and its fracture mode mixity has been checked with reference to the interface crack problem, comparisons have been carried out in terms of the kink angle between the proposed approach and the MCS based one. Results obtained with the maximum ERR criterion show a reasonable agreement with those obtained by means of the MCS criterion for large semi-debonding angles ($\theta_d \geq 60°$) with a difference between kink angles calculated adopting the two criteria smaller than 4%. For small semi-debonding angles ($\theta_d < 60°$) the difference between kink angles predicted by the two criteria is smaller than 10%.

The reasonable agreement between kink angles predicted by using the maximum ERR and the MCS criteria for large semi-debonding angles, confirms the experimental evidences reported in [9].

It is worth noting that the computation of mode mixity angles in the present approach is based on the open crack model of Williams, whereas crack face contact is modeled in finite element computations. In this way contact modeling is introduced to avoid crack interpenetration outside the near-tip zone by using a relatively coarse mesh. On the other hand the near-tip contact model should require a very fine mesh (especially near the crack tip) to be modeled due to the small size characterizing the zone of near-tip crack face interpenetration.

Comparisons carried out with the results of [9] and shown in Figs. 3.53 and 3.54, demonstrate that the above simplified assumption is able to give accurate results in both cases of very small (*small-scale contact*) and non-negligible contact zone. As a matter of fact, in the latter case, crack tip displacements, used to obtain mode mixity according to the component separation method, take into account contact, which is well captured in the finite element model. Consequently, mode I energy release rate component, being related to the opening crack tip relative displacement, approaches practically zero. On the contrary, in the case of very small near-tip contact zone, the open model is suitable for representing fracture mode mixity at the crack tip and the

crack tip displacements are not affected by the crack tip contact zone, being so small as it cannot be captured by the finite element model.

3.6 Validation of the proposed semiconcurrent multiscale method: numerical results and discussion

The proposed multiscale approach, described in Section 3.4, is validated by comparing it with a fully meshed model. In the latter, a composite material is modeled by taking into account a precise description of its microstructure. Numerical calculations are devoted to 2D composite materials with a periodic fiber-reinforced microstructure; two different macroscopic structural configurations have been considered: a 2D heterogeneous beam model, discussed in Section 3.6.1, and a more general solid structure (whose dimensions are of the same order of magnitude), described in Section 3.6.2.

3.6.1 Cantilever beam

The first structural configuration involved in the present numerical applications consists in a heterogeneous beam is composed of a rectangular arrangement of 5×40 unit cells with fibers initially perfectly bonded to the matrix. The proposed problem is discretized by means of two-dimensional finite elements in a plane strain setting. As described in Fig. 3.55, the specimen is clamped at its left edge and two alternative types of global boundary conditions at its right side are considered: (a) prescribed rotation about its centroid axis; (b) prescribed vertical displacement. The considered macroscopic loading conditions, producing pure bending stresses and combined flexural and shearing stresses, respectively, are selected to assess the accuracy of the proposed multiscale technique for general loading conditions, involving mixed-mode damage evolution at the fiber/matrix interfaces.

A 2D square unit cell is considered, including a rigid centered circular fiber. The side length of the RVE is $h = 30$ μm, the diameter of the inclusion $d_f = 0.5h$, so that the resulting fiber volume fraction is $V_f / V \approx 0.20$. Matrix and inclusions are assumed to be homogeneous and made of isotropic linearly

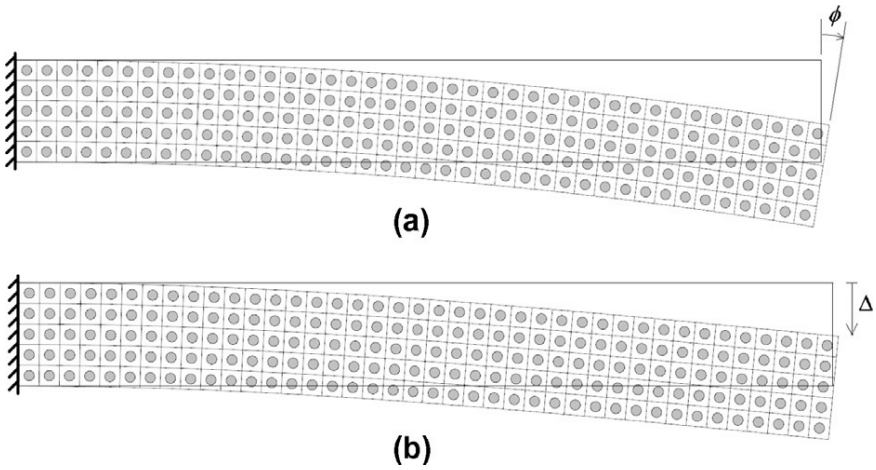

Fig. 3.55 Initial and deformed configuration of a fiber-matrix composite beam subjected to two different global boundary conditions: (a) prescribed rotation; (b) prescribed vertical displacement.

elastic materials, whose constants are: $E_m = 2.79$ GPa and $\nu_m = 0.3$ for the matrix, $E_f = 70.8$ GPa and $\nu_m = 0.22$ for the fiber. The interface is characterized by four failure parameters: the tensile and shear strengths, $\sigma_c = 90$ MPa and $\tau_c = 120$ MPa, the fracture mode I toughness $\mathcal{G}_{\mathrm{Ic}} = 2.0$ J/m^2 and the fracture mode-sensitivity parameter λ that adjusts the influence of mode II contribution, set as 0.3. The reference length l_{ref} used to normalize the oscillatory singularity is set as 1×10^{-2} μm. According to this choice, based on a material length scale, l_{ref} necessarily lies within the zone of dominance of the K-field.

The geometric model at both macro- and micro-scales have been discretized with quadratic triangular elements by means of an unstructured mesh. Moreover, in the homogenized analysis, internal geometric constraints have been applied to the mesh, for a direct evaluation of the displacement field on the RVE boundaries, as shown in Fig. 3.56. In the direct analysis an appropriate mesh refinement along the interfaces and the J-integral contours is employed. This mesh is arranged in about 354,900 elements, resulting in about 1,421,900 degrees of freedom (DOF). On the contrary, in the homogenized

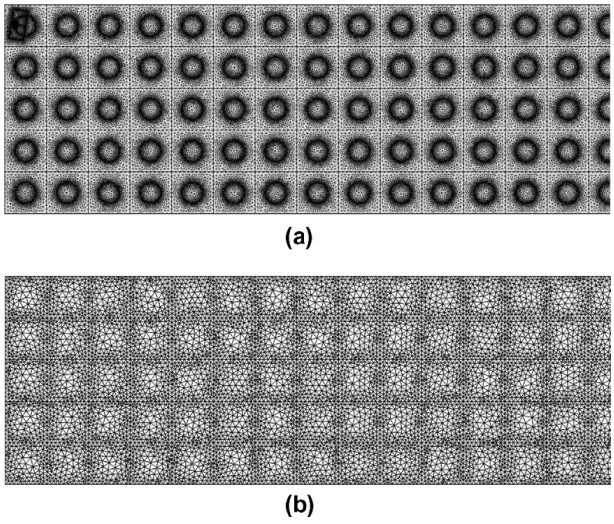

Fig. 3.56 Mesh plot of a portion of the specimen near the left end for the direct (a) and for the multiscale (b) numerical simulations.

analysis the mesh is composed of 42,410 elements, so that the number of DOFs is equal to 186,040.

The mesh size employed to solve the homogenized problem was chosen as the best one among several test values: results obtained by using coarser meshes showed a loss in accuracy, whereas additional mesh refinement did not affect the finite element solution. This mesh sensitivity can be related to the necessity to provide a better representation of discontinuities at the macroscale for the regions of the multiscale model linked to the damaging unit cells.

3.6.1.1 Cantilever beam with a prescribed rotation

This application involves a 2D cantilever beam subjected to an imposed rotation $\beta\phi_{\text{ref}}$ on its right end, where ϕ_{ref} is a reference rotation set as $L/500H$, where L is the specimen length, H its height, and β denotes the loading parameter. The main scope of this section is to perform a macroscopic failure analysis of the considered heterogeneous structure under the assumption of

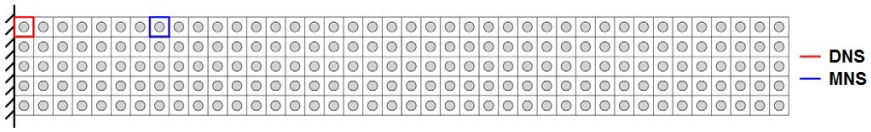

Fig. 3.57 Location of the unit cell undergoing crack initiation in the direct (DNS) and multiscale (MNS) numerical simulations for global boundary conditions (a).

crack initiation and propagation along a weak fiber/matrix interface during the loading history. As the bending moment is (approximately) constant along the x_1-axis in the macroscopic model, each unit cell placed on the upper side could be a suitable site for crack onset. However, the presence of a fixed boundary disturbs the macroscopic fields and therefore the left end of the beam becomes the favorite zone for crack initiation. In the direct analysis, the application of the criterion $(3.7)_2$ leads to obtain the upper left cell as that undergoing the first crack initiation; on the other hand the multiscale analysis is not able to detect the same unit cell because of the approximations related to the homogenization/localization process and to the macroscopic uniformity of the stress and strain distributions (see Fig. 3.57). However, as will be shown later, the macroscopic failure behavior of the composite beam is scarcely influenced by the location of the damaging cell.

Interface stresses play a fundamental role in failure mechanisms of fiber-reinforced composite materials, since they govern the location of the crack onset point at the fiber/matrix interface. Fig. 3.58 shows the distribution of dimensionless normal and tangential interfacial stresses (here denoted by σ_r and $\tau_{r\theta}$, respectively) computed by means of the direct (continuous line) and the multiscale (dashed line) analyses within the cell undergoing crack onset and for a unit load factor. Results highlight that the multiscale analysis provides a good approximation of the maximum absolute value of normal and tangential interface stresses, although the direct and multiscale analyses do not predict the same cell undergoing crack initiation.

It is worth noting that the maximum value of the interface stresses is attained at different values of the polar angle θ (measured counterclockwise

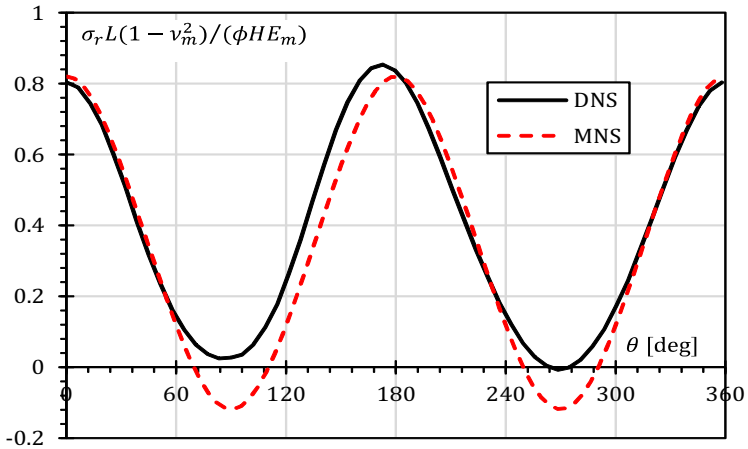

(a)

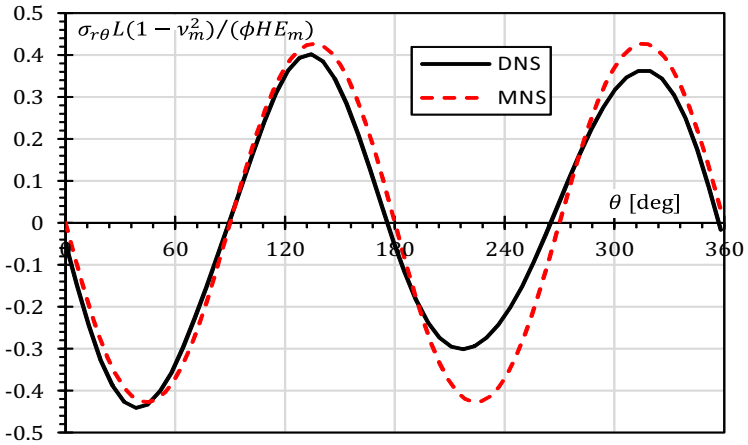

(b)

Fig. 3.58 Comparisons in terms of normal (a) and tangential (b) interface stresses between the multiscale (MNS) and the direct (DNS) numerical simulations for the cell undergoing crack initiation for global boundary conditions (a).

from the positive x_1-axis) for the direct and multiscale analyses. As a consequence, each analysis leads to a different location of the onset point $P(r, \theta_c)$.

Table 3.3 Comparisons in terms of local failure parameters at crack onset between direct and multiscale numerical simulations for the cell undergoing crack initiation in the case of global boundary conditions (a).

	θ_c (°)	β_c	$\varphi_c^{(1)}$ (°)	$\varphi_c^{(2)}$ (°)	φ_c (°)	$\frac{\sigma_{r,\max} L(1-\nu_m^2)}{\phi H E_m}$	$\frac{\sigma_{r\theta,\max} L(1-\nu_m^2)}{\phi H E_m}$
DNS	171.0	17.12	8.12	7.24	15.36	0.854	0.441
MNS	180.0	17.83	7.72	7.67	15.39	0.820	0.427
Error [%]	5.26	4.15	-4.97	5.96	0.179	-3.89	-3.18

Once the onset point is located, the application of the coupled stress- and energy-based criterion (3.11) leads to the determination of the critical load factor β_c at crack onset and the two crack partial lengths $l_c^{(1)}$ and $l_c^{(2)}$ measured from the onset point along the fiber/matrix interface (see Fig. 3.13). In Table 3.3 the load factor and the maximum values of interfacial stresses at crack onset are presented in dimensionless form, whereas $l_c^{(1)}$ and $l_c^{(2)}$ are given as angular distances from the onset point, denoted by $\varphi_c^{(1)}$ and $\varphi_c^{(2)}$.

Figs. 3.59 and 3.60 show the comparison between the results obtained through the direct and the multiscale analyses, in terms of global parameters. The moment-rotation diagram at the right end of the specimen shows that the macroscopic response of the considered structure is characterized by a sharp snap-back behavior and a subsequent snap-through (see Fig. 3.59). This implies an initially unstable behavior followed by a stable one with the consequent possibility of crack arrest for a prescribed load factor. The above-described behavior can be better appreciated by means of Fig. 3.60, showing the evolution of the load parameter as a function of the crack total length (expressed in terms of debonding angle $\varphi_c = \varphi_c^{(1)} + \varphi_c^{(2)}$). This diagram highlights a recover in strength for $\varphi_c > 56°$ in both analyses; in fact, as the crack length increases, the stabilizing effect due to the mixed-mode crack propagation becomes more relevant. The change in the stability behavior can be justified on the basis of the plot of the total energy release rate to interface toughness ratio versus the crack total length, which is characterized by an initial

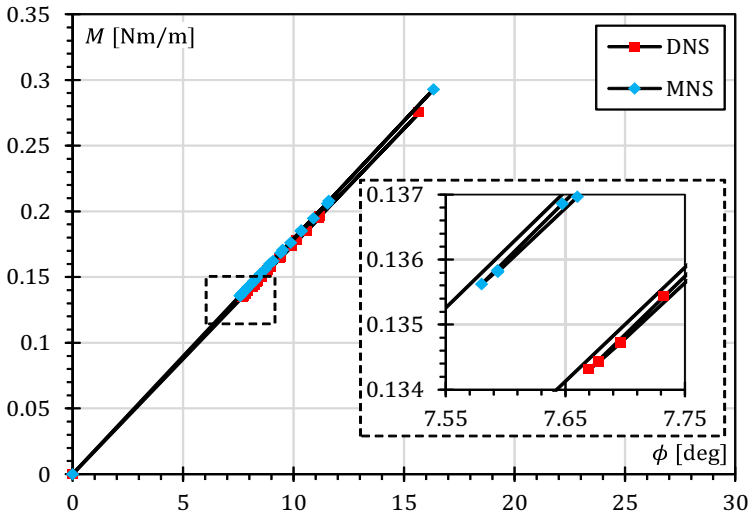

Fig. 3.59 Bending moment versus prescribed rotation curve for both direct (DNS) and multiscale (MNS) numerical simulations.

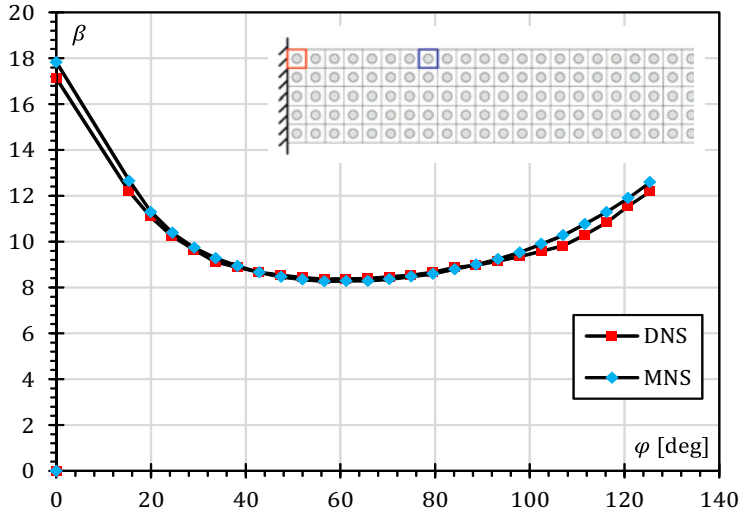

Fig. 3.60 Evolution of the load factor as a function of the total debonding angle for both direct (DNS) and multiscale (MNS) numerical simulations.

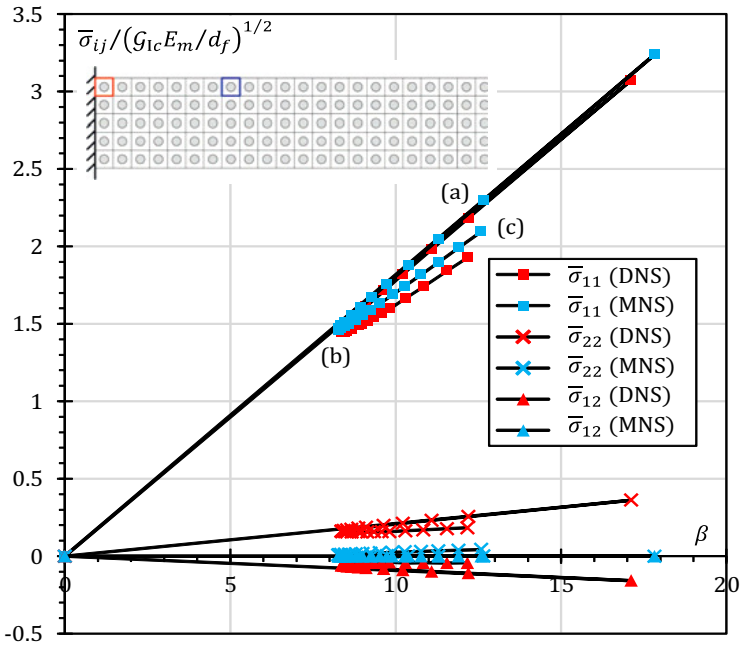

Fig. 3.61 Macroscopic dimensionless stresses versus loading parameter for the unit cell undergoing crack initiation and propagation in the direct (DNS) and the multiscale (MNS) numerical simulations.

increasing behavior followed by a decreasing one (see Fig. 3.64), related to increasing values of the mode mixity for increasing debonding lengths (see Fig. 3.65).

The multiscale analysis provides an overestimation of the maximum bending moment of 6.39%, whereas the multiscale and the direct analyses practically lead to the same global stiffness, which is practically unaffected by a growing defect in a single unit cell.

In order to investigate the constitutive response of the damaging unit cell, Fig. 3.61 shows the evolution of the dimensionless macroscopic stresses as functions of the loading parameter. A notable degradation for increasing values of the length crack can be noticed, with the maximum loss in stiffness

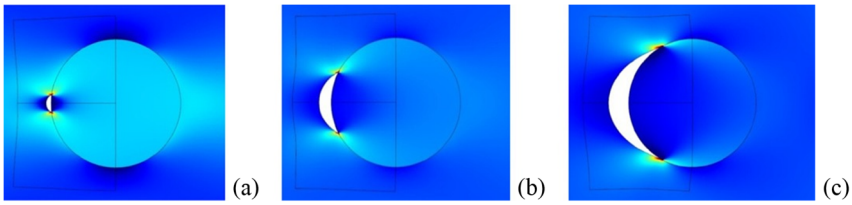

Fig. 3.62 Evolution of damage in the unit cell of the multiscale numerical simulation: (a) crack onset; (b) intermediate stage corresponding to the snap-back through (turning point); (c) final stage.

exhibited in the x_1-direction. The multiscale analysis provides a small overestimation of the peak value of σ_{11} (with a relative percentage error of about 5%) with respect to the direct analysis. The comparison between the direct and the multiscale analyses in terms of σ_{22} and σ_{12} shows very large errors due to the different location of the damaged unit cell. However, these stresses do not affect significantly the global structural behavior of the examined composite structure.

The evolution of crack initiation and propagation for the multiscale simulation in the critical unit cell is shown in Fig. 3.62, with reference to the stages shown in the stress-load parameter behavior of Fig. 3.61. As can be seen the crack initiates at fiber/matrix interface with an angle of about 15.4° and then progresses along the interface until $\varphi \approx 125°$; after this value, for increasing crack lengths contact phenomena may arise and kinking begins to be favored over debonding.

In order to obtain the homogenized behavior of the damaging microstructure, the estimation of the macroscopic moduli of the cracked unit cell was needed for increasing debonding angles. As shown in Fig. 3.63, the highest loss in stiffness is exhibited by $\overline{C}_{1111}$.

The evolution of the energy release rate at each tip for both direct and multiscale analyses is shown in Fig. 3.64. The jagged behavior exhibited by the curve can be explained by the alternating propagation of the two tips, and the oscillating contribution can be notably reduced by choosing a very small increment of the crack length during its growth. The comparison between the

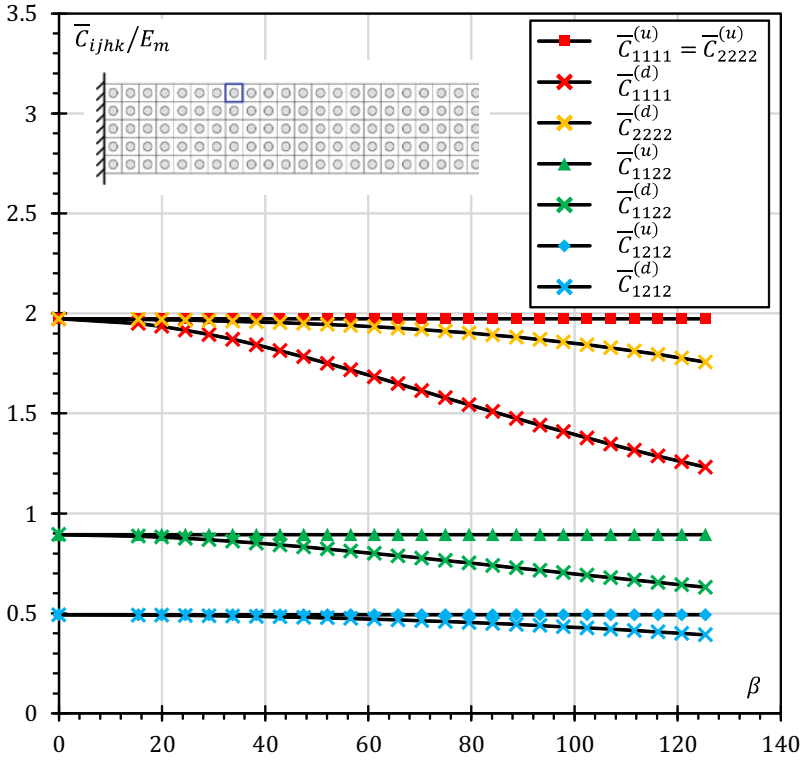

Fig. 3.63 Behavior of the macroscopic moduli for increasing debonding angle for unit cell undergoing damage growth (comparison between undamaged (*u*) and damaged (*d*) moduli).

two analyses shows small errors in average sense, owing to the different location of the onset point. The peak value of energy release rates for both tips and the relative percentage errors between the direct and the multiscale analyses are shown in Table 3.4.

Finally, Fig. 3.65 shows the behavior of the mixed-mode angle as a function of debonding angle for both tips; the plot highlights a linear relationship between the two angles after the onset process, and results are in good agreement with the analytical solution proposed in [49]. The offset between curves corresponding to direct and multiscale analyses can be explained by the different location of the onset point, owing to boundary layer effects.

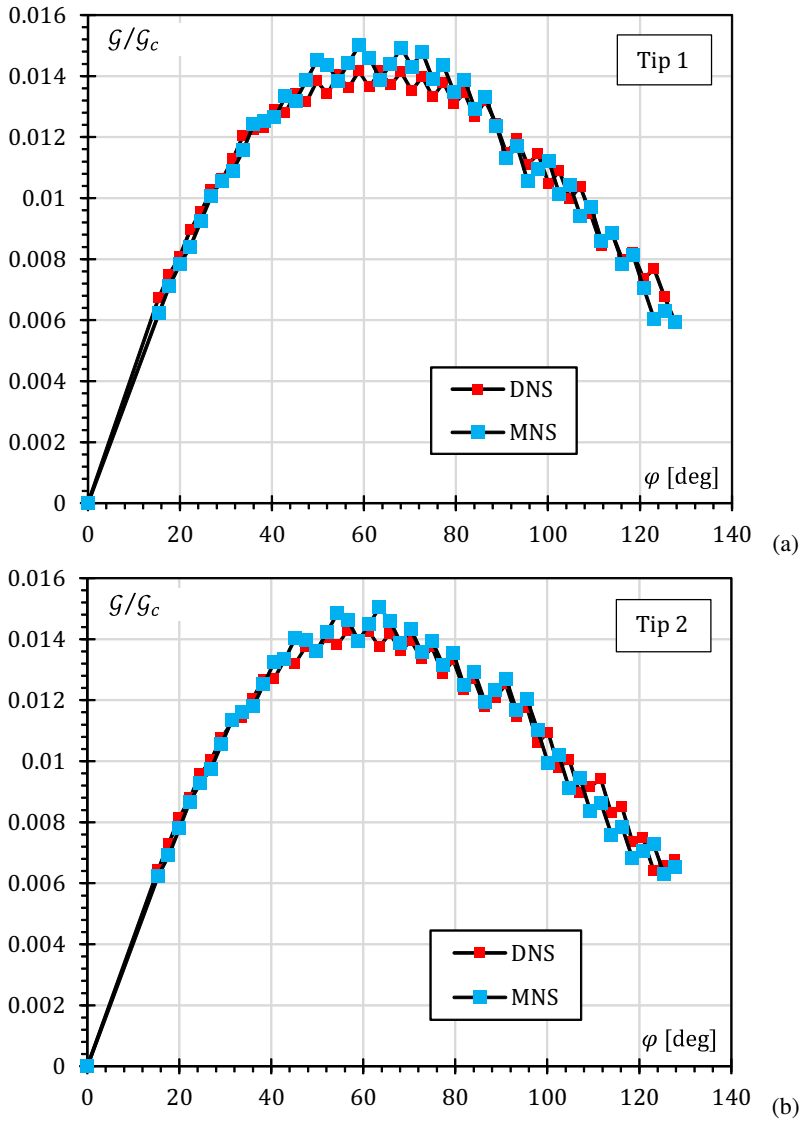

Fig. 3.64 Dimensionless energy release rate for a unit load factor as a function of debonding angle for tip 1 (a) and tip 2 (b) in both the direct (DNS) and the multiscale (MNS) numerical simulations.

Table 3.4 Comparison between direct and multiscale numerical simulations in terms of peak values of the dimensionless energy release rate for a unit load factor for both tips in the case of global boundary conditions (a).

	$\mathcal{G}_{\max}^{(1)} / \mathcal{G}_c^{(1)}$	$\mathcal{G}_{\max}^{(2)} / \mathcal{G}_c^{(2)}$
DNS	0.014165	0.014286
MNS	0.015017	0.015043
Error [%]	6.02	5.30

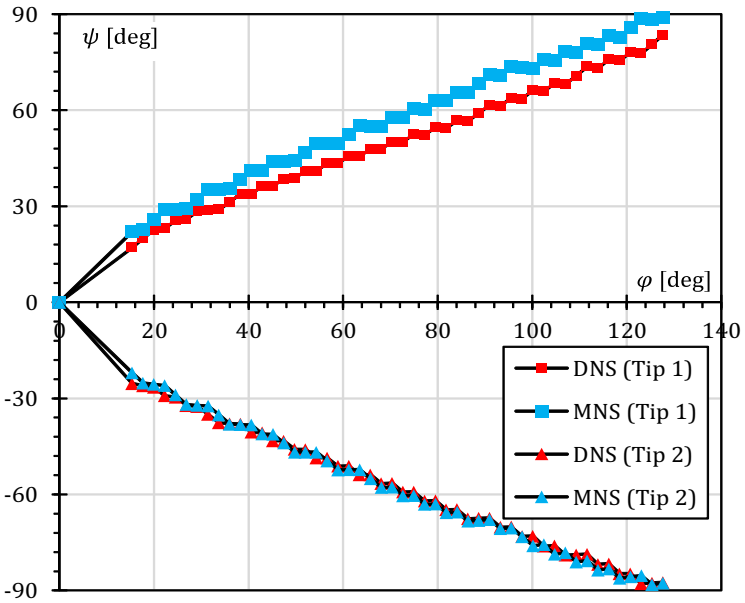

Fig. 3.65 Mixed mode angle as a function of debonding angle for both tips and for both the direct (DNS) and the multiscale (MNS) numerical simulations.

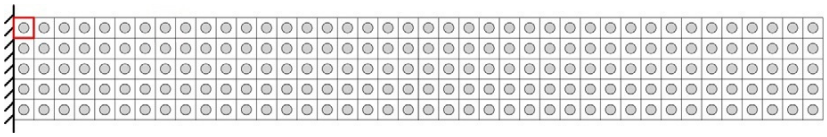

Fig. 3.66 Location of the unit cell undergoing crack initiation in the direct (DNS) and multiscale (MNS) numerical simulations for global boundary conditions (b).

3.6.1.2 Cantilever beam with a prescribed displacement

The second application is devoted to the problem of non-uniform bending in a composite beam. The same cantilever beam considered before is subjected to a prescribed vertical displacement $\Delta = \beta\Delta_{\text{ref}}$ on its right end, with reference displacement $\Delta_{\text{ref}} = L/1000$. In this case the macroscopic fields are subjected to a spatial variation along both x_1- and x_2-directions and uniformity cannot be found in the expected structural behavior, unlike the previous case. As a consequence a single crack initiation will be located within the most stressed unit cell.

In both the direct and the multiscale analyses, the application of the criterion $(3.7)_2$ leads to finding the upper left cell as the one undergoing the first crack initiation; this result can be justified on the basis that the fixed end is subjected to the maximum value of the bending moment (see Fig. 3.66).

Fig. 3.67 shows the distribution of dimensionless normal and tangential interfacial stresses computed by means of the direct (continuous line) and the multiscale (dashed line) analyses within the cell undergoing crack onset and for a unit load factor. Results highlight that the multiscale analysis provides an underestimation of the maximum absolute value of normal and tangential interface stresses, owing to relevant boundary layer effects.

Once the onset point is located, the application of the coupled stress- and energy-based criterion (3.11) leads to the determination of the critical load factor β_c at crack onset and the two crack partial lengths $l_c^{(1)}$ and $l_c^{(2)}$, measured from the onset point along the fiber/matrix interface. In Table 3.5 the load

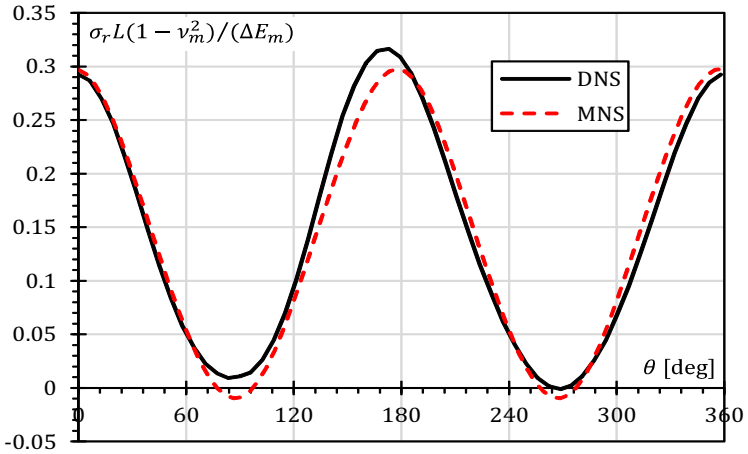

(a)

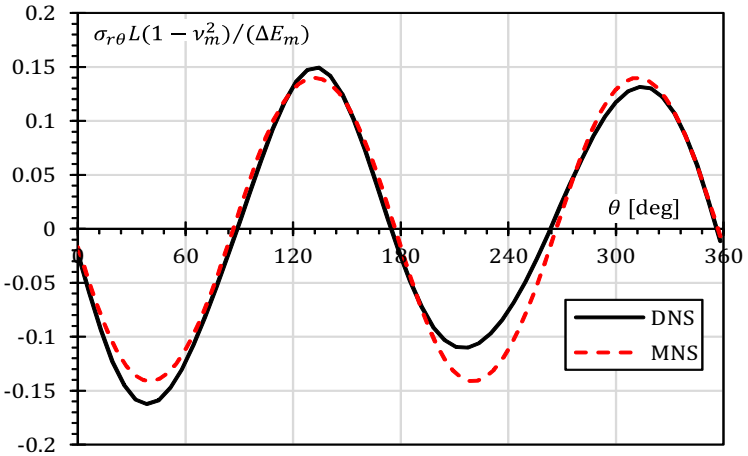

(b)

Fig. 3.67 Comparisons in terms of normal (a) and tangential (b) interface stresses between the multiscale (MNS) and the direct (DNS) numerical simulations for the cell undergoing crack initiation for global boundary conditions (b).

Table 3.5 Comparisons in terms of local failure parameters at crack onset between direct and multiscale numerical simulations for the cell undergoing crack initiation in the case of global boundary conditions (b).

	θ_c (°)	β_c	$\varphi_c^{(1)}$ (°)	$\varphi_c^{(2)}$ (°)	φ_c (°)	$\frac{\sigma_{r,\max} L\left(1-\nu_m^2\right)}{\Delta E_m}$	$\frac{\sigma_{r\theta,\max} L\left(1-\nu_m^2\right)}{\Delta E_m}$
DNS	168.8	92.24	9.09	6.12	15.21	0.317	0.162
MNS	178.3	98.11	7.10	8.22	15.32	0.298	0.141
Error [%]	5.63	6.36	-21.89	34.31	0.723	-5.95	-13.1

factor and the maximum values of interfacial stresses are presented in dimensionless form, whereas $l_c^{(1)}$ and $l_c^{(2)}$ are given as angular distances from the onset point, as in the previous case.

Figs. 3.68 and 3.69 show the comparison between the results obtained through the direct and the multiscale analyses, in terms of macroscopic parameters. The shear force-deflection diagram at the right end of the specimen shows that the macroscopic response is characterized by a severe snap-back behavior and a subsequent snap-through, as in the bending moment-rotation diagram of the previous case (see Fig. 3.68). Therefore similar considerations can be made as far as the macroscopic stability behavior of the composite beam is concerned. Fig. 3.69 shows the evolution of the load parameter as a function of the crack total length. A recovery in strength for $\varphi > 61°$ is pointed out in both analyses as a consequence of the stabilizing effect related to the mixed-mode crack propagation. The change in the stability behavior is confirmed by the plot of the total energy release rate to interface toughness ratio versus the crack total length, which highlights an initial increasing behavior followed by a decreasing one (see Fig. 3.72), accordingly with the increasing values of the mode mixity for increasing debonding lengths (see Fig. 3.73).

As depicted in Fig. 3.68, the multiscale analysis provides an overestimation of the maximum shear force of about 8.6%, whereas the global stiffness is scarcely affected by the adopted analysis.

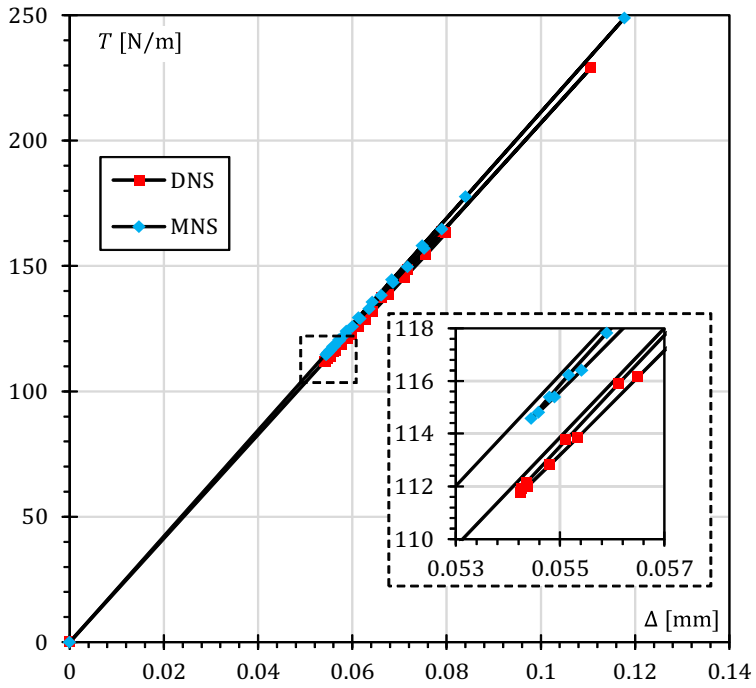

Fig. 3.68 Shear force versus prescribed vertical displacement curve for both direct (DNS) and multiscale (MNS) numerical simulations.

The small damage sensitivity of the macroscopic stiffness is strongly related to the fact that crack initiation and propagation phenomena are located inside only one unit cell and to the assumption that damage growth occurs at the fiber/matrix interface. To this end interfacial stress analyses were carried out for both loading cases in order to find other possible onset points; results showed that the application of the stress-based criterion $(3.7)_2$ cannot lead to locating other crack sites, because of the unstable nature of crack propagation process leading to snap-back instability in the global response. In other words, by applying the crack length control scheme, during crack initiation the heterogeneous beam is suddenly subjected to unloading and stress redistribution is not able to produce a stress state level high enough for crack onset. In general,

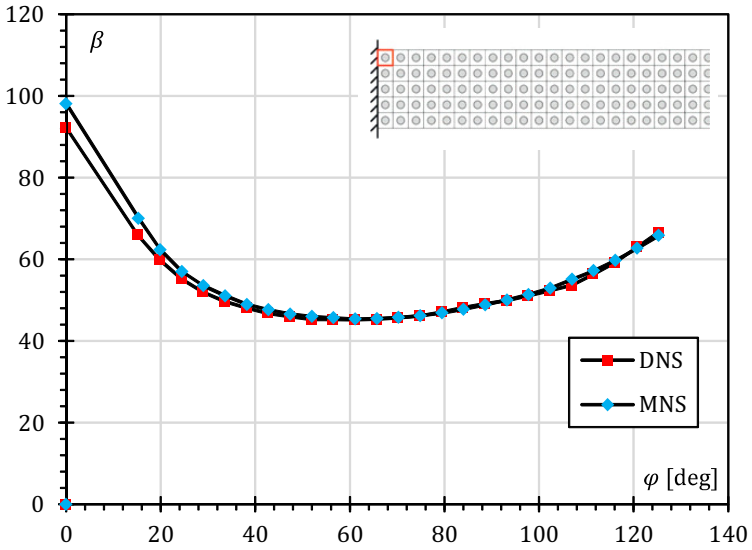

Fig. 3.69 Evolution of the load factor as a function of the total debonding angle for both direct (DNS) and multiscale (MNS) numerical simulations.

when kinking and percolation effects must be taken into account, a multi-site crack initiation and propagation analysis cannot be avoided leading to a more sophisticated multilevel model. In this case it is believed that the global stiffness may change notably during the unstable regime.

The homogenized constitutive response of the damaging unit cell is depicted in Fig. 3.70. The maximum loss in stiffness is exhibited in the x_1-direction. The multiscale analysis gives a small overestimation of the peak value of σ_{11} (with a relative percentage error of about 7.8%) with respect to the direct analysis.

Fig. 3.71 shows the evolution of crack configuration during its propagation within the critical unit cell for the multiscale simulation, with reference to the stages shown in the stress-load parameter behavior of Fig. 3.70. As can be seen the crack initiates at fiber/matrix interface with an angle of about 15.3° and then progresses along the interface until $\varphi \approx 125°$; after this value,

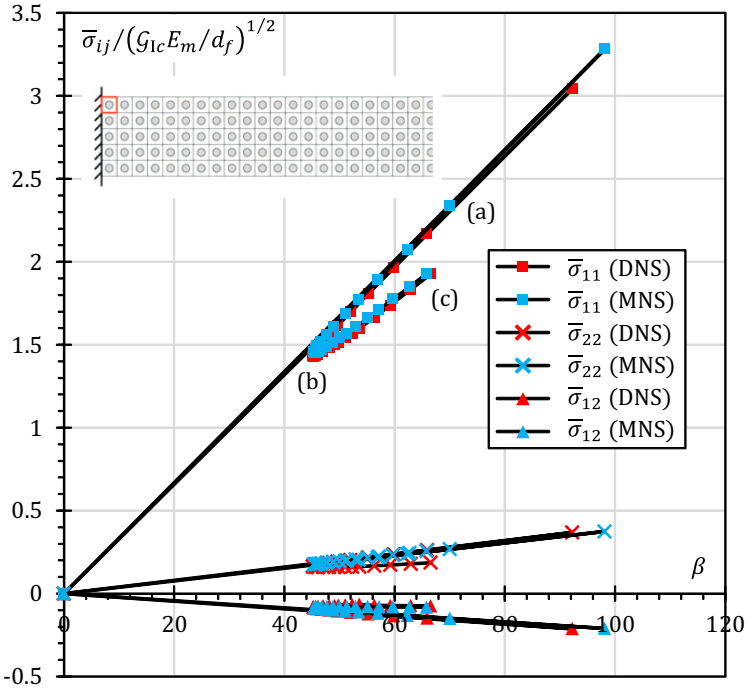

Fig. 3.70 Macroscopic dimensionless stresses versus loading parameter for the unit cell undergoing crack initiation and propagation in the direct (DNS) and the multiscale (MNS) numerical simulations.

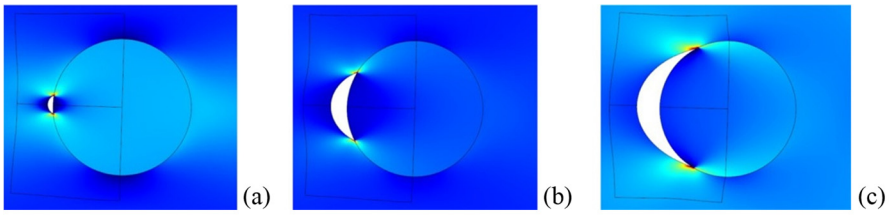

Fig. 3.71 Evolution of damage in the unit cell of the multiscale numerical simulation: (a) crack onset; (b) intermediate stage corresponding to the snap-back through (turning point); (c) final stage.

for increasing crack lengths contact phenomena may arise and kinking begins to be favored over debonding.

The behavior of the damaged macroscopic moduli of the critical unit cell for increasing debonding angles appears to be very similar to the one corresponding to the previous loading case, depicted in Fig. 3.63. This is due to the fact that the crack onset points found in both analyses are very close to each other.

The evolution of the energy release rate at each tip for both direct and multiscale analyses is shown in Fig. 3.72. The comparison between the two analyses shows very small errors, leading to a very good assessment of the multiscale analysis in estimating fracture parameters.

The peak value of energy release rates for both tips and the relative percentage errors between the direct and the multiscale analyses are shown in Table 3.6, whereas Fig. 3.73 shows the behavior of the mixed-mode angle as a function of the debonding angle for both tips.

3.6.2 Composite microstructure under extensional loading

The second structural configuration considered for performing numerical calculations consists in a 2D model of a general heterogeneous solid (whose dimensions are of the same order of magnitude) composite structure reinforced with long fibers initially perfectly bonded to the matrix. The same unit cell geometry and material properties as in Section 3.6.1 are considered. However, here, the reference length l_{ref} is expressed in terms of incremental polar angle along the interface from the crack tip location and set as 0.1°.

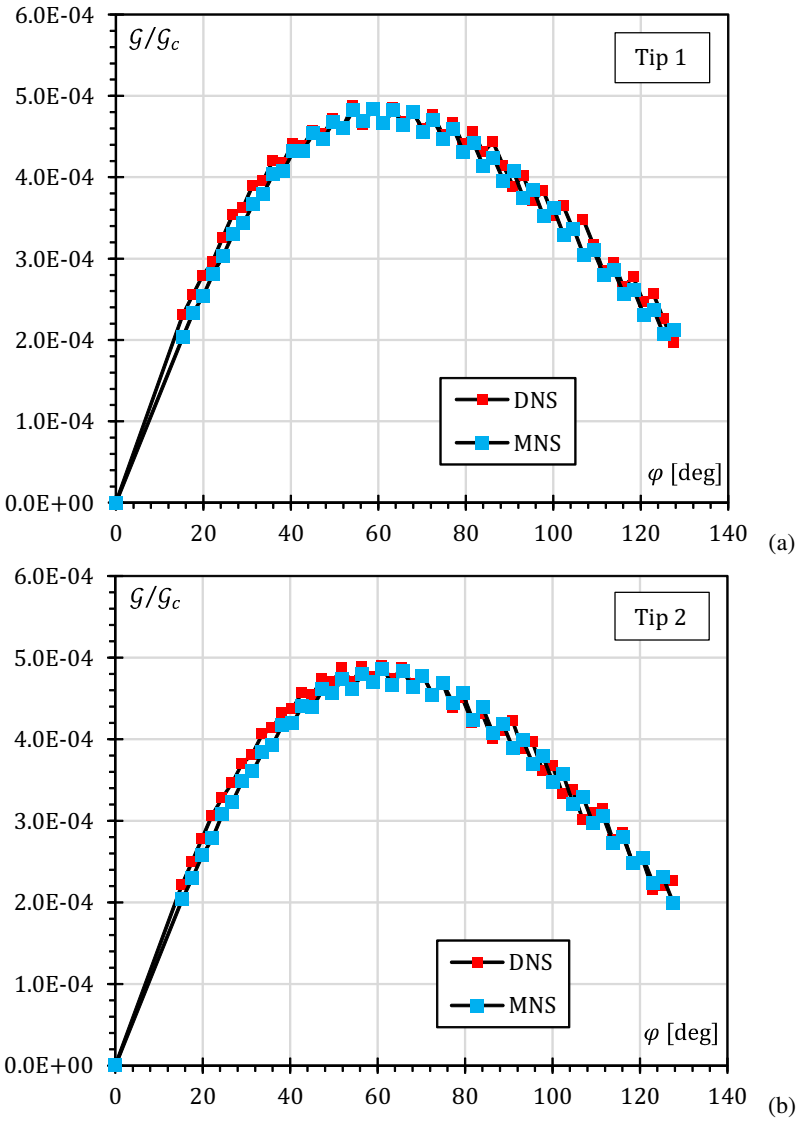

Fig. 3.72 Dimensionless energy release rate for a unit load factor as a function of debonding angle for tip 1 (a) and tip 2 (b) in both the direct (DNS) and the multiscale (MNS) numerical simulations.

Table 3.6 Comparison between direct and multiscale numerical simulations in terms of peak values of the dimensionless energy release rate for a unit load factor for both tips in the case of global boundary conditions (b).

	$\mathcal{G}_{\max}^{(1)} / \mathcal{G}_c^{(1)}$	$\mathcal{G}_{\max}^{(2)} / \mathcal{G}_c^{(2)}$
DNS	0.0004876	0.014286
MNS	0.0004834	0.015043
Error [%]	-0.860	-0.774

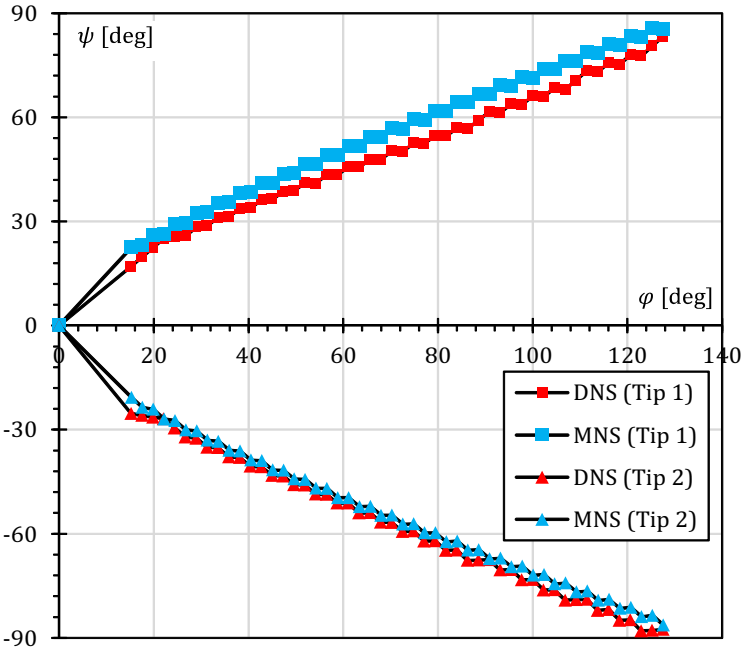

Fig. 3.73 Mixed mode angle as a function of debonding angle for both tips and for both the direct (DNS) and the multiscale (MNS) numerical simulations.

The microstructure is composed of a regular arrangement of 10×10 unit cells and subjected at its upper side to a prescribed reference extensional displacement $\Delta_{\text{ref}} = H/1000$, where H is the height of the composite structure.

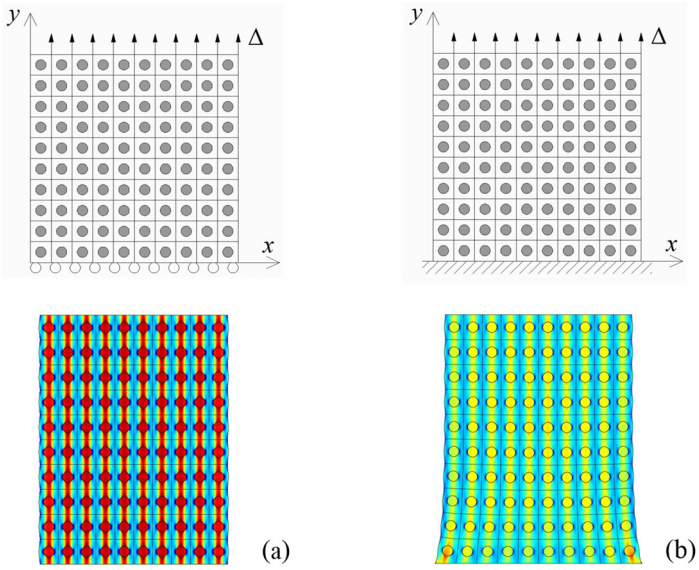

Fig. 3.74 Geometry and deformed configuration of a perfectly bonded fiber-reinforced composite: (a) uniform macroscopic deformation gradient; (b) non-uniform macroscopic deformation gradient.

Its right and left sides are assumed to be traction-free, and two types of boundary conditions at its lower side are considered: (a) sliding boundary and (b) fixed boundary, as shown in Fig. 3.74. The global boundary conditions (a) and (b) involve, respectively, uniform and non-uniform macroscopic stress and strain gradients.

In the direct analysis, an unstructured triangular mesh is adopted and a suitable mesh refinement along the interface at each cell is used. This mesh is arranged in about 402,000 quadratic elements, resulting in about 1,610,000 degrees of freedom, as shown in Fig. 3.75. Interface stresses play a fundamental role in failure mechanisms of fiber reinforced composite materials, since they govern the location of the crack onset point at the fiber/matrix interface. By applying Eq. $(3.7)_1$ the unit cell undergoing crack initiation is detected in both the direct and homogenized analyses: for global boundary conditions (a)

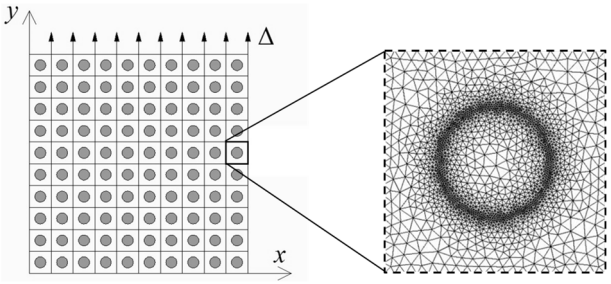

Fig. 3.75 Mesh plot of the fiber-reinforced composite macrostructure in the direct numerical simulation.

crack initiation can occur within every unit cell; however the crack onset point is supposed to be located within one of the four central cells.

For global boundary conditions (b) the homogenized and the direct analyses are able to detect the same cell. Figs. 3.76 and 3.77 show the distribution of dimensionless normal and tangential interfacial stress (here denoted respectively by σ_r and $\sigma_{r\theta}$) computed by means of the direct (continuous line) and the homogenized (dashed line) analyses within the considered cell, for both types of boundary conditions. Results show that the direct and homogenized analyses give practically the same values for interfacial stresses in the case of global boundary conditions (a), whereas the homogenized analysis provides an underestimation of the maximum absolute value of normal and tangential interface stresses.

Note that the maximum values of the interface stress are attained at different values of the polar angle θ (measured counterclockwise from the positive x_1-axis) in the case of global boundary conditions (b) for the direct and homogenized analyses (see Fig. 3.77).

Finally the estimation of the critical load factor β_c and the interface crack length l_c at onset has been carried out by solving the system (3.11) for β_c, $l_c^{(1)}$ and $l_c^{(2)}$. Tables 3.7 and 3.8 show the comparisons performed between direct and homogenized analyses, in term of the polar angle θ_c which locates the

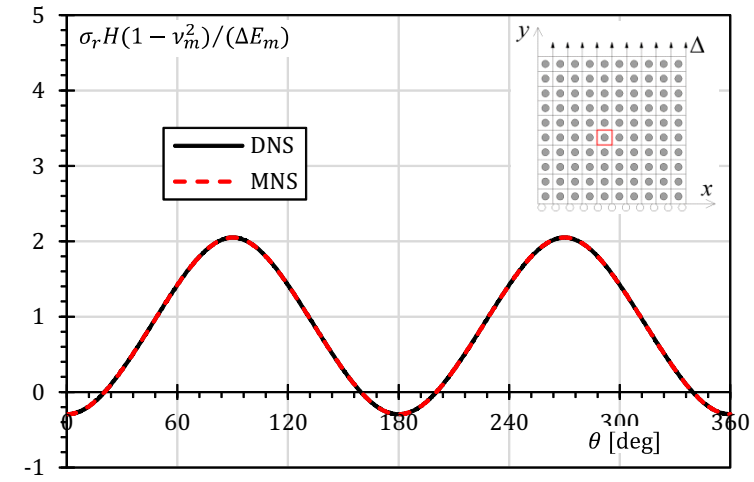

(a)

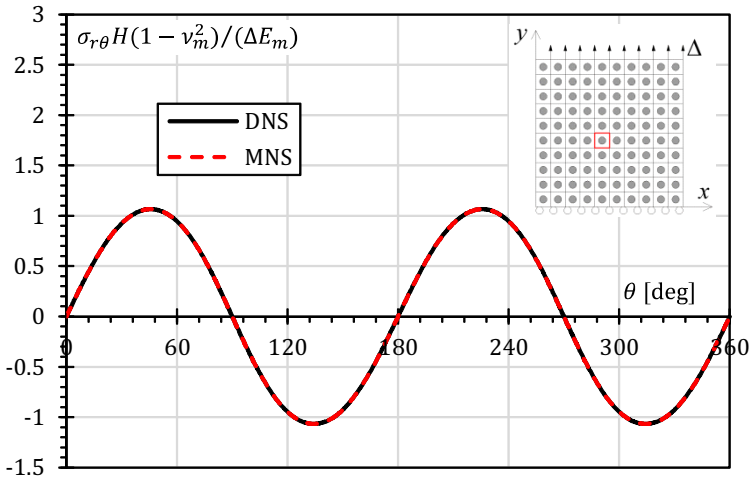

(b)

Fig. 3.76 Comparisons in terms of normal (a) and tangential (b) interface stresses between the multiscale (MNS) and the direct (DNS) numerical simulations for the cell undergoing crack initiation in the case of uniform macroscopic gradient.

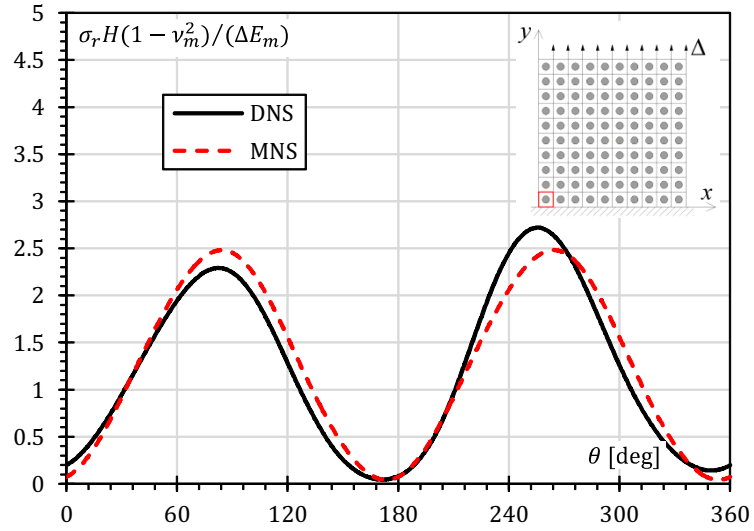

(a)

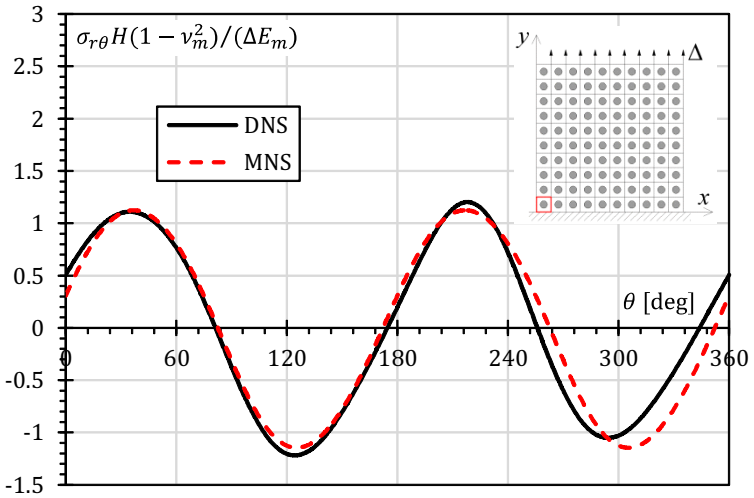

(b)

Fig. 3.77 Comparisons in terms of normal (a) and tangential (b) interface stresses between the multiscale (MNS) and the direct (DNS) numerical simulations for the cell undergoing crack initiation in the case of non-uniform macroscopic gradient.

Table 3.7 Comparisons in terms of local failure parameters at crack onset between direct and multiscale numerical simulations for global boundary conditions (a).

	θ_c (°)	Δ_c / H	l_c / d_f	$\frac{\sigma_{r,\max} L(1-\nu_m^2)}{\Delta E_m}$	$\frac{\sigma_{r\theta,\max} L(1-\nu_m^2)}{\Delta E_m}$
DNS	270.0	1.432e-2	0.1453	2.0492	1.0668
MNS	270.0	1.427e-2	0.1321	2.0493	1.0669
Error [%]	0.000	-0.3408	-9.097	0.0081	0.0078

Table 3.8 Comparisons in terms of local failure parameters at crack onset between direct and multiscale numerical simulations for global boundary conditions (b).

	θ_c (°)	Δ_c / H	l_c / d_f	$\frac{\sigma_{r,\max} L(1-\nu_m^2)}{\Delta E_m}$	$\frac{\sigma_{r\theta,\max} L(1-\nu_m^2)}{\Delta E_m}$
DNS	255.4	1.077e-2	0.1322	2.7213	1.1245
MNS	264.4	1.176e-2	0.1336	2.4830	1.2180
Error [%]	3.525	9.145	1.059	-8.759	-7.6799

interfacial crack onset point, the critical value of the prescribed displacement at onset $\Delta_c = \beta_c \Delta_{\text{ref}}$, the crack onset length l_c and the maximum values of interfacial stresses $\sigma_{r,\max}$ and $\sigma_{r\theta,\max}$. All failure parameters are given in dimensionless form.

4

An adaptive concurrent multiscale model for failure analyses of composite materials

As already stated in Section 2.2.3, concurrent multiscale methods abandon the concept of scale transition in favor of the concept of *scale embedding*, according to which models at different scales coexist in adjacent regions of the domain (see [207, 208] for recent implementations).

In the present chapter, a novel concurrent multiscale model able to perform complete failure analyses of fiber-reinforced composite materials is presented, by using a non-overlapping domain decomposition method in a finite element tearing and interconnecting (FETI) framework (see [57, 209]) in conjunction with an adaptive strategy able to continuously update the fine-scale

subdomain around a propagating macroscopic crack. When modeling fracture phenomena in composites, the competition between fiber/matrix interface debonding and kinking phenomena from and towards the matrix is accounted for, whereas the continuous matrix cracking is described by using a novel shape optimization strategy.

This chapter is outlined as follows: in Section 4.1 the theoretical background is presented; in Section 4.2 a set of numerical tools for describing microcrack propagation in composite materials is given; in Section 4.3 a detailed description of the proposed multiscale approach is provided, together with its implementation details; finally, Section 4.4 presents some numerical results obtained via the proposed method and their validation by means of comparisons with direct numerical simulations (DNS).

4.1 Theoretical framework

In the present section, the theoretical framework of the multiscale domain decomposition approaches is illustrated following [38]; these approaches are inspired by the (dual-primal) FETI-DP method, introduced by Farhat et al. [33], which belongs to the family of domain decomposition methods. For the sake of clarity, the formulation of the FETI-DP method is restricted to the case of linear elasticity problems.

4.1.1 Basics of the FETI-DP method

Let Ω denote the computational support of a two-dimensional structural problem, and $\{\Omega^s\}$ its decomposition into N_s non-overlapping subdomains denoted by $s = 1, \dots, N_s$. The stiffness matrix, the displacement vector and the force vector associated with Ω^s are denoted by $\mathbf{K}^s$, $\mathbf{u}^s$, and $\mathbf{f}^s$, respectively. After distinguishing the subdomain internal and boundary degrees of freedom (DOFs), denoted by the superscripts i and b, respectively, $\mathbf{K}^s$, $\mathbf{u}^s$, and $\mathbf{f}^s$ can be partitioned as follows:

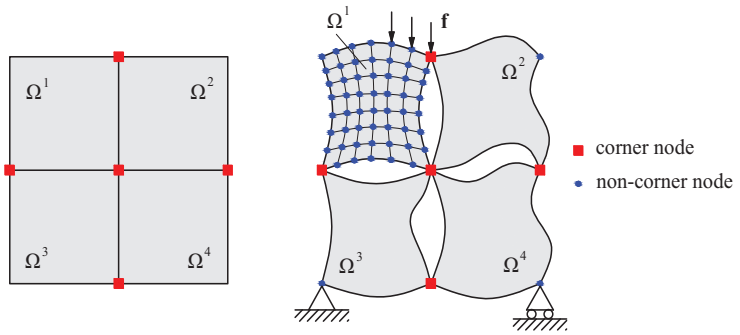

Fig. 4.1 Scheme of the FETI-DP method: (a) identification of corner nodes; (b) representation of the "tearing" step.

$$\mathbf{K}^s = \begin{bmatrix} \mathbf{K}^s_{ii} & \mathbf{K}^s_{ib} \\ \mathbf{K}^s_{bi} & \mathbf{K}^s_{bb} \end{bmatrix}, \quad \mathbf{u}^s = \begin{bmatrix} \mathbf{u}^s_i \\ \mathbf{u}^s_b \end{bmatrix}, \quad \mathbf{f}^s = \begin{bmatrix} \mathbf{f}^s_i \\ \mathbf{f}^s_b \end{bmatrix}. \tag{4.1}$$

Then, the "corners" of a mesh partition are identified as the nodes located at the ends of each edge of each subdomain, as shown in Fig. 4.1a; accordingly, the component $\mathbf{u}^s_b$ is partitioned as follows:

$$\mathbf{u}^s_b = \begin{bmatrix} \mathbf{u}^s_{b_r} \\ \mathbf{u}^s_{b_c} \end{bmatrix}, \tag{4.2}$$

where the subscripts c and r denote the DOFs attached to the corners and the remainder of the boundary DOFs, respectively. Corners are mesh nodes whose DOFs remain primal variables; the direct mechanical interpretation of this assumption is a mesh splitting performed by making incisions but leaving the corner points attached. This is the "tearing" step of classical FETI methods (see Fig. 4.1b); the "interconnecting step" occurs only on the interfaces excluding the corner points.

In other words, the domain decomposition method is formulated such that the solution at the corner points is continuous; thus, the corner unknowns are

defined at the global level, whereas all other displacement unknowns are defined at the subdomain level. For this purpose, the global vector of DOFs, denoted by $\mathbf{u}$, is partitioned as follows

$$\mathbf{u} = \begin{bmatrix} \mathbf{u}_r \\ \mathbf{u}_c \end{bmatrix} = \begin{bmatrix} \mathbf{u}_r^1 \\ \vdots \\ \mathbf{u}_r^{N_s} \\ \mathbf{u}_c \end{bmatrix}, \tag{4.3}$$

where $\mathbf{u}_r^s$ is the remaining subdomain solution vector and $\mathbf{u}_c$ is a global/primal solution vector containing all defined corner DOFs. Using this notation, the subdomain stiffness matrix can be split as:

$$\mathbf{K}^s = \begin{bmatrix} \mathbf{K}_{rr}^s & \mathbf{K}_{rc}^s \\ \mathbf{K}_{rc}^{s\mathrm{T}} & K_{cc}^s \end{bmatrix}. \tag{4.4}$$

Then, the FETI-DP equilibrium equation can be written using the following matrix partitioning:

$$\begin{bmatrix} \mathbf{K}_{rr}^1 & \cdots & \mathbf{0} & \mathbf{K}_{rc}^1 \mathbf{L}_c^1 \\ \vdots & \ddots & \vdots & \vdots \\ \mathbf{0} & \cdots & \mathbf{K}_{rr}^{N_s} & \mathbf{K}_{rc}^{N_s} \mathbf{L}_c^{N_s} \\ \mathbf{L}_c^{1\mathrm{T}} \mathbf{K}_{rc}^{1\mathrm{T}} & \cdots & \mathbf{L}_c^{N_s\mathrm{T}} \mathbf{K}_{rc}^{N_s\mathrm{T}} & \sum_{s=1}^{N_s} \mathbf{L}_c^{s\mathrm{T}} \mathbf{K}_{cc}^s \mathbf{L}_c^s \end{bmatrix} \begin{bmatrix} \mathbf{u}_r^1 \\ \vdots \\ \mathbf{u}_r^{N_s} \\ \mathbf{u}_c \end{bmatrix} = \begin{bmatrix} \mathbf{f}_r^1 - \mathbf{B}_r^{1\mathrm{T}} \boldsymbol{\lambda} \\ \vdots \\ \mathbf{f}_r^{N_s} - \mathbf{B}_r^{N_s\mathrm{T}} \boldsymbol{\lambda} \\ \sum_{s=1}^{N_s} \mathbf{L}_c^{s\mathrm{T}} \mathbf{f}_c^s \end{bmatrix}, \tag{4.5}$$

where the corner stiffness matrix $\mathbf{K}_{cc} = \sum_{s=1}^{N_s} \mathbf{L}_c^{s\mathrm{T}} \mathbf{K}_{cc}^s \mathbf{L}_c^s$ is a global stiffness quantity, $\mathbf{f}_r^s$ is the external force acting on the rth DOF, and $\boldsymbol{\lambda}$ are the Lagrange multipliers on the global interface, introduced to enforce the interface continuity condition:

$$\sum_{s=1}^{N_s} \mathbf{B}_r^s \mathbf{u}_r^s = \mathbf{0}. \tag{4.6}$$

In Eq. (4.5), $\mathbf{L}_c^s$ are localization matrices able to extract the corner DOFs $\mathbf{u}_c^s$ of each subdomain from the global vector of corner DOFs, i.e. $\mathbf{L}_c^s \mathbf{u}_c = \mathbf{u}_{b_c}^s$, and $\mathbf{B}_r^s$ are signed Boolean matrices able to extract the non-corner DOFs of each subdomain belonging to the interfaces:

$$\mathbf{B}_r^s \mathbf{u}_r^s = \pm \mathbf{u}_{b_r}^s \quad \text{for } s = 1, \ldots, N_s, \tag{4.7}$$

where the sign of this equality is determined by a suitable convention. It is worth noting that the choice of corner nodes must be made so that the matrix $\mathbf{K}_{rr}^s$ is guaranteed to be nonsingular.

Hence, from Eq. (4.5) it follows that

$$\mathbf{u}_r^s = \mathbf{K}_{rr}^{s^{-1}} \left(\mathbf{f}_r^s - \mathbf{B}_r^{s^{\mathrm{T}}} \boldsymbol{\lambda} - \mathbf{K}_{rc}^s \mathbf{L}_c^s \mathbf{u}_c \right) \quad \text{for } s = 1, \ldots, N_s. \tag{4.8}$$

Then, Eq. (4.8) is substituted into Eqs. (4.5) and (4.6), and the following dual-primal problem is obtained after some algebraic manipulations aimed at eliminating $\mathbf{u}_r^s$:

$$\begin{bmatrix} \mathbf{F}_{I_{rr}} & \mathbf{F}_{I_{rc}} \\ \mathbf{F}_{I_{rc}}^T & -\mathbf{K}_{cc}^* \end{bmatrix} \begin{bmatrix} \boldsymbol{\lambda} \\ \mathbf{u}_c \end{bmatrix} = \begin{bmatrix} \mathbf{d}_r \\ -\mathbf{f}_c^* \end{bmatrix}, \tag{4.9}$$

where:

$$\begin{aligned} \mathbf{F}_{I_{rr}} &= \sum_{s=1}^{N_s} \mathbf{B}_r^s \mathbf{K}_{rr}^{s^{-1}} \mathbf{B}_r^{s^{\mathrm{T}}}, \quad & \mathbf{F}_{I_{rc}} &= \sum_{s=1}^{N_s} \mathbf{B}_r^s \mathbf{K}_{rr}^{s^{-1}} \mathbf{K}_{rc}^s \mathbf{L}_c^s \\ \mathbf{d}_r &= \sum_{s=1}^{N_s} \mathbf{B}_r^s \mathbf{K}_{rr}^{s^{-1}} \mathbf{f}_r^s, & \mathbf{f}_c^* &= \sum_{s=1}^{N_s} \mathbf{L}_c^{s^{\mathrm{T}}} \left(\mathbf{f}_c^s - \mathbf{K}_{rc}^{s^{\mathrm{T}}} \mathbf{K}_{rr}^{s^{-1}} \mathbf{f}_r^s \right) \\ \mathbf{K}_{cc}^* &= \mathbf{K}_{cc} - \sum_{s=1}^{N_s} (\mathbf{K}_{rc}^s \mathbf{L}_c^s)^{\mathrm{T}} \mathbf{K}_{rr}^{s^{-1}} (\mathbf{K}_{rc}^s \mathbf{L}_c^s). \end{aligned} \tag{4.10}$$

By condensing $\mathbf{u}_c$ in Eq. (4.9), the following symmetric positive definite dual interface problem is obtained:

$$\mathbf{F}_I \lambda = \mathbf{D}_r \tag{4.11}$$

with

$$\begin{aligned} \mathbf{F}_I &= \mathbf{F}_{I_{rr}} + \mathbf{F}_{I_{rc}} \mathbf{K}_{cc}^{*^{-1}} \mathbf{F}_{I_{rc}}^T \\ \mathbf{D}_r &= \mathbf{d}_r - \mathbf{F}_{I_{rc}} \mathbf{K}_{cc}^{*^{-1}} \mathbf{f}_c^* . \end{aligned} \tag{4.12}$$

The interface problem (4.11) is usually not solved by a direct method, since assembling the matrix $\mathbf{F}_I$ and the vector $\mathbf{D}_r$ can require huge storage and computational resources for large-scale problems; therefore, the FETI-DP method can be regarded as the transformation of the original problem $\mathbf{Ku} = \mathbf{f}$ into the interface problem (4.11) to be solved by an iterative method, like a preconditioned conjugate gradient (PCG) algorithm.

4.1.2 Formulation of the multiscale domain decomposition method for cracked composite materials

Consider the mechanical problem of a cracked composite structure, occupying the open set $\Omega \subset \mathbb{R}^3$, shown in Fig. 4.2a; its boundary $\partial\Omega = \partial_t\Omega \cup \partial_u\Omega$ is supposed to be Lipschitz continuous such that $\partial_t\Omega \cap \partial_u\Omega = \varnothing$ and the measure of $\partial_u\Omega$ is greater than zero to avoid rigid-body motions. Such heterogeneous structure is composed of periodically arranged cells, whose microstructure is the same as in the reference cell (*repeating unit cell* or RUC), whereas its microconstituents are made of linearly hyperelastic materials. The given crack configuration K is modeled as a finite set of physical surfaces, denoted by $\Gamma_c^{(i)}$ ($i = 1, \ldots, n$), where the displacement field becomes discontinuous. Such a problem, under the hypotheses of small displacements and quasistatic loading, can be mathematically formulated by means of a classical elliptic PDE system with associated boundary conditions:

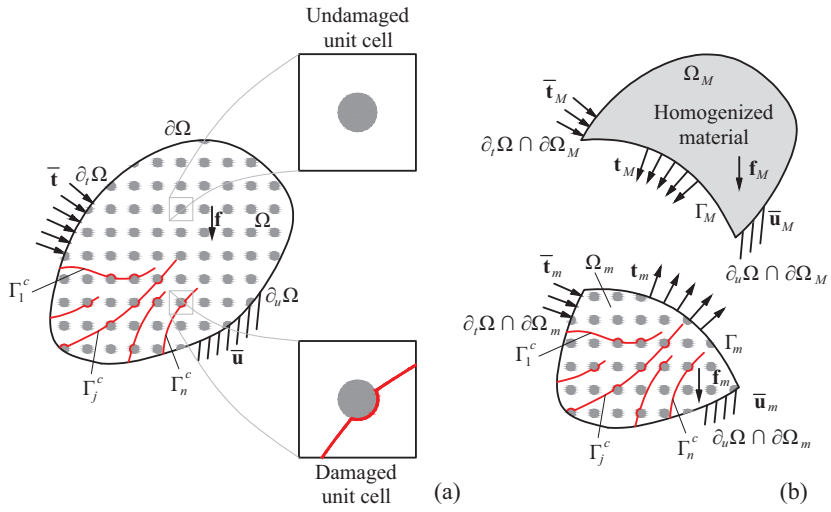

Fig. 4.2 Boundary value problem for a cracked periodic composite structure: (a) identification of damaged and undamaged unit cells; (b) domain decomposition into subdomains described at different resolutions.

$$\begin{cases} -\nabla \cdot \left(\mathbb{C}(\mathbf{x}) : (\nabla \otimes_s \mathbf{u}) \right) = \mathbf{f} & \text{in } \Omega \\ \mathbf{u} = \overline{\mathbf{u}} & \text{on } \partial_u \Omega \\ \left(\mathbb{C}(\mathbf{x}) : (\nabla \otimes_s \mathbf{u}) \right) \cdot \mathbf{n} = \overline{\mathbf{t}} & \text{on } \partial_t \Omega \end{cases} \tag{4.13}$$

where the vector functions $\mathbf{f}$ and $\overline{\mathbf{t}}$ denote the prescribed body forces and tractions, respectively, $\overline{\mathbf{u}}$ is the prescribed displacement, and $\mathbb{C}$ is the elasticity tensor, supposed to be rapidly varying over the macroscopic variable $\mathbf{x}$.

The elastic problem, whose solution is guaranteed to be unique by the assumption of strictly convex strain energy densities, becomes rather complex to solve, if no suitable modeling strategies are pursued. However, in the presence of microcracks (or, in general, microscopic defects) subjected to propagation and coalescence phenomena, classical homogenization approaches cannot be applied, because the assumption of periodicity ceases to hold, and thus alternative methods have to be necessarily introduced.

In the following, a concurrent multiscale strategy is adopted, based on a domain decomposition method. The main feature of this approach is to decompose the original problem into smaller and more manageable different sub-problems to be solved simultaneously. This is possible by partitioning Ω into two sets Ω_M and Ω_m of non-overlapping subdomains, as depicted in Fig. 4.2b. The tensor $\mathbb{C}$ is supposed to be periodic only in Ω_M, whereas no assumptions about periodicity are made in Ω_m, therefore it follows:

$$\mathbb{C}(\mathbf{x}) = \begin{cases} \mathbb{C}_M^{\varepsilon}(\mathbf{x}), & \mathbf{x} \in \Omega_M \\ \mathbb{C}_m(\mathbf{x}), & \mathbf{x} \in \Omega_m \end{cases} \tag{4.14}$$

where the superscript ε highlights the dependence on a small period, which is the RUC size. After defining the so-called "fast variable" $\mathbf{y} := \mathbf{x}/\varepsilon$, the component of the $\mathbb{C}_M^{\varepsilon}$ can be obtained by extending those of the tensor $\widetilde{\mathbb{C}} = \widetilde{\mathbb{C}}(\mathbf{y})$, defined over the reference cell, periodically to Ω_M.

In this context, the problem (4.13) can be easily reformulated in an equivalent multi-domain form, composed of two coupled sub-problems:

$$\begin{cases} -\nabla \cdot \left(\mathbb{C}_M^{\varepsilon}(\mathbf{x}) : (\nabla \otimes_s \mathbf{u}_M^{\varepsilon})\right) = \mathbf{f}_M & \text{in } \Omega_M \\ \mathbf{u}_M^{\varepsilon} = \overline{\mathbf{u}}_M & \text{on } \partial_u \Omega_M \\ \left(\mathbb{C}_M^{\varepsilon}(\mathbf{x}) : (\nabla \otimes_s \mathbf{u}_M^{\varepsilon})\right) \cdot \mathbf{n}_M = \overline{\mathbf{t}}_M & \text{on } \partial_t \Omega_M \\ \mathbf{u}_M^{\varepsilon} = \mathbf{u}_m & \text{on } \Gamma_M \\ \left(\mathbb{C}_M^{\varepsilon} : (\nabla \otimes_s \mathbf{u}_M^{\varepsilon})\right) \cdot \mathbf{n}_M = \left(\mathbb{C}_m : (\nabla \otimes_s \mathbf{u}_m)\right) \cdot \mathbf{n}_m & \text{on } \Gamma_M \end{cases} \tag{4.15}$$

$$\begin{cases} -\nabla \cdot \left(\mathbb{C}_m(\mathbf{x}) : (\nabla \otimes_s \mathbf{u}_m)\right) = \mathbf{f}_m & \text{in } \Omega_m \\ \mathbf{u}_m = \overline{\mathbf{u}}_m & \text{on } \partial_u \Omega_m \\ \left(\mathbb{C}_m^{\varepsilon} : (\nabla \otimes_s \mathbf{u}_m^{\varepsilon})\right) \cdot \mathbf{n}_m = \overline{\mathbf{t}}_m & \text{on } \partial_t \Omega_m \\ \mathbf{u}_m = \mathbf{u}_M^{\varepsilon} & \text{on } \Gamma_m \\ \left(\mathbb{C}_m : (\nabla \otimes_s \mathbf{u}_m)\right) \cdot \mathbf{n}_m = \left(\mathbb{C}_M^{\varepsilon} : (\nabla \otimes_s \mathbf{u}_M^{\varepsilon})\right) \cdot \mathbf{n}_M & \text{on } \Gamma_m \end{cases} \tag{4.16}$$

where $\partial_u\Omega_M = \partial_u\Omega \cap \partial\Omega_M$, $\partial_t\Omega_M = \partial_t\Omega \cap \partial\Omega_M$, $\partial_u\Omega_m = \partial_u\Omega \cap \partial\Omega_m$ and $\partial_t\Omega_m = \partial_t\Omega \cap \partial\Omega_m$, the interfaces Γ_M and Γ_m are the additional boundaries generated by the partition of the original domain. The first sub-problem defined over Ω_M, where the assumption of periodicity is still valid, can be solved by considering the following asymptotic expansion of $\mathbf{u}_M^\varepsilon(\mathbf{x})$:

$$\mathbf{u}_M(\mathbf{x},\mathbf{y}) = \mathbf{u}_{M,0}(\mathbf{x},\mathbf{y}) + \varepsilon\mathbf{u}_{M,1}(\mathbf{x},\mathbf{y}) + \varepsilon^2\mathbf{u}_{M,2}(\mathbf{x},\mathbf{y}) + O\left(\varepsilon^3\right), \quad (4.17)$$

where $\mathbf{u}_{M,i}$ are periodic functions in $\mathbf{y}$. As already discussed in Section 2.1.2, a classical result in homogenization theory is that $\mathbf{u}_{M,0}$ depends only on $\mathbf{x}$; thus the original microstructure can be replaced by an equivalent homogenized material and Eq. (4.15) becomes:

$$\begin{cases} -\nabla\cdot\left(\overline{\mathbb{C}}(\mathbf{x}) : (\nabla \otimes_s \mathbf{u}_M)\right) = \mathbf{f}_M & \text{in } \Omega_M \\ \mathbf{u}_M^\varepsilon = \overline{\mathbf{u}}_M & \text{on } \partial_u\Omega_M \\ \left(\overline{\mathbb{C}}(\mathbf{x}) : (\nabla \otimes_s \mathbf{u}_M)\right)\cdot\mathbf{n}_M = \overline{\mathbf{t}}_M & \text{on } \partial_t\Omega_M \\ \mathbf{u}_M = \mathbf{u}_m & \text{on } \Gamma_M \\ \left(\overline{\mathbb{C}}(\mathbf{x}) : (\nabla \otimes_s \mathbf{u}_M)\right)\cdot\mathbf{n}_M = \left(\mathbb{C}_m^\varepsilon : (\nabla \otimes_s \mathbf{u}_m^\varepsilon)\right)\cdot\mathbf{n}_m & \text{on } \Gamma_M \end{cases} \quad (4.18)$$

where the subscript 0 has been omitted for the sake of simplicity. As already stated in Section 2.1.2.3, the tensor $\overline{\mathbb{C}} = \left(\overline{C}_{ijhk}\right)$ of homogenized (*effective*) moduli is given by:

$$\overline{C}_{ijhk} = \frac{1}{|Y|}\int_Y \left(\tilde{C}_{ijhk} + \tilde{C}_{ijlm}\frac{\partial\chi_l^{hk}}{\partial y_m}\right) \mathrm{d}Y, \quad (4.19)$$

where C_{ijhk} are the moduli corresponding to the different constituents of the microstructure and the periodic functions χ^{hk} represent the characteristic displacements of the RUC.

An inherent scale separation exists between the two sets Ω_M and Ω_m, as suggested by the use of subscripts M and m, which stand for macroscopic and microscopic, respectively; as a consequence, when numerically solving the

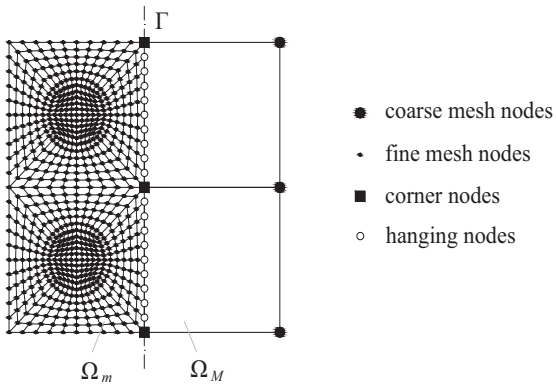

Fig. 4.3 Nonmatching meshes at the micro-macro interface.

coupled sub-problems (4.16) and (4.18), Ω_M is identified as the region where a coarse scale resolution is sufficient, unlike Ω_m which requires a fine discretization.

4.1.3 Micro-macro connection within a finite element framework

A proper multilevel domain decomposition method should account for two main aspects: (i) the connection between the fine and coarse meshes at the micro-macro interface, and (ii) the choice of the so-called *zone of interest* where to perform the zoom-in procedure. The aspect (i) is discussed in the following, whereas the aspect (ii) will be presented in Section 4.3, which describes an adaptive strategy for updating the zoomed zones of interest "on the fly" during the analysis.

When applied in a 2D finite element setting, the above-described multilevel domain decomposition method is characterized by the presence of nonconforming meshes at the double-sided interface $\Gamma = \Gamma_M \cup \Gamma_m$. Since linear shape functions have been chosen for both coarse and fine resolutions, in this work a coarse element interface shares only two nodes with the corresponding fine subdomain interface, as shown in Fig. 4.3. These nodes, referred to as *corner nodes*, define two collections of single-sided interfaces $\Gamma_{M,i}$ and $\Gamma_{m,i}$

($i = 1, \ldots, n_\Gamma$) such that $\Gamma_M = \bigcup_{i=1}^{n_\Gamma} \Gamma_{M,i}$ and $\Gamma_m = \bigcup_{i=1}^{n_\Gamma} \Gamma_{m,i}$, whereas the nonmatching nodes are called *hanging nodes*.

In the spirit of FETI-DP approach, the displacement continuity at corner nodes is enforced pointwise by using a primal method, whereas a dual method is applied to enforce compatibility at the hanging nodes, based on the following weak formulation at $\Gamma_i = \Gamma_{M,i} \cup \Gamma_{m,i}$:

$$\int_{\Gamma_i} \mathbf{w}\left(x^{(i)}\right) \cdot \left(\mathbf{u}_m\left(x^{(i)}\right) - \mathbf{u}_M\left(x^{(i)}\right)\right) \mathrm{d}x^{(i)} = 0, \tag{4.20}$$

where $x^{(i)}$ is a local abscissa on Γ_i and $\mathbf{w}$ represents a weigh function acting as a field of Lagrange multipliers, which can be differently chosen leading to different types of micro-macro connection.

4.1.3.1 Strong coupling by collocation method

The simplest choice for $\mathbf{w}$ in Eq. (4.20) consists of a linear combination of Dirac delta functions centered in all the nonmatching nodes belonging to the fine mesh side of the interface Γ_i:

$$\mathbf{w}\left(x^{(i)}\right) = \sum_{j=1}^{n_h} \boldsymbol{\lambda}_j^{(i)} \delta\left(x^{(i)} - x_j^{(i)}\right), \tag{4.21}$$

where n_h is the number of hanging nodes (taken as a constant for all the interfaces) and $\boldsymbol{\lambda}_j^{(i)}$ is the two-component Lagrange multiplier vector representing the unknown force at node j of Γ_i; if the hanging nodes are equally spaced along the interface, taking into account Eq. (4.21), the weak constraint (4.20) can be rewritten as follows:

$$\sum_{j=1}^{n_h} \boldsymbol{\lambda}_j^{(i)} \cdot \left(\mathbf{u}_m\left(x_j^{(i)}\right) - \mathbf{u}_M\left(x_j^{(i)}\right)\right) = 0. \tag{4.22}$$

This approach, commonly referred to as *collocation method*, enforces the equality between the displacement field of the fine side and the interpolation

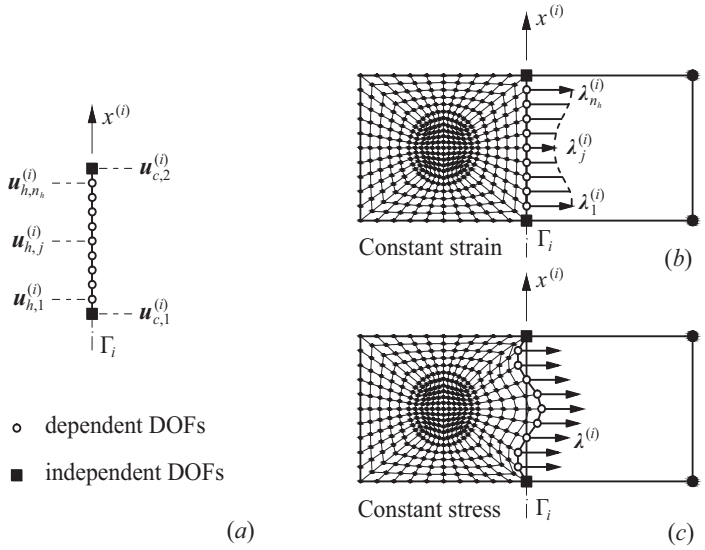

Fig. 4.4 Micro-macro connection in the FETI-DP setting: (a) identification of corner (independent) and hanging (dependent) DOFs; (b) strong coupling by collocation method; (c) weak coupling by mortar method.

of the coarse displacement field at the location of the interior interface nodes, leading to the following set of $2n_h$ equations for each interface Γ_i:

$$\mathbf{u}_m\left(x_j^{(i)}\right) = \mathbf{u}_M\left(x_j^{(i)}\right) \quad \text{for } j = 1 \text{ to } n_h. \tag{4.23}$$

After introducing the displacement vectors $\mathbf{u}_c^{(i)}$ and $\mathbf{u}_h^{(i)}$ for corner and hanging nodes, respectively, the compatibility equation (4.23) can be expressed as a set of linear multipoint constraints (LMPCs) admitting the following matrix representation (see Fig. 4.4a):

$$\mathbf{u}_h^{(i)} = \mathbf{B}^{(i)}\mathbf{u}_c^{(i)}. \tag{4.24}$$

In Eq. (4.24), $\mathbf{B}^{(i)}$, referred to as *interpolation matrix*, is the $2n_h \times 4$ matrix of shape function values on the coarse side at the location of the fine mesh nodes:

$$\mathbf{B}^{(i)} = \begin{bmatrix} \mathbf{N}\left(x_1^{(i)}\right) \\ \vdots \\ \mathbf{N}\left(x_{n_h}^{(i)}\right) \end{bmatrix} \tag{4.25}$$

with

$$\mathbf{N}\left(x_j^{(i)}\right) = \begin{bmatrix} N_1\left(x_j^{(i)}\right) & 0 & N_2\left(x_j^{(i)}\right) & 0 \\ 0 & N_1\left(x_j^{(i)}\right) & 0 & N_2\left(x_j^{(i)}\right) \end{bmatrix}, \tag{4.26}$$

where N_1 and N_2 are the linear shape functions for the corner nodes.

4.1.3.2 Weak coupling by mortar method

The *mortar method* [192, 210] is a general approach to enforce the compatibility condition in an average sense, based on the weak formulation (4.20) for a variety of continuous weight functions **w**. In the following the weight functions are set to be constant, coherently with the choice of linear shape functions; in this case the displacement fields on the two sides of the interface Γ_i satisfy the following constraint:

$$\lambda^{(i)} \cdot \int_{\Gamma_i} \left(\mathbf{u}_m\left(x^{(i)}\right) - \mathbf{u}_M\left(x^{(i)}\right) \right) \mathrm{d}x^{(i)} = 0, \tag{4.27}$$

where $\lambda^{(i)}$ plays the role of a Lagrange multiplier, as in the collocation method.

Once the continuous displacement field $\mathbf{u}_m\left(x^{(i)}\right)$ has been interpolated by means of the matrix $\mathbf{B}^{(i)}$, defined by Eq. (4.25), the same discretization is employed for both sides of the interface; therefore a unique piecewise linear shape function matrix $\widetilde{\mathbf{N}}\left(x^{(i)}\right)$ can approximate $\mathbf{u}_m\left(x^{(i)}\right)$ and $\mathbf{u}_M\left(x^{(i)}\right)$:

$$\begin{aligned} \mathbf{u}_m\left(x^{(i)}\right) &= \widetilde{\mathbf{N}}\left(x^{(i)}\right)\mathbf{u}_h^{(i)} \\ \mathbf{u}_M\left(x^{(i)}\right) &= \widetilde{\mathbf{N}}\left(x^{(i)}\right)\mathbf{B}^{(i)}\mathbf{u}_c^{(i)}. \end{aligned} \tag{4.28}$$

By substituting Eq. (4.28) in Eq. (4.27), the following equation can be obtained:

$$\lambda^{(i)} \cdot \underbrace{\int_{\Gamma_i} \widetilde{\mathbf{N}}\left(x^{(i)}\right) \mathrm{d}x^{(i)}}_{\mathbf{H}^{(i)}} \left(\mathbf{u}_h^{(i)} - \mathbf{B}^{(i)}\mathbf{u}_c^{(i)}\right) = 0, \tag{4.29}$$

where $\mathbf{H}^{(i)}$ is a $2 \times 2n_h$ matrix containing the integral of the shape functions over Γ_i.

As a consequence the relationships between the DOFs on the two sides of the interface can be cast in a matrix form:

$$\mathbf{H}^{(i)}\mathbf{u}_h^{(i)} = \mathbf{H}^{(i)}\mathbf{B}^{(i)}\mathbf{u}_c^{(i)}, \tag{4.30}$$

representing a system of two linear equations for each micro-macro interface. Moreover, for equally spaced hanging nodes, Eq. (4.30) is equivalent to the following relation:

$$\sum_{j=1}^{n_h} \left(\mathbf{u}_{h,j}^{(i)} - \mathbf{N}\left(x_j^{(i)}\right)\mathbf{u}_c^{(i)}\right) = \mathbf{0}, \tag{4.31}$$

where $\mathbf{u}_{h,j}^{(i)}$ is the displacement vector of the jth hanging node of Γ_i.

It is worth noting that the average compatibility conditions (4.30) and (4.31) involve a lower number of LMPCs than the pointwise constraint enforced by collocation, leading to a reduction of the computational cost in solving the interface problem.

4.1.3.3 Similarities with microscopic BCs in classical homogenization

As argued in [207], a parallelism can be established between the set of LMPCs involved in collocation and mortar methods, and two alternative types of boundary conditions commonly prescribed on the RVE in classical homogenization, i.e. (i) linear displacements and (ii) uniform tractions, respectively. In other words the micro-macro connection between nonmatching meshes leads to define locality constraints on the difference:

$$\mathbf{u}_m\left(x^{(i)}\right) - \mathbf{u}_M\left(x^{(i)}\right) \tag{4.32}$$

appearing in Eq. (4.20), interpreted as the microscopic fluctuation of classical homogenization approaches, due to the linear nature of $\mathbf{u}_M\left(x^{(i)}\right)$.

The collocation method is firstly considered; the constraint expressed by Eq. (4.23) is equivalent to the assumption of zero microscopic fluctuation on the subdomain boundary in a pointwise sense; indeed the distributions of the microscopic displacement and strain become linear and constant, respectively, along the micro-macro interface (see Fig. 4.4b), coherently with the strain approach, which assumes linear displacements on the RVE's boundaries.

On the other hand, the set of LMPCs involved in Eq. (4.27), enforced by the mortar method, is equivalent to the assumption of zero microscopic fluctuation in an average sense; indeed the non-corner boundary DOFs, which can be different from zero, are associated to a constant distribution of Lagrange multipliers (see Fig. 4.4c). Therefore, there are some analogies with the so-called *stress approach*, according to which uniform tractions are applied on the RVE's boundaries.

4.2 Modeling strategies of microcrack propagation in composite materials

The multiscale model presented in this chapter is devoted to the failure analysis of composite materials, essentially due to microcrack propagation phenomena. Under transverse loading, crack growth can be properly studied by using simplified 2D models, in which the allowed damage mechanisms are essentially the matrix cracking, the interfacial debonding, and the crack kinking/deflection phenomena towards and from the interface. Fiber splitting is not considered, because the related fracture energy is supposed to be several orders of magnitude larger than the fracture energy of both the matrix and the material interfaces.

In the following only the case of a single propagating crack is treated, but it is rather straightforward to provide an extension to the case of multiple crack propagation. As in the method presented in Section 3.3.2.1, crack propagation is modeled by applying incremental geometric topological changes to the current crack configuration, thus also in this case an automatic remeshing procedure is required. Crack propagation is driven by the classical Griffith criterion, and a crack control length scheme is adopted, in order to deal with unstable behaviors (see Section 3.2.2).

Only matrix crack propagation and crack deflection toward an interface are discussed in the following; the discussions about the interface crack propagation and the kinking out of an interface have already been presented in Sections 3.2.2.1 and 3.2.2.2, respectively.

4.2.1 Matrix crack propagation in an ALE setting

Numerical computations presented in Chapter 3 have been shown that when the crack path is not known *a priori*, such a technique may become highly time consuming, because the application of the maximum energy release rate criterion requires a (global or local) remeshing for each trial crack direction (see, for instance, [211]).

In order to reduce the computational cost, a novel methodology able to provide the actual crack direction (expressed in terms of kinking angle) is proposed. Firstly, the maximum energy release criterion is recast in a variational setting, by considering the following expression of $\mathcal{G}$, as a function of both the crack length l and the kinking angle θ (describing the crack direction):

$$\mathcal{G}(l,\theta) = -\Pi^*_{,l}(l,\theta) \approx -\frac{\Pi^*(l+\Delta l,\theta) - \Pi^*(l)}{\Delta l}, \tag{4.33}$$

where Δl is the crack length increment, chosen to be much smaller than l, and Π^* denotes the total potential energy at equilibrium:

$$\Pi^*(l) = \Pi(\mathbf{u}(l), l) = \inf_{\mathbf{u}\in U_a(l)} \Pi(\mathbf{u}, l). \tag{4.34}$$

In Eq. (4.34) U_a represents the set of admissible displacements:

$$U_a = \left\{ \mathbf{u} |\ \mathbf{u} \cdot \mathbf{n} \geq 0 \quad \forall \mathbf{x} \in \Omega, \quad \mathbf{u} = \overline{\mathbf{u}}, \quad \forall \mathbf{x} \in \partial_u \Omega \right\}, \tag{4.35}$$

where $\mathbf{u} \cdot \mathbf{n}$ denotes the normal component of the displacement jump, supposed to be nonnegative due to the enforced condition of frictionless unilateral contact.

By using Eqs. (4.33) and (4.34), the maximization of the energy release rate can be enforced as a double minimization of Π with respect to both the displacement field and the crack direction:

$$\sup_{\theta} \mathcal{G}(l, \theta) \Longrightarrow \inf_{\theta} \left[\inf_{\mathbf{u} \in U_a(l + \Delta l, \theta)} \Pi(\mathbf{u}, l + \Delta l, \theta) \right], \tag{4.36}$$

which is performed by using a moving mesh approach, similarly to other works, as [58] or [59]. The main feature of the proposed method is that a classical remeshing and an *r*-adaptation are performed in an alternating sequence, able to account for the crack advance and to provide the actual crack direction according to the maximum energy release rate criterion, respectively.

The crack update performed during the searching procedure for the crack direction, is accomplished by relocating nodes, without any changes in the mesh topology. This technique relies on the Arbitrary Lagrangian-Eulerian (ALE, in short) description [212], developed to achieve the advantages of the two classical kinematical descriptions. In the ALE setting, neither the material configuration Ω_X nor the spatial configuration Ω_x is taken as the reference. Thus, a third domain has to be introduced, i.e. the referential configuration Ω_χ, whose points are identified by the referential coordinates χ, as depicted in Fig. 4.5. The (current) material coordinates $\mathbf{X}$ are mapped onto the (current) spatial coordinates $\mathbf{x}$ through the well-known deformation map $\boldsymbol{\varphi}$:

$$\boldsymbol{\varphi} : \Omega_X \to \Omega_x, \quad \mathbf{x} = \boldsymbol{\varphi}(\mathbf{X}), \tag{4.37}$$

defining the (physical) displacement field as $\mathbf{u} = \mathbf{x} - \mathbf{X}$.

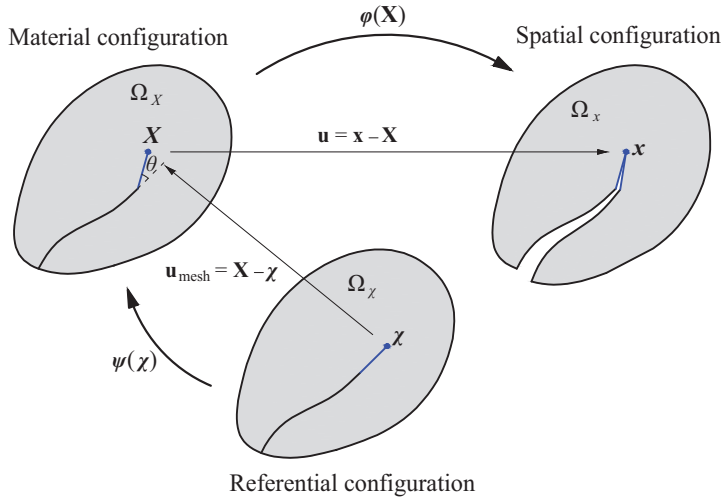

Fig. 4.5 ALE description for matrix crack propagation by shape optimization.

On the other hand, the mapping $\boldsymbol{\psi}$ of the referential coordinates $\boldsymbol{\chi}$ (describing the body configuration before the crack reorientation) onto the (current) material coordinates $\mathbf{X}$ is:

$$\boldsymbol{\psi} : \Omega_{\chi} \rightarrow \Omega_{X}, \quad \mathbf{X} = \boldsymbol{\psi}(\boldsymbol{\chi}), \tag{4.38}$$

corresponding to the mesh displacement field $\mathbf{u}_{\text{mesh}} = \mathbf{X} - \boldsymbol{\chi}$; this mapping represents a structural change, which, in the context of this work, consists in the (finite) rotation θ of the small kink emanated from the current crack tip, computed with respect to the direction of the crack prior to the current extension; during this transformation, the mesh nodes are moved in order to follow such shape modification, which is not induced from physics. Indeed, the computational nodes may be arbitrarily moved by decoupling them from the material points, in order to give a continuous rezoning capability.

In the present work, such rezoning is performed by means of an elliptic mesh generation, i.e. by solving a Laplace equation for each component of the mesh displacement, allowing to avoid excessive element distortions and to prevent mesh entanglement phenomena:

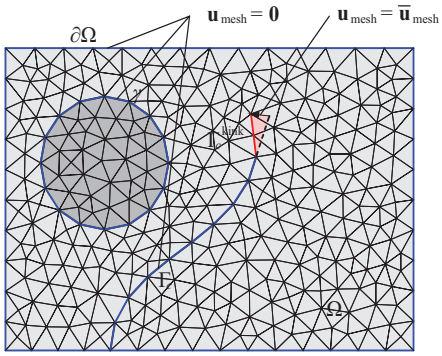

Fig. 4.6 Computational domain and boundary conditions for the moving mesh.

$$\nabla_\chi \cdot \nabla_\chi \mathbf{u}_{\text{mesh}} = \mathbf{0}, \tag{4.39}$$

where $\nabla_\chi \cdot \nabla_\chi$ denotes the vector Laplacian with respect to χ.

Suitable constraint conditions on the relative motion between referential and material configurations have to be imposed on the computational grid; since the shape of both the body and the current crack cannot change during the searching for the crack direction, zero displacement boundary conditions have to be enforced everywhere, except for a small kinked boundary Γ_c^{kink}, subjected to a prescribed rotation θ around the old tip position (see Fig. 4.6):

$$\begin{aligned} \mathbf{u}_{\text{mesh}} &= \mathbf{X} - \chi = \mathbf{0} && \text{on } \partial\Omega \cup \gamma \cup \Gamma_c \\ \mathbf{u}_{\text{mesh}} &= \mathbf{X} - \chi = \overline{\mathbf{u}}_{\text{mesh}}(\theta) && \text{on } \Gamma_c^{\text{kink}} \end{aligned} \tag{4.40}$$

where $\partial\Omega$ denotes the external boundaries, γ is the union of the material interfaces in Ω, and Γ_c denotes the fixed portion of the crack set. During its motion, the length of the kinked crack does not change.

It is worth noting that the moving mesh can be defined, as in the present work, only on a subdomain enclosing the crack tip (also referred to as transition zone), chosen to be small enough to reduce the number of the unknown mesh displacements and sufficiently large to make the mesh regularization as efficient as possible.

For each value l of the crack length, the minimization problem (4.36) have to be solved by adopting a loop-in-loop algorithm, in which two nested optimizations are performed: in the inner loop, the boundary value problem associated to the minimization of Π with respect to u at fixed θ is solved, in order to find the equilibrated solution for a given crack configuration (this problem may require an iterative solution method also in linear elasticity, because contact phenomena may arise between the crack faces, leading to a nonlinear structural response); in the outer loop, needed to find the actual crack direction, the energy minimization is performed with respect to a single variable, i.e. the kinking angle θ, and only a one-dimensional optimization algorithm is required. In this scheme, the potential energy for each trial value of θ is always computed from equilibrated displacement fields. Such a scheme seems to be more efficient than the approaches proposed in [58] or [59], according to which all the nodal coordinates $\mathbf{X}$ are regarded as control variables during the search for the optimal shape configuration.

4.2.2 Deflection of a matrix crack towards an interface

During its propagation within the matrix, a transverse crack may interact with the fibers in different ways: if inclusions are stiffer than the matrix (this is the most common case for fiber-reinforced composites, also referred to as *weak singularity* case), the crack may be deflected away from the interface, experiencing at the same time a crack arrest event. This is a well-known phenomenon due to vanishing behavior of the energy release rate at fixed external load as the crack approaches an interface; many works have been addressed to solve the problem of a finite or semi-infinite crack perpendicular to an interface at a small distance from it, subjected to a remote tensile loading, by using both analytical and numerical approaches (see, for instance, [213, 214]).

On the other hand, as the tip singularity propagates near the interface, increasing values of the interfacial stresses are induced, as sketched in Fig. 4.7a, leading to the nucleation of an interfacial crack; this mechanism, which appears to be coherent with the coupled stress- and energy-based criterion proposed in [47], arises in an abrupt manner as shown in Fig. 4.7b; finally the

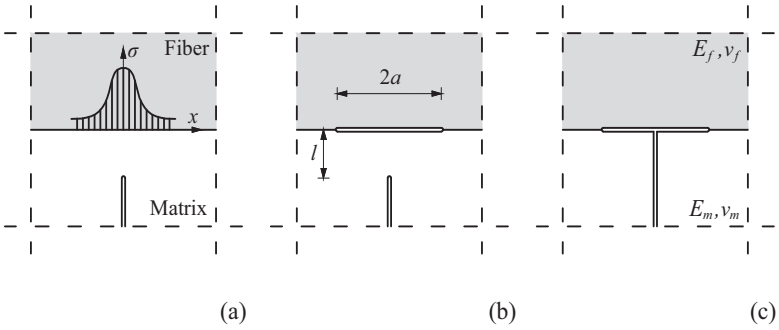

Fig. 4.7 Deflection of a matrix towards an interface as a debonding nucleation: (a) interfacial stress concentration induced by an approaching matrix crack; (b) nucleation of an interfacial crack ahead of the main crack; (c) rupture of the ligament.

crack deflection toward the interface can be modeled as the rupture of the ligament, which is energetically preferred over the crack propagation along the interface in most cases (see Fig. 4.7c).

A novel criterion is proposed to analyze the competition between the crack propagation within the matrix and the crack nucleation at the interface, by combining a generalization of the above-mentioned coupled criterion for the interfacial crack, as proposed in [49], and the classical Griffith's criterion for the matrix crack. For a matrix crack propagating perpendicularly to the interface in a pure mode I, a set of three nonlinear equations with unknowns the critical load factor β_c, the critical ligament width l_c and the critical debonding semi-length a_c, is obtained:

$$\begin{cases} \beta_c^2 \hat{\mathcal{G}}(l_c) = \mathcal{G}_c \\ \beta_c^2 \left[\left(\dfrac{\langle \hat{\sigma}(l_c, a_c) \rangle}{\sigma_c} \right)^2 + \left(\dfrac{\hat{\tau}(l_c, a_c)}{\tau_c} \right)^2 \right] = 1 \\ \beta_c^2 \hat{\mathcal{E}}(l_c, a_c) = \mathcal{E}_c(l_c, a_c) \end{cases} \tag{4.41}$$

where $\hat{\mathcal{G}}$ is the energy release rate per unit load factor for the main crack propagating toward the fiber, $\hat{\sigma}$ and $\hat{\tau}$ are the normal and tangential interfacial stresses, $\hat{\mathcal{E}}$ is the released potential energy (also called *incremental energy*

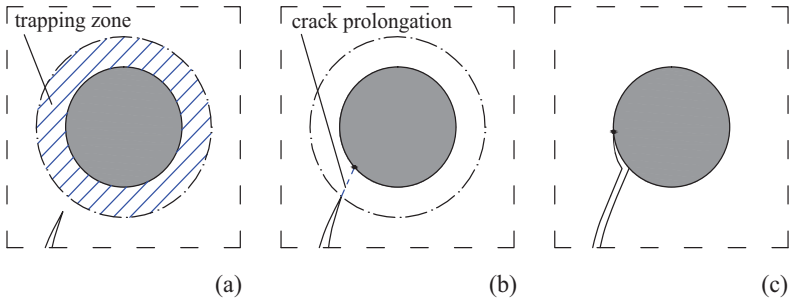

Fig. 4.8 Simplified modeling of crack deflection: (a) identification of the trapping zone; (b) prolongation of the main crack up to the interface; (c) crack advance along the interface.

release) during the interface crack nucleation at constant (unit) load factor, and $\mathscr{G}_c$ denotes its critical value, computed by integrating the critical energy release rate over the interface crack length, as suggested in [49]. It is worth noting that the coupled criterion is incorporated into the two last equations of (4.41), in the modified manner as proposed in Section 3.2.1, taking into account the interaction between normal and tangential stresses.

However, the set of equations (4.41) requires an iterative scheme to be solved, leading to an increase in the computational cost of the crack propagation process; thus, the following simplified strategy has been applied to obtain the numerical results presented in this chapter.

Firstly, the crack path is obtained by an extended version of the maximum energy release rate criterion incorporating the crack kinking criterion, as already discussed in Section 3.2.2, except than in the neighborhood of the inclusions, where the matrix crack can be trapped by an interface; the trapping region is defined by offsetting the circle describing the inclusion ahead the matrix crack by the quantity $a_0 = \mathscr{G}_{\mathrm{I}c} E^* / \pi \sigma_c^2$, which plays the role of a critical distance and defines the size of the process zone around the nucleated interface crack, according to the coupled criterion (4.41) (see Fig. 4.8a).

Once trapped, the main crack is prolonged up to the interface, and the intersection point between the crack prolongation and the interface is identified, as shown in Fig. 4.8b; finally, this point is considered as the starting point for the subsequent interface crack propagation (see Fig. 4.8c).

In order to avoid unrealistic values for the critical load factor, the nonlocal stress criterion appearing in Eq. (4.41) is replaced by a stress criterion applied to the above-mentioned intersection point, leading to the following simplified version of the original coupled criterion:

$$\begin{cases} \beta_c^2 \hat{\mathcal{G}}(l_c) = \mathcal{G}_c \\ \beta_c^2 \left[\left(\dfrac{\langle \hat{\sigma}(l_c) \rangle}{\sigma_c} \right)^2 + \left(\dfrac{\hat{\tau}(l_c)}{\tau_c} \right)^2 \right] = 1 \end{cases} \tag{4.42}$$

where the dependence on a_c disappears, because an equilibrium state prior to crack nucleation is considered; it is worth noting that criterion (4.42) is more conservative than criterion (4.41), because of the presence of a local stress criterion instead of a nonlocal stress criterion. The application of this criterion allows to eliminate all the equilibrium states, as determined by Eq. $(4.42)_2$, which are violating Eq. $(4.42)_2$ at the considered interface.

4.3 An adaptive concurrent multiscale model for microcrack propagation in composite materials

In this section, a novel multiscale strategy is presented, able to combine the concepts of domain decomposition and crack propagation models discussed in Sections 4.1 and 4.2 in an adaptive manner. Adaptivity is considered to be a necessary ingredient of the proposed multiscale approach, in order to obtain the accuracy of a fully microscopic model and the efficiency of a macroscopic model at the same time; indeed the crack path is not known a priori, thus the zone of interest, for which a microscopic resolution is needed, has to be continuously updated following the propagating crack tip. This strategy, which falls into the wide class of *adaptive model refinement* techniques [60], shares

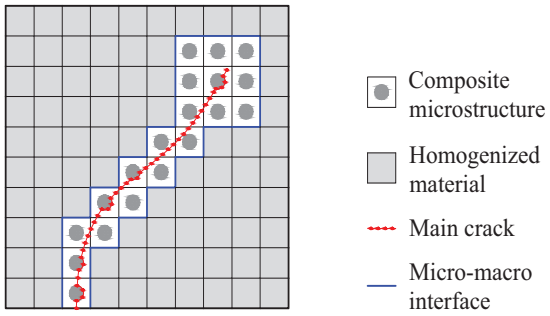

Fig. 4.9 Adaptive zoom-in procedure for multiscale crack propagation in composite materials.

some similarities with the classical *adaptive mesh refinement* strategies, but it is more efficient when dealing with highly heterogeneous solids.

The strategy for adaptive mesh refinement in the zones surrounding a given single macrocrack in a periodic medium is illustrated. The starting point of this procedure is to build a structured grid made of square elements, whose size is specified by the RVE size. Given the initial configuration of the macroscopic crack, as shown in Fig. 4.9, the unit cells which have to keep a fine discretization during the zoom-in procedure, are those which belong to the crack neighborhood, whose construction will be described in Section 4.3.2.1. The other unit cells coincide with macroelements whose material properties are computed by adopting the effective moduli obtained by means of classical first-order homogenization schemes. The entire cell detection is repeated, as the crack tip propagates across the cells. The main aspect of this strategy is to push the interface far enough to avoid the strong influence of spurious effects due to interface nonmatching meshes on the structural response. It is worth noting that this heuristic zoom-in criterion is uniquely based on geometric considerations, even if more sophisticated approaches are already existent in the literature (see, for instance, [61]), involving indicators for strain localization and loss of periodicity.

4.3.1 Finite element implementation

The proposed multiscale approach has been implemented by using the finite element commercial package COMSOL Multiphysics® and taking advantage of the extended scripting capabilities provided by LiveLink for MATLAB®, a tool integrated into the simulation environment and able to run MATLAB® codes for preprocessing, model manipulation and postprocessing.

The adaptive framework, used in conjunction with the crack length control scheme and the moving mesh approach for crack propagation, gives rise to a dedicated algorithm for automatic simulation of multiscale crack propagation in 2D fiber-reinforced composites. This algorithm, which is conceptually divided in two parts, is sketched in Fig. 4.10. In the first part, occupying the top of the figure, a hierarchical periodic homogenization scheme is used to obtain the overall moduli of the equivalent homogenized material; this operation is considered as a preprocessing step, to be performed at the beginning of the incremental-iterative strategy used to implement the proposed concurrent multiscale method.

The latter part of the algorithm, occupying the bottom of Fig. 4.10, is conceptually divided in three columns: the left column is devoted to the matrix crack propagation process, the middle column handles the crack deflection towards an interface, and the right one implements the competition between continuous debonding and kinking out of the interface.

It is worth noting that mesh optimization discussed in Section 4.2.1 is performed only outside the trapping zone described in Section 4.2.2; this fact contributes to improve the efficiency of the proposed numerical method. Moreover, when studying the crack deflection at the interface, two different virtual processes have been considered, i.e. two crack extensions performed clockwise and counterclockwise; the actual process is the one whose energy release rate to interface toughness ratio is greater. Finally, it should be noted that the model refinement is performed only a few times with respect to the total number of crack updates.

A MATLAB® script has been developed to perform the nested loops for crack propagation, whereas the FE software has been employed to solve the

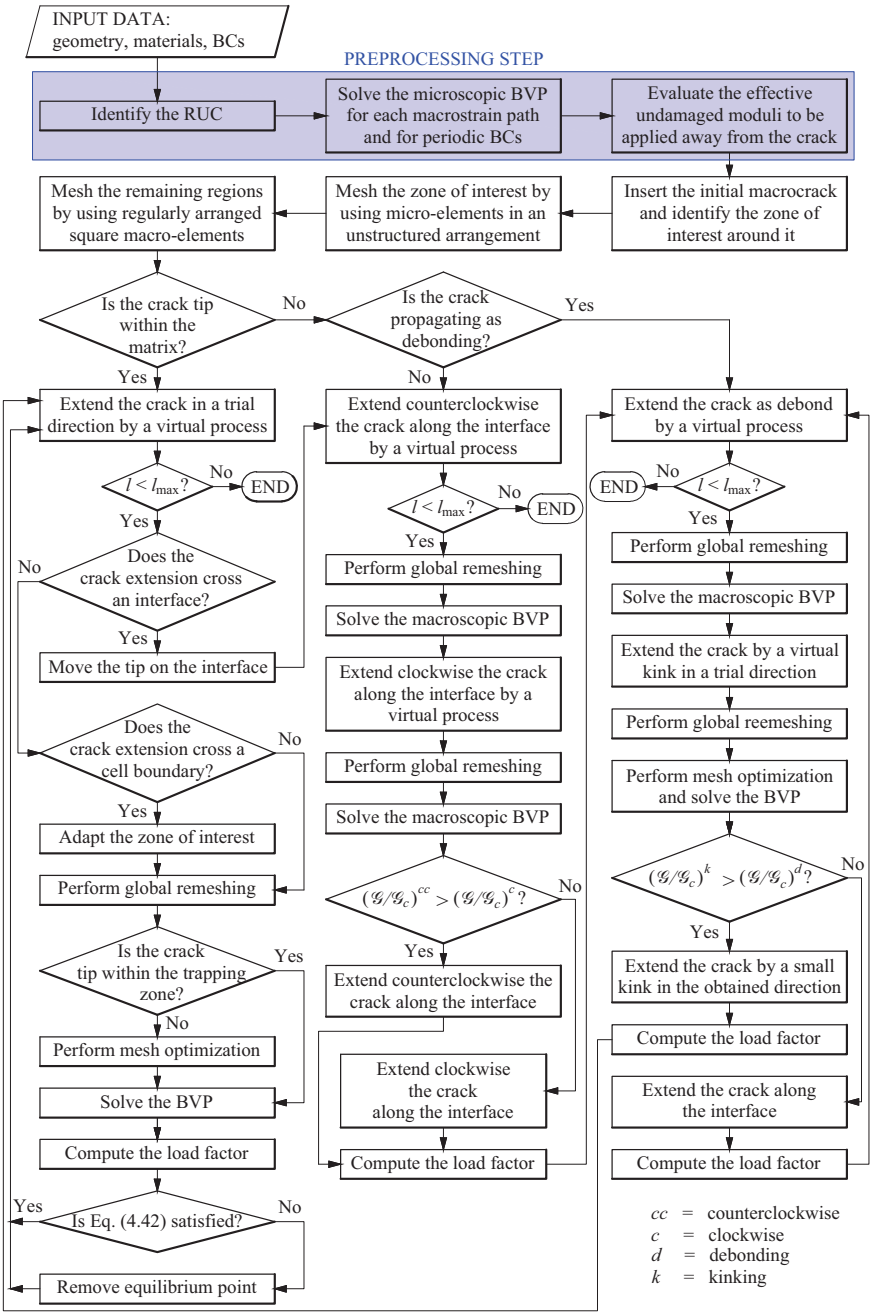

Fig. 4.10 Flowchart of the multiscale crack propagation algorithm.

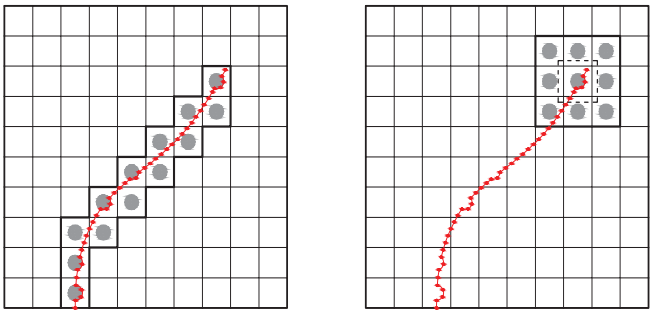

Fig. 4.11 Construction of the crack neighborhood.

structural problem, and to perform the shape optimization steps described in Section 4.2.1.

4.3.2 Computational details

In this section some computational details are given, in order to clarify how the proposed approach has been implemented in a standard finite element setting. The topics covered in this section are the construction of the crack neighborhood, and the crack interface model used to incorporate unilateral contact.

4.3.2.1 Construction of the crack neighborhood

In the proposed approach, there are no other source of nonlinearity except for the presence of microcracks (with neglected process zone in the bulk material, in the spirit of classical LEFM approaches); thus, the zone of interest is essentially related to the crack neighborhood, whose construction is performed in two steps. In the first step, shown in Fig. 4.11a, the unit cells intersected by the current crack path are detected in order to form the zone of interest Ω_m; in the latter one, the unit cells adjacent to the one containing the crack tip are identified, as shown in Fig. 4.11b, and subsequently added to Ω_m. This step is needed to avoid spurious boundary effects which could affect the accuracy in the numerical evaluation of the J-integral when the crack tip approaches a micro-macro interface.

It is worth noting that, here the *J*-integral outer path (the dashed line in Fig. 4.11b), is kept fixed during the microcrack propagation inside each unit cell, being updated only when the crack crosses the unit cell boundaries.

4.3.2.2 Implementation of the moving mesh methodology

As already stated in Section 4.2.1, the moving mesh methodology allows to formulate the problem of finding the crack direction for each propagation step during matrix cracking, as a geometry optimization problem. To this end, a COMSOL's "deformed geometry" interface is added to the finite element model, introducing a new geometry coordinate system, described by a new set of variables $\mathbf{X}_g$, which are independent of both spatial and material coordinates (denoted by $\mathbf{x}$ and $\mathbf{X}$, respectively). In this way, the original geometry can be deformed and/or parameterized without having to create a new mesh, and if an optimization solver is used, searching for the crack direction is equivalent to performing a structural or shape optimization (see [205]).

Both derivative-based and derivative-free optimization methods have been tested to solve for the kinking angle θ; the considered derivative-based method, i.e. a one-dimensional version of the SNOPT (Sparse Nonlinear OPTimizer), which is directly available in the employed simulation environment [205], has proved to be very efficient in most cases, but sometimes it fails, due to the noise of the objective function. Therefore, a derivative-free optimization method is here considered to be more suitable for these purposes; one of the optimization tools already available within the employed commercial package is the Nelder-Mead method, which reduces to a classical dichotomy method in a one-dimensional setting. This method, which has been used to obtain all the results reported in the present chapter, is very robust and accurate, provided that the objective function is unimodal in the interval chosen to bracket a local minimum.

A suitable initial bracket $[-\theta^*, \theta^*]$ for θ can be found by recalling that the maximum kinking angle predicted by the maximum energy release rate criterion in isotropic homogenous materials is $\theta^* \approx 75.2°$, corresponding to the case of a crack loaded in pure mode II. As a consequence of such severe trial

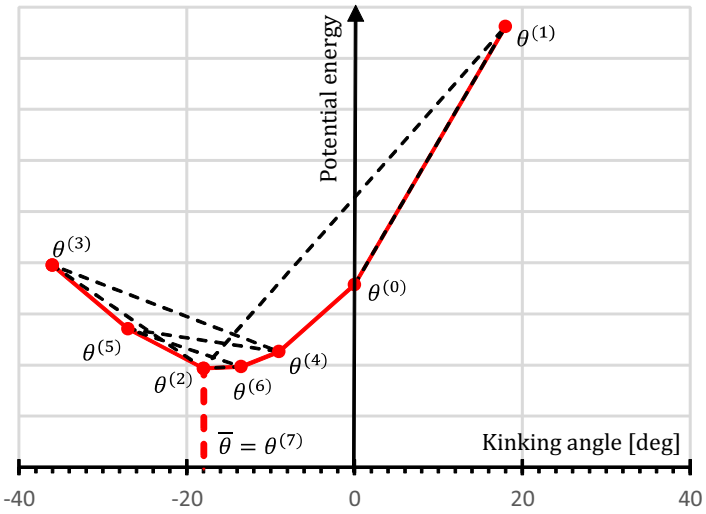

Fig. 4.12 Iterations performed to find the crack direction $\overline{\theta}$ by using the dichotomy approach, starting from the initial guess $\theta^{(0)} = 0°$.

crack realignment, the quality of the elements in the neighborhood of the crack tip is inevitably reduced; however, since from a theoretical point of view the crack path is a curve with continuous tangent, except for a finite set of discontinuity points, characterized by severe kinking and branching phenomena, if a suitable value for Δl is chosen, a discrete crack propagation algorithm generally provides very small values for the actual kinking angle; in the present computations θ^* has been always set equal to 60°, considered as an optimal value coming from experience.

The initial guess for θ is set as zero, which is regarded as a good predictor of the actual angle, as the crack path is supposed to be smooth almost everywhere, except for a few kinking points; then, iterations are performed by testing different values of θ, each of which is associated with a value of the total potential energy, resulting from the solution of the equilibrium problem. A number of iterations between ten and fifteen is usually enough to find the kinking angle with a satisfactory accuracy (less than 0.5°), as shown in Fig.

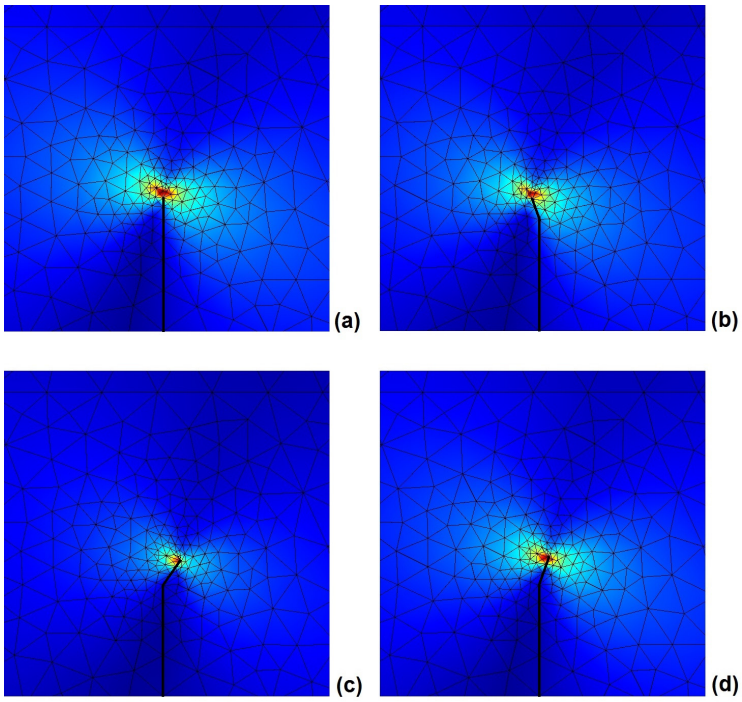

Fig. 4.13 Mesh plots at the neighborhood of the kinked crack for different trial values of the propagation direction: (a) $\theta^{(0)} = 0°$ (initial guess); (b) $\theta^{(1)} = 18.0°$; (c) $\theta^{(3)} = -36.0°$; (d) $\theta^{(3)} = -16.5°$ (actual value).

4.12; the mesh plots corresponding to four different trial values of θ are depicted in Fig. 4.13.

4.3.2.3 Crack interface elements incorporating unilateral contact

In the present work, cracks are inserted in a 2D standard finite element model by using special zero-thickness interface elements able to provide nodal doubling, necessary to decoupling the given mesh across the crack faces. The chosen interface element is already available in the simulation environment used for the present numerical calculations; this element, whose length L is set to be equal to the crack increment, has four nodes labeled from 1 to 4, as shown in Fig. 4.14; lines 1–2 and 3–4 are straight and the nodes 1 and 4, and the

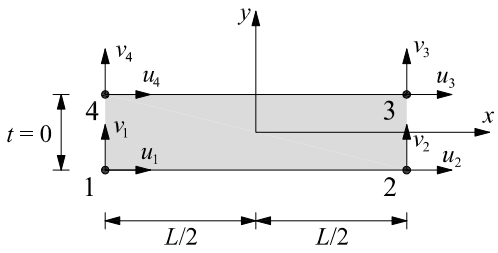

Fig. 4.14 Zero-thickness interface element.

nodes 2 and 3 are coincident before deformation. The nodal displacement vector in the local coordinate system is:

$$\mathbf{d} = \{u_1, v_1, u_2, v_2, u_3, v_3, u_4, u_4\}^{\mathrm{T}}. \tag{4.43}$$

The vector of relative displacements $[\![\mathbf{u}]\!]$ is defined as

$$[\![\mathbf{u}]\!] = \mathbf{u}_u - \mathbf{u}_l, \tag{4.44}$$

where $\mathbf{u}_l$ and $\mathbf{u}_u$ are the displacements computed on the "lower" and "upper" sides of the interface, respectively; $[\![\mathbf{u}]\!]$ is written by components as follows:

$$\begin{Bmatrix} [\![u_t]\!] \\ [\![u_n]\!] \end{Bmatrix} = \begin{Bmatrix} u_u - u_l \\ v_u - v_l \end{Bmatrix} \tag{4.45}$$

where $[\![u_t]\!]$ and $[\![u_n]\!]$ represent the tangential and normal relative displacements, respectively. Displacements u and v can be approximated by using linear interpolation functions N_1 and N_2, that is:

$$\begin{Bmatrix} u_l \\ v_l \end{Bmatrix} = \begin{bmatrix} N_1 & 0 & N_2 & 0 & 0 & 0 & 0 & 0 \\ 0 & N_1 & 0 & N_2 & 0 & 0 & 0 & 0 \end{bmatrix} \mathbf{d} \tag{4.46}$$

and

$$\begin{Bmatrix} u_u \\ v_u \end{Bmatrix} = \begin{bmatrix} 0 & 0 & 0 & 0 & N_2 & 0 & N_1 & 0 \\ 0 & 0 & 0 & 0 & 0 & N_2 & 0 & N_1 \end{bmatrix} \mathbf{d}, \tag{4.47}$$

where $N_1 = \frac{1}{2} - \frac{x}{L}$ and $N_2 = \frac{1}{2} + \frac{x}{L}$.

Thus the vector of relative displacements can be written as:

$$[\![\mathbf{u}]\!] = \mathbf{B}\mathbf{d}, \tag{4.48}$$

where

$$\mathbf{B} = \begin{bmatrix} -N_1 & 0 & -N_2 & 0 & N_2 & 0 & N_1 & 0 \\ 0 & -N_1 & 0 & -N_2 & 0 & N_2 & 0 & N_1 \end{bmatrix}. \tag{4.49}$$

The stress-displacement relationship for the interface is given as:

$$\mathbf{t} = \mathbf{k}[\![\mathbf{u}]\!] \tag{4.50}$$

or, by components:

$$\begin{Bmatrix} t_t \\ t_n \end{Bmatrix} = \begin{bmatrix} k_t & 0 \\ 0 & k_n \end{bmatrix} \begin{Bmatrix} [\![u_t]\!] \\ [\![u_n]\!] \end{Bmatrix}, \tag{4.51}$$

where t_t and t_n are the tangential and normal stresses (i.e. the normal and tangential forces per unit area along the interface), k_t and k_n represent the tangential and normal stiffness per unit area along the interface. It is worth noting that $\mathbf{k}$ does not contain off-diagonal terms, implying that the shear and normal deformations are independent of each other.

In this work, the interface element is used to enforce the frictionless unilateral contact condition; thus k_t is set equal to zero, whereas k_n is

$$k_n = \frac{k}{2}\left(1 - \operatorname{sgn}([\![u_n]\!])\right), \tag{4.52}$$

where k is the so-called penalty parameter, used to regularize the Signorini's contact condition.

Considering $[\![\mathbf{u}]\!]$ as a generalized strain, the element stiffness matrix can be obtained in a standard manner:

$$\mathbf{k}_e = h \int \mathbf{B}^{\mathrm{T}} \mathbf{k} \mathbf{B} \, \mathrm{d}x, \tag{4.53}$$

where h is the thickness of the solid; each term can be exactly integrated, giving:

$$\mathbf{k}_e = \frac{Lh}{6} \begin{bmatrix} 2k_t & 0 & k_t & 0 & -k_t & 0 & -2k_t & 0 \\ & 2k_n & 0 & k_n & 0 & -k_n & 0 & -2k_n \\ & & 2k_t & 0 & -2k_t & 0 & -k_t & 0 \\ & & & 2k_n & 0 & -2k_n & 0 & -k_n \\ & & & & 2k_t & 0 & k_t & 0 \\ & & \text{sym} & & & 2k_n & 0 & k_n \\ & & & & & & 2k_t & 0 \\ & & & & & & & 2k_n \end{bmatrix}. \tag{4.54}$$

Finally the element stiffness equation is given as:

$$\mathbf{k}_e \mathbf{d} = \mathbf{f}, \tag{4.55}$$

where $\mathbf{f}$ is the nodal force vector in the local coordinate system:

$$\mathbf{f} = \left\{ f_{1x}, f_{1y}, f_{2x}, f_{2y}, f_{3x}, f_{3y}, f_{4x}, f_{4y} \right\}^{\mathrm{T}}. \tag{4.56}$$

4.4 Validation of the proposed model: results and discussions

In the present section the proposed multiscale approach is validated by carrying out comparisons with *direct numerical simulations* (DNS, in short), for which all the microstructural details of the given composite structure are explicitly modeled. Complete failure analyses have been performed for both

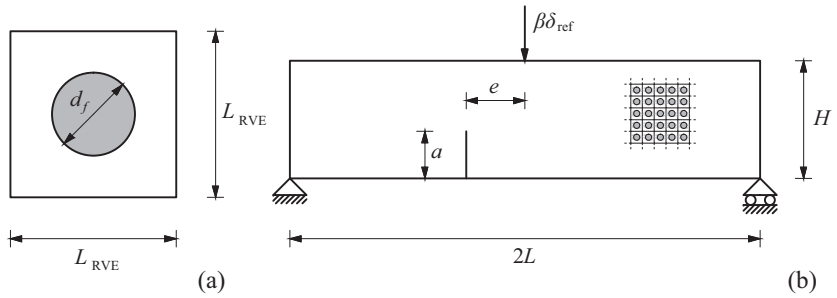

Fig. 4.15 Geometric configuration of the fiber-reinforced composite beam used for numerical experiments: (a) prototype of RUC; (b) geometry and boundary conditions for the reference problem.

Table 4.1 Elastic properties of the microconstituents in the bimaterial system.

Component	Material	E (GPa)	ν	$\mathcal{G}_c$ $\left(\text{J}/\text{m}^2\right)$
Matrix	Epoxy	2.79	0.33	100
Fiber	Glass	70.8	1.22	–

models, in order to estimate the numerical errors of the proposed strategy in evaluating the peak and the post-peak behavior during the crack propagation in a composite structure. Furthermore it was not possible to perform experiments providing failure material properties at both the macro- and the micro-scale. On the other hand, closed-form solutions or other analytical results are not available at the best author's knowledge, for the considered problem. Thus, the direct numerical results are considered to be a reference solution in order to assess the validity of the proposed multiscale method.

4.4.1 Description of the numerical model

In the present work, a 2D fiber-reinforced composite structure is considered, formed by the repetition of square unit cells periodically distributed. The prototype of these unit cells, playing the role of representative volume element,

is composed of a soft matrix including a stiffer circular fiber at its center, as shown in Fig. 4.15a; the side of this unit cell is 30 μm, whereas the fiber radius is $d_f = 15$ μm, resulting in a fiber/matrix volume fraction approximately equal to 20%. An epoxy/glass bimaterial system is considered, whose elastic properties are listed in Table 4.1. Fibers are supposed to be perfectly bonded to the matrix, except for the cells traversed by the macroscopic crack introduced as the starting point for the successive propagation steps. The mechanical properties of the fiber/matrix interface in terms of strength and toughness are shown in Table 4.2. The reference length l_{ref} needed to normalize the oscillatory singularity, is expressed as angular distance along the circular inclusion and set as 0.1°. According to this choice, based on a material length scale, l_{ref} necessarily lies within the zone of dominance of the K-field.

The reference problem analyzed to assess the validity of the proposed method consists in the complete failure analysis of a single notched and simply supported heterogeneous beam, subjected to a three-point bending test, whose geometry is sketched in Fig. 4.15b. The beam's mid-span is $L = 6.0 \times 10^{-4}$ m, and its height is $H = 3.0 \times 10^{-4}$ m, whereas the initial crack length a_0 is equal to $H/5 = 6.0 \times 10^{-5}$ m. For this structure, the scale separation principle is considered to be valid, since the characteristic size of the macroscopic structure $l_{\text{macro}} = \min\{2L, H\}$ is ten times bigger than l_{micro}. The applied load consists in a centered vertical displacement $\delta = \beta\delta_{\text{ref}}$ imposed on the upper side of the beam; β is the load factor and δ_{ref} is a reference displacement, set as 1.0×10^{-3} m. In order to avoid numerical inaccuracies in recovering stress and strain fields in the neighborhood of the loaded points, it is assumed that both supports and prescribed displacements are spread out over a small arbitrary line patch (whose length is set equal to the RVE size). It follows that the considered composite structure consists in a 2D spatial array of 41×10 unit cells. In the present numerical computations, plane strain conditions have been imposed, considering a thickness t equal to 1 mm.

Table 4.2 Mechanical properties of the fiber/matrix interface.

σ_c (MPa)	τ_c (MPa)	$\mathcal{G}_{Ic}$ (J/m^2)	λ
150	200	25	0.3

In order to explore the capabilities of the proposed method to study mixed-mode propagation of macroscopic cracks, four case studies have been considered, obtained varying the eccentricity e of the initial crack with respect to the mid-section. In the first case, a centered crack has been inserted into the finite element model, leading to a propagation in pure mode I at the macroscopic level; for the other cases the following three value for e have been considered (given in dimensionless form): $e/L = \{0.25, 0.50, 0.75\}$.

The multiscale numerical model has been described by using two different meshes according to the considered multilevel domain decomposition: the mesh used for the macroscopic level is a coarse mesh composed of bilinear quadrilateral elements (macroelements) arranged in a mapped mesh, whose size is equal to the RVE size, whereas the microscopic mesh used to describe the zone of interest is discretized by using linear triangular elements arranged in an unstructured mesh, such that the maximum mesh size is ten times smaller the RVE size. As a consequence, the micro-macro interface is characterized by nine hanging nodes for each macroelement. Moreover, a suitable mesh refinement along the material interfaces and the J-integral contours is adopted.

For the initial crack configuration, such nonconforming mesh, a portion of which is depicted in Fig. 4.16a, is composed of about 10,500 elements, with about 11,300 degrees of freedom (DOFs). On the other hand, the direct numerical model has been discretized by using everywhere the same fine mesh as in the multiscale model. For the initial crack configuration, such mesh is composed of about 201,500 linear triangular elements, resulting in about 211,700 degrees of freedom, as shown in Fig. 4.16b.

The numerical test has been performed by using the collocation approach, described in Section 4.1.3.1, by introducing a set of Lagrange multipliers

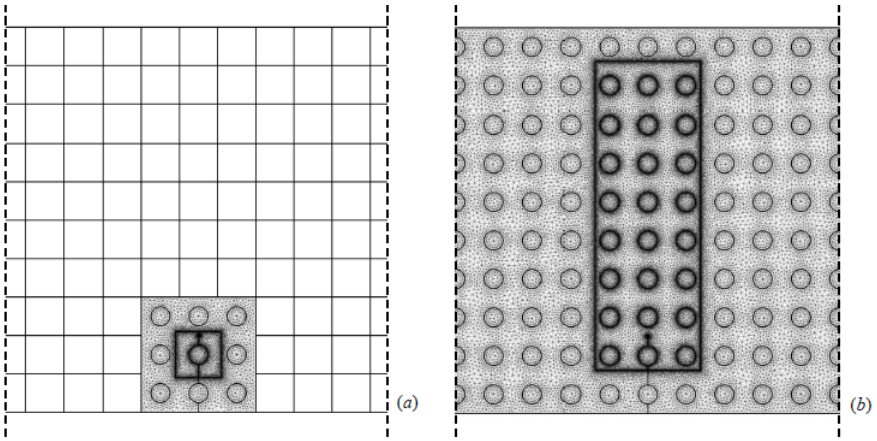

Fig. 4.16 Finite element discretization of the reference composite structure: (a) nonconforming mesh for multiscale numerical simulations; (b) fine resolution conforming mesh for direct numerical simulations.

which enforce pointwise a gluing condition at the micro-macro interface. The constraint (4.22) has to be fulfilled for the interface between two corner nodes of each macroelement adjacent to the fine resolution subdomain.

4.4.2 Numerical results: the case of the center crack

The aim of this section is to present the numerical results of the multiscale failure analysis performed on the heterogeneous beam, with reference to the case of the center crack.

The macroscopic structural response of the considered specimen in shown in Fig. 4.18, in terms of deformed configuration for a generic crack propagation step; the crack path is quite jagged due to the microstructure of the beam. The figure also highlights the micro/macro interface as determined by means of the adaptive model refinement technique described in Section 4.3.

In Fig. 4.17, the corresponding load-deflection curve is depicted, limited to its first portion in order to better explain the competition between different

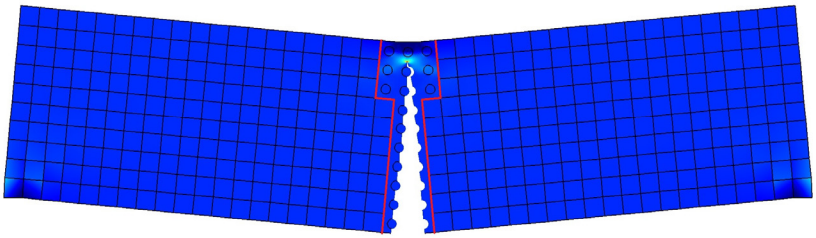

Fig. 4.18 Numerical results of the multiscale analysis for the case $e/L = 0$: deformed configuration for a generic crack propagation step.

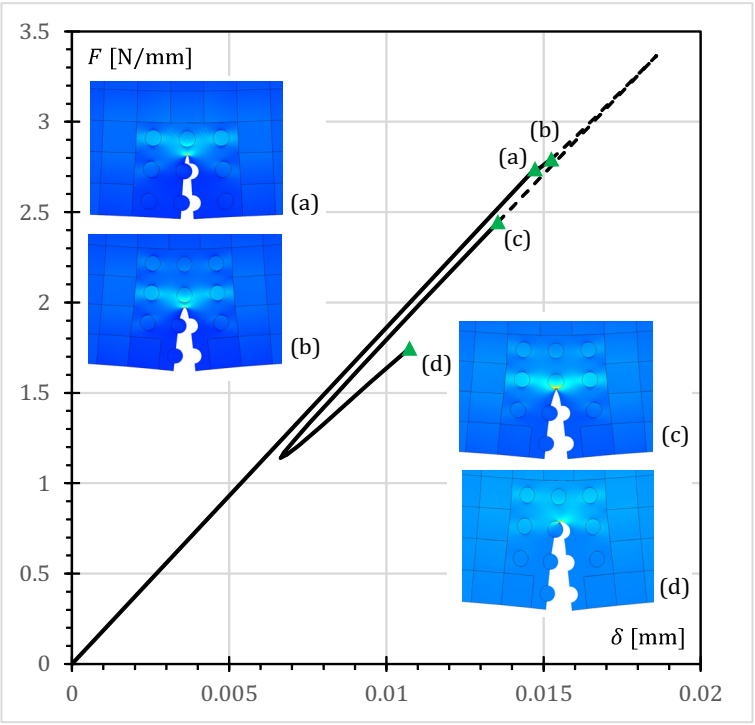

Fig. 4.17 Numerical results of the multiscale analysis for the case $e/L = 0$: first portion of the load-displacement curve with the main significant points: (a) initial crack; (b) debonding nucleation; (c) crack deflection towards the interface; (d) kinking out of the interface.

cracking phenomena already discussed in Section 4.2. It is worth noting that the load corresponding to the prescribed displacement is computed as the summation of the nodal reaction forces over the portion of the constrained boundary.

The first point of this force-displacement curve, marked by (a), represents the equilibrium state for the initial crack configuration, obtained by applying directly Griffith's criterion for the preexisting crack. The subsequent points are the equilibrium points for a quasistatic crack propagation, each of which corresponds to a crack configuration which is obtained by updating the previous crack by a fixed length increment. Fig. 4.17 also highlights the main drawback when dealing with an energy-based criterion for bimaterial systems: the application of such criterion provides a very high value for the first peak load, due to a strengthening effect of the fibers as the crack approaches a material interface. At the same time this phenomenon exhibits a strong dependence on the length increment used to model the crack propagation process.

This inconsistency can be explained by recalling the coupled stress- and energy-based criterion for a crack propagating towards a rigid inclusion. In the present computations, the "true" peak load, corresponding to point (b), is assumed to be the highest load which corresponds to the simultaneous fulfillment of both the classical energy-based criterion and the stress criterion at the nearest interface to the current crack tip, according to Eq. (4.42).

Thus, the remaining part of the loading curve (the dashed one in Fig. 4.17) has to be cut, starting from point (b) up to the point corresponding to the crack deflection towards the considered interface, marked by (c), for which the Griffith criterion is applied. In other words, the arrest of the matrix crack growing is circumvented by introducing a competition with an interface debonding, modeled as a crack nucleation, followed by the rupture of the crack ligament.

The last point shown in Fig. 4.17, marked by (d) corresponds to the last debonding step before the kinking out event, and thus the portion (c-d) of the curve represents the set of equilibrium states characterized by the interface crack propagation.

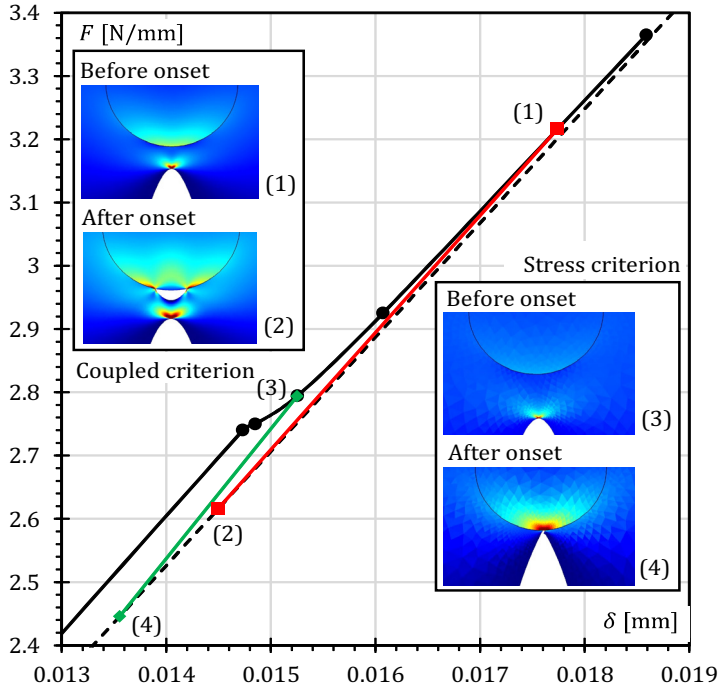

Fig. 4.19 Zoom-in of the load-displacement curve showing the comparison between criteria (4.41) and (4.42).

At this point it is useful to compare the simplified (stress) criterion (4.42), by which points (b) and (c) are determined, with the coupled criterion (4.41), which requires the solution of a nonlinear system for the unknowns β_c, a_c and l_c (see Section 4.2.2); to this end, a zoom-in of the load-displacement curve of Fig. 4.17 is made, which is shown in Fig. 4.19, where criteria (4.41) and (4.42) are highlighted in red and green, respectively; as expected, by applying the stress criterion (4.42), the load peak, corresponding to point (3), is underestimated of 12.5% with respect to the load peak obtained by means of the coupled criterion, corresponding to point (1). This fact is essentially due to the nonlocal nature of the stress criterion incorporated in Eq. (4.41).

The complete load-displacement curve is depicted in Fig. 4.20a, where

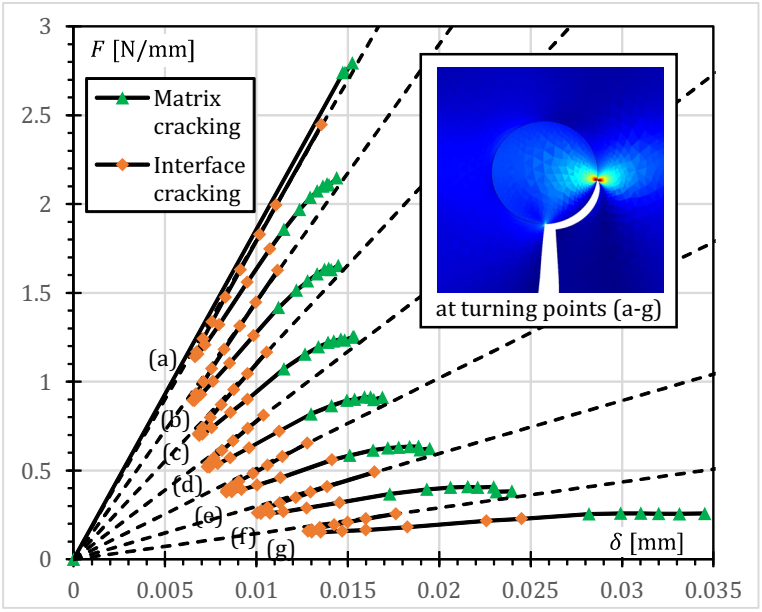

(a)

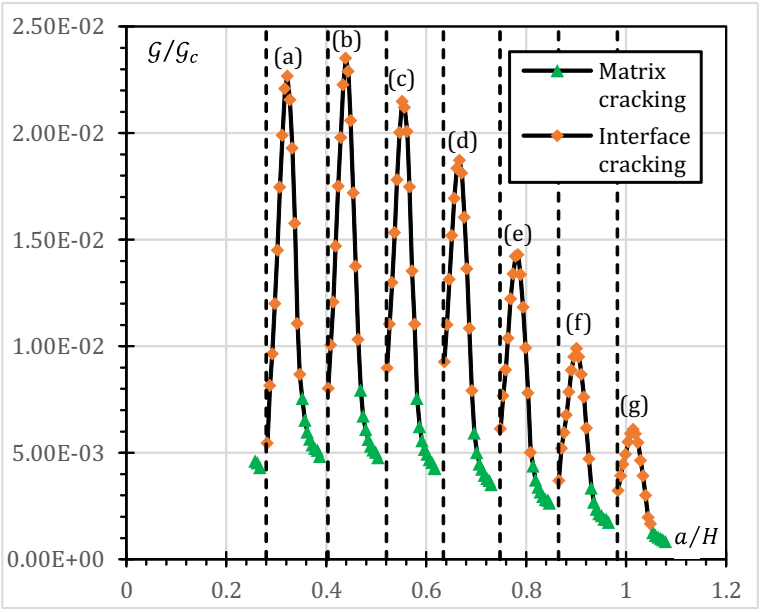

(b)

Fig. 4.20 Numerical results of the multiscale analysis for the case $e/L = 0$: (a) force versus prescribed vertical displacement; (b) dimensionless energy release rate for a unit load factor as a function of the crack length.

the distinction between matrix cracking and interface cracking has been highlighted; the global response presents some discontinuity points, one for each intercepted interface, where the above-mentioned coupled criterion is applied; the oblique asymptotes shown as dashed lines are added to the graph in order to highlight the limit behavior as the crack ligament goes to zero (i.e. $l \to 0$).

This phenomenon can be better appreciated by considering Fig. 4.20b, which shows the evolution of the dimensionless energy release rate $\tilde{\mathcal{G}} / \mathcal{G}_c$ per unit load factor as a function of the dimensionless crack length a/H. It is worth noting that $\mathcal{G}_c$ assumes a different meaning depending on whether the crack propagation takes place within the matrix or at an interface. In the first case $\mathcal{G}_c$ represents the mode I fracture energy of the matrix (which is a material property); in the latter one, $\mathcal{G}_c = \mathcal{G}_c(\psi)$, i.e. the mixed-mode interface toughness, which is a function of the mode mixity ψ, according to the phenomenological law used in [88]. As already explained in Section 4.2.2, the strengthening effect of the fiber is essentially due to the vanishing behavior of the related energy release rate for a crack approaching an interface in case of weak singularity. Vertical asymptotes, corresponding to those of Fig. 4.20a, are added to the graph in order to highlight the limiting behavior of $\mathcal{G}$ for $l \to 0$.

The turning points (a-g) of Fig. 4.20a, characterized by local peaks of the energy release rate as shown in Fig. 4.20b, are associated with the same local crack configuration around the interface depicted in Fig. 4.20a, whose direction is aligned with the vertical plane.

As shown in Fig. 4.20a, after a crack reaches the first material interface by the rupture of the crack ligament, the structural behavior shows a severe snap-back event, corresponding to the crack propagation along the fiber/matrix interface, and those magnitude is strictly related to the ratio between the interface toughness and the fracture energy of the matrix. A weaker interface would lead to a more conspicuous unstable behavior, whereas a stronger interface would produce a more stable response, associated to easier kinking phenomena. The presence of the turning points (a-g) and of the subsequent snap-through events in Fig. 4.20a reveals the stabilizing effect associated to higher values for the interfacial crack length. This phenomenon is clarified by

analyzing the behavior of the energy release rate, as shown in Fig. 4.20b. For small debonding lengths the energy release shows an initial increasing behavior until the maximum is reached (corresponding to the above-mentioned turning points); this takes place for a debonding length (expressed in terms of angular distance) of about 90° (as shown in Fig. 4.20a), after which the slope of the energy release curve becomes negative. The local peaks of the energy release rate can be explained by considering that the interface crack in this configuration is subjected to an approximately uniaxial remote stress state along the x-axis.

The recover in strength is essentially due to the fact that the crack is constrained to lie along the interface; while turning around the fiber, the interface crack tends to be close and contact phenomena between the crack faces can occur. As a consequence, crack propagation along the interface becomes more energetically costly and kinking phenomena can take place. Indeed a crack deflection is predicted for a debonding angle (measured from the crack tip which corresponds to the turning point) between 55° and 60°. This range seems to be consistent with the numerical and the experimental results already existent in the literature (see, for instance, [9]).

Kinking out of the interface does not produce any discontinuity in the structural response, and the subsequent matrix propagation occurs in a stable manner, as shown in Figs. 4.20a and 4.20b. The geometry of the considered specimen and the prescribed boundary conditions produce a crack propagation in macroscopic mode I, and the resulting crack path tends to intercept all the fibers which lie along the mid-section. Thus an alternating stable/unstable behavior can be recognized in a cyclic sense, until the final collapse.

The behavior of the mode mixity angle as a function of the crack length is shown in Fig. 4.21: the first stages of the interface crack propagation for each intercepted fiber are characterized by small absolute values of the mode mixity; for increasing debonding lengths the mode I contribution tends to decrease, leading to mixed-mode interfacial propagation in which the mode II contribution is dominant. For $45° < \psi < 55°$ the crack deflection seems to be favored over the propagation along the interface.

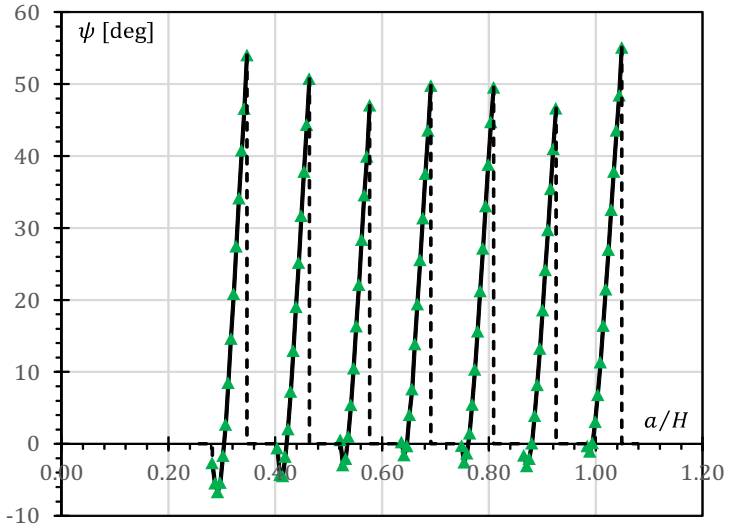

Fig. 4.21 Numerical results of the multiscale analysis for the case $e/L = 0$: mode mixity angle as a function of the crack length.

In Fig. 4.22 the structural response for the same test is shown, obtained by adopting a displacement control scheme: in this case only the stable equilibrium configurations are considered, i.e. the states for which the critical load factor β_c is an increasing function of the crack length. Such a curve is more suitable to be compared with classical load-displacement curves obtained from experimental tests. After the initial linear behavior, associated to the initial crack configuration, the considered test is characterized by a short nonlinear structural response, in which both loads and displacements increase, showing at the same time a small reduction in apparent stiffness. The load carrying capacity is reached when a critical stress is attained within the nearest interface to the main crack.

After this, the crack is deflected towards the considered interface, leading to a sudden fracture process involving more than one fiber and a relevant portion of the matrix. This is highlighted by the sharp decrease of load after reaching the maximum value; the resulting lose in stiffness is about of 70%. Failure

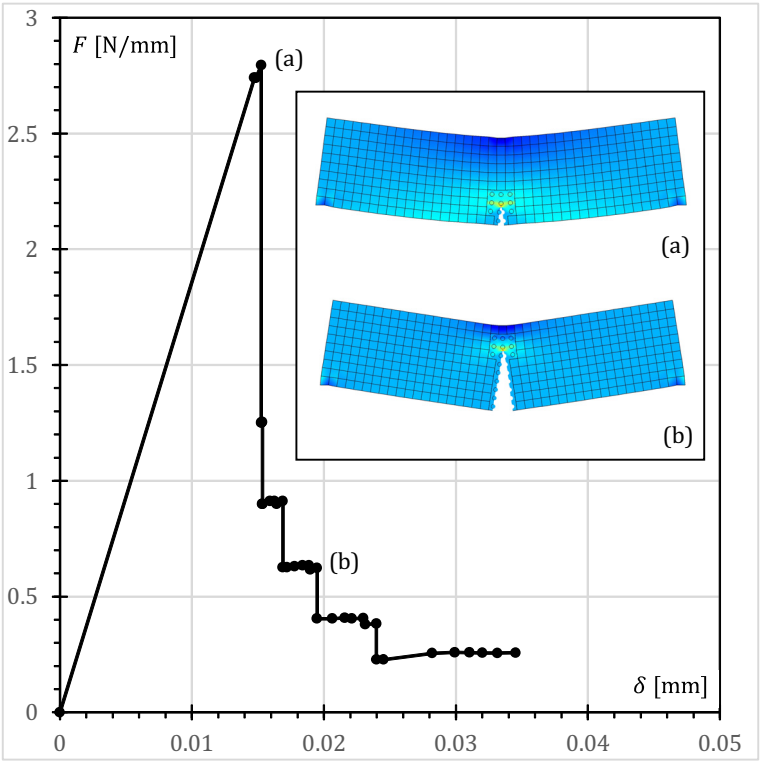

Fig. 4.22 Numerical results of the multiscale analysis for the case $e/L = 0$ using a displacement control scheme: force versus prescribed vertical displacement.

is not totally catastrophic, and the considered structure may experience a crack arrest for a prescribed load factor. Indeed, the post-peak structural response shows a little residual load carrying capacity, strictly related to the strengthening effect due to the crack interaction with fibers. Each discontinuity in the softening region corresponds to the crack propagation along an interface, which takes place in an unstable manner. It is worth noting that the test was performed without reaching the total collapse, in order to avoid numerical errors due to the crack interaction with the external loaded boundary, which may affect the accuracy in catching the collapse behavior.

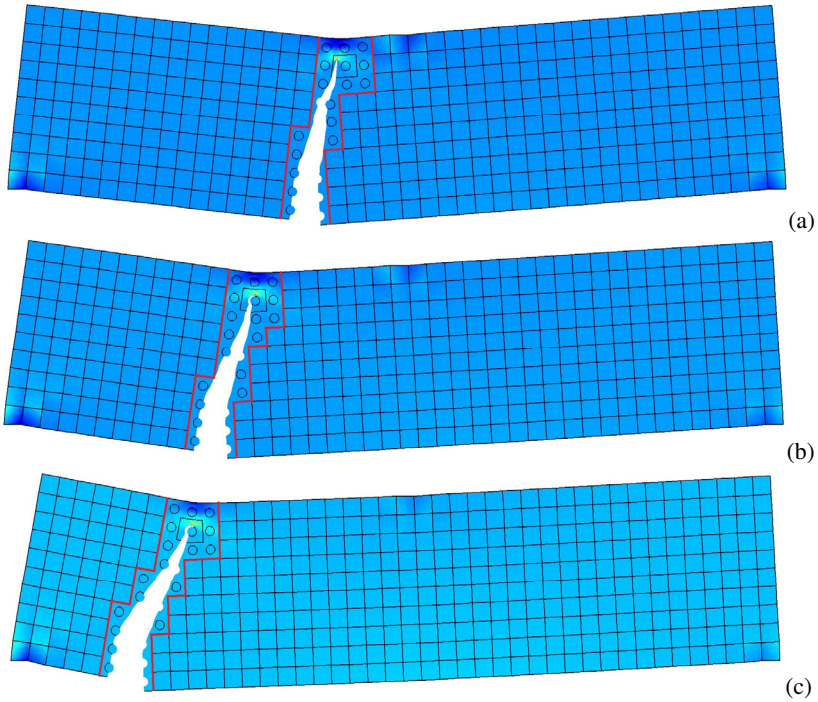

Fig. 4.23 Numerical results of the multiscale analysis for $e/L = [0.25, 0.50, 0.75]$: deformed configuration for a generic crack propagation step.

4.4.3 Numerical results: the case of the eccentric crack

In order to analyze the influence of the position of the initial crack on the macroscopic structural response of the given composite beam, three different eccentric cracks have been considered, i.e. $e/L = [0.25, 0.50, 0.75]$; the deformed configuration for a generic crack propagation step and for all considered case is shown in Fig. 4.23; the crack path is quite jagged due to the microstructure of the beam. The figure also highlights the micro/macro interface as determined by means of the adaptive model refinement technique described in Section 4.3.

For the case of the eccentric crack, the effect of the elastic mismatch at the material interface tends to produce a crack deflection away from the inclusion, thus the only intercepted interfaces during the crack propagation are those approached by a crack with a large inclination with respect to the material interface. As a consequence, the load-displacement curve appears to be more irregular than in the previous case.

The load-displacement curve for $e/L = 0.25$ is shown in Fig. 4.24a; after a severe snap-back event associated to the crack propagation along the nearest interface to the initial crack tip, several alternating stable/unstable stages take place during the crack propagation within the matrix. This oscillating behavior can be revealed more clearly by considering the plot of the energy release rate as a function of the crack length as shown in Fig. 4.24b. The two peaks for the dimensionless energy release rate correspond to the turning points highlighted in Fig. 4.24a, after which a recover in strength occurs. As in the previous case, the global structural response seems to be mostly unstable, but global failure is not related to a catastrophic collapse, since a little residual load carrying capacity is still present, after the prescribed displacement corresponding to the peak load is reached.

The main results for the eccentricity $e/L = 0.50$ are depicted in Fig. 4.25. In this case, similar considerations can be made about the local stability of the crack propagation process, with respect to the previous case. The main difference concerns the global structural behavior: the response of the composite beam appears to be completely brittle, with no residual load carrying capacity after the peak load is reached, for a displacement controlled loading path. As a consequence the complete failure occurs in a catastrophic manner, leading to a sudden total lose in apparent stiffness.

The global structural behavior in the case of eccentricity $e/L = 0.75$ is characterized by the same unstable nature, as shown in Fig. 4.26: indeed, even if the local behavior appears to be unstable/stable according to the slope of the energy release rate's curve depicted in Fig. 4.26b, a very sharp global snap-back event can be recognized. The complete failure takes place again by a catastrophic collapse.

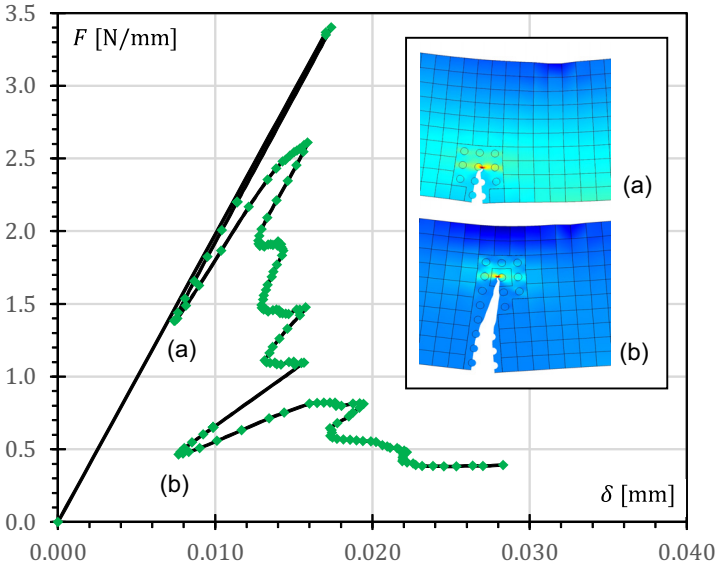

(a)

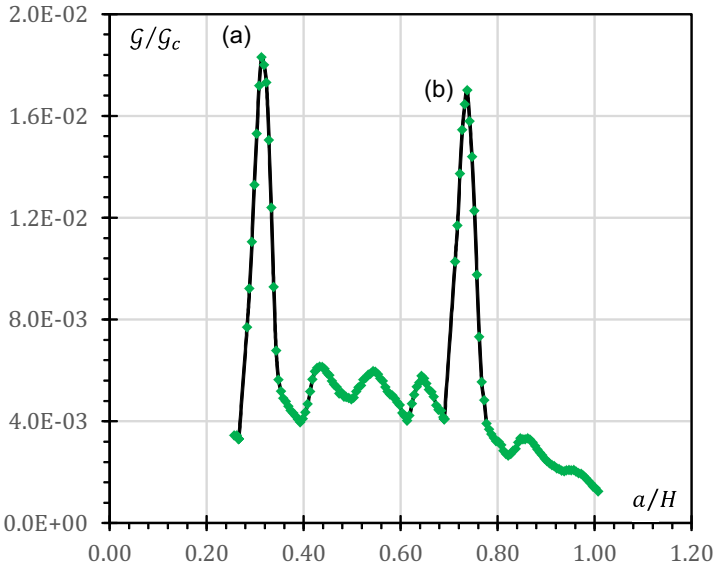

(b)

Fig. 4.24 Numerical results of the multiscale analysis for the case $e/L = 0.25$: (a) force versus prescribed vertical displacement; (b) dimensionless energy release rate for a unit load factor as a function of the crack length.

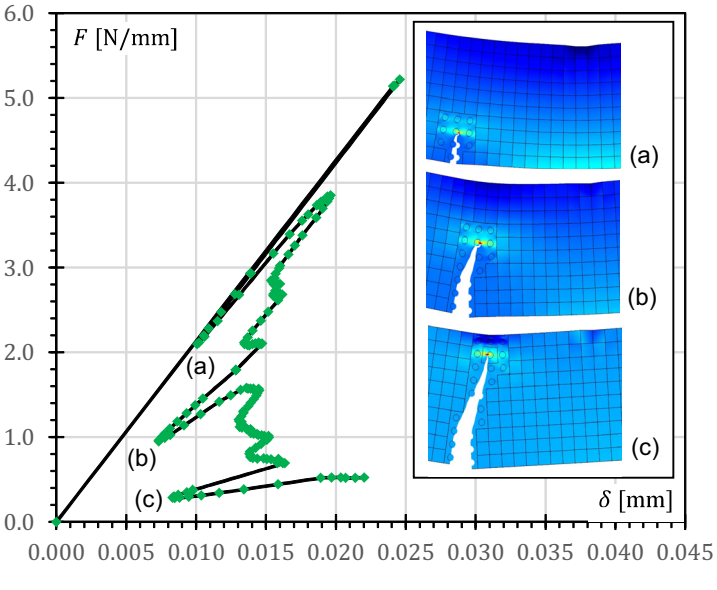

(a)

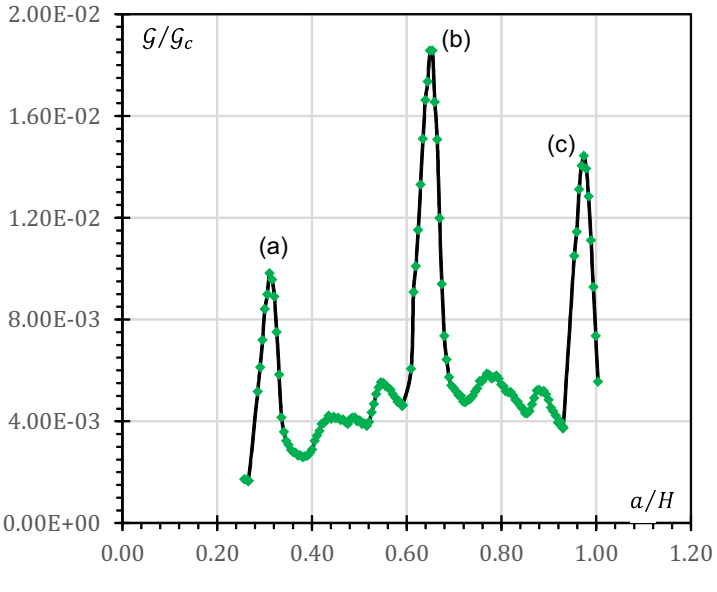

(b)

Fig. 4.25 Numerical results of the multiscale analysis for the case $e/L = 0.50$: (a) force versus prescribed vertical displacement; (b) dimensionless energy release rate for a unit load factor as a function of the crack length.

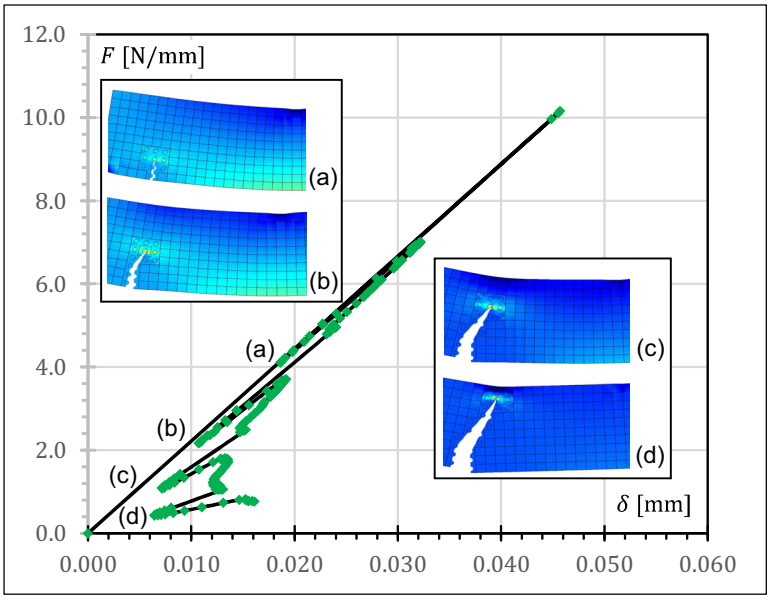

(a)

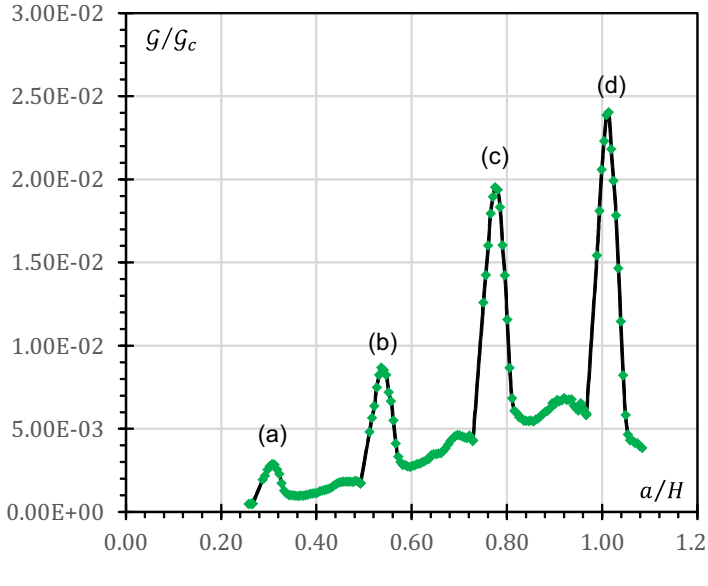

(b)

Fig. 4.26 Numerical results of the multiscale analysis for the case $e/L = 0.75$: (a) force versus prescribed vertical displacement; (b) dimensionless energy release rate for a unit load factor as a function of the crack length.

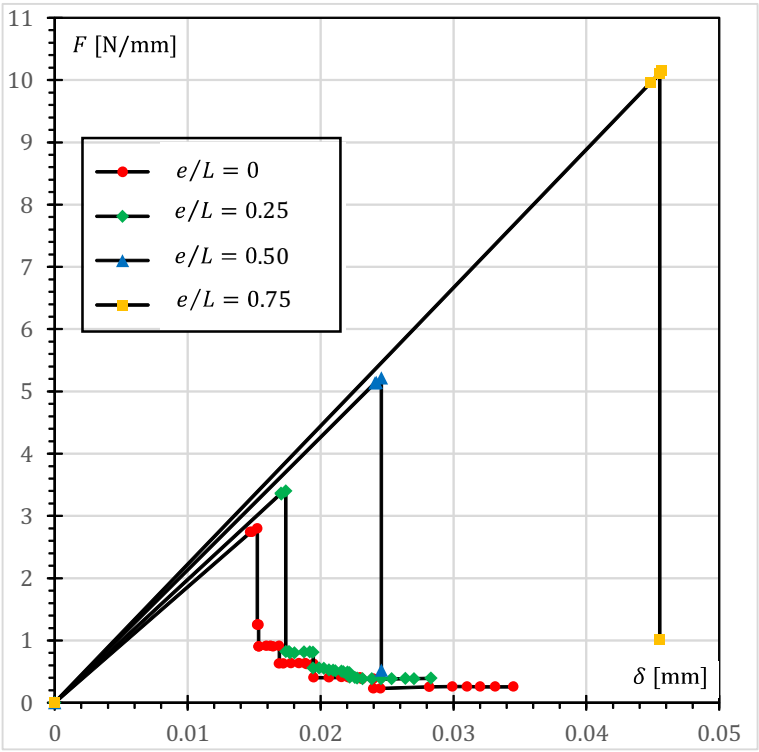

Fig. 4.27 Numerical results of the multiscale analysis for $e/L = [0, 0.25, 0.50, 0.75]$ using a displacement control scheme: force versus prescribed vertical displacement.

If a displacement control scheme is adopted, the global response for all the considered numerical tests takes the form depicted in Fig. 4.27, where the load-displacement curves have been superposed. An increase in the crack eccentricity corresponds to a slight increase in the apparent stiffness and to an increase in the load-carrying capacity. However, the benefit related to the increased strength is offset by the embrittlement of the specimen. The peak load for each considered value of crack eccentricity is reported in Table 4.3.

Table 4.3 Load peak for different values of crack eccentricity.

e/L	0	0.25	0.50	0.75
F (N/mm)	2.794	3.401	5.215	10.10

4.4.4 Comparisons with a direct numerical simulation (DNS)

In the present section, the accuracy of the proposed multiscale method is shown by means of comparisons with a direct numerical simulation, for each considered specimen. The main results are presented in Figs. from 4.28 to 4.31, with reference to the load-deflection curve and the energy release rate as a function of the total crack length. In each case, the multiscale analysis provides a very good estimation of the macroscopic structural behavior, as confirmed by the results shown in Table 4.4, which presents the absolute value of the relative percentage errors on the maximum energy release rate, the peak load, and the deflection of the loaded point corresponding to this peak.

The reported errors tend to become large as the eccentricity increases; such behavior can be easily explained if one considers that the energy release rate for $\beta_c = 1$ at the initial propagation step decreases for increasing values of e, and thus the inaccuracies associated to the numerical computation of $\mathcal{G}$ get more and more importance, as shown in Figs. 4.28b, 4.29b, 4.30b, and 4.31b.

The absolute relative percentage errors between the multiscale and the direct numerical simulations have been computed for the main failure quantities by means of the following relation:

$$\text{error} = \left| \frac{(\cdot)_{\text{MNS}} - (\cdot)_{\text{DNS}}}{(\cdot)_{\text{DNS}}} \right| \%. \tag{4.57}$$

The errors on the beam's deflection at the first peak of the load-displacement diagram are always less than 4%, which is an acceptable value for practical applications. On the other hand, the corresponding relative percentage errors

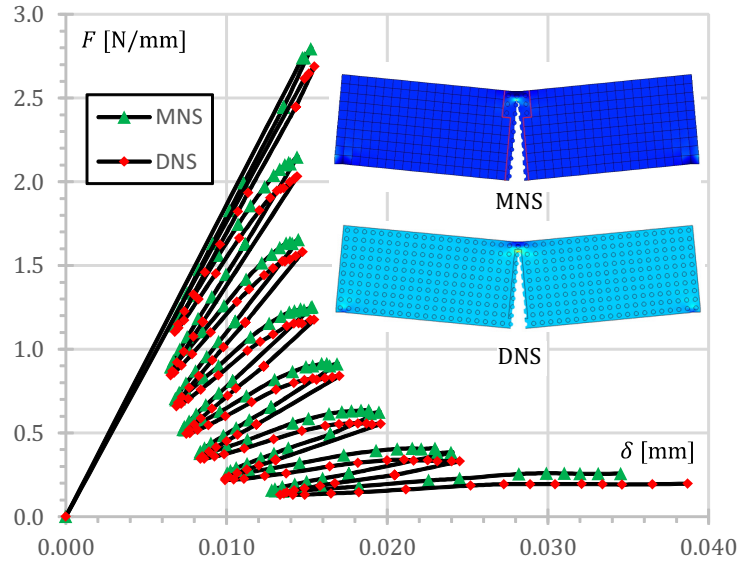

(a)

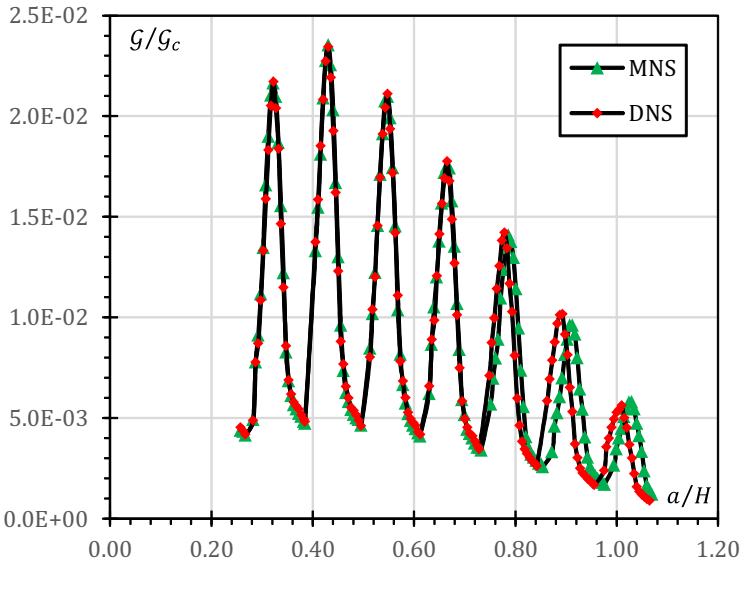

(b)

Fig. 4.28 Comparisons between the multiscale (MNS) and the direct (DNS) numerical simulations for the case $e/L = 0$: (a) force versus prescribed vertical displacement; (b) dimensionless energy release rate for a unit load factor as a function of the crack length.

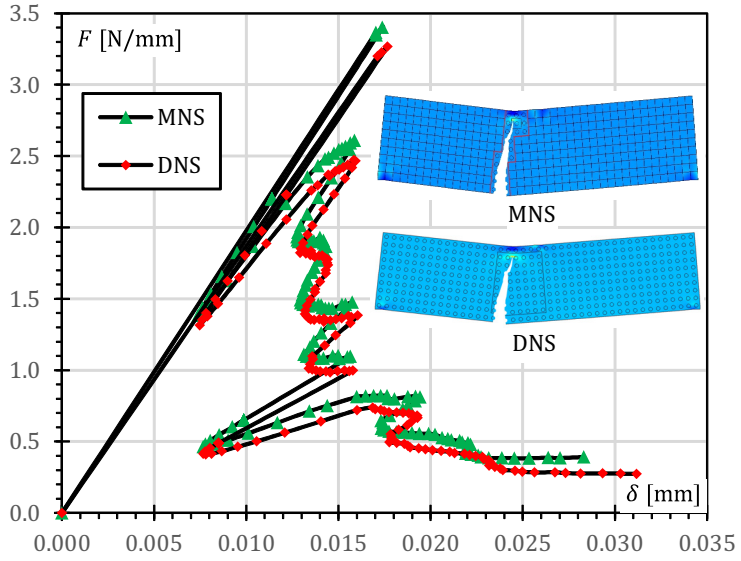

(a)

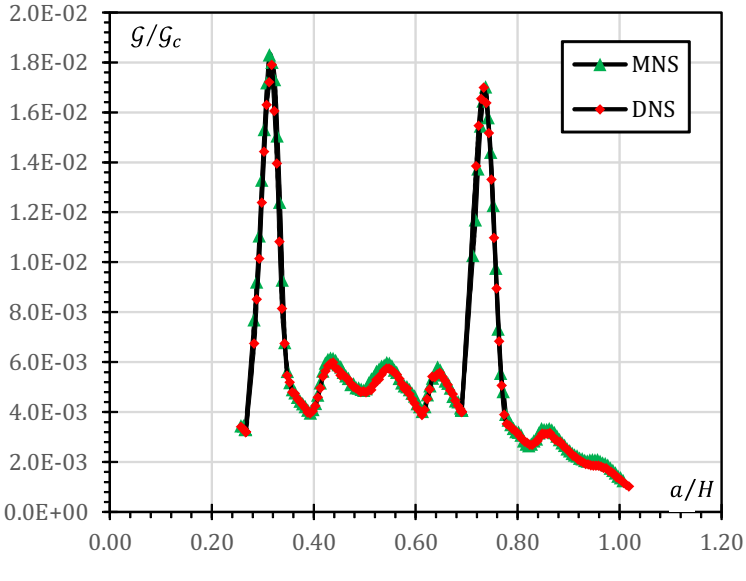

(b)

Fig. 4.29 Comparisons between the multiscale (MNS) and the direct (DNS) numerical simulations for the case $e/L = 0.25$: (a) force versus prescribed vertical displacement; (b) dimensionless energy release rate for a unit load factor as a function of the crack length.

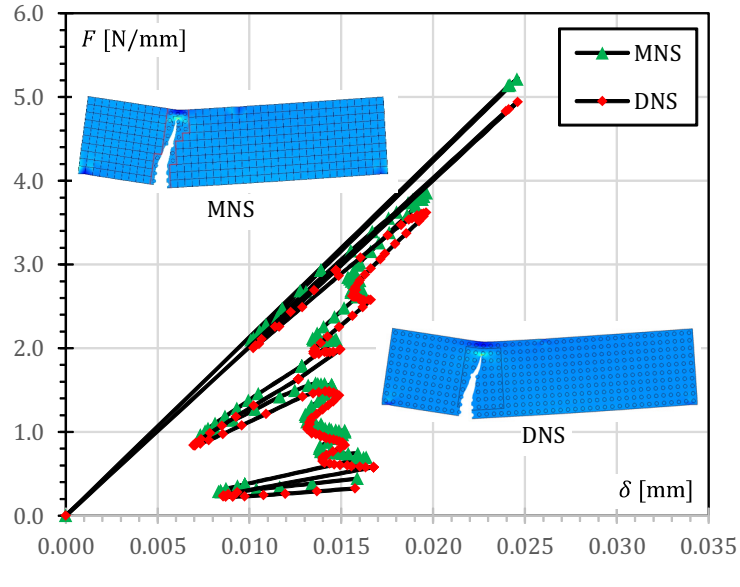

(a)

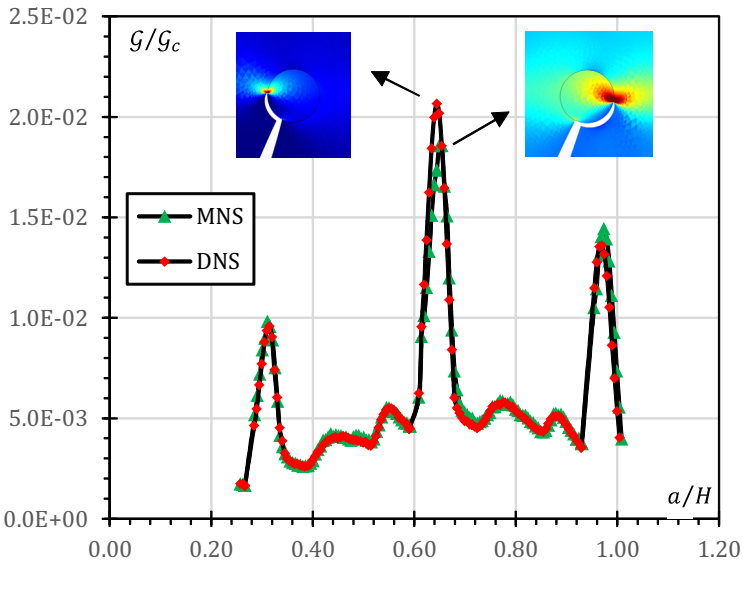

(b)

Fig. 4.30 Comparisons between the multiscale (MNS) and the direct (DNS) numerical simulations for the case $e/L = 0.50$: (a) force versus prescribed vertical displacement; (b) dimensionless energy release rate for a unit load factor as a function of the crack length.

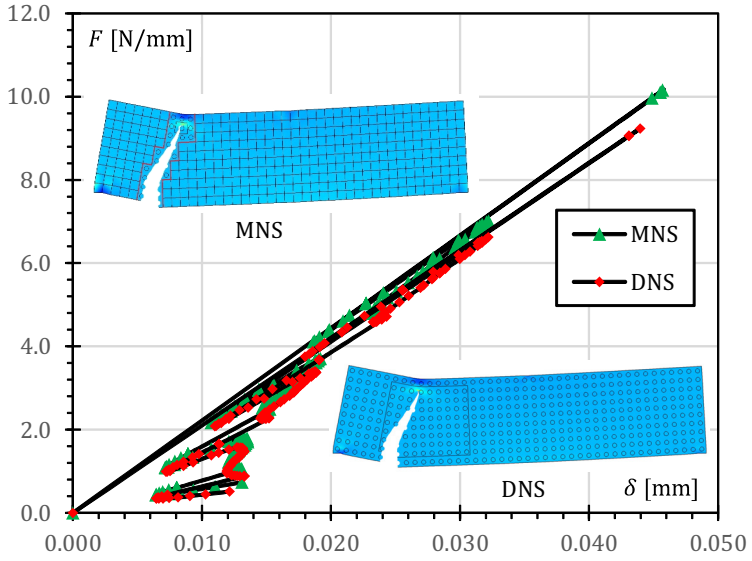

(a)

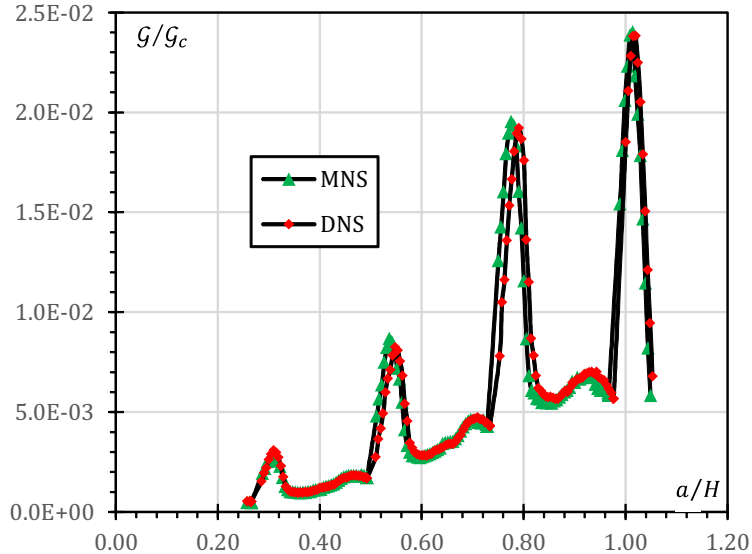

(b)

Fig. 4.31 Comparisons between the multiscale (MNS) and the direct (DNS) numerical simulations for the case $e/L = 0.75$: (a) force versus prescribed vertical displacement; (b) dimensionless energy release rate for a unit load factor as a function of the crack length.

Table 4.4 Absolute relative percentage errors between the direct and multiscale numerical simulations in terms of maximum energy release rate, peak load, and deflection at peak.

e/L	0	0.25	0.50	0.75
Error_G (%)	0.24	2.26	10.1	0.84
Error_F (%)	3.96	5.52	4.09	9.42
Error_δ (%)	1.46	0.14	1.51	3.55

on the peak load are larger, from 3.96% for $e/L = 0$ to 9.42% for $e/L = 0.75$. This behavior can be easily explained by considering that the stiffness of the beam appears to be systematically overestimated by the multiscale analysis, as shown in Figs. 4.28a, 4.29a, 4.30a and 4.31a.

Indeed two different sources of error seem to affect the accuracy of the results of the multiscale analysis: (i) a discretization error, essentially due to the coarse mesh for the regions subjected to the applied concentrated loads, and (ii) a homogenization error, related to the use of homogenized moduli, computed by assuming periodic boundary conditions everywhere, even in regions where such conditions cease to hold (transition zones, free edges, loaded boundary zones). All these errors inevitably lead to an increase in stiffness, due to the use of a poor kinematic.

Moreover, for the case $e/L = 0.50$, an abnormally high error on the peak value of the energy release rate (more than 10%), as shown in Fig. 4.30b and Table 4.4; this can be justified by the fact that the direct and the multiscale analyses refer to different equilibrium paths. These local inaccuracies consist in a different selection of the kinking direction for a crack perpendicularly approaching an interface, between the two analyses, which is essentially due to numerical errors in computing the interfacial energy release rate.

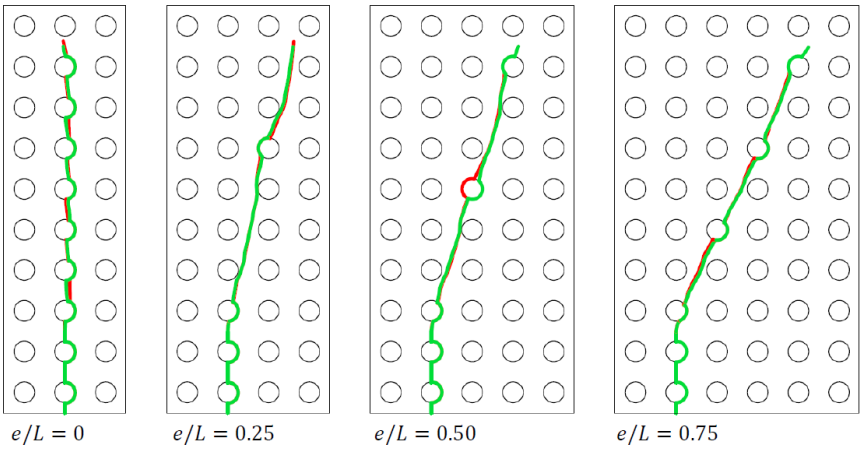

Fig. 4.32 Crack trajectories obtained by the direct (in red) and multiscale (in green) numerical simulations for different values of crack eccentricity.

In order to explore the capability of the proposed approach to predict the crack paths in composite materials, the crack trajectories obtained by the direct and the multiscale analyses for each considered crack eccentricity have been superposed, as shown in Fig. 4.32. Despite the above-mentioned local errors, the global crack paths are accurately estimated by the multiscale numerical simulation for each considered eccentricity.

4.4.5 Boundary layer effects

The numerical results reported in Section 4.4.4 have highlighted moderate inaccuracies of the proposed model in estimating the apparent stiffness of the composite, leading to an overestimation of the peak load for each considered case. In order to reduce these errors, a refined analysis is proposed, able to account for the boundary layer effects due to the presence of concentrated applied loads.

The key point of this analysis is to replace the macroelements adjacent to the loaded boundaries by a fully meshed model; therefore, the above-mentioned subdomains are added to the zone on interest, i.e. the composite regions which require a fine scale description. For the sake of brevity, only the case

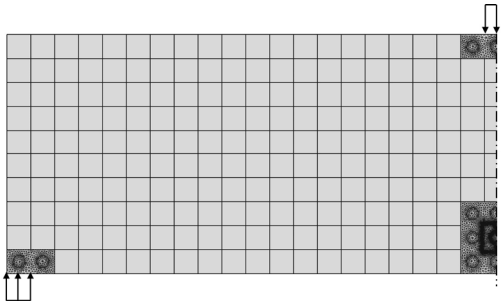

Fig. 4.33 Mesh plot of a half beam for the multiscale numerical simulation performed by accounting for the boundary layer effects.

$e/L = 0$ is reported in detail, whose initial mesh for the multiscale numerical simulation is shown in Fig. 4.33.

The main results are presented in Fig. 4.34, with reference to the load-deflection curve and the energy release rate as a function of the total crack length; the multiscale analysis provides a very accurate estimation of the macroscopic structural behavior, as confirmed by the results shown in Table 4.5, which presents the absolute value of the relative percentage errors on the peak load and the deflection of the loaded point corresponding to this peak, also for the cases of $e/L = \{0.25, 0.50, 0.75\}$.

The numerical errors on the displacement of the loaded point at peak are totally negligible, whereas the errors on the peak load are between 1.54% and 2.11%.

By comparing numerical results shown in Tables 4.4 and 4.5, it follows that accounting for the boundary layer effects leads to dramatically reduced errors on the peak quantities, against a small increase of the number of DOFs in the model.

Moreover, the results have shown that neglecting the effects due to the presence of free edges has a minimal influence on the macroscopic response of the composite structure.

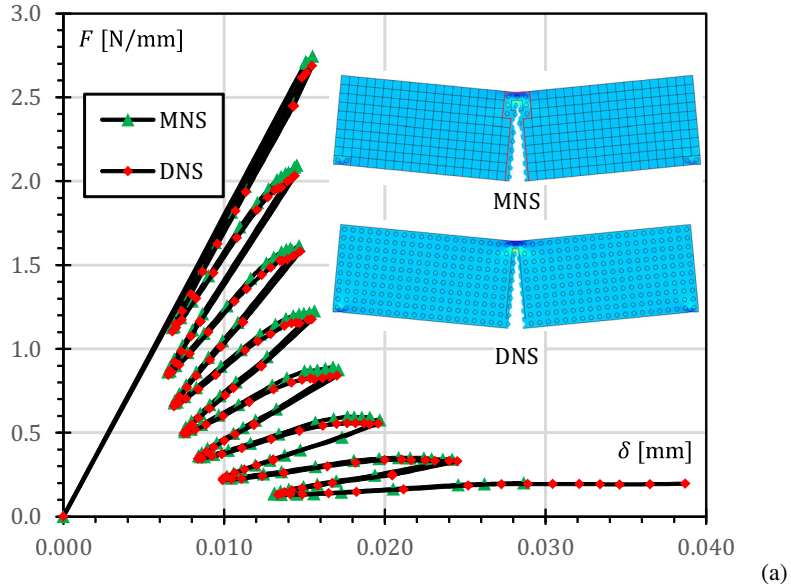

(a)

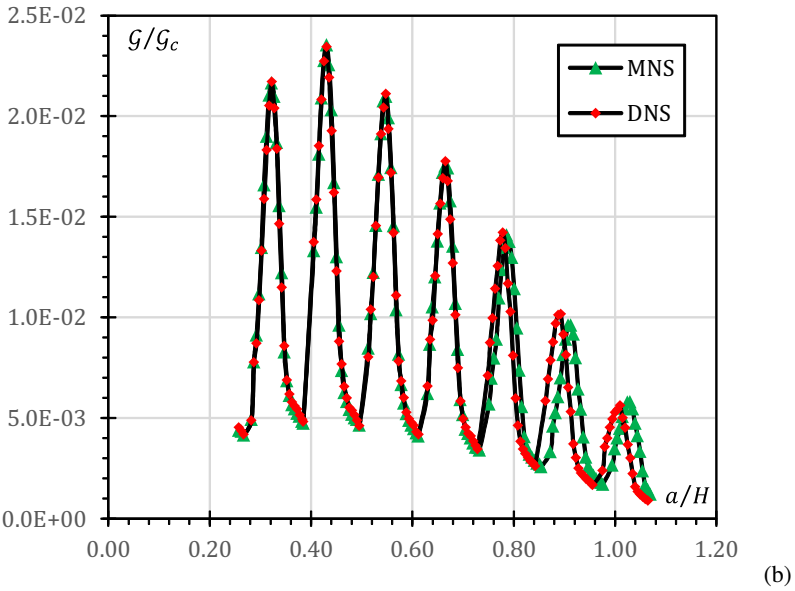

(b)

Fig. 4.34 Comparisons between the multiscale and the direct numerical simulations for the case $e/L = 0$ accounting for the boundary layer effects: (a) force versus prescribed vertical displacement; (b) dimensionless energy release rate for a unit load factor as a function of the crack length.

Table 4.5 Absolute relative percentage errors between the direct and multiscale numerical simulations accounting for the boundary layer effects, in terms of peak load and deflection at peak.

e/L	0	0.25	0.50	0.75
Error_F (%)	2.11	1.84	2.09	1.54
Error_δ (%)	0.21	0.08	0.31	0.18

5

Conclusions

In this thesis the macroscopic nonlinear mechanical response of fiber-reinforced composite materials has been investigated by using different multiscale approaches, belonging to the classes of computational homogenization methods and concurrent models.

In the first part of the thesis, a review of the different analytical and numerical strategies for modeling damage in composite materials has been presented, with reference to both macroscopic and microscopic approaches; macroscopic (or mesoscopic) approaches based on phenomenological damage models have been proved to be very efficient, but usually do not provide accurate results in the presence of complex damage patterns, involving interactions between different failure mechanisms and self-contact phenomena.

Homogenization-based models, devoted to the analytical or numerical determination of overall constitutive laws of composite materials, are more effective in the case of a prescribed damage configuration, but usually fail when dealing with more general not known *a priori* crack patterns.

Therefore, in the subsequent part of this thesis, an overview of existing multiscale methods has been provided; they form a wide class of approaches based on different modeling frameworks, sharing the coexistence of coarse-scale and fine-scale resolved domains within the same numerical model. The advantages and drawbacks of each method have been highlighted, as well their preferred field of application. In detail, computational homogenization approaches, also referred to as semiconcurrent models, are suitable when dealing with problems for which a microscopic model is needed everywhere either as a complement to or as a replacement of the macroscopic model; an example of such problems is a standard mechanical system for which a macroscopic constitutive phenomenological law is missing. The standard approach used in these cases is to couple the macro- and micro-models everywhere, and thus, the scale transition is performed over the whole computational domain. On the other hand, concurrent multiscale models are applied to the solution of problems involving local defects or singularities, such as dislocations, cracks, shocks, and boundary layers, for which a macroscopic model is sufficient for most of the physical domain, and a fine-scale model is only needed in the neighborhood of the singularities or heterogeneities. The standard approach for these problems is to use a *domain decomposition method* (DDM), since the physical domain is split in two subdomains resolved at different scales; the main task in this approach is a suitable coupling at the interface between the subdomains. It is worth noting that for this type of problems, the macro-micro coupling is localized.

Then, the influence of microstructure evolution, due to interface crack initiation and propagation under mixed-mode loading conditions, on the macroscopic constitutive response of elastic fiber-reinforced composite materials

has been investigated by using suitable homogenization techniques and multiscale models in conjunction with a classical finite element method (FEM), as described in Chapters 3 and 4.

Firstly, a novel micromechanical approach has been presented, based on homogenization theory and using stress based failure criteria in conjunction with fracture mechanics concepts, starting from results presented in [44, 54]. Crack onset within a microconstituent or at a bimaterial interface has been incorporated into the numerical model by using a coupled stress-energy criterion regarded as a generalization of the approach introduced by Leguillon [47], also taking into account the possibility of initiation of multiple cracks. The subsequent crack propagation process has been controlled by the maximum energy release rate criterion, adopted to predict incremental changes in crack path. The adopted propagation condition includes the competition between kinking and progressive interface crack under mixed-mode loading conditions. Based on the above assumptions, a novel strategy for quasi-automatic simulation of arbitrary crack propagation in 2D finite element models has been formulated which takes advantage of a generalized *J*-integral formulation and of the component separation method introduced in [55] to compute the energy release rate and the mode mixity.

Numerical applications, obtained by coupling a finite element formulation and an interface model, have been devoted to an initially undamaged inclusion/matrix system, considered as a 2D model of a fiber-reinforced composite material under transverse loading conditions. The macroscopic constitutive response of the fiber reinforced microstructure, computed for both uniaxial and shear macrostrain paths, exhibits a strong nonlinear behavior due to the changes in microstructural configuration introduced by interface crack onset and propagation and crack face contact interaction. Results have shown the stabilizing effects on the macroscopic response of mixed mode crack propagation and of contact between crack faces. The influence of interfacial toughness on macroscopic constitutive response has been analyzed, showing that an increase in the interface toughness leads to an increase in the strength of the

composite material, favoring, at the same time, kinking over continued interface cracking. Then, numerical simulations have been carried out for a prescribed uniaxial tensile macrostrain path, in order to investigate the size effect related to the inclusion diameter and to fiber volume fraction, on the macroscopic constitutive response. Computations have demonstrated that decreasing the size of the inclusion leads to increasing the mechanical strength of the composite system and gives a stabilizing influence on its macroscopic response. These results are essentially in agreement with those obtained in the literature, although, contrarily to the present thesis, the majority of these studies does not analyze the complete process of crack initiation and subsequent propagation. Moreover, numerical developments carried out in the context of generalized plane strain conditions, have shown the notable influence of loading along the fiber direction on the macroscopic properties of the composite, leading to an increase in composite strength up to 62% when a compressive out-of-plane macrostrain having the same magnitude of the transverse one, is imposed.

The validity of the approach proposed to compute energy release rate and fracture mode mixity for an interface crack and to analyze kinking out of an interface debonding leaving the interface and penetrating into the matrix, has been assessed through comparisons with existing models. These comparisons have shown a reasonable agreement in terms of energy release rate, fracture mode mixity and kinking angles.

It follows that the proposed homogenized model can be useful to improve the ability of predicting failure due to microcrack initiation and propagation and, consequently, can be of notable importance for the design and assessment of composite structures. However, as widely discussed in Chapter 3, more sophisticate approaches are needed in the presence of strain localization phenomena associated with the formation of a complex crack pattern within the composite material.

In order to overcome the limitations of classical homogenization techniques, two different multiscale approaches have been presented, able to simulate the strongly nonlinear response of composite materials characterized by

evolving microstructures due to crack initiation and propagation, together with contact phenomena. Both approaches, belonging to the classes of semi-concurrent and concurrent multiscale methods, respectively, have been proved to be more effective in the case of mixed-mode crack propagation along arbitrary paths which are not known a priori.

The first approach consists in a two-scale model for the failure analyses of locally periodic fiber-reinforced composites, in which the coupling between the macro- and micro-scales is obtained by using a unit cell model with evolving microstructure due to mixed-mode crack initiation and propagation at fiber/matrix interface. To this end original computational techniques have been introduced to perform the localization and homogenization exchanges between the two scales during microstructural damage evolution. By means of the proposed techniques local failure quantities, such as fiber/matrix interfacial stresses, energy release and mode mixity for an interface crack, can be accurately predicted in an arbitrary cell by using the results of the macroscale analysis and, consequently, can be used to predict crack initiation and propagation at the fiber/matrix interface. As in the previous approach, crack initiation process has been studied by using a generalization of the coupled stress- and energy-based failure criterion to the case of mixed-mode interface fracture, whereas crack propagation has been analyzed by means of a mode mixity dependent fracture criterion taking advantage of the above-mentioned generalization of the *J*-integral technique in combination with the component separation method. The macroscopic description of the constitutive law based on unit cell calculations is based on a secant formulation of the nonlinear constitutive law.

The nonlinear homogenized constitutive response of the composite solid has been determined by using a deformation-controlled approach and the micro-to-macro transition is performed by adopting periodic boundary conditions. A finite element formulation incorporating a novel strategy for automatic simulation of arbitrary crack initiation has been developed for two-dimensional composite structures. The numerical multiscale model consists in a macroscopic model of the composite structure and in unit cell models linked

by means of appropriate displacement boundary conditions derived from the macroscale solution, with the corresponding regions of the macroscopic structure. Microstructural evolution due to crack initiation and propagation is locally analyzed at the level of the unit cell.

In order to investigate the accuracy of the method in the prediction of failure mechanisms related to the interfacial crack growth at microstructural level, comparisons with direct numerical simulations have been developed for a fiber-reinforced composite structure with initially undamaged fibers, as discussed in Section 3.6. The fully-meshed numerical model adopts a fine scale modeling of the composite microstructure and therefore is considered as a reference analysis to evaluate the effectiveness of the proposed multi-scale method. Two different macroscopic structural configurations have been considered for numerical tests: a 2D heterogeneous beam model, discussed in Section 3.6.1, and a more general solid structure (whose dimensions are of the same order of magnitude), described in Section 3.6.2.

The first considered structure is composed of a rectangular arrangement of 5×40 unit cells. The specimen is clamped at one end and is subjected to two alternative macroscopic loading conditions at the opposite end leading to macroscopic pure bending and combined shear and bending, respectively. The first loading conditions leads to quasi-uniform macroscopic gradients.

Comparisons between the multiscale and the direct numerical simulations have shown that for the relative percentage errors of both local and global failure properties are reasonably small and generally decrease for global boundary conditions involving uniform macroscopic gradients. Moreover, results have shown that changes in macroscopic properties due to microstructure evolution during crack onset are negligible. On the contrary, these changes cannot be neglected when crack propagation must be analyzed. Both the macroscopic load-deflection curves (moment-rotation or shear force-deflection diagrams in the case of pure bending or combined shear and bending, respectively) have shown that the macroscopic response of the composite is characterized by a severe snap-back behavior and a subsequent snap-through. Ac-

cordingly, the macroscopic constitutive response has an initially unstable behavior followed by a stable one with the consequent possibility of crack arrest for a prescribed load factor.

Furthermore, results highlight a reasonable accuracy in the prediction of the macroscopic load-deflection curve and the errors in the prediction of the peak loads are within 6% about, with smaller discrepancies for the pure bending case.

The local crack path in the critical unit cell predicted by the multiscale solution may show moderate discrepancies in comparison with that of the direct simulation. At crack onset the errors in the location of the onset point at fiber/matrix interface and in the total crack angle within about 6% and 1%, respectively, with slightly smaller errors in the pure bending case, although larger errors are shown for the partial crack angles. In the case of the pure bending loading condition, the multiscale analysis is not able to detect the same critical unit cell predicted by the direct simulation, because of the quasi-uniformity of the stress and strain distributions and owing to the approximations related to the homogenization/localization process. However, the macroscopic failure behavior of the composite beam in pure bending is scarcely influenced by the location of the damaging cell. On the contrary, the same critical cell is predicted in both the direct and the multiscale numerical simulations, in the case of combined shear and bending.

The errors in the fiber/matrix interface stresses at the load level corresponding to crack initiation, playing an important role in determining the location of the crack onset point, are generally small and within 4%, except in the case of the combined shear and bending where errors increase up to about 13%. On the contrary, the errors in the peak values of the dimensionless energy release rate are larger for the pure bending case but remain always within about 6%. The macroscopic load-deflection curves show a small sensitivity of the macroscopic stiffness due to the fact that crack initiation and propagation phenomena are located inside only one unit cell and to the assumption that damage growth occurs at the fiber/matrix interface. The former assumption has been verified by carrying out interfacial stress analyses in order to find

other possible onset points and results showed that the application of the stress-based criterion cannot lead to locating other crack sites, because of the unstable nature of crack propagation process leading to a sudden unloading after crack initiation which prevents damage occurring in other unit cells.

The second considered structure is composed of a regular arrangement of 10×10 unit cells and subjected to two alternative global boundary conditions, involving uniform and non-uniform macroscopic stress and strain gradients, respectively.

Numerical results obtained for the first type of boundary conditions have shown that the direct and multiscale numerical simulations give practically the same values for interfacial stresses; this is essentially due to the minimal perturbing effect of boundary layers. As a consequence, also the critical load factor at crack onset is well estimated, with very small absolute relative percentage errors (of about 0.34%).

On the other hand, the application of the second type of boundary conditions is associate with higher numerical errors with reference to both interfacial stresses and critical load factor at onset (which are, however, less than 10%).

It is worth noting that, in general, when kinking and percolation effects must be taken into account, a multi-site crack initiation and propagation analysis must be performed leading to a more sophisticated multi-scale model. In this case the global stiffness can change notably during the unstable regime. For instance, when a crack reaches a boundary, the displacement jump violates the periodic conditions on that boundary, and so special multiscale models are needed to move from micro-diffusive damage to macrocracks.

Moreover, the proposed computational homogenization scheme is quite expensive in terms of computational time and memory usage since several microscopic boundary value problems are sequentially solved for each loading step of the incremental procedure; however, the computational effort can be significantly reduced by taking advantage of parallelization, since the above-mentioned problem are not coupled each other.

In Chapter 4, an alternative approach is presented, consisting in an adaptive concurrent multiscale method, able to perform a complete failure analysis of composite materials undergoing microcrack propagation and other nonlinear phenomena. The complex microstructural damage have been investigated, by incorporating into the multiscale model the competition between different damage mechanisms in fiber-reinforced structures, such as interfacial debonding and matrix cracking. To this end a strategy to predict the fracture path has been developed, based on a moving mesh approach and a crack length control scheme, within the LEFM framework.

A two-way strong coupling between the different scales is invoked by means of a non-overlapping multilevel domain decomposition method, which assumes a fine scale model embedded into the macroscopic model at some zones of interest, i.e. the regions subjected to microstructural damage phenomena. The adaptive capabilities of the proposed approach are used to continuously update the domain decomposition during the damage evolution, thus keeping a balance between accuracy and computational efficiency.

The moving mesh approach proposed in this work enforces the maximum energy release rate criterion as a particular form of shape optimization problem, leading to achieve a high efficiency during the crack propagation process. Furthermore, the crack length control scheme used to enforce Griffith's criterion enables us to follow the unstable branches of the equilibrium path, which are very common for composite structures characterized by a brittle behavior.

Numerical calculations have been performed with reference to the failure analysis of a fiber-reinforced composite beam subjected to a three-point bending test with different values of the (dimensionless) eccentricity e/L of the initial crack. The validity of the proposed multiscale model has been assessed by comparing such numerical results with those obtained by means of a direct analysis, considered as a reference solution. Numerical results show a good accuracy (with errors in terms of load factor ranging from 0.14% and 3.55%), which demonstrates the ability of the proposed method in handling problems involving damage in large composite structures.

The absolute value of the relative percentage error in terms of maximum energy release rate reached during the crack propagation history is also very small, ranging from 0.24 to 2.26, except for $e/L = 0.50$; in this case the maximum energy release rates in the direct and multiscale numerical simulations refer to different crack trajectories, due to different deflection directions followed by the crack terminating at the interface.

Furthermore, additional numerical calculations (not reported for the sake of brevity) carried out by using the mortar connection instead of the collocation method produce results very close to those shown in this work, with practically negligible percentage errors. This insensitivity to the type of micro-macro connection is an indicator of the efficacy of the proposed adaptive scheme, which is uniquely based on the crack geometric configuration.

However, as already discussed in Section 4.4.4, the comparisons between the direct and multiscale analyses show a systematic overestimation of the global stiffness of the considered structure, highlighting the limitations of the proposed approach when practical structural problems have to be solved. In fact, relative percentage errors on the peak load, regarded as the sum of discretization and homogenization errors, are of about 5% in most cases, except than for the case $e/L = 0.75$ (in which this error, however, does not exceed 10%); these inaccuracies are essentially related to the boundary layer effects due to the presence of concentrated loads on the specimen.

In fact, the last numerical results of this thesis, shown in Section 4.4.5, have highlighted that adding the regions adjacent to the loaded boundaries to the set of the fully meshed zones lead to a dramatic reduction of numerical errors for the multiscale analyses, against a small increase in the number of DOFs.

As a consequence, additional investigations starting from this results are needed to include the boundary layer effects within the proposed multiscale model in a systematic manner. Two different directions can be followed to this end: the first approach consists in defining boundary layer correctors to be applied to boundary zones where periodic homogenization is employed, following other works present in the literature (see, for instance, [215]); the latter

one concerns the introduction of a periodicity indicator into the concurrent model, able to switch from the macroscopic to the microscopic discretization also near to the boundaries, where the assumption of periodic distribution of micro-fields ceases to hold.

A further extension of this thesis is to develop a more general multiscale framework for dealing with strain localization, damage and crack propagation phenomena in composite structures in a unified manner, involving also boundary layer effects and contact phenomena between crack faces. According to this perspective, the following improvements of the proposed models are suggested, which are susceptible to be addressed in future works.

- Investigate the possibility of implementing a large strain formulation approach in a multiscale setting.

- Extend the multiscale formulation to multiple crack initiation and propagation, and reduce the computational cost related to the global remeshing performed at each crack propagation step.

- Develop more sophisticated switching criteria between the different modeling levels, incorporating also a zoom-out procedure for already damaged regions that exhibit unloading; an element erosion scheme is believed to be a suitable method for reducing the number of degrees of freedom, especially in the presence of extended damaging zones with respect to the global domain size.

- Develop an adaptive hybrid semiconcurrent-concurrent multiscale method, able to incorporate the advantages of both proposed methods; the final aim of this future perspective of research is to develop complete failure analyses characterized by diffuse damage before the structural collapse due to strain localization at the macroscopic scale, performed reducing the zoomed-in regions to a minimum.

Bibliography

[1] T. Triantafillou, and C. Antonopoulos, "Design of Concrete Flexural Members Strengthened in Shear with FRP," *Journal of Composites for Construction,* vol. 4, no. 4, pp. 198-205, 2000.

[2] J. Chen, and J. Teng, "Shear Capacity of Fiber-Reinforced Polymer-Strengthened Reinforced Concrete Beams: Fiber Reinforced Polymer Rupture," *Journal of Structural Engineering,* vol. 129, no. 5, pp. 615-625, 2003.

[3] O. Buyukozturk, O. Gunes, and E. Karaca, "Progress on understanding debonding problems in reinforced concrete and steel members strengthened using FRP composites," *Construction and Building Materials,* vol. 18, no. 1, pp. 9-19, 2004.

[4] J. Teng, J. Chen, and S. Smith, "Debonding Failures in FRP-Strengthened RC Beams: Failure Modes, Existing Research and Future Challenges," *Composites in Construction*, pp. 139-148.

[5] D. Bruno, R. Carpino, and F. Greco, "Modelling of mixed mode debonding in externally FRP reinforced beams," *Composites Science and Technology,* vol. 67, no. 7–8, pp. 1459-1474, 2007.

[6] E. J. Barbero, *Introduction to Composite Materials Design, Second Edition*: Taylor & Francis, 2010.

[7] D. Bruno, F. Greco, and P. Lonetti, "A fracture-ALE formulation to predict dynamic debonding in FRP strengthened concrete beams," *Composites Part B: Engineering,* vol. 46, no. 0, pp. 46-60, 2013.

[8] P. O. Bouchard, F. Bay, and Y. Chastel, "Numerical modelling of crack propagation: automatic remeshing and comparison of different criteria," *Computer Methods in Applied Mechanics and Engineering,* vol. 192, no. 35–36, pp. 3887-3908, 2003.

[9] F. París, E. Correa, and V. Mantič, "Kinking of Transversal Interface Cracks Between Fiber and Matrix," *Journal of Applied Mechanics,* vol. 74, no. 4, pp. 703-716, 2006.

[10] D. B. P. Huynh, and T. Belytschko, "The extended finite element method for fracture in composite materials," *International Journal for Numerical Methods in Engineering,* vol. 77, no. 2, pp. 214-239, 2009.

[11] S. Ghosh, Y. Ling, B. Majumdar *et al.*, "Interfacial debonding analysis in multiple fiber reinforced composites," *Mechanics of Materials,* vol. 32, no. 10, pp. 561-591, 2000.

[12] F. Pérales, Y. Monerie, F. Dubois *et al.*, "Numerical simulation of dynamical fracture in heterogeneous materials," in K.S. Bathe, pp. 437-441.

[13] D. Yang, Y. Sheng, J. Ye *et al.*, "Dynamic simulation of crack initiation and propagation in cross-ply laminates by DEM," *Composites Science and Technology,* vol. 71, no. 11, pp. 1410-1418, 2011.

[14] L. M. Kachanov, "Rupture time under creep conditions," *International Journal of Fracture,* vol. 97, no. 1-4, pp. 11-18, 1999.

[15] J.-L. Chaboche, "A continuum damage theory with anisotropic and unilateral damage," *La Recherche Aérospatiale*, no. 2, pp. 139-147, 1995.

[16] M. Ortiz, "A constitutive theory for the inelastic behavior of concrete," *Mechanics of Materials,* vol. 4, no. 1, pp. 67-93, 1985.

[17] P. Ladevèze, O. Allix, J.-F. Deü *et al.*, "A mesomodel for localisation and damage computation in laminates," *Computer Methods in Applied Mechanics and Engineering,* vol. 183, no. 1–2, pp. 105-122, 2000.

[18] E. J. B. Lonetti, Paolo, "Damage model for composites defined in terms of available data," *Mechanics of Composite Materials and Structures,* vol. 8, no. 4, pp. 299-315, 2001.

[19] G. Papanicolau, A. Bensoussan, and J.-L. Lions, *Asymptotic analysis for periodic structures*: Access Online via Elsevier, 1978.

[20] E. Sánchez-Palencia, *Non-homogeneous media and vibration theory*: Springer-Verlag, 1980.

[21] M. Hori, and S. Nemat-Nasser, "On two micromechanics theories for determining micro–macro relations in heterogeneous solids," *Mechanics of Materials,* vol. 31, no. 10, pp. 667-682, 1999.

[22] I. M. Gitman, H. Askes, and L. J. Sluys, "Representative volume: Existence and size determination," *Engineering Fracture Mechanics,* vol. 74, no. 16, pp. 2518-2534, 2007.

[23] V. Kouznetsova, M. G. D. Geers, and W. A. M. Brekelmans, "Multi-scale constitutive modelling of heterogeneous materials with a gradient-enhanced computational homogenization scheme," *International*

Journal for Numerical Methods in Engineering, vol. 54, no. 8, pp. 1235-1260, 2002.

[24] V. G. Kouznetsova, M. G. D. Geers, and W. A. M. Brekelmans, "Multi-scale second-order computational homogenization of multi-phase materials: a nested finite element solution strategy," *Computer Methods in Applied Mechanics and Engineering,* vol. 193, no. 48–51, pp. 5525-5550, 2004.

[25] T. Belytschko, S. Loehnert, and J.-H. Song, "Multiscale aggregating discontinuities: A method for circumventing loss of material stability," *International Journal for Numerical Methods in Engineering,* vol. 73, no. 6, pp. 869-894, 2008.

[26] V. Phu Nguyen, O. Lloberas-Valls, M. Stroeven *et al.*, "On the existence of representative volumes for softening quasi-brittle materials–a failure zone averaging scheme," *Computer Methods in Applied Mechanics and Engineering,* vol. 199, no. 45, pp. 3028-3038, 2010.

[27] T. Belytschko, and J.-H. Song, "Coarse-graining of multiscale crack propagation," *International Journal for Numerical Methods in Engineering,* vol. 81, no. 5, pp. 537-563, 2010.

[28] M. Hain, and P. Wriggers, "Numerical homogenization of hardened cement paste," *Computational Mechanics,* vol. 42, no. 2, pp. 197-212, 2008.

[29] F. Feyel, and J.-L. Chaboche, "FE2 multiscale approach for modelling the elastoviscoplastic behaviour of long fibre SiC/Ti composite materials," *Computer Methods in Applied Mechanics and Engineering,* vol. 183, no. 3–4, pp. 309-330, 2000.

[30] I. Gitman, H. Askes, and L. Sluys, "Coupled-volume multi-scale modelling of quasi-brittle material," *European Journal of Mechanics-A/Solids,* vol. 27, no. 3, pp. 302-327, 2008.

[31] F. Greco, and G. Sgambitterra, "Validation of Homogenization Techniques for Locally Periodic Fiber-reinforced Composites with Interfacial Debonding," *Mechanics of Advanced Materials and Structures,* vol. 20, no. 8, pp. 638-651, 2013.

[32] H. B. Dhia, and G. Rateau, "The Arlequin method as a flexible engineering design tool," *International Journal for Numerical Methods in Engineering,* vol. 62, no. 11, pp. 1442-1462, 2005.

[33] C. Farhat, M. Lesoinne, P. LeTallec *et al.*, "FETI-DP: a dual–primal unified FETI method—part I: A faster alternative to the two-level FETI method," *International journal for numerical methods in engineering,* vol. 50, no. 7, pp. 1523-1544, 2001.

[34] M. Xu, R. Gracie, and T. Belytschko, "A continuum-to-atomistic bridging domain method for composite lattices," *International Journal for Numerical Methods in Engineering,* vol. 81, no. 13, pp. 1635-1658, 2010.

[35] S. Ghosh, J. Bai, and P. Raghavan, "Concurrent multi-level model for damage evolution in microstructurally debonding composites," *Mechanics of Materials,* vol. 39, no. 3, pp. 241-266, 2007.

[36] D. Sohn, J. H. Lim, Y.-S. Cho *et al.*, "Finite element analysis of quasistatic crack propagation in brittle media with voids or inclusions," *Journal of Computational Physics,* vol. 230, no. 17, pp. 6866-6899, 2011.

[37] F. J. Vernerey, and M. Kabiri, "An adaptive concurrent multiscale method for microstructured elastic solids," *Computer Methods in Applied Mechanics and Engineering,* vol. 241–244, no. 0, pp. 52-64, 2012.

[38] O. Lloberas-Valls, D. J. Rixen, A. Simone *et al.*, "Domain decomposition techniques for the efficient modeling of brittle

heterogeneous materials," *Computer Methods in Applied Mechanics and Engineering,* vol. 200, no. 13–16, pp. 1577-1590, 2011.

[39] S. Rudraraju, A. Salvi, K. Garikipati *et al.*, "Predictions of crack propagation using a variational multiscale approach and its application to fracture in laminated fiber reinforced composites," *Composite Structures,* vol. 94, no. 11, pp. 3336-3346, 2012.

[40] Y. F. Xing, Y. Yang, and X. M. Wang, "A multiscale eigenelement method and its application to periodical composite structures," *Composite Structures,* vol. 92, no. 9, pp. 2265-2275, 2010.

[41] Y. X. Zhang, and H. S. Zhang, "Multiscale finite element modeling of failure process of composite laminates," *Composite Structures,* vol. 92, no. 9, pp. 2159-2165, 2010.

[42] S. F. Zheng, M. Denda, and G. J. Weng, "Interfacial partial debonding and its influence on the elasticity of a two-phase composite," *Mechanics of Materials,* vol. 32, no. 12, pp. 695-709, 2000.

[43] S. Li, G. Wang, and E. Morgan, "Effective elastic moduli of two dimensional solids with distributed cohesive microcracks," *European Journal of Mechanics - A/Solids,* vol. 23, no. 6, pp. 925-933, 2004.

[44] D. Bruno, F. Greco, P. Lonetti *et al.*, "Influence of micro-cracking and contact on the effective properties of composite materials," *Simulation Modelling Practice and Theory,* vol. 16, no. 8, pp. 861-884, 2008.

[45] T. Matsuda, D. Okumura, N. Ohno *et al.*, "Three-dimensional microscopic interlaminar analysis of cross-ply laminates based on a homogenization theory," *International Journal of Solids and Structures,* vol. 44, no. 25–26, pp. 8274-8284, 2007.

[46] D. Bruno, F. Greco, and P. Lonetti, "A 3D delamination modelling technique based on plate and interface theories for laminated structures," *European Journal of Mechanics - A/Solids,* vol. 24, no. 1, pp. 127-149, 2005.

[47] D. Leguillon, "Strength or toughness? A criterion for crack onset at a notch," *European Journal of Mechanics-A/Solids,* vol. 21, no. 1, pp. 61-72, 2002.

[48] Z. Yosibash, E. Priel, and D. Leguillon, "A failure criterion for brittle elastic materials under mixed-mode loading," *International Journal of Fracture,* vol. 141, no. 1-2, pp. 291-312, 2006.

[49] V. Mantič, "Interface crack onset at a circular cylindrical inclusion under a remote transverse tension. Application of a coupled stress and energy criterion," *International Journal of Solids and Structures,* vol. 46, no. 6, pp. 1287-1304, 2009.

[50] E. Riks, "An incremental approach to the solution of snapping and buckling problems," *International Journal of Solids and Structures,* vol. 15, no. 7, pp. 529-551, 1979.

[51] R. de Borst, "Computation of post-bifurcation and post-failure behavior of strain-softening solids," *Computers & Structures,* vol. 25, no. 2, pp. 211-224, 1987.

[52] Z. Chen, and H. L. Schreyer, "A numerical solution scheme for softening problems involving total strain control," *Computers & Structures,* vol. 37, no. 6, pp. 1043-1050, 1990.

[53] C. V. Verhoosel, J. J. Remmers, and M. A. Gutiérrez, "A dissipation-based arc-length method for robust simulation of brittle and ductile failure," *International journal for numerical methods in engineering,* vol. 77, no. 9, pp. 1290-1321, 2009.

[54] F. Greco, "Homogenized mechanical behavior of composite micro-structures including micro-cracking and contact evolution," *Engineering Fracture Mechanics,* vol. 76, no. 2, pp. 182-208, 2009.

[55] T. Nishioka, S. Syano, and T. Fujimoto, "Concepts of separated J-lntegrals, separated energy release rates, and the component separation

method of the J-integral for interfacial fracture mechanics," *Journal of applied mechanics,* vol. 70, no. 4, pp. 505-516, 2003.

[56] A. Carpinteri, "Cusp catastrophe interpretation of fracture instability," *Journal of the Mechanics and Physics of Solids,* vol. 37, no. 5, pp. 567-582, 1989.

[57] C. Farhat, J. Mandel, and F. X. Roux, "Optimal convergence properties of the FETI domain decomposition method," *Computer methods in applied mechanics and engineering,* vol. 115, no. 3, pp. 365-385, 1994.

[58] P. Thoutireddy, and M. Ortiz, "A variational r-adaption and shape-optimization method for finite-deformation elasticity," *International Journal for Numerical Methods in Engineering,* vol. 61, no. 1, pp. 1-21, 2004.

[59] F. Fraternali, "Free discontinuity finite element models in two-dimensions for in-plane crack problems," *Theoretical and Applied Fracture Mechanics,* vol. 47, no. 3, pp. 274-282, 2007.

[60] A. L. Garcia, J. B. Bell, W. Y. Crutchfield *et al.*, "Adaptive Mesh and Algorithm Refinement Using Direct Simulation Monte Carlo," *Journal of Computational Physics,* vol. 154, no. 1, pp. 134-155, 1999.

[61] P. Raghavan, and S. Ghosh, "Concurrent multi-scale analysis of elastic composites by a multi-level computational model," *Computer methods in applied mechanics and engineering,* vol. 193, no. 6, pp. 497-538, 2004.

[62] R. M. Jones, *Mechanics Of Composite Materials*: Taylor & Francis, 1998.

[63] CNR, "Istruzioni per la Progettazione, l'Esecuzione ed il Controllo di Interventi di Consolidamento Statico mediante l'utilizzo di Compositi Fibrorinforzati - Prima revisione," 2012.

[64] G. Lubin, and S. T. Peters, *Handbook of Composites*: Chapman & Hall, 1998.

[65] A. A. Griffith, “The phenomena of rupture and flow in solids,” *Philosophical transactions of the royal society of london. Series A, containing papers of a mathematical or physical character,* vol. 221, pp. 163-198, 1921.

[66] E. K. Gamstedt, and B. A. Sjögren, “Micromechanisms in tension-compression fatigue of composite laminates containing transverse plies,” *Composites Science and Technology,* vol. 59, no. 2, pp. 167-178, 1999.

[67] C.-H. Hsueh, “Interfacial debonding and fiber pull-out stresses of fiber-reinforced composites,” *Materials Science and Engineering: A,* vol. 123, no. 1, pp. 1-11, 1990.

[68] J. W. Hutchinson, and H. M. Jensen, “Models of fiber debonding and pullout in brittle composites with friction,” *Mechanics of Materials,* vol. 9, no. 2, pp. 139-163, 1990.

[69] D. T. G. Katerelos, J. Varna, and C. Galiotis, “Energy criterion for modelling damage evolution in cross-ply composite laminates,” *Composites Science and Technology,* vol. 68, no. 12, pp. 2318-2324, 2008.

[70] C. A. Wood, and W. L. Bradley, “Determination of the effect of seawater on the interfacial strength of an interlayer E-glass/graphite/epoxy composite by in situ observation of transverse cracking in an environmental SEM,” *Composites Science and Technology,* vol. 57, no. 8, pp. 1033-1043, 1997.

[71] Z. Hashin, “Analysis of cracked laminates: a variational approach,” *Mechanics of Materials,* vol. 4, no. 2, pp. 121-136, 1985.

[72] P. Ladeveze, and E. LeDantec, “Damage modelling of the elementary ply for laminated composites,” *Composites Science and Technology,* vol. 43, no. 3, pp. 257-267, 1992.

[73] N. J. Pagano, “On the micromechanical failure modes in a class of ideal brittle matrix composites. Part 1. Coated-fiber composites,” *Composites Part B: Engineering,* vol. 29, no. 2, pp. 93-119, 1998.

[74] N. J. Pagano, “On the micromechanical failure modes in a class of ideal brittle matrix composites. Part 2. Uncoated-fiber composites,” *Composites Part B: Engineering,* vol. 29, no. 2, pp. 121-130, 1998.

[75] J.-K. Kim, and Y.-w. Mai, “High strength, high fracture toughness fibre composites with interface control—A review,” *Composites Science and Technology,* vol. 41, no. 4, pp. 333-378, 1991.

[76] B. Budiansky, “Micromechanics,” *Computers & Structures,* vol. 16, no. 1–4, pp. 3-12, 1983.

[77] F. Greco, P. Lonetti, and R. Zinno, “An analytical delamination model for laminated plates including bridging effects,” *International Journal of Solids and Structures,* vol. 39, no. 9, pp. 2435-2463, 2002.

[78] R. B. Pipes, and N. Pagano, “Interlaminar stresses in composite laminates under uniform axial extension,” *Journal of Composite Materials,* vol. 4, no. 4, pp. 538-548, 1970.

[79] A. Diaz Diaz, J.-F. Caron, and A. Ehrlacher, “Analytical determination of the modes I, II and III energy release rates in a delaminated laminate and validation of a delamination criterion,” *Composite Structures,* vol. 78, no. 3, pp. 424-432, 2007.

[80] R. P. Carreira, J.-F. Caron, and A. Diaz Diaz, “Model of multilayered materials for interface stresses estimation and validation by finite element calculations,” *Mechanics of materials,* vol. 34, no. 4, pp. 217-230, 2002.

[81] G. Alfano, and M. Crisfield, “Finite element interface models for the delamination analysis of laminated composites: mechanical and computational issues,” *International journal for numerical methods in engineering,* vol. 50, no. 7, pp. 1701-1736, 2001.

[82] E. F. Rybicki, and M. F. Kanninen, "A finite element calculation of stress intensity factors by a modified crack closure integral," *Engineering Fracture Mechanics,* vol. 9, no. 4, pp. 931-938, 1977.

[83] I. S. Raju, "Calculation of strain-energy release rates with higher order and singular finite elements," *Engineering Fracture Mechanics,* vol. 28, no. 3, pp. 251-274, 1987.

[84] J. R. Rice, "A Path Independent Integral and the Approximate Analysis of Strain Concentration by Notches and Cracks," *Journal of Applied Mechanics,* vol. 35, no. 2, pp. 379-386, 1968.

[85] M. Gurtin, "On the energy release rate in quasi-static elastic crack propagation," *Journal of Elasticity,* vol. 9, no. 2, pp. 187-195, 1979.

[86] T. K. Hellen, "On the method of virtual crack extensions," *International Journal for Numerical Methods in Engineering,* vol. 9, no. 1, pp. 187-207, 1975.

[87] D. M. Parks, "A stiffness derivative finite element technique for determination of crack tip stress intensity factors," *International Journal of Fracture,* vol. 10, no. 4, pp. 487-502, 1974.

[88] J. Hutchinson, and Z. Suo, "Mixed mode cracking in layered materials," *Advances in applied mechanics,* vol. 29, no. 63, pp. 191, 1992.

[89] D. S. Dugdale, "Yielding of steel sheets containing slits," *Journal of the Mechanics and Physics of Solids,* vol. 8, no. 2, pp. 100-104, 1960.

[90] G. Barenblatt, "The mathematical theory of equilibrium cracks in brittle fracture," *Advances in applied mechanics,* vol. 7, no. 1, pp. 55-129, 1962.

[91] O. Allix, and A. Corigliano, "Modeling and simulation of crack propagation in mixed-modes interlaminar fracture specimens," *International Journal of Fracture,* vol. 77, no. 2, pp. 111-140, 1996.

[92] J. Chaboche, R. Girard, and A. Schaff, "Numerical analysis of composite systems by using interphase/interface models," *Computational Mechanics,* vol. 20, no. 1-2, pp. 3-11, 1997.

[93] M. C. Chen, AJ Kinloch, EP Busso, FL Matthews, Y. Qiu, J, "Predicting progressive delamination of composite material specimens via interface elements," *Mechanics of composite materials and structures,* vol. 6, no. 4, pp. 301-317, 1999.

[94] P. P. Camanho, C. Davila, and M. De Moura, "Numerical simulation of mixed-mode progressive delamination in composite materials," *Journal of composite materials,* vol. 37, no. 16, pp. 1415-1438, 2003.

[95] J. Masters, and K. Reifsnider, "An investigation of cumulative damage development in quasi-isotropic graphite/epoxy laminates," *ASTM STP,* vol. 775, pp. 40-62, 1982.

[96] K. Reifsnider, and R. Jamison, "Fracture of fatigue-loaded composite laminates," *International Journal of Fatigue,* vol. 4, no. 4, pp. 187-197, 1982.

[97] A. L. Highsmith, and K. L. Reifsnider, "Stiffness-reduction mechanisms in composite laminates," *Damage in composite materials, ASTM STP,* vol. 775, pp. 103-117, 1982.

[98] R. Talreja, and C. Veer Singh, *Damage and Failure of Composite Materials*: Cambridge University, 2012.

[99] K. Garrett, and J. Bailey, "The effect of resin failure strain on the tensile properties of glass fibre-reinforced polyester cross-ply laminates," *Journal of Materials Science,* vol. 12, no. 11, pp. 2189-2194, 1977.

[100] A. Parvizi, and J. Bailey, "On multiple transverse cracking in glass fibre epoxy cross-ply laminates," *Journal of Materials Science,* vol. 13, no. 10, pp. 2131-2136, 1978.

[101] A. Parvizi, K. Garrett, and J. Bailey, "Constrained cracking in glass fibre-reinforced epoxy cross-ply laminates," *Journal of Materials Science,* vol. 13, no. 1, pp. 195-201, 1978.

[102] K. Garrett, and J. Bailey, "Multiple transverse fracture in 90 cross-ply laminates of a glass fibre-reinforced polyester," *Journal of materials science,* vol. 12, no. 1, pp. 157-168, 1977.

[103] K. Reifsnider, and A. Talug, "Analysis of fatigue damage in composite laminates," *International Journal of Fatigue,* vol. 2, no. 1, pp. 3-11, 1980.

[104] R. Talreja, "Transverse cracking and stiffness reduction in composite laminates," *Journal of composite materials,* vol. 19, no. 4, pp. 355-375, 1985.

[105] L. Lammerant, and I. Verpoest, "Modelling of the interaction between matrix cracks and delaminations during impact of composite plates," *Composites Science and Technology,* vol. 56, no. 10, pp. 1171-1178, 1996.

[106] A. B. de Morais, M. F. de Moura, A. T. Marques *et al.*, "Mode-I interlaminar fracture of carbon/epoxy cross-ply composites," *Composites Science and Technology,* vol. 62, no. 5, pp. 679-686, 2002.

[107] D. Bruno, F. Greco, and P. Lonetti, "Interaction Between Interlaminar and Intralaminar Damage in Fiber-Reinforced Composite Laminates," *International Journal for Computational Methods in Engineering Science and Mechanics,* vol. 9, no. 6, pp. 358-373, 2008.

[108] V. Azzi, and S. Tsai, "Anisotropic strength of composites," *Experimental Mechanics,* vol. 5, no. 9, pp. 283-288, 1965.

[109] S. W. Tsai, and E. M. Wu, "A general theory of strength for anisotropic materials," *Journal of composite materials,* vol. 5, no. 1, pp. 58-80, 1971.

[110] Z. Hashin, *Fatigue Failure Criteria for Unidirectional Fiber Composites*, DTIC Document, 1980.

[111] J. Chaboche, "Continuum damage mechanics," *J. appl. Mech,* vol. 55, no. 1, pp. 59-64, 1988.

[112] J. L. Chaboche, "Continuum Damage Mechanics: Part II—Damage Growth, Crack Initiation, and Crack Growth," *Journal of Applied Mechanics,* vol. 55, no. 1, pp. 65-72, 1988.

[113] K. Lee, S. Moorthy, and S. Ghosh, "Multiple scale computational model for damage in composite materials," *Computer Methods in Applied Mechanics and Engineering,* vol. 172, no. 1–4, pp. 175-201, 1999.

[114] J. Fish, Q. Yu, and K. Shek, "Computational damage mechanics for composite materials based on mathematical homogenization," *International Journal for Numerical Methods in Engineering,* vol. 45, no. 11, pp. 1657-1679, 1999.

[115] C. Dascalu, G. Bilbie, and E. K. Agiasofitou, "Damage and size effects in elastic solids: A homogenization approach," *International Journal of Solids and Structures,* vol. 45, no. 2, pp. 409-430, 2008.

[116] X. Ren, J.-S. Chen, J. Li *et al.*, "Micro-cracks informed damage models for brittle solids," *International Journal of Solids and Structures,* vol. 48, no. 10, pp. 1560-1571, 2011.

[117] T. Belytschko, and T. Black, "Elastic crack growth in finite elements with minimal remeshing," *International Journal for Numerical Methods in Engineering,* vol. 45, no. 5, pp. 601-620, 1999.

[118] N. Moës, J. Dolbow, and T. Belytschko, "A finite element method for crack growth without remeshing," *Int. J. Numer. Meth. Engng,* vol. 46, pp. 131-150, 1999.

[119] J. Dolbow, N. Moës, and T. Belytschko, "Discontinuous enrichment in finite elements with a partition of unity method," *Finite elements in analysis and design,* vol. 36, no. 3, pp. 235-260, 2000.

[120] C. Daux, N. Moës, J. Dolbow *et al.*, "Arbitrary branched and intersecting cracks with the extended finite element method," *International Journal for Numerical Methods in Engineering,* vol. 48, no. 12, pp. 1741-1760, 2000.

[121] P. Matthew, and K. Nam, "Modeling Failure in Composite Materials with the Extended Finite Element and Level Set Methods," *50th AIAA/ASME/ASCE/AHS/ASC Structures, Structural Dynamics, and Materials Conference*, Structures, Structural Dynamics, and Materials and Co-located Conferences: American Institute of Aeronautics and Astronautics, 2009.

[122] M. Jean, "The non-smooth contact dynamics method," *Computer Methods in Applied Mechanics and Engineering,* vol. 177, no. 3–4, pp. 235-257, 1999.

[123] J. J. Moreau, "Numerical aspects of the sweeping process," *Computer methods in applied mechanics and engineering,* vol. 177, no. 3, pp. 329-349, 1999.

[124] F. Camborde, C. Mariotti, and F. V. Donzé, "Numerical study of rock and concrete behaviour by discrete element modelling," *Computers and Geotechnics,* vol. 27, no. 4, pp. 225-247, 2000.

[125] Z. You, and W. Buttlar, "Discrete element modeling to predict the modulus of asphalt concrete mixtures," *Journal of Materials in Civil Engineering,* vol. 16, no. 2, pp. 140-146, 2004.

[126] X. Li, S. He, Y. Luo *et al.*, "Discrete element modeling of debris avalanche impact on retaining walls," *Journal of Mountain Science,* vol. 7, no. 3, pp. 276-281, 2010.

[127] F. Radjaï, F. Dubois, and J. Wiley, *Discrete-element modeling of granular materials*: ISTE, 2011.

[128] A. Khattab, M. J. Khattak, and I. M. Fadhil, "Micromechanical discrete element modeling of fiber reinforced polymer composites," *Polymer Composites,* vol. 32, no. 10, pp. 1532-1540, 2011.

[129] D. Yang, Y. Sheng, J. Ye *et al.*, "Discrete element modeling of the microbond test of fiber reinforced composite," *Computational Materials Science,* vol. 49, no. 2, pp. 253-259, 2010.

[130] M. J. Khattak, and A. Khattab, "Modeling tensile response of fiber-reinforced polymer composites using discrete element method," *Polymer Composites,* vol. 34, no. 6, pp. 877-886, 2013.

[131] E. Schlangen, and E. J. Garboczi, "Fracture simulations of concrete using lattice models: Computational aspects," *Engineering Fracture Mechanics,* vol. 57, no. 2–3, pp. 319-332, 1997.

[132] A. C. Aydin, A. Arslan, and R. Gül, "Mesoscale simulation of cement based materials' time-dependent behavior," *Computational Materials Science,* vol. 41, no. 1, pp. 20-26, 2007.

[133] X. P. Xu, and A. Needleman, "Numerical simulations of fast crack growth in brittle solids," *Journal of the Mechanics and Physics of Solids,* vol. 42, no. 9, pp. 1397-1434, 1994.

[134] P. H. Geubelle, and J. S. Baylor, "Impact-induced delamination of composites: a 2D simulation," *Composites Part B: Engineering,* vol. 29, no. 5, pp. 589-602, 1998.

[135] M. G. A. Tijssens, B. L. J. Sluys, and E. van der Giessen, "Numerical simulation of quasi-brittle fracture using damaging cohesive surfaces," *European Journal of Mechanics - A/Solids,* vol. 19, no. 5, pp. 761-779, 2000.

[136] A. Turon, C. G. Dávila, P. P. Camanho *et al.*, "An engineering solution for mesh size effects in the simulation of delamination using cohesive zone models," *Engineering Fracture Mechanics,* vol. 74, no. 10, pp. 1665-1682, 2007.

[137] H. D. Espinosa, and P. D. Zavattieri, "A grain level model for the study of failure initiation and evolution in polycrystalline brittle materials. Part I: Theory and numerical implementation," *Mechanics of Materials,* vol. 35, no. 3–6, pp. 333-364, 2003.

[138] V. Tomar, J. Zhai, and M. Zhou, "Bounds for element size in a variable stiffness cohesive finite element model," *International Journal for Numerical Methods in Engineering,* vol. 61, no. 11, pp. 1894-1920, 2004.

[139] N. Blal, L. Daridon, Y. Monerie *et al.*, "Artificial compliance inherent to the intrinsic cohesive zone models: criteria and application to planar meshes," *International Journal of Fracture,* vol. 178, no. 1-2, pp. 71-83, 2012.

[140] G. Pijaudier-Cabot, and Z. P. Bazant, "Nonlocal damage theory," *Journal of Engineering Mechanics,* vol. 113, no. 10, pp. 1512-1533, 1987.

[141] Z. P. Bazant, and F.-B. Lin, "Nonlocal smeared cracking model for concrete fracture," *Journal of structural engineering,* vol. 114, no. 11, pp. 2493-2510, 1988.

[142] M. Jirásek, and T. Zimmermann, "Rotating crack model with transition to scalar damage," *Journal of engineering mechanics,* vol. 124, no. 3, pp. 277-284, 1998.

[143] R. H. J. Peerlings, R. De Borst, B. W. A. M. *et al.*, "Gradient enhanced damage for quasi-brittle materials," *International Journal for Numerical Methods in Engineering,* vol. 39, pp. 3391-3403, 1996.

[144] A. Simone, "Explicit and implicit gradient-enhanced damage models," *Revue européenne de génie civil,* vol. 11, no. 7-8, pp. 1023-1044, 2007.

[145] T. Belytschko, and J. I. Lin, "A three-dimensional impact-penetration algorithm with erosion," *International Journal of Impact Engineering,* vol. 5, no. 1–4, pp. 111-127, 1987.

[146] S. R. Beissel, G. R. Johnson, and C. H. Popelar, “An element-failure algorithm for dynamic crack propagation in general directions,” *Engineering Fracture Mechanics,* vol. 61, no. 3–4, pp. 407-425, 1998.

[147] R. Fan, and J. Fish, “The rs-method for material failure simulations,” *International Journal for Numerical Methods in Engineering,* vol. 73, no. 11, pp. 1607-1623, 2008.

[148] A. Pandolfi, and M. Ortiz, “An eigenerosion approach to brittle fracture,” *International Journal for Numerical Methods in Engineering,* vol. 92, no. 8, pp. 694-714, 2012.

[149] B. Schmidt, F. Fraternali, and M. Ortiz, “Eigenfracture: an eigendeformation approach to variational fracture,” *Multiscale Modeling & Simulation,* vol. 7, no. 3, pp. 1237-1266, 2009.

[150] T. Mura, *Micromechanics of Defects in Solids*: M. Nijhoff, 1987.

[151] S. Nemat-Nasser, and M. Hori, *Micromechanics: overall properties of heterogeneous materials*: Elsevier Amsterdam, 1999.

[152] P. Suquet, "Effective properties of nonlinear composites," *Continuum micromechanics*, P. Suquet, ed., pp. 197-264: Springer-Verlag New York, Inc., 1997.

[153] S. Torquato, *Random heterogeneous materials: microstructure and macroscopic properties*: Springer, 2002.

[154] G. W. Milton, *The theory of composites*: Cambridge University Press, 2002.

[155] R. Hill, “Elastic properties of reinforced solids: some theoretical principles,” *Journal of the Mechanics and Physics of Solids,* vol. 11, no. 5, pp. 357-372, 1963.

[156] Z. Hashin, and S. Shtrikman, “A variational approach to the theory of the elastic behaviour of multiphase materials,” *Journal of the Mechanics and Physics of Solids,* vol. 11, no. 2, pp. 127-140, 1963.

[157] W. J. Drugan, and J. R. Willis, "A micromechanics-based nonlocal constitutive equation and estimates of representative volume element size for elastic composites," *Journal of the Mechanics and Physics of Solids,* vol. 44, no. 4, pp. 497-524, 1996.

[158] M. Ostoja-Starzewski, "Microstructural Randomness Versus Representative Volume Element in Thermomechanics," *Journal of Applied Mechanics,* vol. 69, no. 1, pp. 25-35, 2001.

[159] M. Stroeven, H. Askes, and L. J. Sluys, "Numerical determination of representative volumes for granular materials," *Computer Methods in Applied Mechanics and Engineering,* vol. 193, no. 30–32, pp. 3221-3238, 2004.

[160] P. Evesque, "Fluctuations, correlation and representative elementary Volume (REV) in granular materials," *arXiv preprint cond-mat/0506385*, 2005.

[161] Z. Hashin, "Analysis of Composite Materials—A Survey," *Journal of Applied Mechanics,* vol. 50, no. 3, pp. 481-505, 1983.

[162] S. Graham, and N. Yang, "Representative volumes of materials based on microstructural statistics," *Scripta Materialia,* vol. 48, no. 3, pp. 269-274, 2003.

[163] T. Kanit, S. Forest, I. Galliet *et al.*, "Determination of the size of the representative volume element for random composites: statistical and numerical approach," *International Journal of Solids and Structures,* vol. 40, no. 13–14, pp. 3647-3679, 2003.

[164] K. Terada, M. Hori, T. Kyoya *et al.*, "Simulation of the multi-scale convergence in computational homogenization approaches," *International Journal of Solids and Structures,* vol. 37, no. 16, pp. 2285-2311, 2000.

[165] J. C. Michel, H. Moulinec, and P. Suquet, "Effective properties of composite materials with periodic microstructure: a computational

approach," *Computer Methods in Applied Mechanics and Engineering,* vol. 172, no. 1–4, pp. 109-143, 1999.

[166] Z. F. Khisaeva, and M. Ostoja-Starzewski, "On the Size of RVE in Finite Elasticity of Random Composites," *Journal of Elasticity,* vol. 85, no. 2, pp. 153-173, 2006.

[167] M. Sautter, C. Dietrich, M. H. Poech *et al.*, "Finite element modelling of a transverse-loaded fibre composite effects of section size and net density," *Computational Materials Science,* vol. 1, no. 3, pp. 225-233, 1993.

[168] J. Guedes, and N. Kikuchi, "Preprocessing and postprocessing for materials based on the homogenization method with adaptive finite element methods," *Computer Methods in Applied Mechanics and Engineering,* vol. 83, no. 2, pp. 143-198, 1990.

[169] B. Hassani, and E. Hinton, "A review of homogenization and topology optimization I—homogenization theory for media with periodic structure," *Computers & Structures,* vol. 69, no. 6, pp. 707-717, 1998.

[170] W.-X. Wang, D. Luo, Y. Takao *et al.*, "New solution method for homogenization analysis and its application to the prediction of macroscopic elastic constants of materials with periodic microstructures," *Computers & Structures,* vol. 84, no. 15–16, pp. 991-1001, 2006.

[171] Y. Davit, C. G. Bell, H. M. Byrne *et al.*, "Homogenization via formal multiscale asymptotics and volume averaging: How do the two techniques compare?," *Advances in Water Resources*, no. 0.

[172] E. Weinan, B. Engquist, X. Li *et al.*, "Heterogeneous multiscale methods: a review," *Commun Comput Phys,* vol. 2, no. 3, pp. 367-450, 2007.

[173] F. Feyel, "A multilevel finite element method (FE2) to describe the response of highly non-linear structures using generalized continua,"

Computer Methods in Applied Mechanics and Engineering, vol. 192, no. 28–30, pp. 3233-3244, 2003.

[174] F. Yuan, N. Pagano, and X. Cai, "Elastic moduli of brittle matrix composites with interfacial debonding," *International journal of solids and structures,* vol. 34, no. 2, pp. 177-201, 1997.

[175] P. Bisegna, and R. Luciano, "Bounds on the overall properties of composites with debonded frictionless interfaces," *Mechanics of materials,* vol. 28, no. 1, pp. 23-32, 1998.

[176] H. Teng, "Transverse stiffness properties of unidirectional fiber composites containing debonded fibers," *Composites Part A: Applied Science and Manufacturing,* vol. 38, no. 3, pp. 682-690, 2007.

[177] A. Caporale, R. Luciano, and E. Sacco, "Micromechanical analysis of interfacial debonding in unidirectional fiber-reinforced composites," *Computers & Structures,* vol. 84, no. 31–32, pp. 2200-2211, 2006.

[178] S. A. Wimmer, and D. G. Karr, "Compressive failure of microcracked porous brittle solids," *Mechanics of Materials,* vol. 22, no. 4, pp. 265-277, 1996.

[179] C. Miehe, J. Schröder, and J. Schotte, "Computational homogenization analysis in finite plasticity Simulation of texture development in polycrystalline materials," *Computer Methods in Applied Mechanics and Engineering,* vol. 171, no. 3–4, pp. 387-418, 1999.

[180] T. Y. Hou, and X.-H. Wu, "A multiscale finite element method for elliptic problems in composite materials and porous media," *Journal of computational physics,* vol. 134, no. 1, pp. 169-189, 1997.

[181] K. Matouš, M. G. Kulkarni, and P. H. Geubelle, "Multiscale cohesive failure modeling of heterogeneous adhesives," *Journal of the Mechanics and Physics of Solids,* vol. 56, no. 4, pp. 1511-1533, 2008.

[182] C. Alfaro, A. Suiker, C. Verhoosel *et al.*, "Numerical homogenization of cracking processes in thin fibre-epoxy layers," *European Journal of Mechanics-A/Solids,* vol. 29, no. 2, pp. 119-131, 2010.

[183] C. V. Verhoosel, J. J. Remmers, M. A. Gutiérrez *et al.*, "Computational homogenization for adhesive and cohesive failure in quasi-brittle solids," *International Journal for Numerical Methods in Engineering,* vol. 83, no. 8-9, pp. 1155-1179, 2010.

[184] V. P. Nguyen, O. Lloberas-Valls, M. Stroeven *et al.*, "Homogenization-based multiscale crack modelling: From micro-diffusive damage to macro-cracks," *Computer Methods in Applied Mechanics and Engineering,* vol. 200, no. 9–12, pp. 1220-1236, 2011.

[185] T. J. Massart, R. H. J. Peerlings, and M. G. D. Geers, "An enhanced multi-scale approach for masonry wall computations with localization of damage," *International Journal for Numerical Methods in Engineering,* vol. 69, no. 5, pp. 1022-1059, 2007.

[186] F. V. Souza, and D. H. Allen, "Multiscale modeling of impact on heterogeneous viscoelastic solids containing evolving microcracks," *International Journal for Numerical Methods in Engineering,* vol. 82, no. 4, pp. 464-504, 2010.

[187] V. P. Nguyen, M. Stroeven, and L. J. Sluys, "An enhanced continuous–discontinuous multiscale method for modeling mode-I cohesive failure in random heterogeneous quasi-brittle materials," *Engineering Fracture Mechanics,* vol. 79, no. 0, pp. 78-102, 2012.

[188] F. F. Abraham, J. Q. Broughton, N. Bernstein *et al.*, "Spanning the continuum to quantum length scales in a dynamic simulation of brittle fracture," *EPL (Europhysics Letters),* vol. 44, no. 6, pp. 783, 1998.

[189] E. B. Tadmor, M. Ortiz, and R. Phillips, "Quasicontinuum analysis of defects in solids," *Philosophical Magazine A,* vol. 73, no. 6, pp. 1529-1563, 1996.

[190] G. J. Wagner, and W. K. Liu, “Coupling of atomistic and continuum simulations using a bridging scale decomposition,” *Journal of Computational Physics,* vol. 190, no. 1, pp. 249-274, 2003.

[191] S. P. Xiao, and T. Belytschko, “A bridging domain method for coupling continua with molecular dynamics,” *Computer Methods in Applied Mechanics and Engineering,* vol. 193, no. 17–20, pp. 1645-1669, 2004.

[192] C. Bernardi, Y. Maday, and A. T. Patera, "Domain Decomposition by the Mortar Element Method," *Asymptotic and Numerical Methods for Partial Differential Equations with Critical Parameters*, NATO ASI Series H. Kaper, M. Garbey and G. Pieper, eds., pp. 269-286: Springer Netherlands, 1993.

[193] R. Hill, “On constitutive macro-variables for heterogeneous solids at finite strain,” *Proceedings of the Royal Society of London. A. Mathematical and Physical Sciences,* vol. 326, no. 1565, pp. 131-147, 1972.

[194] S. J. Hollister, and N. Kikuchi, “A comparison of homogenization and standard mechanics analyses for periodic porous composites,” *Computational Mechanics,* vol. 10, no. 2, pp. 73-95, 1992.

[195] L. Ye, “Role of matrix resin in delamination onset and growth in composite laminates,” *Composites science and technology,* vol. 33, no. 4, pp. 257-277, 1988.

[196] D. Taylor, “The theory of critical distances,” *Engineering Fracture Mechanics,* vol. 75, no. 7, pp. 1696-1705, 2008.

[197] Z. P. Bazant, and J. Planas, *Fracture and Size Effect in Concrete and Other Quasibrittle Materials*: Taylor & Francis, 1997.

[198] H. Azadi, and A. Khoei, “Numerical simulation of multiple crack growth in brittle materials with adaptive remeshing,” *International journal for numerical methods in engineering,* vol. 85, no. 8, pp. 1017-1048, 2011.

[199] M. L. Williams, “The stresses around a fault or crack in dissimilar media,” *Bulletin of the Seismological Society of America,* vol. 49, no. 2, pp. 199-204, 1959.

[200] J. R. Rice, and G. C. Sih, “Plane Problems of Cracks in Dissimilar Media,” *Journal of Applied Mechanics,* vol. 32, no. 2, pp. 418-423, 1965.

[201] M. Comninou, “The Interface Crack,” *Journal of Applied Mechanics,* vol. 44, no. 4, pp. 631-636, 1977.

[202] J. Rice, “Elastic fracture mechanics concepts for interfacial cracks,” *J. Appl. Mech.(Trans. ASME),* vol. 55, no. 1, pp. 98-103, 1988.

[203] B. Malyshev, and R. Salganik, “The strength of adhesive joints using the theory of cracks,” *International Journal of Fracture Mechanics,* vol. 1, no. 2, pp. 114-128, 1965.

[204] C. H. Wu, “Maximum-energy-release-rate criterion applied to a tension-compression specimen with crack,” *Journal of Elasticity,* vol. 8, no. 3, pp. 235-257, 1978.

[205] COMSOL-AB, “Comsol Multiphysics, Reference Manual,” 2013.

[206] N. Pagano, and F. Yuan, “The significance of effective modulus theory (homogenization) in composite laminate mechanics,” *Composites science and technology,* vol. 60, no. 12, pp. 2471-2488, 2000.

[207] A. M. Amini, D. Dureisseix, and P. Cartraud, “Multi-scale domain decomposition method for large-scale structural analysis with a zooming technique: Application to plate assembly,” *International Journal for Numerical Methods in Engineering,* vol. 79, no. 4, pp. 417-443, 2009.

[208] O. Lloberas-Valls, D. J. Rixen, A. Simone *et al.*, “On micro-to-macro connections in domain decomposition multiscale methods,” *Computer Methods in Applied Mechanics and Engineering,* vol. 225–228, no. 0, pp. 177-196, 2012.

[209] C. Farhat, and F. X. Roux, "A method of finite element tearing and interconnecting and its parallel solution algorithm," *International Journal for Numerical Methods in Engineering,* vol. 32, no. 6, pp. 1205-1227, 1991.

[210] F. B. Belgacem, "The Mortar finite element method with Lagrange multipliers," *Numerische Mathematik,* vol. 84, no. 2, pp. 173-197, 1999.

[211] M. Bäker, "Simulation of crack propagation in mixed mode and at bimaterial interfaces using trial cracks," *Computational Materials Science,* vol. 45, no. 3, pp. 680-683, 2009.

[212] J. Donea, A. Huerta, J. P. Ponthot *et al.*, "Arbitrary Lagrangian–Eulerian methods," *Encyclopedia of computational mechanics*, 2004.

[213] E. Martin, D. Leguillon, and C. Lacroix, "A revisited criterion for crack deflection at an interface in a brittle bimaterial," *Composites Science and Technology,* vol. 61, no. 12, pp. 1671-1679, 2001.

[214] K. Kaddouri, M. Belhouari, B. B. Bouiadjra *et al.*, "Finite element analysis of crack perpendicular to bi-material interface: Case of couple ceramic–metal," *Computational Materials Science,* vol. 35, no. 1, pp. 53-60, 2006.

[215] J. Fish, and A. Wagiman, "Multiscale finite element method for a locally nonperiodic heterogeneous medium," *Computational Mechanics,* vol. 12, no. 3, pp. 164-180, 1993.